

universität ulm

Institute of Pharmaceutical Biotechnology

Multi-layered characterization of the tRNA methyltransferase TRMT2A and its therapeutic potential for polyQ diseases

Dissertation to obtain the degree
Dr. rer. nat.
of the Faculty of Natural Sciences
of the University of Ulm

Submitted by
Monika Barbara Witzenberger from Augsburg

2021

Faculty of Natural Sciences

Ulm University

Dean of Faculty: Prof. Dr. Thorsten Bernhardt

First reviewer: Prof. Dr. Dierk Niessing

Second reviewer: Prof. Dr. Nils Johnsson

First additional reviewer: Prof. Dr. Anita Marchfelder

Second additional reviewer: Prof. Dr. Bernhard Eikmanns

Day of oral examination: 17.02.2022

“Nothing in life is to be feared, it is only to be understood.
Now is the time to understand more, so that we may fear less.”

Marie Skłodowska Curie

Table of Contents

Abstract 1

Zusammenfassung 2

1. Introduction 3

1.1. Rise of epitranscriptomics 3
1.1.1 RNA modifications 3
1.1.2 tRNA modifications 5
1.1.3 RNA modifications as drug target 7

1.2 The family of m^5U tRNA methyltransferases 9
1.2.1 Structure of TrmA and related methyltransferases 9
1.2.2 Functional characterization of TrmA and its homologs 11
1.2.3 Additional functions of TrmA and its homologs 13

1.3 PolyQ diseases 16
1.3.1 The polyQ disease family 16
1.3.2 Huntington's disease 16
1.3.3 Treatment strategies for polyQ diseases including Huntington's disease 19

1.4 TRMT2A as polyQ disease modifier 21

1.5 Objectives of this thesis 23

2. Materials and methods 25

2.1. Chemicals and materials 25
2.1.1 Chemicals 25
2.1.2 Buffers for molecular biology and protein biochemistry 27
2.1.3 Enzymes and kits 28
2.1.4 Media and supplements 29
2.1.5 Oligonucleotides 30
2.1.6 RNA 34
2.1.7 Plasmids 35
2.1.8 Bacterial strains, mammalian and insect cell lines 38

2.2 Molecular biology 40
2.2.1 Transformation of chemically competent *E. coli* 40
2.2.2 Small-scale DNA amplification 40
2.2.3 Large-scale DNA amplification 40
2.2.4 Molecular cloning 41

2.3 Protein purification 43
2.3.1 Small-scale protein expression screen 43
2.3.2 Protein expression in *E. coli* 43
2.3.3 Protein expression in insect cells 44
2.3.4 Cell lysis 44
2.3.5 Purification of hTRMT2A RBD and *dm*TRMT2A RBD 45
2.3.6 Purification of SUMO-tagged hTRMT2A, *dm*TRMT2A and *ct*Trm2 domains 46
2.3.7 Purification of GST-tagged hTRMT2A globular domain and *ct*Trm2 FL 48
2.3.8 Purification of the catalytic domain of GST-tagged hTGS1 48

2.4 Protein biochemistry 49
2.4.1 Determination of protein concentration 49
2.4.2 Gel electrophoresis 49
2.4.3 Analytical limited proteolysis 50
2.4.4 Methyltransferase assay 50

2.5 RNA work 53

2.5.1 Small-scale *in vitro* transcription 53
2.5.2 Large-scale *in vitro* transcription 53
2.5.3 Mouse liver tRNA purification using ion-exchange chromatography 54
2.5.4 Isotopic labeling of RNA 54
2.5.5 Electrophoretic mobility shift assay (EMSA) 55
2.5.6 3' end biotinylation of RNA 55

2.6 Biochemical/-physical experiments *56*
2.6.1 Thermofluor assay 56
2.6.2 Right angle light scattering (RALS) 56
2.6.3 Surface plasmon resonance (SPR) 56
2.6.4 Western blot 57
2.6.5 Proximity-dependent biotinylation (BioID) 58
2.6.6 Co-immunoprecipitation (Co-IP) 59
2.6.7 Mass spectrometry and crosslinking 60

2.7 Structural biology *62*
2.7.1 Crystallization screens and optimization of crystals 62
2.7.2 Crystal soaking 63
2.7.3 *In situ* proteolysis 63
2.7.4 Data collection and solving X-ray structures 63
2.7.5 Visualization of X-ray structures 64

2.8 Cell culture *65*
2.8.1 Culturing of HEK cells and cryopreservation 65
2.8.2 Generation of stably transfected cell lines 65
2.8.3 Fluorescence-activated cell sorting (FACS) 66
2.8.4 Immunocytochemistry and fluorescence microscopy 66

2.9. Bioinformatics tools *68*
2.9.1 Statistical analysis with R 68
2.9.2 Michaelis Menten fitting with R 68
2.9.3 GO-term analysis 68
2.9.4 Data processing for BioID and Co-IP mass spectrometry results 69

3. Results 71

3.1 Structure determination of TRMT2A *71*
3.1.1 Expression and purification of hTRMT2A proteins 71
3.1.2 Expression and purification of hTRMT2A FL from insect cells 73
3.1.3 Expression and purification of *dm*TRMT2A proteins 74
3.1.4 Expression and purification *ct*Trm2 proteins 77
3.1.5 Crystal structure of hTRMT2A RBD 78
3.1.6 Crystal structure of *dm*TRMT2A RBD 79
3.1.7 Stability of hTRMT2A proteins 80

3.2 Identification of small inhibitory molecules of hTRMT2A *82*
3.2.1 Co-crystallization and soaking of hTRMT2A RBD with small molecules 82
3.2.2 Small molecules bind to TRMT2A RBD 83
3.2.3 Establishment of an assay to determine hTRMT2A FL inhibition 84
3.2.4 Small molecules reduce catalytic activity of hTRMT2A *in vitro* 86
3.2.5 A small molecule hTRMT2A inhibitor reduces polyQ aggregation in cells 88
3.2.6 Indirect testing of m^5U levels from different cellular sources 88

3.3 RNA binding and methylation by hTRMT2A *91*
3.3.1 RNA binding by hTRMT2A 91
3.3.2 Enzymatic activity of hTRMT2A 93
3.3.3 tRNA binding by hTRMT2A involves multiple domains 94
3.3.4 tRNA binding by hTRMT2A involves amino acids from all domains 95
3.3.5 A model of hTRMT2A and $tRNA^{Gln}$ binding 97

3.4 Interactome of hTRMT2A *99*
3.4.1 Impaired RNA binding hTRMT2A mutant 99
3.4.2 BioID identifies the hTRMT2A proximity interactome 101

3.4.3 Co-IP identifies hTRMT2A interacting proteins ... 103
3.4.4 hTRMT2A localizes to the nucleus ... 107

4. Discussion ... 108

4.1 Purification and crystallization of hTRMT2A and its homologs ... 108
4.1.1 Predicted RNA recognition mode of hTRMT2A RBD and *dm*TRMT2A RBD ... 108
4.1.2 Future directions for solving the TRMT2A structure ... 109
4.1.3 The AlphaFold homology model of hTRMT2A ... 111

4.2 Hybrid model of hTRMT2A and tRNA gives insights into RNA recognition ... 112
4.2.1 Crosslinking and mass spectrometry reveals the hTRMT2A-tRNA^{Gln} binding interface to single amino acid resolution ... 112
4.2.2 The hybrid model ... 113
4.2.3 hTRMT2A is potentially a tRNA chaperone ... 114

4.3 hTRMT2A is potentially a multi-substrate RNA methyltransferase ... 115
4.3.1 hTRMT2A FL binds preferentially tRNA ... 115
4.3.2 U54 in tRNA is the major parameter for methylation by hTRMT2A FL ... 116
4.3.3 Multisubstrate recognition by hTRMT2A ... 116
4.3.4 RNA binding ability of hTRMT2A FL is robust towards mutations ... 117
4.3.5 Oligomerization status of hTRMT2A FL ... 118

4.4 The hTRMT2A interactome suggests different functions ... 119
4.4.1 Strengths and limitations of BioID and Co-IP ... 119
4.4.2 High confidence protein interaction partners of hTRMT2A ... 120
4.4.3 hTRMT2A associates with several nuclear processes ... 126

4.5 hTRMT2A associates with polyQ disease pathology ... 127
4.5.1 Hypothesis for hTRMT2A silencing phenotype in a polyQ disease model ... 127
4.5.2 hTRMT2A as potential drug ... 128
4.5.3 hTRMT2A drug discovery campaign using *in silico* methods ... 128

4.6 Conclusion ... 130

5. Supplementary Data ... 132

Supplementary Figures ... 132

Supplementary Tables ... 143

6. Appendix ... 159

List of Abbreviations ... 159

Figure Index ... 160

Table Index ... 162

7. References ... 164

Acknowledgements ... 184

Abstract

The tRNA methyltransferase 2 homolog A (TRMT2A) is the dedicated enzyme for methylation of uridine 54 in transfer-RNA (tRNA). Human TRMT2A has also been described as modifier of polyglutamine- (polyQ-) derived neuronal toxicity. Corresponding human polyQ pathologies include Huntington's disease and constitute a family of devastating neurodegenerative diseases. A polyQ tract in the corresponding disease-linked protein causes neuronal death and symptoms like impaired motor function, as well as cognitive impairment. In polyQ-disease models, silencing of TRMT2A reduced polyQ-associated cell death and polyQ-protein aggregation, suggesting this protein to be a valid drug target against this class of disorders.

As human TRMT2A is underexplored, the first aim of this thesis was to characterize the basic principles of RNA binding and enzymatic activity. To do so, *in vitro* binding and methylation assays were employed that showed a preference for tRNA and stem-loop RNA structures. These RNA structures in combination with an uracil in the sterically correct position allowed for selective methylation of RNA. Moreover, crucial residues of TRMT2A for catalytic activity and RNA binding were identified and allowed for the rational generation of a mutant with abolished enzymatic activity. These data were also used to create a hybrid model of the tRNA-TRMT2A binding interface. To explore the potential impact of human TRMT2A on polyQ diseases, structure-based drug discovery was established with the X-ray structure of the RNA binding domain of TRMT2A, resulting in the identification of spermidine as TRMT2A inhibitor. For insights into the protein interactome of human TRMT2A, proximity-dependent biotinylation and co-immunoprecipitation were employed. Several associated pathways were identified, which are likely to aid in understanding the biological function of human TRMT2A considerably.

Results from this thesis provide a basis for comprehending the molecular and cellular function of the underexplored human enzyme TRMT2A and will help to leverage its potential as drug target against polyQ diseases.

Zusammenfassung

tRNA-Methyltransferase 2 Homolog A (TRMT2A) ist das Enzym für die Methylierung von Uridin 54 in Transfer-RNA (tRNA). Humanes TRMT2A wurde als Modifikator neuronaler Toxizität beschrieben, welche durch Polyglutamin (PolyQ) verursacht wird. Zu den entsprechenden humanen PolyQ-Pathologien, eine Familie verheerender neurodegenerativer Erkrankungen, gehört Chorea Huntington. Ein PolyQ-Trakt im krankheitszugehörigen Protein führt zum Absterben von Nervenzellen und zu Symptomen wie eingeschränkter Motorik und kognitiver Beeinträchtigung. In Modellen für PolyQ-Krankheiten reduzierte das Ausschalten von TRMT2A den PolyQ-assoziierten Zelltod und die PolyQ-Protein-Aggregation. Dies deutet darauf hin, dass TRMT2A ein valider Angriffspunkt für Wirkstoffe gegen PolyQ-Pathologien sein könnte.

Da das humane TRMT2A noch nicht ausreichend erforscht ist, bestand das primäre Ziel dieser Arbeit darin, die grundlegenden Prinzipien der RNA-Bindung und der enzymatischen Aktivität von TRMT2A zu charakterisieren. Zu diesem Zweck wurden *in vitro* Bindungs- und Methylierungsassays durchgeführt, die eine Präferenz für tRNA- und Stem-Loop RNA-Strukturen zeigten. Diese RNA-Strukturen in Kombination mit einem Uracil an der sterisch korrekten Position ermöglichten eine selektive Methylierung der RNA. Darüber hinaus wurden entscheidende TRMT2A Aminosäuren für die katalytische Aktivität und die RNA-Bindung identifiziert und ermöglichten die rationale Erzeugung einer Mutante mit abgeschwächter enzymatischer Aktivität. Diese Daten wurden auch zur Erstellung eines Hybridmodells des tRNA-TRMT2A-Interfaces verwendet. Um die potenziellen Auswirkungen von humanem TRMT2A auf PolyQ-Erkrankungen zu erforschen, wurde strukturbasierte Wirkstoffforschung mit der dreidimensionalen Struktur der RNA-Bindedomäne von TRMT2A durchgeführt, was zur Identifizierung von Spermidin als TRMT2A Inhibitor führte. Um Einblicke in das Proteininteraktom von humanem TRMT2A zu erhalten, wurden die Techniken der nähen-abhängige Biotinylierung und Co-Immunpräzipitation eingesetzt. Es wurden mehrere assoziierte Signalwege identifiziert, die unser Verständnis der biologischen Funktion von TRMT2A aller Voraussicht nach erheblich verbessern werden.

Die Ergebnisse dieser Arbeit bilden eine Grundlage für das Verständnis der molekularen und zellulären Funktion des bisher wenig erforschten humanen Enzyms TRMT2A und werden dazu beitragen, sein Potenzial als Wirkstoffziel für Medikamente gegen PolyQ-Krankheiten auszuschöpfen.

1. Introduction

1.1. Rise of epitranscriptomics

Similar to DNA and protein, RNA is post-transcriptionally modified with more than 170 different types of modifications installed by a multitude of enzymes (Boccaletto et al., 2018). The most heavily modified RNA species is transfer RNA (tRNA, discussed in **1.1.2**). Other frequently modified RNA species are ribosomal RNA (rRNA), messenger RNA (mRNA) and several non-coding RNA (ncRNA). Recently, the realization emerged that RNA modifications functionally affect a variety of cellular processes such as translation or transcription and thus provide an additional layer of gene regulation. Disruption of the dedicated enzymes for RNA modifications often causes disease, which underlines their physiological importance (Jonkhout et al., 2017; Boo and Kim, 2020; Shi et al., 2020).

Historically, the first RNA modification was discovered in the late 1950s, however, for decades was classified as functionally irrelevant. In 2008, a study showed that the depletion of an RNA m^6A methyltransferase, wich transfers a methylgroup to adenosine, induces growth defects in plants (Zhong et al., 2008). The additional identification of a human m^6A demethylase suggested a reversible, modification-based RNA control system with methyltransferases and demethylases, similar to the well-studied epigenome (Jia et al., 2011). First transcriptome-wide maps of the m^6A modification reiterated the functional importance of m^6A for development and differentiation (Dominissini et al., 2012; Meyer et al., 2012). These findings revived the interest in the field and coined the term “epitranscriptomics”. More recent technology advancements provided single nucleotide modification maps for several RNA modifications (m^1A, m^5C, m^7G, pseudouridine ψ), which allowed correlating them with cellular functions (Khoddami and Cairns, 2013; Carlile et al., 2014; Safra et al., 2017b; Lin et al., 2019).

1.1.1 RNA modifications

Here, the five most frequent RNA modifications are reviewed briefly and visualized in **Figure 1.** RNA modification enzymes, the “writers”, install RNA modifications. For some modification types the epitranscriptomic mark can be reversed by “eraser” protein such as demethylases. Moreover, “reader” proteins read-out modification status and connect it to downstream processes. The best-studied mRNA modification in terms of writer, reader and eraser proteins is methylation of adenosine at position 6, m^6A. m^6A is predominantly found around the stop codon, the coding region and the 5’ untranslated region (UTR) of mRNA, but also in rRNA and primary-microRNA (pri-miRNA). An enzymatic complex or stand-alone enzymes can install m^6A on RNA (Liu et al., 2014; Pendleton et al., 2017; Ma et al., 2019;

van Tran et al., 2019). The m^6A mark can be erased by two different RNA demethylases (Zheng et al., 2013) and reader proteins connect m^6A modification status for example to mRNA translation (Wang et al., 2015).

Generally, RNA modifications can be subdivided into constitutive and dynamic modifications. Constitutive modifications are installed on all RNA targets and are generally more widespread in tRNA, rRNA and snRNA (small nuclear RNA). Dynamic modifications are deposited on mostly mRNA upon certain external stimuli. Depending on the target RNA, the same modification can be dynamic and constitutive. One example is pseudouridine (ψ), the most abundant modification in human total RNA. Constitutively, ψ is installed on position 34 and 55 of tRNA and on 95 different positions of rRNA (Sloan et al., 2017). However, ψ is also placed dynamically on mRNA stem-loop structures (Rintala-Dempsey and Kothe, 2017). Another well understood constitutive modification on mRNA is 7-methylguanosine (m^7G) on the mRNA cap structure, which protects mRNA from degradation and initiates cap-dependent protein synthesis. Dynamically, m^7G it is also found in rRNA, tRNA, and to a certain extent internally in the 5' UTR of mRNA (Alexandrov et al., 2002; Haag et al., 2015; Malbec et al., 2019).

RNA modification enzymes require a specific three-dimensional structure and/or sequence motif to recognize their target RNA. Interestingly, some modification enzymes modify the same structure on different RNA species. Representative are some members of the NSUN enzyme family, which methylate position 5 of cytidines (m^5C). Usually, tRNA and other ncRNA are recognized and modified due to their specific structures, although m^5C can also be installed on an mRNA motif that resembles the substrate tRNA sequence and structure (Yang et al., 2017; Bohnsack et al., 2019).

Another aspect of RNA modifications regards their dedicated enzymes, which can be either standalone enzymes or enzymatic complexes formed out of a homodimers, heterodimers or several different proteins. The modular build up of the enzymatic machinery can guide specificity as reported for methylation at position 1 of adenosines (m^1A). m^1A has been studied most detailed in tRNA, where m^1A is deposited on tRNA position 9 by a stand-alone enzyme and on tRNA positions 14 and 58 by an enzymatic complex. Yet other enzymes install m^1A on rRNA and mRNA (Chujo and Suzuki, 2012; Liu et al., 2016; Sloan et al., 2017; Vilardo et al., 2020).

Attributing function to mRNA modifications is not trivial since respective tools to interrogate with modifications have only been developed recently. Nevertheless, the notion gains momentum that mRNA modifications affect mRNA turnover processes such as mRNA splicing, stability, degradation, and translation. Moreover, RNA modifications can change the mRNA secondary structure and thus provide new platforms for RNA-protein interactions that in turn can mediate downstream cellular processes (Lewis et al., 2017). In the nucleus, for

example, m^5C modification of mRNA serves as signal for mRNA maturity and is required for nuclear export (Yang et al., 2017). In contrast, the role of tRNA and rRNA modifications has been understood already in greater detail. Modifications of rRNA, either guided by small nucleolar RNA (snoRNA) or added by enzymes, stabilize the ribosome structure, but can also cluster around functional important sites like the peptidyltransferase center or the decoding site to influence protein synthesis. For example, pseudouridylation of certain rRNA positions is crucial for ribosome assembly itself. Also, a particular m^5C rRNA modification contributes to readthrough at stop codons (Schosserer et al., 2015). Furthermore, rRNA-modification patterns change in response to environmental stimuli and thus seem to be a source of flexible, rapid adaptation of the ribosomes and the translational machinery (Sloan et al., 2017). In the following paragraph tRNA modifications are discussed in greater detail.

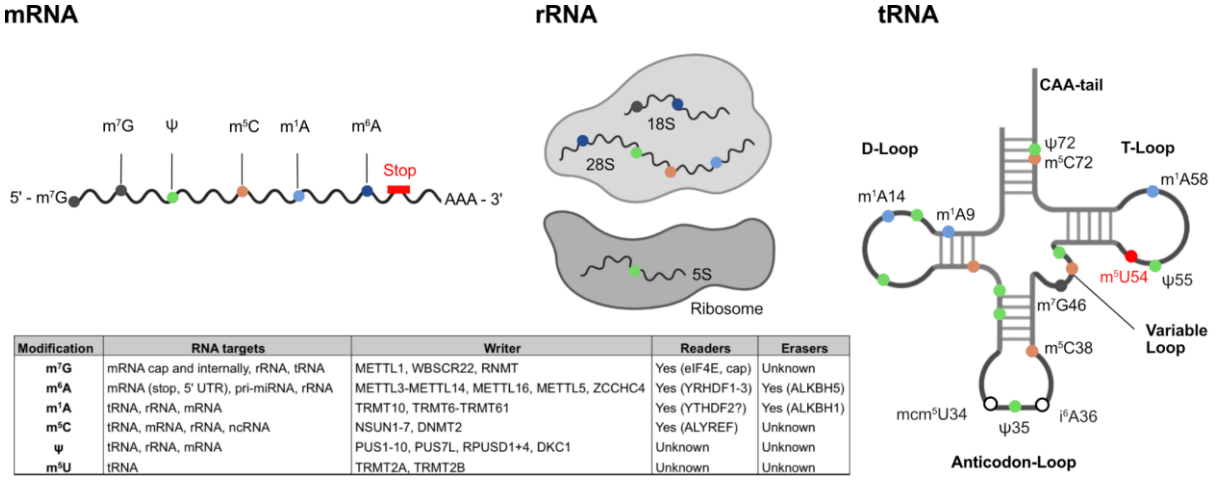

Modification	RNA targets	Writer	Readers	Erasers
m^7G	mRNA cap and internally, rRNA, tRNA	METTL1, WBSCR22, RNMT	Yes (eIF4E, cap)	Unknown
m^6A	mRNA (stop, 5' UTR), pri-miRNA, rRNA	METTL3-METTL14, METTL16, METTL5, ZCCHC4	Yes (YRHDF1-3)	Yes (ALKBH5)
m^1A	tRNA, rRNA, mRNA	TRMT10, TRMT6-TRMT61	Yes (YTHDF2?)	Yes (ALKBH1)
m^5C	tRNA, mRNA, rRNA, ncRNA	NSUN1-7, DNMT2	Yes (ALYREF)	Unknown
Ψ	tRNA, rRNA, mRNA	PUS1-10, PUS7L, RPUSD1+4, DKC1	Unknown	Unknown
m^5U	tRNA	TRMT2A, TRMT2B	Unknown	Unknown

Figure 1 – RNA modifications.
Occurrence of the most common RNA modifications m^7G (dark grey), Ψ (green), m^5C (orange), m^1A (light blue), m^6A (dark blue), and the less abundant modification m^5U (red). Representative modifications of mRNA are visualized on the left, of rRNA in the middle and of tRNA on the right. The clover-leaf structure of tRNA with its T-loop, D-loop, Anticodon-Loop, Variable Loop and CAA-tail is indicated. Of note, selection was restricted to these RNA species and modification types, but does not show a complete picture of the epitranscriptome (Barbieri and Kouzarides, 2020).

1.1.2 tRNA modifications

1.1.2.1 tRNA maturation pathway

tRNA is a 76-86 nucleotide containing, highly structured RNA species that connects the mRNA-coded genetic information with the amino acid code. In the human genome, 423 Polymerase-III (Pol-III) dependent tRNA genes were identified, half of which are actively transcribed, resulting in 32 tRNA with different isoforms (Chan and Lowe, 2009). The biogenesis of tRNA starts after the transcription of precursor-tRNA (pre-tRNA; **Figure 2**). Transcripts undergo several maturation steps that include removal of 3' and 5' trailer sequences by ribonucleases (RNAse), intron splicing by tRNA splicing endonucleases (TSEN) and the enzymatic addition of the amino-acid accepting 3' CAA-tail. During these early maturation steps that occur in the nucleolus, protein cofactors are recruited, such as

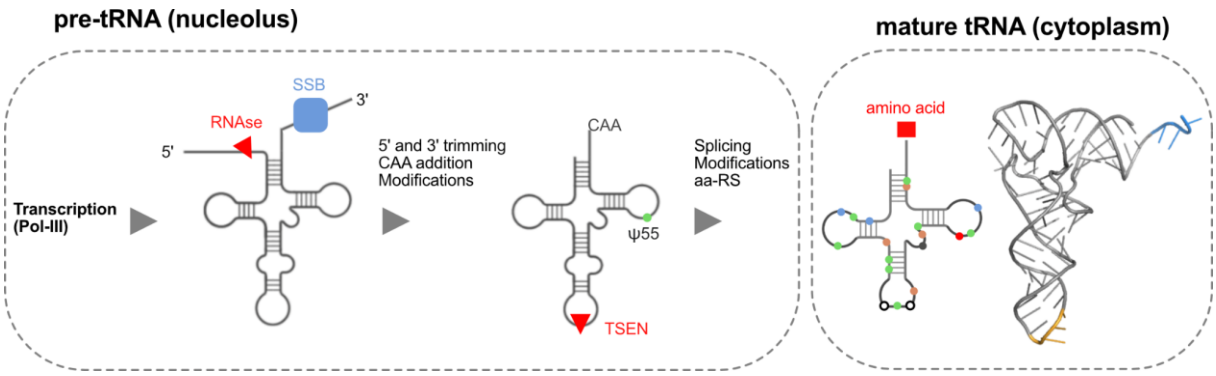

Figure 2 – tRNA biogenesis pathway.
Maturation of Pol-III dependent human tRNA from pre-tRNA in the nucleolus to mature tRNA in the cytoplasm. First step involves recruitment of RNAses for 3' and 5' trimming and of chaperoning cofactors like SSB. Then, initial modifications are installed, for example ψ55, and the CAA-tail is added. Next, the intron in the Anticodon-Loop is removed by TSEN enzymes. Finally, the tRNA is exported to the cytoplasm, further modified and aminoacylated. Mature tRNA is folded into the respective L-shape as exemplified with an experimental tRNA structure (PDB: 4TRA, blue = CAA tail, orange = Anticodon-Loop, D/T-loop = elbow region).

the Lupus La protein (SSB), which protects the 3' end from exonucleolytic degradation. Moreover, post-transcriptional chemical modifications are installed with an average of 10-20 % of tRNA nucleotides beeing modified in the mature tRNA (Jühling et al., 2009). The modifications are partially catalyzed in the nucleolus, such as constitutive pseudouridylation at position 55. Once the tRNA is exported to the cytoplasm various tRNA modification enzymes install additional modifications. Upon correct maturation tRNA folds into its functional L-shape, where D- and T-loop form tertiary interactions and is loaded with respective amino acids (Vakiloroayaei et al., 2017; Chatterjee et al., 2018; Hayne et al., 2020).

1.1.2.2 Different tRNA modifications and their roles in the cell

In human cytosolic tRNA 37 different modifications were identified. Mitochondrial tRNA (mt-tRNA) possess only 18 modifications due to the minimal mitochondrial modification machinery. The most frequent modifications are simple nucleotide methylation (m^2G, m^7G, m^5C, m^1A, m^5U), nucleotide isomerization (ψ), nucleotide reduction (dihydrouridine, D) and nucleotide thiolation (s^4U). Also, more complex modification types usually involving several enzymatic steps are found in tRNA (mcm^5U, t^6A). Hotspots of modifications are the Anticodon-Loop at position 32, 34 and 37, the T-loop at position 54 and 55, as well as the D-loop at position 16 and 20 (**Figure 1**). Modifications in the Anticodon-Loop affect correct codon recognition, reading frame maintenance and translational dynamics. Especially, the 30 different modifications of the wobble position 34 can change codon recognition and translational fidelity (Nedialkova and Leidel, 2015; Rozov et al., 2016). Lack of modification on position 37 has been shown to reduce binding of the tRNA by its cognate aminoacyl-tRNA synthetase (aaRS) and thus the correct amino acid charging is impaired (Niimi et al., 1994).

Modifications in the D- and T-loop mainly impact tRNA stability, its three-dimensional structure and binding affinity to the ribosome (Suzuki, 2021).

The importance of tRNA modifications is reiterated by the fact that hypomodified tRNA is aminoacylated less efficiently and often degraded early by 5'-3' exonucleases via the rapid tRNA decay, a nuclear surveillance system (Pütz et al., 1994; Alexandrov et al., 2006).

Hypomodified tRNA, however, can also be the reservoir for a recently discovered class of RNA molecules, the tRNA derived fragments (tRFs). For instance, under stress conditions tRNA becomes m^5U54 hypomodified and thus is cleaved by angiogenin into tRFs with still unknown functions (Pereira et al., 2021). Generally, tRFs possess regulatory functions in various processes such as apoptosis or cell cycle control (Xie et al., 2020).

The tRF findings by Pereira and colleagues raises another important role of tRNA modifications, namely, linking environmental stimuli to protein expression. Due to a long half-life of the stable tRNA of about 100 hours, tRNA turnover is rather slow (Choe and Taylor, 1972). However, instalment of modifications enables the dynamic and fast adaptation of tRNA function. For example, $tRNA^{Leu}$-specific m^5C modification in response to stress increases the translation of stress response genes (Chan et al., 2012).

1.1.2.3 Specificity of tRNA modification enzymes

As already mentioned in **1.1.1,** tRNA modification enzymes must be able to specifically modify their target tRNA over other closely related tRNA species. Determinants of specificity for substrate tRNA recognition are RNA sequence, the local structural domain and the overall tRNA fold. Interestingly, some tRNA modification enzymes also install the same modification on other RNA at structural or sequence elements that resemble the tRNA substrate. For instance, pseudouridylation has been reported to be installed on one type of mRNA (Sibert and Patton, 2011; Safra et al., 2017a). This indicates that certain tRNA modification enzymes act not only on tRNA, but on multiple RNA substrates.

1.1.3 RNA modifications as drug target

Mutations in RNA modification enzymes, but also their overexpression have been linked to human diseases. Some mitochondrial diseases are also called encephalomyopathies due to the specific symptoms in patients involving brain and muscles. This disease group can be caused for instance by mutations in RNA modification enzymes. Missense mutations in the pseudouridine synthase PUS1 and resulting hypomodification of mt-tRNA is found in patients with MLSA, myopathy, lactic acidosis and sideroblastic anaemia (Bykhovskaya et al., 2004). Moreover, several methyltransferase mutations, such as in the RNA methyltransferases TRMT1 and FTSJ1 were identified in patients with intellectual disability (Li et al., 2020; Zhang et al., 2020). Recent studies also established a clear association between altered

RNA modification enzymes and cancer, as RNA methyltransferases NSUN2, METTL3 and TRMT2A were found to be overexpressed in various cancer types. In further detail, the m^6A methyltransferase METTL3 is highly expressed in acute myeloid leukemia (AML). This overexpression increases the translation of certain oncogenic mRNA targets like MYC, thus driving tumorigenesis (Barbieri et al., 2017). NSUN2 is upregulated in gastric cancer and influences the MYC oncogenic pathway as well (Frye and Watt, 2006; Mei et al., 2020). hTRMT2A is overexpressed in certain types of proliferative breast cancer. Therefore, it is used as marker for a stratification test (Hicks et al., 2010). As RNA modification enzymes have a catalytic center with a defined binding pocket, small molecules targeting the catalytic site could be used as straightforward therapeutic for treatment. Indeed, the company STORM therapeutics based in Cambridge showed that development of a METTL3 specific inhibitor for treatment of AML is a valid treatment strategy (Yankova et al., 2021).

1.2 The family of m^{5}U tRNA methyltransferases

The prior mentioned RNA modifications are the most abundant ones found in RNA. However, also less abundant but highly conserved modifications were described and one of them is of special interest for this thesis: Methylated uridine at position C5 in rRNA and tRNA, short m^{5}U. The epitranscriptomic mark m^{5}U is installed by m^{5}U methyltransferases and found throughout all three domains of life: archaea, bacteria, and eukarya (**Figure 3**). Most of m^{5}U methyltransferases use S-adenosyl methionine (SAM) as methyl donor. The *E. coli* tRNA m^{5}U methyltransferase is TrmA, the *S. cerevisiae* ortholog Trm2p and the human ortholog hTRMT2A and hTRMT2B, with hTRMT2A being the center of this study.

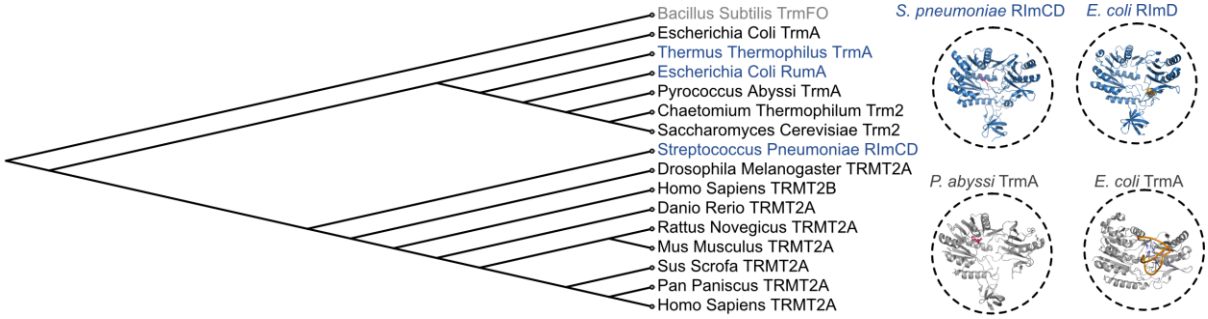

Figure 3 – Evolutionary tree of m^{5}U RNA methyltransferases.
Phylogenetic tree of m^{5}U methlytransferases based on sequence alignment with Clustal**O** and visualized with iTOL, version 5 (Letunic and Bork, 2021). tRNA methyltransferases (black), rRNA methyltransferases (blue) and folate dependent methyltransferase (grey) are highlighted. Representative structures of selected rRNA methyltransferases (blue; *S. pneumoniae* RlmCD, *E. coli* RlmD) and tRNA methyltransferases (grey; *P. abyssi* TrmA, *E. coli* TrmA) show a related three-dimensional fold.

1.2.1 Structure of TrmA and related methyltransferases

In this section, the structurally most closely related SAM-dependent rRNA/tRNA m^{5}U methyltransferases of *E. coli* TrmA – *E. coli* RlmD, *S. pneumoniae* RlmCD and *P. abyssi* TrmA – are compared to extract common topologies (Lee et al., 2004; Alian et al., 2008; Walbott et al., 2008; Jiang et al., 2017). Their similar domain organization includes a potential N-terminal RNA binding domain (RBD), a central domain and a C-terminal catalytic domain (**Figure 4A/B**). Generally, SAM-dependent methyltransferases are characterized by the presence of a Rossmann-fold in its C-terminal catalytic domain, which binds the cofactor SAM (Martin and McMillan, 2002). Structural and sequence alignment of the four m^{5}U methyltransferases show that they possess a Rossmann-fold towards their C-terminus, consisting of an eight-stranded ß-sheet flanked by six α-helices (**Figure 4C**). Typical features in the Rossmann-fold are a glycin-rich loop in motif I and a negative charged residue in motif II, all present in the selected enzymes (**Figure 4D**). Overall, the C-terminal domain contains the conserved catalytic cysteine (*E. coli* RlmD C389, *P. abyssi* TrmA C367, *E. coli* TrmA C324, *S. pneumoniae* RlmCD C408). Furthermore, the proton-abstracting base is conserved in the catalytic domain (*E. coli* RlmD E424, *P. abyssi* TrmA E399, *E. coli* TrmA Q358, *S. pneumoniae* RlmCD E434). The product of methylation reaction SAH is found in the same

position and with the same extended conformation in *E. coli* RlmD, *P. abyssi* TrmA and *S. pneumoniae* RlmCD.

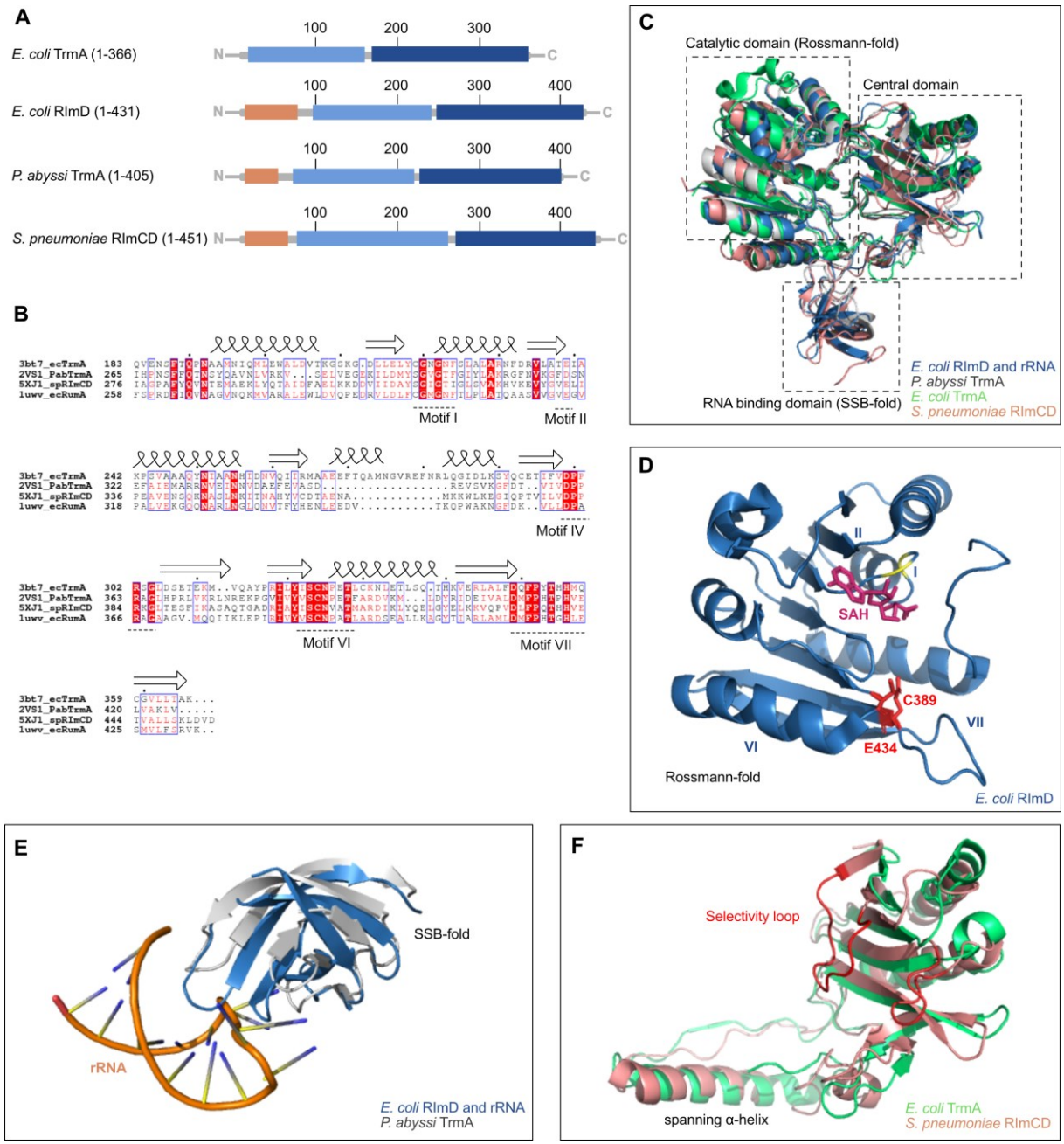

Figure 4 – Structures and common aspects of selected m^{5}U methyltransferases.
A Domain organization of four m^{5}U methyltransferases according to experimental structures with RBD (orange), central domain (light blue) and catalytic domain (dark blue). **B** Multiple sequence alignment and visualization of catalytic domains using ClustalO and ESPript 3. Highly conserved amino acids are highlighted with red background, conserved amino acids with red script. Secondary structure elements of *E. coli* TrmA, α-helixes and ß-sheets, are indicated. Conserved motifs of the Rossmann-fold are assigned too. **C** Structural alignment of *E. coli* TrmA (green, PDB: 3BT7), *E. coli* RlmD (blue, PDB: 2BH2), *P. abyssi* TrmA (grey, PDB: 2JJQ) and *S. pneumoniae* RlmCD (tile, PDB: 5ZQ0) using PyMol shows their conserved domain organization. **D** Zoom in on a representative catalytic domain (*E. coli* RlmD) illustrates bound cofactor SAH (pink), catalytic residue C389 (red), proton-abstracting base E424 (red), the glycin rich motif I (yellow) and all other conserved Rossmann-fold motifs (dark blue script; I, II, IV, VI, VII). **E** Zoom in on representative RBDs (*E. coli* RlmD, *P. abyssi* TrmA) illustrates the RNA binding, small ß-barrel domain (SBB-fold) in contact with an rRNA substrate. **F** Zoom in on representative central domains (*E. coli* TrmA, *S. pneumoniae* RlmCD) shows substrate selectivity loop (red) of *S. pneumoniae* RlmCD and α-helix spanning catalytic and central domains.

The fold of the N-terminal RBD is structurally conserved in all selected structures except for *E. coli* TrmA and displays an oligonucleotide-binding fold, more specifically a small ß-barrel domain known to bind RNA (Youkharibache et al., 2019). In the *E. coli* RlmD co-structure with rRNA shown in **Figure 4E**, the RNA substrate directly interacts with ß-barrel domain residues (Lee et al., 2005).

The C-terminal catalytic domain and N-terminal RBD are connected via a central domain found in all structures. The central domain is comprised of a six-stranded ß-sheet and three α-helixes **Figure 4F**. Moreover, the central domain harbours structural elements that are important to either maintain the overall fold or to mediate substrate selectivity. In *E. coli* RlmD, four cysteines coordinate an iron cluster, which is crucial for protein stability. In all structures, an α-helix spanning catalytic and central domain contribute to the overall protein stability. Moreover, in *S. pneumoniae* RlmD two unusually long loops in the central domain impact substrate selectivity. When applying a bioinformatics search for conserved domains, hTRMT2A is suggested to also possess an N-terminal RBD and a C-terminal catalytic domain including a Rossman-fold (Lu et al., 2020).

1.2.2 Functional characterization of TrmA and its homologs

1.2.2.1 E. coli TrmA and primary function of m^5U54 in bacterial tRNA

E. coli tRNA methyltransferase A (TrmA) was the first enzyme of the m^5U methyltransferase family to be extensively studied. Already in the 1960s, the *E. coli* enzyme catalyzing m^5U in the tRNA T-loop was identified (Fleissner and Borek, 1962). The corresponding gene *trmA* was cloned and sequenced 20 years later (Ny & Björk 1980). A series of studies proposed a mechanism of catalysis outlined in **Figure 5A**: The enzyme's catalytic cysteine 324 executes a nucleophilic attack on carbon 6 of uridine and forms a covalent Michael adduct. Consequently, on carbon 5 of uridine an anion equivalent is generated, which is sufficiently reactive to be methylated by SAM. The position U54 is completely solvent inaccessible, wherefore a uridine flip-out was suggested as part of the enzymatic mechanism (Santi and Hardy, 1987; Kealey et al., 1994).

In vitro, the m^5U54 modification in tRNA was reported to influence the stability of the tRNA tertiary structure, as well as fidelity and rate of protein synthesis (Davanloo et al., 1979; Kersten et al., 1981). *In vivo*, the exact function of TrmA remains elusive, however, the TrmA enzyme itself and not its catalytic function is essential for *E. coli* survival (Persson et al., 1992).

The minimal features of an *E. coli* TrmA substrate are contained in the 17-base T-arm of tRNA. Generally, TrmA binding affinity for the T-arm is similar to its affinity for unmodified tRNA. Mutational analysis allowed for the definition of a substrate consensus: Structurally, a base-paired stem and a loop-size of 7-bases are crucial. The only sequence requirement for

TrmA recognition *in vitro* was presence of U54 and C56 in the loop, X53-U54-X55-C56-X57-X58. (Gu and Santi, 1991; Gu et al., 1996).

Additionally, critical TrmA residues for binding and catalysis were identified. Mutation of the putative SAM binding site G220D and of the catalytic residue C324A, abolished RNA binding and methylation. Mutation of the proton-abstracting base E358K, which supposedly traps the tRNA, destroyed TrmA enzymatic function. Q190A, which was predicted to have a role in uracil recognition, had the same effect. G360D, F188A, D299A and W132A mutations had minor influence on catalytic activity (Urbonavičius et al., 2007). In addition, mutation of F106 and H125, which interrupt tertiary interactions of tRNA T- and D-loop in its L-form, are critical for efficient RNA binding (Keffer-Wilkes et al., 2020). A co-structure of *E. coli* TrmA mutant (E358Q) with a trapped RNA 6-stem T-loop was solved by X-ray crystallography. This structure confirmed orthogonally several residues that are important for RNA binding like C324, Q190, Q358, D299 and F188 (**Figure 5B**). As predicted, the target uracil was flipped out into the catalytic site for methylation and A58 occupied instead the U54 space (Alian et al., 2008).

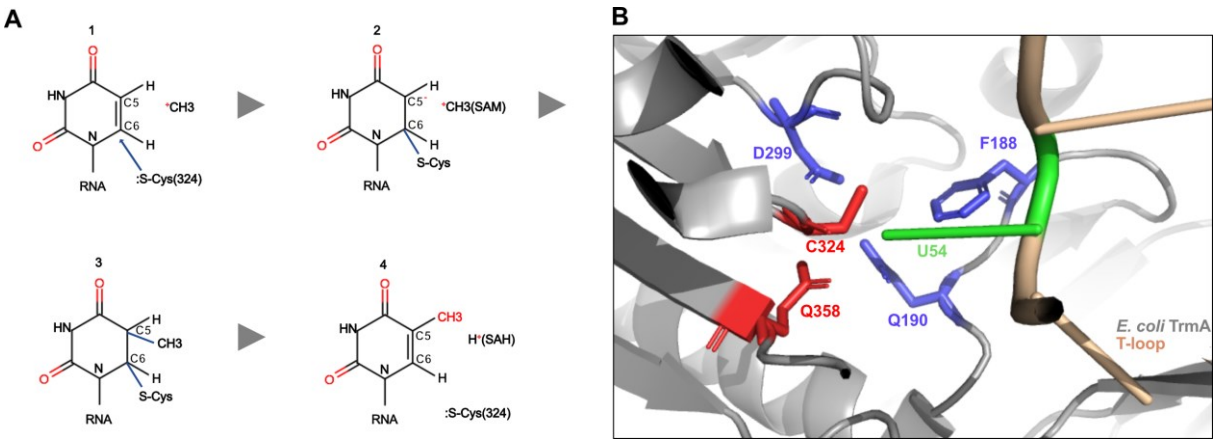

Figure 5 – Catalytic mechanism of m^{5}U formation by *E. coli* TrmA.
A Catalytic mechanism starts with a nucleophilic attack of the catalytic cysteine 324 on C6 of the uridine (1). Michael adduct between C6 of uridine and C324 is formed, which creates a reactive anione on C5 of uridine (2). C5 is methylated with the methylgroup of SAM (3). Dissociation of product SAH and C324 of the enzyme releases modified RNA (4). **B** Co-structure of *E. coli* TrmA and tRNA T-loop shows crucial residue for methylation in the catalytic center (PDB-ID: 3BT7). Catalytic cysteine C324 and proton abstracting base Q358 are highlighted in red. Other important residues, D299, F188 and Q190 are shown in blue. Target uridine 54 (green) of the RNA (beige) is inserted into the catalytic center of *E. coli* TrmA (grey).

1.2.2.2 S. cerevisiae Trm2p and primary function of m^{5}U54 in yeast tRNA

Although not as extensively studied as TrmA, some noteworthy biochemical studies have been conducted on the *S. cerevisiae* homolog Trm2p. A mutant *S. cerevisiae* strain that lacked m^{5}U modifications was isolated and later the respective gene for the methyltransferase *TRM2* was discovered to be responsible for m^{5}U conversion (Hopper et al., 1982; Nordlund et al., 2000). *TRM2* mutant strains that lack m^{5}U are viable and do not

exhibit an apparent phenotype. Thus, in contrast to *E. coli* TrmA, *S. cerevisiae* Trm2p is not essential for survival. Nevertheless, in a yeast screen to find synergistic lethal mutations, absence of Trm2p in four $tRNA^{Ser}$(CGA) mutant strains caused an temperature-dependent growth defect. Catalytically inactive Trm2p mutants (G428D, C521A) restored growth phenotype in one $tRNA^{Ser}$ mutant, which indicates that Trm2p might have an additional role independent of its catalytic function (Johansson and Byström, 2002).

1.2.2.3 Human TRMT2A and TRMT2B

It was predicted that the TRMT2A and TRMT2B are the orthologs of *E. coli* TrmA. Indeed, a recent transcriptome-wide approach confirmed that hTRMT2A is the cytosolic methyltransferase for m^5U54 conversion in humans (Carter et al., 2019). Precisely, 87 % of hTRMT2A targets in cells are cytosolic tRNA. From the tRNA targets bound by hTRMT2A around 75 % were also methylated, which indicates that binding in most but not in all cases correlates with methylation. Some of the remaining 13 % of hTRMT2A targets in cells were mRNA (6 %), rRNA (0.2 %), ncRNA (2 %), snoRNA (0.2 %) and other non-coding RNA (3.6 %). Moreover, a well-defined sequence motif of hTRMT2A was identified: G-U-U-C-G/A-A58. This sequence motif is conserved, as it was already described in parts for *E. coli* TrmA (see **1.2.2.1**). As predicted, C358 was confirmed as conserved catalytic cysteine and E581 as proton-abstracting base. Moreover, two independent mass spectrometry based studies detected hTRMT2A-catalyzed m^5U in tRNA and interestingly also in low levels in mRNA (Cheng et al., 2020; Dai et al., 2021).

Recently, hTRMT2B has been shown to bind and methylate tRNA too. However, hTRMT2B is localized to mitochondria and modifies the resident mitochondrial tRNA instead of their cytosolic counterparts. Surprisingly, hTRMT2B catalyzes in addition m^5U429 conversion in mitochondrial 12S rRNA (Powell and Minczuk, 2020). This mechanism is not restricted to human homologs, as mouse TRMT2B also forms m^5U in mitochondrial tRNA and rRNA at position U54 and U429, respectively (Laptev et al., 2020).

Functionally, m^5U in human mt-tRNA or rRNA does not affect tRNA stability, tRNA aminoacylation, mitoribosome stability or mitochondrial translation. Similarly, in mouse TRMT2B-catalyzed m^5U has no effect on mitochondrial protein synthesis. However, TRMT2B deletion impacted slightly the activity of three electron transfer chain complexes, namely complex I, II and IV (Laptev et al., 2020). Whether TRMT2A has a similar substrate specificity pattern for tRNA and rRNA remains to be studied.

1.2.3 Additional functions of TrmA and its homologs

The main function of TrmA is m^5U catalysis. However, the protein TrmA, but not its enzymatic function, has been shown to be essential for cell survival (Persson et al., 1992;

Johansson and Byström, 2002). This observation points into the direction of an m^5U catalysis-independent secondary function. One possibility of such a secondary function has been elucidated recently for *E. coli* TrmA (Keffer-Wilkes et al., 2020). TrmA RNA binding itself, independent from its enzymatic function, was important for bacterial fitness. On a molecular level, catalytically inactive TrmA still folds tRNA *in vitro* and thus acts as a tRNA chaperone important for cellular function. In the following paragraphs other plausible secondary functions, which are topic of ongoing research, are discussed.

1.2.3.1 Role as endo-exonuclease

An enzyme with endo-exonuclease activity on double-stranded DNA and weakly on single-stranded RNA was purified from *S. cerevisiae*, which later turned out to be Trm2p (Chow and Resnick, 1987). However, the potential endo-exonuclease activity of Trm2p was once questioned (Nordlund et al., 2000) and once proven with alternative *in vitro* endo-exonuclease assays (Choudhury et al., 2007). In summary, the endo-exonuclease activity is either an artefact from co-purification of an endo-exonuclease or indeed *S. cerevisiae* Trm2p possesses this function. Along this line the enzyme possibly acts as RNAse in *S. cerevisiae* tRNA maturation.

1.2.3.2 Role in cell cycle progression

TrmA synthesis in *E. coli* has been shown to be growth-rate dependent and tightly regulated (Ny and Björk, 1977; Gustafsson et al., 1991). Moreover, expression of mouse TRMT2A is cell cycle dependent with a peak during S-phase, when DNA is replicated, and a decrease during mitosis, all regulated by the transcription factor E2FA. Mouse Ran-binding protein 1 (RanBP1), which regulates the cell cycle by controlling transport of protein and nucleic acids into the nucleus, shared the TRMT2A promotor in the opposite direction. Consequently, TRMT2A and RanBP1 have similar temporal requirements during cell cycle progression and are most likely co-regulated (Guarguaglini 1997). Next to being cell-cycle regulated, hTRMT2A has been suggested to regulate cell cycle progression itself and was associated with certain types of proliferative breast cancer (Hicks et al., 2010).

1.2.3.3 Dual specificity of m^5U methyltransferases

As already mentioned before, hTRMT2B binds and methylates mitochondrial tRNA and 12S rRNA (Powell and Minczuk, 2020). However, this is not the only study, which reported dual specificity of a tRNA m^5U methyltransferase. Earlier, *E. coli* TrmA has been shown to bind *in vivo* to the 3' end of 16S rRNA (Gustafsson and Björk, 1993), although no further functions have been assigned. Moreover, *E. coli* TrmA bound to a $tRNA^{Phe}$ analogue consisting of DNA building blocks (Guenther 1994). Transfer-messenger RNA (tmRNA) is a

bacterial RNA that unifies tRNA and mRNA properties. It plays a role in trans-translation, a process that resolves stalled ribosomes. Structurally, tmRNA consists of a conserved tRNA-like domain (TLD) and an mRNA-like region. *E. coli* TrmA also bound and methylated the structurally conserved T-loop of the tmRNA TLD (Ranaei-Siadat 2013).

1.2.4.4 Role in the early maturation steps of pre-tRNA

As mentioned, tRNA modifications are installed in a concerted manner and can be divided into early tRNA modification in the nucleolus and late cytoplasmic tRNA modifications (**Figure 2**). In *S. cerevisiae*, non-spliced pre-tRNA accommodates the m^5U54 modification. This is in line with m^5U being installed before splicing, early in the tRNA maturation process (Etcheverry et al., 1979). The time-dependent tRNA modification sequence was resolved for *S. cerevisiae* $tRNA^{Phe}$ using nuclear magnetic resonance (NMR) experiments. The earliest modification observed was ψ55, followed m^5U54 conversion in the T-loop, which indicates that U55 and U54 are modified at a similar, early time point in *S. cerevisiae* (Barraud et al., 2019). In another study, the pre-existing modification of ψ55 on tRNA increased the binding affinity of *E. coli* TrmA and thus induced efficient m^5U54 modification. In addition, enzymes for ψ55 and m^5U54 conversion could bind and methylate unmodified tRNA, which suggests them to act during early tRNA maturation stages most likely on unmodified pre-tRNA (Schultz and Kothe, 2020). Hence, *E. coli* TrmA and *S. cerevisiae* Trm2p are proposed to participate in early nucleolar steps of tRNA maturation.

1.3 PolyQ diseases

PolyQ disease is another term for trinucleotide expansion disorder and constitutes a group of diseases that is autosomal dominantly inherited. PolyQ diseases have a prevalence of 1-10 per 100.000 patients (Schöls et al., 2004) and include disorders like spinocerebellar ataxias (SCA), Machado-Joseph's disease (SCA3) and Huntington's disease (HD), with latter being the most prevalent one.

1.3.1 The polyQ disease family

Causative for the polyQ diseases is an expanded cytosine-adenine-guanine (CAG) tract in the respective disease-linked gene. The CAG repeat-containing RNA is translated into an uninterrupted polyQ tract, which renders the disease-linked protein prone to aggregate. Accumulation of polyQ proteins and associated toxic gain-of-functions, but also the impact of CAG repeat-containing RNA, interferes on various levels with normal cellular function: impairment of the ubiquitin-proteasome system, mitochondrial dysfunction, transcriptional dysregulation and altered RNA metabolism (Gatchel and Zoghbi, 2005; Bennett et al., 2007; Berendzen et al., 2016).

Overall, neurotoxic species of polyQ proteins and CAG repeat RNA cause progressive neuronal degeneration. Depending on the disease-linked gene, different neuronal subpopulation degenerate in specific brain regions. Consequently, typical clinical features differ in patients with different polyQ diseases. Common to polyQ diseases, however, are progressive movement difficulties and later in disease mild to strong cognitive impairment. Furthermore, onset in middle age and disease progression for about 15-20 years is typical. Each disease has a specific threshold CAG repeat number for disease outbreak. Common to all diseases is that the CAG repeat length can be correlated with disease severity and disease onset. Moreover, the unstable CAG repeat tends to expand genomically (hence, the name expansion disorders), which causes more severe disease phenotypes in later generations (Fan et al., 2014; Lee et al., 2019).

1.3.2 Huntington's disease

George Huntington first identified HD in the late nineteenth century (Huntington, 1872). HD is a monogenic, autosomal dominant polyQ disease with a disease prevalence reaching from 12-17 patients per 100.000 in the best-ascertained population of Europe and Northern America. Asian and African populations display an overall lower prevalence (Fisher and Hayden, 2014). Causative for disease is a CAG repeat expansion above 35 repeats in the gene *huntingtin* (*htt*) located on chromosome 4p16 (Hoogeveen et al., 1993). Mutated huntingtin protein (mHtt) exhibits a polyQ tract corresponding to CAG repeat length. Repeat containing protein and RNA mediate neurotoxicity, for which striatal neurons and basal

ganglia are especially vulnerable (Bohanna et al., 2011). Overall, progressive whiter matter atrophy was observed in patients. Basal ganglia are responsible for muscle driven movements. Therefore the first clinical feature for diagnosis is often chorea, involuntary brief and “dance-like” movements. Other movement disabilities, as well as psychiatric symptoms such as personality change, dementia and cognitive decline are part of disease progression. Mean disease onset is 45 years, but exceptionally can start in childhood. Gradual decline of patient’s state requires intensive full-time care until death. The disease is fatal within an average 18 years after motor symptom onset (Bates et al., 2015). Until today, only symptomatic treatment but no FDA-approved cure is available, although various drug candidates are currently in clinical trials (Rodrigues et al., 2019).

1.3.2.1 Wildtype huntingtin structure and function

The protein huntingtin (Htt) is 348 kDa in size and harbors 67 exons (Ambrose 1994). Htt locates both to cell nucleus and cytoplasm and is expressed throughout the whole body with tissue-specific differences as reported in the Human Protein Atlas (Uhlén et al., 2015). The Htt protein consists of several HEAT-repeat containing, ordered domains interspersed with intrinsically disordered regions. Due to the presence of the expandable polyQ stretch at the N-terminal Htt exon 1, this part of the protein is well described: The usually 23 glutamines long polyQ tract starts with amino acid 17 and is followed by a proline rich domain (PRD). Htt exon 1 constitutes a hotspot for posttranslational modifications like proteolytic cleavage, phosphorylation, and glycosylation (**Figure 6**).

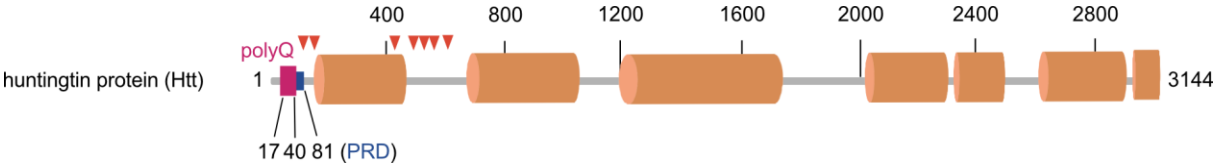

Figure 6 – Domain organization of wildtype huntingtin.
The 348 kDa sized wildtype Htt protein is a multidomain protein, where structured HEAT repeats (orange) are interspersed with unstructured regions (grey). At the N-terminus the polyQ tract (pink) is followed by a PRD (dark blue). Proteolysis sites are indicated with red arrows.

The exact biologic function of Htt is not known. It is proven, however, that Htt is critically involved in several cellular processes, as supported by lethality of Htt knockout in mouse embryos (Zeitlin et al., 1995). On a molecular basis, Htt interacts with molecular motor complexes to transport different vesicles such as autophagosome or synaptic precursor vesicles (Wong and Holzbaur, 2014). Secondly, Htt might be a regulator of selective autophagy, both by loading cargo and by initiating autophagy (Pircs et al., 2018). Thirdly, polyQ tracts are frequently found in regulatory proteins of transcription. This and binding of Htt to different transcription factors like CREP-binding protein (CBP) suggests a role of Htt as transcriptional regulator (Steffan et al., 2000). These physiological properties of Htt provide a basis for explaining the pathobiological observations in HD (Saudou and Humbert, 2016).

1.3.2.2 Pathobiology of HD

HD is seen as a toxic gain-of-function disease and an overview over affected processes is given in **Figure 7**. Generally, fragments of mutant Htt (mHtt) that contain the polyQ tract, are assumed to largely contribute to disease. The mainly disease contributing fragment contains the N-terminus, PolyQ tract and PRD and is either produced by aberrant splicing or by proteolytic cleavage of Htt exon 1. This and other mHtt fragments are prone to cytoplasmic oligomerization and aggregation, although it has not been solved, whether these aggregates are detrimental or have a protective character. The notion that fragments translocate back to the nucleus, build nuclear agglomerates, and thus interfere with transcription is more established. As certain histone acetyltransferases and transcription factors like CBP are sequestered within these mHtt aggregates, chromatin becomes hypoacetylated and transcriptional dysregulation of many genes occurs (McCampbell et al., 2000; Benn et al., 2005; Giralt et al., 2011).

Besides, the CAG repeat in the mHtt mRNA can recruit non-physiologically RNA-binding proteins such as MID1 and prevent them from executing their normal cellular function (Griesche et al., 2016). Moreover, CAG repeat RNA induces phase separation and further sequesters important cellular factors (Jain and Vale, 2017).

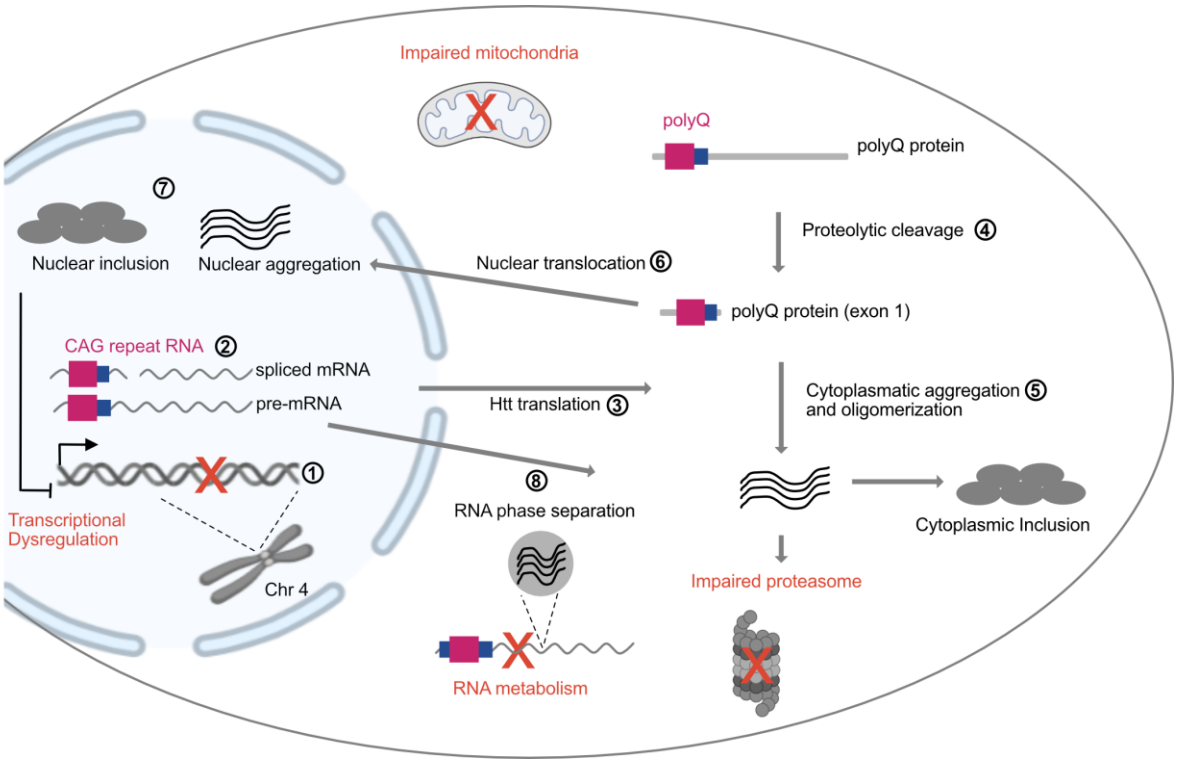

Figure 7 – Pathobiology of HD.
Pathobiology of HD from transcription of CAG-repeat containing mHtt RNA (1), aberrant RNA splicing (2), translation of mHtt protein (3) and proteolysis (4) of polyQ tract harbouring mHtt protein are shown. As a result, mHtt cytoplasmic aggregates and inclusion bodies emerge that can impair the proteasome (5). mHtt fragments translocate back to the nucleus (6) and there build up inclusion bodies and aggregates (7), which causes transcriptional dysregulation. CAG-repeat RNA forms phase separated aggregates that can sequester RNA binding proteins and impair RNA metabolism (8). Impaired cellular processes are indicated in red script (mitochondria, transcription, proteasome, RNA metabolism).

Impaired autophagy, mitochondria and proteasomes with associated cellular toxicity were frequently reported (Bauer and Nukina, 2009; Pircs et al., 2018). The role of Htt in vesicular transport correlates with observed synaptic activity deficiency and axonal transport impairment in HD (Smith-Dijak et al., 2019). In the central nervous cystem (CNS), mHtt can activate the resident immune system and hence cause detrimental neuroinflammation (Crotti and Glass, 2015). Potentiating effects between the different affected pathways progressively induce neuronal death and accelerate disease.

1.3.3 Treatment strategies for polyQ diseases including Huntington's disease

Drugs approved for HD only treat associated symptoms such as the chorea-decreasing drug tetrabenazine, which inhibits a synaptic vesicular amino acid transporter (Sung et al., 2017). Symptomatic treatment includes also anti-depressants and alternative treatment regimes, some of them in clinical trials. Examples are ketogenic diet, physical exercise, and deep brain stimulation (Caron et al., 2018). Curative treatment has not been FDA approved so far. However, several drugs are currently being investigated in preclinical and clinical trials. They can be subdivided into strategies that either lower directly mHtt and or exploit other cellular mechanism to counteract deleterious effects of mHtt.

Lowering of mHtt levels can be achieved by degradation of protein or RNA or by repression of the mHtt gene transcription. Several mHtt-silencing approaches have been tested in pre-clinical studies such as antisense oligonucleotides (ASOs), RNA interference (RNAi) with microRNA (miRNA), transcriptional silencing of mHtt DNA with synthetic zink-finger repressor and small molecules that selectively recruit mHtt for protein degradation (Garriga-Canut et al., 2012; Kordasiewicz et al., 2012; Li et al., 2019; Tabrizi et al., 2019). Currently, the most promising drug candidate is an antisense oligonucleotide (ASO) that selectively degrades mHtt mRNA. A phase 1/2b clinical trial showed a dose-dependent reduction of mHtt mRNA levels after administration of the ASO IONIS-HTT_{RX} (Tabrizi et al., 2019). Unfortunately, the follow-up phase 3 study was halted in March 2021 due to adverse events and no clear benefits for patients (Generation HD1, NCT03761849). Consequently, an effective mHtt lowering strategy has still not been developed. This makes new cellular drug targets and their pharmacological intervention even more attractive in the search for a HD cure.

Here, recent pre-clinical drugs that interfere with one of the better-studied HD associated pathways are described in more detail, specifically neuroinflammation, neuroprotection and transcriptional dysregulation (**Figure 8**). The immunomodulatory drug Laquinimod, originally developed for multiple sclerosis, targets aberrant activation of the immune system. In a HD mouse model, treatment with laquinimod indeed showed a decrease of mHtt and increase in neuroprotective brain-derived neurotrophic factor (BDNF) levels. A phase II clinical trial

showed a good safety profile, but only minor influence on HD-related phenotypes in patients (Ellrichmann et al., 2017; Reilmann et al., 2019a).

Several strategies to promote neuroprotection were followed up on, too. One of them was Pridopidine treatment, which reduced mHtt induced endoplasmatic reticulum stress by modulation of the sigma 1 receptor in a cellular model. However, phase II clinical trials uncovered no strong effect of Pridopidine on HD-related symptoms (Reilmann et al., 2019b; Shenkman et al., 2021). Chromatin hypoacetylation in HD was tried to counteract by selectively inhibiting histone deacetylase 4 (HDAC4), which removes acetyl groups from histone. This treatment is supposed to shift chromatin acetylation back to wildtype levels. Inhibitor treatment correlated with an improved disease phenotype and reduced accumulation of mHtt in a HD mouse model, but requires further elucidation of the underlying molecular mechanism before going into clinical trials (Mielcarek et al., 2013; Suelves et al., 2017).

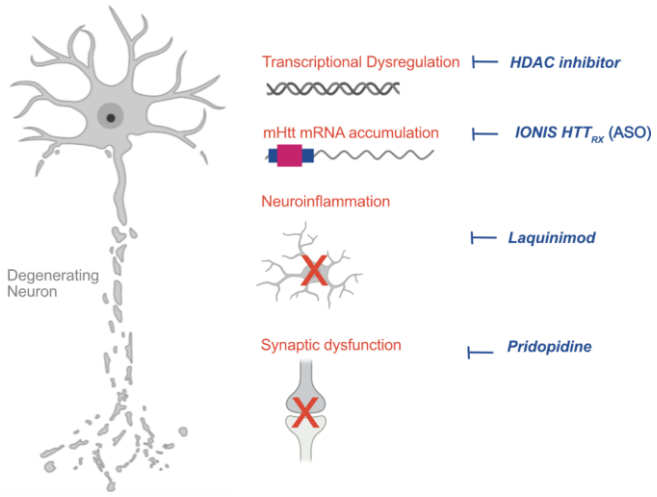

Figure 8 – Selected treatment strategies for HD in preclinical trials.
Affected HD disease mechanisms are highlighted with red script. Pharmaceuetical modalities that target these mechanisms and thus decrease neurodegeneration in HD are indicated in blue.

1.4 TRMT2A as polyQ disease modifier

Overall, no curative, pharmacological treatment for HD has been developed yet. Consequently, high throughput genetic screens in mouse, worm and fly were performed to identify further potent drug targets for HD treatment (Nollen et al., 2004; Zhang et al., 2010). A genome wide *in vivo* CNS screen in a HD mouse model identified several genes that positively modify CNS neuronal survival and mHtt toxicity, such as Nme1, a nucleoside diphosphate kinase 1 (Wertz et al., 2020).

Correspondingly, our collaborator Dr. Aaron Voigt from the RWTH Aachen addressed the search for novel drug targets that modify polyQ protein induced toxicity and cell death. To identify modifiers, an RNAi screen in a fly polyQ disease model was performed (**Figure 9A**). The screen resulted in various modifiers that restored the wildtype fly eye phenotype, amongst them CG3808 (*dm*TRMT2A), the fly homolog of hTRMT2A (Voßfeldt et al., 2012). Moreover, silencing of TRMT2A in flies also abolished polyQ-induced aggregation. Importantly, those findings could be translated to an HD human cell disease model (unpublished data, Voigt laboratory). The disease model was generated by knockdown of hTRMT2A in human embryonic kidney cells (HEK). Subsequently, these cells were transfected with GFP-labelled mHtt containing 103 glutamines. In this HEK polyQ disease model silencing of hTRMT2A reduced polyQ mediated protein aggregation (**Figure 9B**).

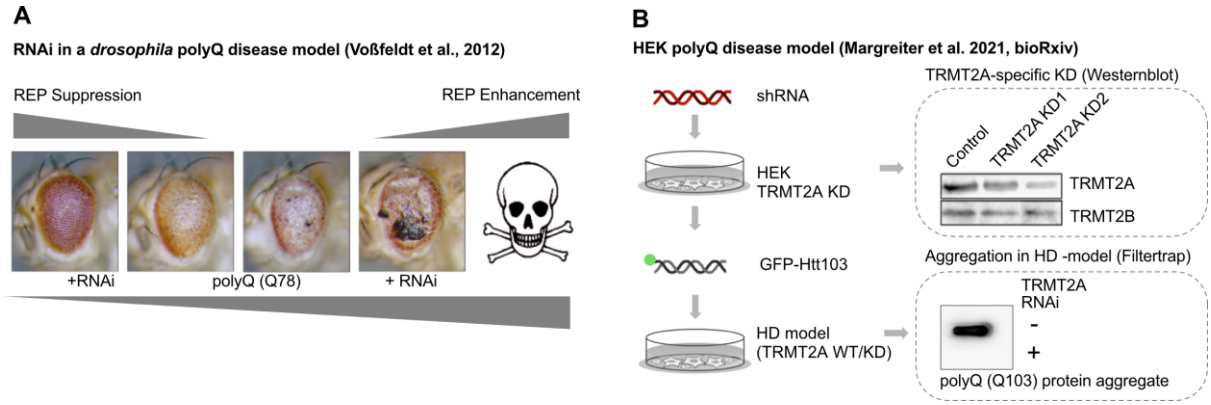

Figure 9 – TRMT2A silencing in fly and HEK cells reduces cell death and polyQ protein aggregation.
A Representative image from the RNAi screen in a fly polyQ disease model. PolyQ protein is specifically expressed in the fly eye causing the rough eye phenotype (REP), which indicates neuroreceptor death. Silencing of 3021 genes resulted in REP suppression or enhancement. Top REP suppressor was TRMT2A (not shown). **B** Generation of a HEK cell HD disease model. KD of hTRMT2A with shRNA in HEK cells reduced hTRMT2A protein levels, but not TRMT2B protein levels. Transfection of GFP-labelled Htt harboring 103 glutamines into hTRMT2A WT and KD HEK cells shows that polyQ protein aggregates were reduced in KD conditions. Data were generated in the Voigt laboratory and can be found in Voßfeldt et al., 2012 and the preprint Margreiter et al., bioRxiv, 2021.

As already stated for another RNA methyltransferase (METTL3), the group of RNA modification enzymes is amenable for pharmacological inhibition due to the presence of a defined catalytic center. Based on results of the fly RNAi screen, we reasoned that inhibition of hTRMT2A might be a valuable strategy to reduce polyQ-associated cell death. Additionally, TRMT2A has features of a possible drug target: Firstly, TRMT2A is crucially

involved in polyQ disease pathobiology, but not in other neurodegenerative diseases like Alzheimer or Parkinson (unpublished data, Voigt laboratory). Secondly, hTRMT2A silencing in human cells and TRMT2A knockout in mice did not result in an any adverse phenotype (unpublished data, Voigt laboratory). Thus, pharmacological modulation of TRMT2A is most likely not detrimental, although further experiments must be conducted to exclude side effects. Previously, several drug discovery campaigns on bacterial tRNA methyltransferases were successfully performed (Coussens et al., 2018; Zhong et al., 2019) and inspired us to envision looking for an hTRMT2A specific inhibitor for treatment of polyQ diseases.

1.5 Objectives of this thesis

The aims of this thesis can be divided into two main goals. Firstly, both molecular and cellular functions of hTRMT2A are underexplored with only a few studies undertaken in the past. Thus, the opportunity was seized to characterize hTRMT2A structurally and functionally with a special emphasis on polyQ disease pathology. To do so, a variety of techniques were employed such as RNA binding and methylation assays, X-ray crystallography, mutagenesis studies and crosslinking followed by mass spectrometry. To gain insight into the cellular protein interactome of hTRMT2A proximity-dependent biotinylation (BioID) assay and co-immunoprecipitation (Co-IP) experiments were performed.

Secondly, the discovery of a hTRMT2A-specific inhibitor was approached with a combination of structure-based drug discovery and *in silico* strategies. For functional readout of enzymatic inhibition, a methylation assay was established.

2. Materials and methods

2.1. Chemicals and materials

General stock solutions were prepared by Vera Roman (Niessing laboratory, HMGU): NaCl (1 M), HEPES (1 M, pH 7.5-8.5), Tris/HCl (1 M, pH 7.5-8.5), Imidazole (1 M), MilliQ-H_2O, DEPC-treated H_2O, PBS (10x), DTT (1 M), IPTG (1 M), APS (10 %, 20 %) and urea (8.3 M). Äkta purifier device, resins and columns for chromatography were purchased from GE Healthcare. Hampton Research provided crystallization tools and crystallization screens.

2.1.1 Chemicals

Table 1 – List of chemicals

Name	Manufacturer (order number)
2-Propanol/Isopropanol, > 99.8 % purity	Sigma Aldrich (33539-1L-R)
Acetic acid, 100 %	Carl Roth (3738.1)
Acrylamid 25%, Rotiphorese® sequencing gel concentrate (+ Urea)	Carl Roth (3031)
Acrylamid 40%, Rotiphorese® gel (19:1; - Urea)	Carl Roth (1931)
Ammonium sulfate ($AmSO_4$)	Merck (1.01217.5000)
α-Chymotrypsin from bovine pandreas	Sigma Aldrich (C3142-10MG)
Agarose	Biozyme (870055)
Anti FLAG® M2 Magnetic Beads	Merck Millipore (M8823-1ML)
Arabinose, L(+)-form	Fluka BioChemika (10845)
Arginine, L-form, > 98.5 % purity	Carl Roth (3144.2)
APS	Merck (101200)
ATP disodium salt (for protein purification)	Sigma Aldrich (A3377-10G)
BlueStar Plus Prestained Protein Marker (10-180 kDa)	Nippon Genetics (MWP03)
Biotin, D(+)-form, > 98.5 % purity	Carl Roth (5822.1)
Bradford assay solution, 5X	Carl Roth (Roti®-Quant, K015.3)
Bromphenol sodium salt	Carl Roth (7512.1)
Boric acid, > 99.8 % purity	Sigma Aldrich (31146-!KG)
BSA, lyophilized	Sigma Aldrich (A9418-5G)
Calcium chloride ($CaCl_2$) dihydrate, > 99 % purity	Carl Roth (T885.2)
Cesium chloride (CeCl), > 99,9 % purity	Biomol (02452)
Casein	VWR (22544.292)
Chloroform/Trichlormethan	Roth 3313.4
Coomassie stain (Methanol-, acetic acid free)	GiottoBiotech (G00PB002)
DAPI, 5 mg/mL	Roche (10236276001)
DEPC, > 97 % purity	Carl Roth (K028.1)
dNTP disodium salts for *in vitro* transcription	Jena Bioscience (Nu-1010-1013-1G)
Deoxycholic acid sodium salt	Carl Roth (3481.1)
DMSO a) cell culture grade b) no cell culture grade	 a) Biotium (90082) b) Roth (A994.2)

Donkey Serum	Sigma Aldrich (D9663-10ML)
DTT, > 99% purity	Carl Roth (6908.2)
Dynabeads MyOne Streptavidine T1, 10 mL	Thermo (65602)
Formamide	Fisher (F/1550/PB08)
ECL western blotting substrate, Pierce®	Thermo (32106)
EDTA (ethylenediaminetetraacetic acid disocium salt dihydrate)	VWR (20302.293)
Ethanol (EtOH), 100%	Merck (100983.1000)
Ethylene-glykol	Riedel-de-Haen (Spectranal, 34907)
FLAG™ Peptide, 3X, lyophyilized	Merck Millipore (F4799)
GelStain Red	Carl Roth (Roti®, 0984.1)
Gene Ruler 100 bp DNA Ladder (100-3000 nt)	Thermo (#SM0241)
Gene Ruler 1000 bp DNA Ladder (250- 10000 nt)	Thermo (#SM0311)
Glucose, D(+)-form, > 99.5 % purity	Carl Roth (6780.2)
Glutathione reduced, > 98 % purity	Sigma Aldrich (G4251-1000)
Glycerol, 100%	PanReac Applichem (A1123/1000)
Glycogen, RNA-grade, 20 mg/mL	Thermo (R0551)
Guanidine hydrochloride, > 98% purity	Carl Roth (6060.2)
Heparine disaccardie I-S sodium salt	Sigma Aldrich (H9267-1MG)
HEPES	PanReac AppliChem (A1069,1000)
M7GTP > 85 % purity	Sigma Aldrich (M61533-5MG)
Imidazole, > 99 % purity	Carl Roth (3899.4)
IPTG, > 99 % purity	Carl Roth (2316.4)
Kalium chloride (KCl)	Merck (EMSURE®, 1.04936.1000)
Lithium chloride (LiCl), > 99 %	Carl Roth (3739.1)
Lithium sulfate (Li_2SO_4)	Fluka BioChemicka (62612)
Magnesium chloride ($MgCl_2$)-hexahydrate	Merck (1.05833.1000)
Methanol (MeOH)	Merck (supelco®, 1.06007.2500)
MTA	Sigma-Aldrich (D5011-25MG)
NP-40	Fluka BioChemika (74385)
PageRuler™ unstained low range protein ladder (3.4-100 kDa)	Thermo (26632)
Pierce™ unstained protein MW marker (14.4-116 kDA)	Thermo (26610)
PFA, 37 % solution	PanReac AppliChem (A0823,0500)
Polyethylene glycol 400	Sigma Aldrich (918193)
Polyethylene glycol 8000	Fluka BioChemica (812608)
PCI	Carl Roth (Roti®, A156.1)
Ponceau S red stain	Sigma Aldrich (P7170)
PEI solution, 50 % (w/v)	Sigma Adlrich (P3143-100ML)
Polyuridylic acid potassium salt	Sigma Aldrich (P9528-10MG)
ProLong™ Diamond Antifade Mountant	Invitrogen (P36961)
Protease Inhibitor tablets, Pierce®	Thermo (A32963)
Putrescine	Sigma Aldrich (51799)
Radiolabelled γ-^{32}P ATP	Hartmann Analytic
RiboLock RNAse Inhibitor, 40 U/µL	Thermo (EO0381)
S-(5'-Adenosyl)-L-Homocysteine	ChemCruz (sc-214826), 10 mg
S-(5'Adenosyl)-L-methionine chloride dihydrochloride, >75%	Sigma Aldrich (A7007-25MG)

SDS pellets	Serva (20765.03)
SelenoMet™ Medium Base	Molecular Dimensions (MD12-502)
SelenoMet™ Nutrient Mix	Molecular Dimensions (MD12-501)
DL-Selenomethionine, > 99 % purity	Acros Organics (10410131)
Sinefungin, > 95 % purtiy	Cayman Chemical (13829)
Sodium acetate, > 99 % purity	Sigma Aldrich (S8750-500G)
Sodium chloride (NaCl)	Merck (EMSURE®, 1.06404.1000)
Sodium citrate 2-hydrate > 99 %	Carl Roth (3480.1)
di-Sodium Hydrogen phsopahte 2 hydrate (Na_2HPO_4)	PanReac AppliChem (142507.1211)
Sodium dihydrogen phosphate monohydrate (NaH_2PO_4)	Merck (30.09.15)
Sodium hyroxide (NaOH)	Th Geyer (chemsolute®, 1375.1000)
Spermidine, purity > 99 %	Sigma Aldrich (S2626)
Spermine	Sigma Aldrich (55313)
ssRNA ladder, low range (50-300 nt)	NEB (N03645)
Sucrose, 100 %	Calbiochem (5737)
SYPRO® orange protein gel stain, 5000x in DMSO	Thermo (S6651)
TCEP, 0.5 M	Sigma Aldrich (64564-10x1ML)
TEMED	PanReac AppliChem (A1148,0100)
TFA, > 99% purity	PanReac AppliChem (163317.1608)
Tris, > 99.3 % purity	Carl Roth (PURFFERAN®, AE15.2)
Triton X-100	Sigma Aldrich (37240)
Trypan Blue Solution, 0.4 %	Thermo (15250061)
Trypsin from bovine pancreas	Sigma Aldrich (T8003-10MG)
TRIzol Reagent	Ambion (15596026)
Tween® 20	GBiosciences (9005-64-5)
Xylene cyanol FF	Sigma Aldrich (X5126-10G)

2.1.2 Buffers for molecular biology and protein biochemistry

Table 2 – Stock solutions and loading dyes

Name	Composition	Application
2x formamide loading dye	95 % (v/v) formamide, 5 mM EDTA, 0.025 % (w/v) bromophenol blue, 0.025 % (w/v) xylene cyanol, 0.025 % (w/v) SDS	Denaturing TBE gel electrophoresis
4x stacking gel buffer	0.5 M Tris/Cl pH 6.8, 0.4 % (w/v) SDS	SDS PAGE
4x separating gel buffer	3 M Tris/Cl pH 8.6, 0.4 % (w/v) SDS	SDS PAGE
4x SDS loading dye	110 mM Tri/Cl pH 6.8, 40 % (v/v) glycerine, 40 mM DTT, 4 % (w/v) SDS, 0.25 % (w/v) bromophenol blue	SDS PAGE
6x DNA loading dye	30 % (w/v) gylcerol, 0.25 % (w/v) bromophenol blue	Agarose gel electrophoresis
10x TGS	0.5 M Tris, 1.9 M glycine, 1% (w/v) SDS	SDS PAGE gel electrophoresis
10x TBE	1M Tris base, 1 M Boric acid, 20 mM EDTA	Native/Denaturing TBE gel electrophoresis
50x TAE	2 M Tris base, 50 mM EDTA pH 8.3	Agarose gel electrophoresis
NuPAGE 20x MOPS SDS Running Buffer	50 mM MOPS, 50 mM Tris Base, 0.1 % SDS, 1 mM EDTA, pH 7.7	Westernblot

NuPAGE 20x Transfer buffer	25 mM Bicine, 25 mM Bis-Tris, 1 mM EDTA, pH 7.2, 20 % MeOH	Westernblot
NuPAGE 4x SDS Loading dye	110 mM Tris/HCl pH 6.8, 40 % (v/v) Glycerol, 40 mM DTT, 4 % (w/v) SDS, 0.25 % (w/v) Bromophenol blue	Westernblot
Ponceau S staining	0.1 % (w/v) in 5% acetic acid	Westernblot

2.1.3 Enzymes and kits

Table 3 – Enzymes and enzyme-based kits

Name	Enzyme type	Company (order number)
Benzonase, Pierce™	Nuclease	Thermo (88700)
Clone Amp HiFi PCR Premix	DNA Polymerase	Takara (639298)
Elastase	Protease (1 mg/mL)	Provided by André Mourão (STB*)
Fast-AP & Fast-AP Buffer	Alkaline Phosphatase	Thermo (EF0654)
Fast-Digest BamHI-HF & FastDigest Grenn Buffer	Restriction enzyme	Thermo (FD0054)
Glucosidase-C (Glu-C)	Protease (1 mg/mL)	Provided by André Mourão (STB*)
Phusion High-Fidelity DNA Polymerase & 5X Phusion HF Buffer	DNA Polymerase	Thermo Fisher (F530S)
PKA & PKA Buffer A/B	Polynucleotide Kinase	NEB (M0201L)
PreScission™ Protease	Protease	Prepared by Vera Roman
Q5 High-Fidelity DNA Polymerase & Reaction Buffer	DNA Polymerase	NEB (M0491S)
Subtilisin	Protease (1 mg/mL)	Provided by André Mourão (STB*)
T4 Ligase	DNA Ligase	Thermo Fisher (EL001)
T7 RNA Polymerase	RNA Polymerase	Prepared by Vera Roman

All restriction enzymes and respective buffers (Cut Smart Buffer, Buffer 2.1, Buffer 3.1) that are not listed here were purchased from NEB.
* Institute of Structural Biology at the Helmholtz Center Munich

Table 4 – Kits

Kit name	Application	Company (order number)
Cellfectin™ II Reagent	Transfection of insect cells	Thermo (10362100)
InFusion HD Cloning kit	InFusion kit for molecular cloning with competent *E.coli* Stellar	Takara (638920)
Lipofectamine 3000 reagent and Transfectionk kit	Transfection of mammalian cells	Thermo (L3000-001)
MEGAshort script T7	RNA *in vitro* transcription for < 100 nucleotide transcripts	Thermo/Invitrogen (AM1354)
NucleoSpin Gel and PCR clean up	PCR and agarose gel purification	Macherey Nagel (740609.50)
Nucleo Spin Plasmid Mini kit	Plasmid purification	Macherey Nagel (740588.50)
NucleoBond® Xtra Maxi	Large scale plasmid purification	Macherey Nagel (740414.100)
FuGene® HD Transfection Reagent	Transfection of mammalian/insect cells	Promega (E2311)

2.1.4 Media and supplements

Table 5 – Media, antibiotics and supplements used for *E. coli* and insect cell culture

Medium	Composition	Application (company)
LB	10 g/L BD Bacto™ tryptone, 5 g/L BD Bacto™ yeast extract, 5 g/L NaCl, pH 7.0 For plates: 15 g/L agar	*E. coli* protein expression
2XY 5052 auto-induction medium	10g/L BD Bacto™ tryptone, 5 g/L BD Bacto™ yeast extract	*E. coli* autoinduction, protein expression
HyClone SFX-Insect MP™ Cell culture medium	42.32 g/L HyClone® SFX-Insect™, 0.35 g/L Na bicarbonate, 1.5 mL/L glycerol, pH 6.1 – 6.4	High five (Hi5) protein expression (Thermo)
SelenoMet™ Medium Base	21.6 g in 1 L MilliQ-H_2O	*E. coli* B834 protein expression (Molecular Dimensions)
Sf-900™ SFM (Sf-900)	-	Sf21 insect cell propagation (Thermo)
SOB	20 g/L BD Bacto™ tryptone, 5 g/L BD Bacto™ yeast extract, 10 mM NaCl, 10 mM $MgCl_2$, 2.5 mM KCl, pH 7.0	*E. coli* transformation
SOC	20 g/L BD Bacto™ tryptone, 5 g/L BD Bacto™ yeast extract, 20 mM glucose, 20 mM $MgSO_4$, 10 mM NaCl, 10 mM $MgCl_2$, 2.5 mM KCl, pH 7.0	*E. coli* transformation
Antibiotics and supplements		
5052 sugar mix (50X)	25 % (v/v) glycerol, 2.5 % (w/v) glucose), 10 % (w/v) lactose	Supplement auto-induction
Ampicillin	Stock 100 mg/mL	*E. coli* selection (Carl Roth)
Carbenicillin	100 mg/mL	*E. coli* selection (AppliChem) on plates
Chloramphenicol	34 mg/mL in EtOH	*E. coli* selection (Carl Roth)
Gentamycin	7 mg/uL	Sf21, Hi5 insect cells
Isopropyl-ß-D-thioglactopyranosid	1 M	*E. coli* induction of protein expression
Kanamycin	50 mg/mL	DH10Ba*c* selection (Carl Roth)
M salt mix (25x)	1.25 M Na_2HPO_4, 1.25 M KH_2PO_4, 2.5 M NH_4Cl, 0.25 M Na_2SO_4	Supplement auto-induction
SelenoMet™ Nutrient Mix	5.1 g in 50 mL MilliQ-H_2O	Supplement SelenoMet™ Medium Base
Trace metal mix (1000X)	40 mM HCl, 50 mM $FeCl_3$, 20 mM $CaCl_2$, 10 mM $MnCl_2$, 10 mM $ZnCl_2$, 2 mM $CoCl_2$, 2 mM $CuCl_2$, 2 mM Na_2MoO_4, 2 mM H_3BO_3	Supplement auto-induction
Tetracycline	10 mg/mL	DH10Bac selection (Carl Roth)
X-gal	100 mg/mL in DMSO	DH10Bac selection on plates

Vera Roman provided with antibiotics stocks, antibiotic supplemented agar plates, LB medium, autoinduction medium and supplements, SOB/SOC medium and Hi5 medium.

Table 6 – Media, antibiotics and supplements used for mammalian (HEK) cell culture

Medium	Composition	Company (order number)
Complete Medium	90 % DMEM (v/v), 10 % FBS (v/v), 1 % Pen/Strep	-
DPBS	PBS [-] $CaCl_2$, [-] $MgCl_2$	Gibco (14190-744)
DMEM	DMEM [+] 4.5 g/l glucose, [+] L-glutamine, [-] Pyruvate	Gibco (41965-039)
FBS	Heat inactivated	Sigma/Gibco
Freezing Medium	DMEM + 20 % FBS + 10 % DMSO	-
OptiMEM	[+] HEPES, [+] 2.4 g/L sodium bicarbonate, [+] L-Glutamine	Gibco (31985-062)
Antiobiotics and supplements (order number)		
Doxycyline	1:1000 dilution in complete medium	Takara
Pen/Strep	Penicilin/Streptomycin	Gibco (15140122)
Hygro	Hygromycin B in PBS, 50 mg/mL	Invitrogen (10687010)
Trpysin-EDTA (10x)	0.05 % (v/v) dilution in PBS	Merck (L215.3)

2.1.5 Oligonucleotides

Table 7 – Oligonucleotides for cloning, mutagenesis, and *in vitro* transcription

Name	Sequence (5'-3')	Application
TRMT2_69-147_F	AAGTTCTGTTTCAGGGCCCGACCTCTGAGATCTTT	InFusion pOPIN
TRMT2_69-147_R	ATGGTCTAGAAAGCTTTACTTGGGCCGGGCCAG	InFusion pOPIN
TRM_166_F	Provided by Elena Davydova	InFusion pOPIN
TRM_1_F	Provided by Elena Davydova	InFusion pOPIN
MW1-TRMT2_178fwd	AAGTTCTGTTTCAGGGCCCGCTGCAGAAACTTGCCAAG	InFusion pOPIN
MW2-TRMT2_195fwd	AAGTTCTGTTTCAGGGCCCGGTGCCCTATGCTGAGCAG	InFusion pOPIN
MW3-TRMT2_591rev	ATGGTCTAGAAAGCTTTAGTGCTCCACCCTCTCAAA	InFusion pOPIN
MW4-TRMT2_593rev	ATGGTCTAGAAAGCTTTAATTGGGGTGCTCCACCCT	InFusion pOPIN
MW5-TRMT2_591rev+His	ATGGTCTAGAAAGCTTTAGTGGTGATGGTGATGATGGTGCTCCACCCTCTCAAA	InFusion pOPIN
MW6-TRMT2_593rev+His	ATGGTCTAGAAAGCTTTAGTGGTGATGGTGATGATGATTGGGGTGCTCCACCCT	InFusion pOPIN
MW7-POPINFseq-fwd	GGAGTTAATCCGGGACCTTTAATT	Sequencing primer
MW8-TRMT2_166fwd_PE	AGGAGATATACCATGGTGCCCTATGCTGAGCAGCTTGAGCGGAAGCAGCTG	InFusion pOPIN
MW9-TRMT2_593rev_PE	GTGATGGTGATGTTTTTAGTGGTGATGGTGATGATGATTGGGGTGCTCCACCCT	InFusion pOPIN
MW10-S3C-TRMT2_1fwd_pFB	CATCGGGCGCGGATCCATGGCACACCATCACCACCA	InFusion pFastBac
MW11-S3C-TRMT2_625rev_pFB	GTAGGCCTTTGAATTCTTAGGATGAGGGGAAGGTCCCA	InFusion pFastBac
MW14-TRMT2_391fwd	AAGTTCTGTTTCAGGGCCCGCGGTGCAT	InFusion pOPIN

	CCACGAGGA	
MW15-TRMT2_625rev	ATGGTCTAGAAAGCTTTAGGATGAGGGGAAGGTCCCA	InFusion pOPIN
MW16-TRMT2_148fwd	AAGTTCTGTTTCAGGGCCCGGCCGACCCCATGGCCA	InFusion pOPIN
MW17-TRMT2_390rev	ATGGTCTAGAAAGCTTTAGTCCCCAGCCACATGCTC	InFusion pOPIN
MW18-TRMT2aR-mutR82A_fwd	GAGCTGCAGAACGTGCCTGCCCACGCCAGC	Mutagenesis
MW19-TRMT2aR-mutR82A_rev	GCTGGCGTGGGCAGGCACGTTCTGCAGCTC	Mutagenesis
MW20-TRMT2aR-mutR137A_fwd	GCACACTGAGTGGGGCGCCTTTCCAGAGGG	Mutagenesis
MW21-TRMT2aR-mutR137A_rev	CCCTCTGGAAAGGCGCCCCACTCAGTGTGC	Mutagenesis
MW22-TRMT2aR-mutK135A_fwd	GAGTGGGCGGCCTGCCCAGAGGGCACCA	Mutagenesis
MW23-TRMT2aR-mutK135A_rev	TGGTGCCCTCTGGGCAGGCCGCCCACTC	Mutagenesis
MW30_CG3808-full_1fwd	AAGTTCTGTTTCAGGGCCCGATGGAGTGTTTCAATGCG	InFusion pOPIN
MW31_CG3808-full_620rev	ATGGTCTAGAAAGCTTTATCACGTTACGGATGTGGTG	InFusion pOPIN
MW32_CG3808_57fwd	AAGTTCTGTTTCAGGGCCCGACTTCGGAAATATTCAAA	InFusion pOPIN
MW33_CG3808_134rev	ATGGTCTAGAAAGCTTTAGGCCTTGGCAACATGAGCC	InFusion pOPIN
MW34_CG3808_137rev	ATGGTCTAGAAAGCTTTAATCGGCCGAGGCCTTGGCA	InFusion pOPIN
MW35_CG3808_155fwd	AAGTTCTGTTTCAGGGCCCGAAGAAACAACGTACGGCG	InFusion pOPIN
MW36_CG3808_160fwd	AAGTTCTGTTTCAGGGCCCGGCGGTGGAAGCCACGTGT	InFusion pOPIN
MW37_CG3808_579rev	ATGGTCTAGAAAGCTTTATTCACGCTCGAACAGAATG	InFusion pOPIN
MW38_TRMT2aCHis_625rev_pFB	GTAGGCCTTTGAATTTTAGTGGTGATGGTGATGATGGGATGAGGGGAAGGTCCC	InFusion pFastBac
MW39_CG3808_620rev_pFB	GTAGGCCTTTGAATTTCACGTTACGGATGTGGTGT	InFusion pFastBac
MW40_TRMT2a_mutE581A_fwd	CAGACCCCGCACTGTGCAATGCTCATCCTGTTTG	Mutagenesis
MW41_TRMT2a_mutE581A_rev	CAAACAGGATGAGCATTGCACAGTGCGGGGTCTG	Mutagenesis
MW42_TRMT2a_mutK104E_fwd	GCCCCACAAAACCGAACTCTTTGGGC	Mutagenesis
MW43_TRMT2a_mutK104E_rev	GCCCAAAGAGTTCGGTTTTGTGGGGC	Mutagenesis
MW44_TRMT2a_mutF113A_fwd	CAACCACCCTGCGCCGCTGTGACATTCCGCAG	Mutagenesis
MW45_TRMT2a_mutF113A_rev	CTGCGGAATGTGACAGCGCGCCAGGGTGGTTG	Mutagenesis
MW46_TRMT2a_mutF86A_fwd	CCTCGCCACGCCAGCGCCAGCGACGTCCGGC	Mutagenesis

MW47_TRMT2a_mutF86A_rev	GCCGGACGTCGCTGGCGCTGGCGTGGCGAGG	Mutagenesis
MW51_tRNA^{Gln}-Tloop_2	CCGAGATTTGAACCGGCCTATAGTGAGTCGTATTA	*In vitro* transcription
MW52_tRNA^{Lys}-Tloop_2	AAGAGTGGTTCTCTTCCTATAGTGAGTCGTATTA	*In vitro* transcription
MW53_T7-promotor	TAATACGACTCACTATAGG	*In vitro* transcription
MW57_TRMT2a_237fwd	AAGTTCTGTTTCAGGGCCCGACTGAGTATCGTAATAAG	InFusion pOPIN
MW58_TRMT2a_414rev	ATGGTCTAGAAAGCTTTATGTGTTCACCTGGAAGAAGGC	InFusion pOPIN
MW59_TRMT2a_414fwd	AAGTTCTGTTTCAGGGCCCGACACCCGCAGCC	InFusion pOPIN
MW60_TRMT2a_590rev	ATGGTCTAGAAAGCTTTACTCCACCCTCTCAAACAGGAT	InFusion pOPIN
MW61_TRMT2a_RVFusion_fwd	CAGACTGAGTATCGTGTGAACACACCCGCA	InFusion pOPIN
MW62_TRMT2a_RVFusion_rev	TGCGGGTGTGTTCACACGATACTCAGTCTG	InFusion pOPIN
MW63_TRMT2a_161fwd	AAGTTCTGTTTCAGGGCCCGAGTGAGCCACCAGTAA	InFusion pOPIN
MW64_TRMT2a_166fwd	AAGTTCTGTTTCAGGGCCCGACACGAGTGGCCGA	InFusion pOPIN
MW65_TRMT2a_1fwd_PiggyBac	ACAAAGACGATGACGACAAGATGAGTGAGAACCTC	InFusion PB
MW66_TRMT2a_625rev_PiggyBac	GAGATCCCCGCGCTGCAGTTAGGATGAGGGGAAGGTCCCAGTTT	InFusion PB
MW67_TRMT2a_mutC538A_fwd	TGCTGTACGTCTCAGCCAACCCCCGGGCAG	Mutagenesis
MW68_TRMT2a-mutC538A_rev	CTGCCCGGGGGTTGGCTGAGACGTACAGCA	Mutagenesis
MW69_TRMT2a_1fwd_PiggyBac+BirA*	AGTGGGGGTGGAGGCAGTATGAGTGAGAACCTC	InFusion PB
MW70_TRMT2a_69rev_seq	GTAAACAAGTCATCCCTGATGTAG	Sequencing primer
MW71_TRMT2a_44rev_seq	TCTTTCTCCACCTCCTCCAG	Sequencing primer
MW72_TRMT2a_seq_1fwd	ATGAGTGAGAACCTCGACAAC	Sequencing primer
MW73_TRMT2a_seq_1683rev1	AATGCCCTTCACCCGGTTAGATGG	Sequencing primer
MW74_TRMT2a_seq_1742rev2	TCACAGTGCGGGGTCTGCGGGAA	Sequencing primer
MW75_TRMT2a_mutA284G_fwd	GCTTCCTGGGCCGCTTTGGTCTGCAG	Mutagenesis
MW76_TRMT2a_mutA284G_rev	CTGCAGACCAAAGCGGCCCAGGAAGC	Mutagenesis
MW78_tmRNA-seq1	TGGTGGAGCTGGCGGGAGTTGAACCCGCGTCCGAAATTCCTACATCCTCGGTACTACATG CCTATAGTGAGTCGTATTA	*In vitro* transcription
MW81_TRMT2aCodon-7mut_rev	GTTGCTTAATTCGTTATCTTGGGCGTTCACCCGGGCGTCCTC	Mutagenesis
MW82_TRMT2aCodon-7mut_fwd	CAAGATAACGAATTAAGCAACGTGGAGTTCCACTGCGGGAGG	*In vitro* transcription
MW83_tRNA^{Phe}-full	TGGTGCCGAAACCCGGGATCGAACCAG	*In vitro* transcription

	GGACCTTTAGATCTTCAGTCTAACGCTCT CCCAACTGAGCTATTTCGGCCCTATAGT GAGTCGTATTA	
MW84_tRNA^{Gln}-full	TGGAGGTCCCACCGAGATTTGAACTCGG ATCGCTGGATTCAAAGTCCAGAGTGCTA ACCATTACACCATGGGACCCCTATAGTG AGTCGTATTA	*In vitro* transcription
MW86_tRNA^{Gln}-mutU54G_full	TGGAGGTCCCACCGAGATTTGACCTCGG ATCGCTGGATTCAAAGTCCAGAGTGCTA ACCATTACACCATGGGACCCCTATAGTG AGTCGTATTAt	*In vitro* transcription
MW89_TRMT2a_AmutQ411A_fwd	CACGCCTTCTTCGCGGTGAACACACCC	Mutagenesis
MW90_TRMT2a_AmutQ411A_rev	GGGTGTGTTCACCGCGAAGAAGGCGTG	Mutagenesis
MW91_TRMT2a_F409A+Q411A_F	GGATCTCTCCACACGCCGCCTTCGCGGT GAACACACCCGCAGC	Mutagenesis
MW92_TRMT2a_F409A+Q411A_R	GCTGCGGGTGTGTTCACCGCGAAGGCG GCGTGTGGAGAGATCC	Mutagenesis
MW93_TRMT2a_CmutF409A_fwd	GATCTCTCCACACGCCGCCTTCCAGGTG AACACAC	Mutagenesis
MW94_TRMT2a_CmutF409A_rev	GTGTGTTCACCTGGAAGGCGGCGTGTGG AGAGATC	Mutagenesis
MW95_TRMT2a_DmutK242A_fwd	GACTGAGTATCGTAATGCGTGTGAGTTTC TGGTTG	Mutagenesis
MW96_TRMT2a_DmutG242A_rev	CAACCAGAAACTCACACGCATTACGATAC TCAGTC	Mutagenesis
MW97_TRMT2a_EmutD510A_fwd	GTGGCCATCCTGGCCCCACCCCGTGCTG	Mutagenesis
MW98_TRMT2a_EmutD510A_rev	CAGCACGGGGTGGGGCCAGGATGGCCA C	Mutagenesis
MW99_TRMT2a_mutE76A_fwd	GATCTTTAAACTGGCGCTGCAGAACGTG C	Mutagenesis
MW100_TRMT2a_mutE76A_rev	GCACGTTCTGCAGCGCCAGTTTAAAGAT C	Mutagenesis
MW101_TRMT2a_mutH95R_fwd	GCGCTTCCTGGGCCGCTTTGGTCTGCAG C	Mutagenesis
MW102_TRMT2a_mutH95R_rev	GCTGCAGACCAAAGCGGCCCAGGAAGC GC	Mutagenesis
MW103b_ctTrm2_94fwd	AAGTTCTGTTTCAGGGCCCGCTGGGCAC CGAACTGGAA	InFusion pOPIN
MW104b_ctTrm2_543rev	ATGGTCTAGAAAGCTTTAATCAACGCGAT TCAGAAC	InFusion pOPIN
MW105b_ctTrm2_161rev	ATGGTCTAGAAAGCTTTATGCCGGGGCA ATCAC	InFusion pOPIN
MW107b_ctTrm2_360fwd	AAGTTCTGTTTCAGGGCCCGAATAATAAT AGTATCCTG	InFusion pOPIN
MW108_droso-tRNA^{Gln}_oligo	GAATTCGGTTCCATGGTGTAATGGTTAGC ACTCAGGACTCTGAATCCTGCGATCCGA GTTCAAATCTCGGTGGAACCTCTGCAG	*In vitro* transcription
MW109_ctTrm2_360fwd2	AAGTTCTGTTTCAGGGCCCGAACAACAA CTCCATTCTC	InFusion pOPIN
MW110_ctTrm2_seq-rev	ATCCGGCACACCTTTACGACGTG	InFusion pOPIN
MW111_ctTrm2_91fwd	AAGTTCTGTTTCAGGGCCCGCTGCCGGA	InFusion pOPIN

	ACTGGGCAC	
MW112_CG3808_581rev	ATGGTCTAGAAAGCTTTATTTAGGTTCAC GCTCGAAC	InFusion pOPIN
MW113_ctTrm2_53fwd	AAGTTCTGTTTCAGGGCCCGCATGAAGA AATTCTG	InFusion pOPIN
MW114_ctTrm2_544rev	ATGGTCTAGAAAGCTTTATTCATCAACGC GATTCAG	InFusion pOPIN
MW115_tRNA^{Ala}-AGC-9-1	TGGAGAATGCGGGCGTCGATCCCGCTAC CTCTCGCATGCTAAGCGAGCGCTCTACC GCCTGAGCTAATTCCCCCTATAGTGAGT CGTATTA	*In vitro* transcription
MW116_tRNA^{Asn}-GTT-1-1	TGGCGTCCCTGGGTGGGATCGAACCACC AACCTTTCGGTTAACAGCCGAACGCGCT AACCGATTGCGCCACAGAGACCCTATAG TGAGTCGTATTA	*In vitro* transcription
MW117_Akt1-Intron	CCACACGACGTCGACACAGTCTTCACCC TGGTCGTGTACCGTACTCACTGAGACTA ATCCCTATAGTGAGTCGTATTA	*In vitro* transcription
MW118_KCND2-Intron	GTCTACAGAATGGATGTGTCAGAAGTGG TATGATGCATATGTGTATTTATGAGAGTT ATAGCCTATAGTGAGTCGTATTA	*In vitro* transcription
MW119_ZNF773	TCTCTGCTCCAGCAGACCTTCTTCACTCA CGTCCCTGTTCGGGCGCCACTTGCCTAT AGTGAGTCGTATTA	*In vitro* transcription
MW120_pcDNA_1fwd	ACCCAAGCTGGCTAGATGAGTGAGAACC TCGACAACG	InFusion pcDNA3.1.
MW121_pcDNA_625rev	AAACGGGCCCTCTAGTTAGGATGAGGGG AAGGTCC	InFusion pcDNA3.1.

Oligonucleotides were synthesized by Eurofins Genomics.

2.1.6 RNA

Table 8 – RNA sequences produced by *in vitro* transcription

RNA name	Short name	Sequence (5'→ 3')	Produced by
Full tRNA^{Phe}-GAA, 76 nt	tRNA^{Phe}	GCCGAAAUAGCUCAGUUGGGAGAGC GUUAGACUGAAGAUCUAAAGGUCCC UGGUUCGAUCCCGGGUUUCGGCACC A	*In vitro* transcription. Template MW83
Full tRNA^{Gln} -TTG, 75 nt	tRNA^{Gln}	GGUCCCAUGGUGUAAUGGUUAGCAC UCUGGACUUUGAAUCCAGCGAUCCG AGUUCAAAUCUCGGUGGGACCUCCA	*In vitro* transcription. Template MW84
Full tRNA^{Gln}-TTG, U54G, 75 nt	tRNA$^{Gln\ U54G}$	GGUCCCAUGGUGUAAUGGUUAGCAC UCUGGACUUUGAAUCCAGCGAUCCG AGGUCAAAUCUCGGUGGGACCUCCA	*In vitro* transcription. Template MW86
tRNA^{Gln} T-stemloop (49-65), 17 nt	tRNA^{Gln} T-loop	CCGAGUUCAAAUCUCGG	*In vitro* transcription. Template MW51
tRNA^{Lys} T-stemloop (49-63), 15 nt	tRNA^{Lys} T-loop	AAGAGAACCACUCUU	*In vitro* transcription. Template MW52
tmRNA T-stemloop, 60 nt	tmRNA	CAUGUAGUACCGAGGAUGUAGGAAU UUCGGACGCGGGUUCAACUCCCGCC AGCUCCACAA	*In vitro* transcription. Template MW78
tRNA^{Ala}-AGC, 73 nt	tRNA^{Ala}	GGGGAAUUAGCUCAGGCGGUAGAGC GCUCGCUUAGCAUGCGAGAGGUAGC	*In vitro* transcription. Template MW115

		GGGAUCGACGCCCGCAUUCUCCA	
$tRNA^{Asn}$-GTT, 77 nt	$tRNA^{Asn}$	GGUCUCUGUGGCGCAAUCGGUUAGC GCGUUCGGCTGUUAACCGAAAGGUU GGUGGUUCGAUCCCACCCAGGGACG CCA	*In vitro* transcription. Template MW116
Akt1 Intron, Intron mRNA, 50 nt	Akt1	GGAUUAGUCUCAGUGAGUACGGUAC ACGACCAGGGUGAAGACUGUGUCGA CGUCGUGUGG	In vitro transcription. Template MW117
KCND2 Intron mRNA, 62 nt	KCND2	GCUAUAACUCTCAUAAAUACACAUAU GCAUCAUACCACUUCUGACACAUCCA UUCUGUAGAC	*In vitro* transcription. Template MW118
ZNF773 coding region mRNA, 52 nt	ZNF	GGUCUCUGUGGCGCAAUCGGUUAGC GCGUUCGGCTGUUAACCGAAAGGUU GGUGGUUCGAUCCCACCCAGGGACG CCA	*In vitro* transcription. Template MW119
S. cerevisiae ASH1 E3 mRNA, 50 nt	Ash1		Purchased RNA (Dharmacon)

Red letter indicates introduced nucleotide mutation compared to wildtype tRNA.

2.1.7 Plasmids

Table 9 – Plasmids obtained and generated in this thesis

Vector	Application	Tag	Resistance	Source
pFastBac™	Protein expression in insect cells	-	Amp, Gent	Invitrogen
pFastBac™ Dual	Protein expression in insect cells	-	Amp, Gent	Invitrogen
pOPIN-J	Protein expression in bacteria	N-terminal-His_6-GST-3C	Amp	Addgene
pOPIN-M	Protein expression in bacteria	N-terminal-His_6-MBP-3C	Amp	Addgene
pOPIN-S3C	Protein expression in bacteria/insect cells	N-terminal-His_6-SUMO-3C	Amp	Addgene
pOPIN-TRX	Protein expression in bacteria	N-terminal-His_6-TRX-3C	Amp	Addgene
pOPIN-E	Protein expression in bacteria	C-terminal-His_6	Amp	Addgene
pGro12	GroES/GroEL co-expression		Kan	
pGEX-TGS1(618-853)	Protein expression of human TGS1	N-terminal-GST-tag	Amp	Dr. Thomas Monecke
pGEX-ctTrm2(1-544)	Protein expression of c.t. Trm2	N-terminal-GST-tag	Amp	General Biosystems
#FI05218, Gold	Vector with *dm*TRMT2A (dCG3808)	-	Cm	Drosophila Genomics Center
pcDNA 3.1.(+)-insert	Mammalian cell expression vector with insert		Amp	HMGU, Toxicology
F1	pOPINF_hTRMT2A(1-625)		Amp	Dr. Elena Davydova
F2	pOPIN-F_hTRMT2A(166-		Amp	Dr. Elena

	588)			Davydova
S1	pOPINS3C_hTRMT2A(1-625)		Amp	Dr. Elena Davydova
S2	pOPINS3C_hTRMT2A(166-588)	-	Amp	Dr. Elena Davydova

3C indicates 3C-protease (PreScission™) cleavage site

Table 10 – Plasmids generated during this thesis

#	Description	PCR primer	Source/cloning
1	pOPINS3C_hTRMT2RS2(69-147)	TRMT2_69-147_F, TRMT2_69-147_R	Elena Davydova
2	pOPINS3C_TRMT2A-G1(178-591)	MW1/MW3	InFusion cloning
3	pOPINS3C_TRMT2A-G2(178-593)	MW1/MW4	InFusion cloning
4	pOPINS3C_TRMT2A-G3(195-591)	MW2/MW3	InFusion cloning
5	pOPINS3C_TRMT2A-G4(195-593)	MW2/MW4	InFusion cloning
6	pOPINS3C_TRMT2A-G5(166-591)	E_166_fwd/MW3	InFusion cloning
7	pOPINS3C_TRMT2A-G6(166-593)	E_166_fwd/MW4	InFusion cloning
8	pOPINS3C_TRMT2A-G7(1-591)	ED1/MW3	InFusion cloning
9	pOPINS3C_TRMT2A-G8(1-593)	ED1/MW4	InFusion cloning
10	pOPINF_TRMT2A-G6(166-593)	E_166_fwd/MW4	InFusion cloning
11	pOPINJ_TRMT2A-G6(166-593)	E_166_fwd/MW4	InFusion cloning
12	pOPINS3C_TRMT2A-G6(166-593)-CHis	E_166_fwd/MW6	InFusion cloning
13	pOPINF_TRMT2A-G6(166-593)-CHis	E_166_fwd/MW6	InFusion cloning
14	pOPINJ_TRMT2A-G6(166-593)-CHis	E_166_fwd/MW6	InFusion cloning
15	pOPINE_TRMT2A-G6(166-693)-CHis	E_166_fwd/MW6	InFusion cloning
16	pFastBac_S3C-TRMT2afull(1-625)	MW10, MW11	InFusion cloning
17	pOPINS3C_TRMT2A-Rmut1(69-147), R82A	MW19, MW18	Mutagenesis of #1
18	pOPINS3C_TRMT2A-Rmut2(69-147), R137A	MW21, MW20	Mutagenesis of #1
19	pOPINS3C_TRMT2A-Rmut3(69-147), R82A + R137A	MW21, MW20	Mutagenesis of #16
20	pOPINJ_hTRMT2R(69-147)	TRMT2_69-147_F, TRMT2_69-147_R	InFusion cloning
22	pOPINS3C_TRMT2A-Central1(148-390)	MW16, MW17	InFusion cloning
21	pOPINS3C_TRMT2A-Catalytic1(391-625)	MW14, MW15	InFusion cloning
23	pOPINS3C_TRMT2A_Central1Catalytic1(148-625)	MW16, MW15	InFusion cloning
24	pOPINS3C_TRMT2A_RCentral1(69-390)	TRMT2_69-147_F, MW17	InFusion cloning
25	pOPINM_TRMT2A-Central1(148-390)	MW16, MW17	InFusion cloning
26	pOPINTRX_TRMT2A-Central1(148-390)	MW16, MW17	InFusion cloning
27	pOPINS3C_*dm*TRMT2ARBD1(57-135)	MW32, MW33	InFusion cloning
28	pOPINJ_*dm*TRMT2ARBD1(57-135)	MW32, MW33	InFusion cloning
29	pOPINS3C_*dm*TRMT2ARBD1(57-137)	MW32, MW34	InFusion cloning

30	pOPINJ_*dm*TRMT2ARBD1(57-137)	MW32, MW34	InFusion cloning
31	pOPINS3C_*dm*TRMT2A-G1(57-579)	MW32, MW37	InFusion cloning
32	pOPINJ_*dm*TRMT2A-G1(57-579)	MW32, MW37	InFusion cloning
33	pOPINS3C_*dm*TRMT2A-G2(155-579)	MW35, MW37	InFusion cloning
34	pOPINJ_dmTRMT2A-G2(155-579)	MW35, MW37	InFusion cloning
35	pOPINS3C_*dm*TRMT2A-G3(160-579)	MW36, MW37	InFusion cloning
36	pOPINJ_*dm*TRMT2A-G3(160-579)	MW36, MW37	InFusion cloning
37	pOPINS3C_*dm*TRMT2A-full(1-620)	MW30, MW31	InFusion cloning
38	pOPINJ_*dm*TRMT2A-full(1-620)	MW30, MW31	InFusion cloning
39	pFastBac_S3C-hTRMT2A-full(1-625)-Chis	MW10, MW38	InFusion cloning
40	pFastBac_S3C-hTRMT2A-full(1-625)-Chis, E581A=ED1	MW41, MW40	Mutagenesis of #42
41	pFastBac_S3C-*dm*TRMT2A-full(1-620)	MW10, MW39	InFusion cloning
42	pOPINS3C_TRMT2A-Rmut4(69-147), E86A+F113A	MW44, MW55, MW46, MW47	Mutagenesis of #1
43	pOPINS3C_TRMT2A-Rmut5(69-147), E86A+F113A+K104E	MW42, MW43	Mutagenesis of # 4
44	pOPINS3C_TRMT2A-Central2(237-414)	MW57, MW58	InFusion cloning
45	pOPINS3C_TRMT2A-Catalytic2(414-590)	MW59, MW60	InFusion cloning
46	pOPINS3C_TRMT2A-RBDCentral2(69-414)	TRMT2_69-147_F, MW58	InFusion cloning
47	pOPINJ_TRMT2A-RBDCentral2(69-414)	TRMT2_69-147_F, MW58	InFusion cloning
48	pOPINS3C_TRMT2A-RBDFusion(69-240/413-590)	TRMT2_69-147_F, MW62, MW61, MW60	InFusion cloning
49	pOPINS3C_TRMT2A-LoopFusion(161-240/413-590)	MW63, MW62, MW61, MW60	InFusion cloning
50	pFastBac_S3C-TRMT2A-full(1-625), C538A=ED2	MW67, MW68	Mutagenesis of #16, InFusion cloning
51	pFastBac_S3C-TRMT2A-full(1-625), C538A+E581A=ED2+ED1	MW67, MW68	Mutagenesis of #40, InFusion cloning
52	pFastBac_S3C-TRMT2A-full(1-625), 8mut=IR	MW91, MW92, MW93, MW94, MW95, MW96, MW97, MW98, MW99, MW100,	Mutagenesis of #50, InFusion cloning
53	PB_FLAG-BirA*-TRMT2A(1-625), MW1	LM1, MP6, MP90, LM27, MW69, MW66	3-fragment InFusion
54	PB_FLAG-BirA*-TRMT2A(1-625)-altCod, MW1altCod	MW81, MW82	Mutagenesis of #54, 3-fragment InFusion
55	PB_FLAG-BirA*, MP6	-	*
56	PB_FLAG-BirA*-TRMT2A(1-625), 8mut=IR, MW2	LM1, MP6, MP90, LM27, MW69, MW66	from #52, 3-fragment InFusion
57	PB_FLAG, MP3	LM1, MP6, MP90, LM27, MW65, MW66	*
58	PB_FLAG-TRMT2A(1-625), MW3	LM1, MP6, MP90, LM27, MW65, MW66	3-fragment InFusion
59	PB_FLAG-TRMT2A(1-625), 8mut=IR, MW4		from #56, 3-

			fragment InFusion
60	PB helper plasmide, MP11	-	*
61	pOPINS3C_ctTrm2-G1(94-543)	MW103, MW104	InFusion cloning
62	pOPINJ_ctTrm2-G1(94-543)	MW103, MW104	InFusion cloning
63	pOPINS3C_ctTrm2-RBD(94-161)	MW103, MW105	InFusion cloning
64	pOPINJ_ctTrm2-RBD(94-161)	MW103, MW105	InFusion cloning
65	pOPINS3C_ctTrm2-G3(163-543)	MW106, MW104	InFusion cloning
66	pOPINJ_ctTrm2-G3(163-543)	MW106, MW104	InFusion cloning
67	pOPINS3C_ctTrm2-G4(390-543)	MW109, MW104	InFusion cloning
68	pOPINJ_ctTrm2-G4(390-543)	MW109, MW104	InFusion cloning
69	pOPINJ_ctTrm2-G1b(91-544)	MW111, MW114	InFusion cloning
70	pOPINJ_ctTrm2-G2(53-544)	MW113, MW114	InFusion cloning
71	pOPINS3C_*dm*TRMT2A-G1b(57-581)	MW32, MW112	InFusion cloning
72	pcDNA3.1_TRMT2A(1-625)-altCod	MW120, MW121	InFusion cloning
73	pcDNA3.1_TRMT2A(1-625)-altCod, 8mut=IR/NR	MW120, MW121	from #52, InFusion cloning

* Backbone PiggyBac vectors, MP3 and MP6 were kindly provided by Dr. Lena Molitor and Dr. Jana Tretter. MP11 was obtained from the Drukker laboratory at HMGU (Krendl et al 2017).

2.1.8 Bacterial strains, mammalian and insect cell lines

Table 11 – List of *E. coli* strains and mammalian cell lines

Strain/Cell	Description	Resistance	Source
E. coli XL-1 Blue	Plasmid production strain	Amp	-
E. coli Stellar™	Plasmid production strain	Amp	Takara
E. coli BL21 Star (DE3)	Expression strain	Amp	-
E. coli BL21 Gold (DE3) pRARE	Expression strain	Amp	-
E. coli B834 (DE3)	Expression strain, SeMet auxotroph	Amp	Novagen
E. coli Rosetta	Expression strain	Amp, Cm	-
E. coli pLysS	Expression strain	Amp, Cm	-
E. coli DH10Bac	Bac-to-Bac system	Tetr, Kan, Gent	Invitrogen
E. coli MultiBac	Bac-to-Bac system	Tetr, Kan, Gent	Invitrogen
HEK 293	Immortalised human embryonic kidney cell line	Pen/Strep	
HEK shk (scrambled)	Stably scrambled control siRNA transfected HEK cell line	Pen/Strep	Obtained from Dr. Aaron Voigt
HEK TRMT2A KD 1 (skh856) and KD 2 (sh1537)	Stably siRNA transfected cell line. TRMT2A Knockdown	Pen/Strep	Obtained from Dr. Aaron Voigt
HEK Flag OE (**MP3**)	Stable overexpression of plasmid #57	Pen/Strep, Hygro	Generated in this thesis
HEK Flag-TRMT2A-WT OE (**MW3**)	Stable overexpression of plasmid #58	Pen/Strep, Hygro	Generated in this thesis
HEK Flag-TRMT2A-	Stable overexpression of plasmid #59	Pen/Strep,	Generated in this

IR OE (**MW4**)		Hygro	thesis
HEK BirA* OE (**MP6**)	Stable overexpression of plasmid #55	Pen/Strep, Hygro	Generated in this thesis
HEK BirA*-TRMT2A-WT OE (**MW1**)	Stable overexpression of plasmid #53	Pen/Strep, Hygro	Generated in this thesis
HEK BirA*-TRMT2A-IR OE (**MW2**)	Stable overexpression of plasmid #56	Pen/Strep, Hygro	Generated in this thesis
Sf21	Cells from Spodoptera frugiperda (Sf) ovarian cells for propagation of recombinant baculovirus stocks	Gentamycin	Invitrogen
Hi5	Cells from Trichopulsia ni for expression of recombinant proteins after baculovirus infection	Gentamycin	Invitrogen

Vera Roman produced chemically competent *E. coli* listed here. **Bold**: Cell line names as used in later paragraphs.

2.2 Molecular biology

2.2.1 Transformation of chemically competent *E. coli*

Chemically competent bacteria were transformed by adding 100 ng plasmid DNA to 100 µL chemically competent *E. coli* cells (50 µL commercial *E. coli* stellar strain). After incubation on ice for 5 min, bacteria were heat shocked for 45 sec at 42 °C and placed for 2 min back on ice. 900 µL SOC medium was added and cells were incubated for 1 h at 37 °C in case of *E. coli* and for 4 h at 37 °C in case *E. coli* DH10Bac, while shaking with 650-800 rpm. *E. coli* cells were pelleted with 10.000 x *g* for 15 sec, resuspended in 100 µL SOC medium, plated on antibiotic supplemented agar plates and incubated ON at 37 °C. DH10Bac were incubated for 48-72 h at 37 °C on antibiotic supplemented X-gal agar plates for blue and white selection. White colonies were consecutively double selected to discard false-positive clones. A list of *E. coli* strains can be found in **Table 11**.

2.2.2 Small-scale DNA amplification

For small scale plasmid isolation 5 mL LB medium containing respective antibiotics was inoculated with single colonies and grown ON at 37 °C with 130 rpm. Cells were harvested by centrifugation for 5 min with 4000 rpm (Hettich centrifuge Rotina 420R). DNA from cell pellets was extracted using the NucleoSpin® Plasmid kit according to manufacturer's instructions. Pure DNA was eluted with 50 µL elution buffer and stored at -20 °C.

Initial steps of small-scale bacmid DNA isolation were performed like usual plasmid isolation with buffers from the NucleoSpin® Plasmid kit. To prevent shearing of large bacmid DNA, the DNA was precipitated with 0.8 mL isopropanol after the neutralization step and cooled down for 10 min on ice. Next, DNA was pelleted by centrifugation for 30 min at 4 °C with 11.000 x *g*. Pellet was washed 2x with 500 µL of 70 % (v/v) EtOH. DNA pellet was air dried, dissolved in elution buffer from the kit and stored at 4 °C.

2.2.3 Large-scale DNA amplification

For large-scale plasmid isolation single colonies were grown ON at 37 °C with 130 rpm in 200 mL LB medium supplemented with respective antibiotics. Cells were harvested and plasmid DNA purified according to manufacturers instruction with the NucleoBond® Xtra Maxi. DNA was resuspended in 100 µL elution buffer and stored at -20 °C.

For large-scale bacmid isolation, protocol was performed according to large-scale plasmid isolation with the NucleoBond® Xtra Maxi until the neutralization step. To prevent sheering of large DNA, the column for DNA purification from the commercial kit was avoided and instead DNA was precipitated with 1 volume isopropanol. After cooling for 10 min on ice, DNA was pelleted by centrifugation for 10 min at 4 °C with 11.000 x *g*. Next, DNA was washed once

with 8 mL 70 % (v/v) EtOH. Pelleted DNA was air-dried, dissolved in 100 µL elution buffer and stored at 4 °C.

2.2.4 Molecular cloning

Standard molecular biology cloning procedures were applied. DNA sequences were PCR amplified from a template using Q5 (NEB), Phusion (Thermo) or Clone Amp HiFi (Takara) polymerases. Parameters of the mostly used PCR program for TRMT2A amplification using the Clone Amp HiFi PCR Premix or Phusion polymerase are listed in **Table 12**. PCR products were monitored by agarose gel electrophoresis. Gels with 0.5-2 % (w/v) agarose were supplemented with GelStain Red for visualization and run in 1x TBE running buffer at constant 120 V. Correct amplicon bands as determined with the 6 µL GeneRuler™ 1 kb or 100 bp DNA ladder were excised for purification with the NucleoSpin Gel and PCR clean up kit. Bands were visualized with the UV option of the Fusion SL 4 imaging device and respective software (Vilber Lourmat).

For majority of plasmids Gibson cloning was employed using the InFusion® HD cloning kit. For that purpose, pOPIN and pFastBac backbone vectors were linearized with KpnI and NcoI or BamHI and EcoRI restriction enzymes, respectively. Re-ligation was prevented by 5' dephosphorylation with FastAP™ thermosensitive slkaline phosphatase. Alternatively, PCR amplicons were ligated to linearized backbone vectors using T4 DNA ligase. For transformation 3-10 µL of InFusion or ligation reaction were proceeded as described in **2.2.1**. All enzymes and buffers were used according to manufacturer's recommendations.

Point mutations were introduced by site-directed mutagenesis using overlap extension PCR as described before (Ho et al., 1989). Briefly, forward and reverse primers with the respective mutation were used to amplify DNA. Then, the two PCR fragments including the mutation were connected with a third PCR.

Initial positive clones of PiggyBack plasmid cloning were assayed using a fast digest BamH1 HF restriction enzyme test according to instructions.

Overall, the DNA sequencing service of Eurofins Genomics confirmed positive clones. Plasmid concentration was determined with a NanoDrop spectrometer. The A_{260nm}/A_{280nm} value was used to estimate DNA purity with ideal values of 1.8-2.0 (A_{260nm} of 1.0 = 50 ng/µL). Primer sequences are listed in **Table 7** and generated plasmids as well as respective cloning procedures can be found in **Table 10**.

Table 12 – Parameters of Phusion and Clone Amp HiFi PCR

PCR	Phusion		Clone Amp HiFi	
Steps	**Temperature**	**Time**	**Temperature**	**Time**
1. Initial denaturing	98 °C	30 sec	-	-
2. Denaturing	98 °C	10 sec	95 °C	15 sec
3. Annealing	70 °C	30 sec	55 °C	15 sec
4. Elongation	72 °C	30 sec	72 °C	15 sec
Repeats	Go to step 2., 35 x		Go to step 2, 35 x	
5. Final Elongation	72 °C	5 min	-	-
Hold	12 °C	forever	4 °C	forever

2.3 Protein purification

2.3.1 Small-scale protein expression screen

To select promising candidates for large-scale protein expression in respect to protein yield and solubility, small-scale protein expression screens were performed. GST- or His/TRX-tagged proteins were enriched with Gluthathione Sepharose™ high performance and Ni Sepharose™ 6 Fast Flow (GE Healthcare) resins, respectively, according to manufacturers recommendations. Briefly, pellets from 20 mL culture were sonified in 5 mL His-lysis buffer (50 mM HEPES 7.5, 500 mM NaCl, 20 mM Imidazol, 0.1 % Tween) or GST-lysis buffer (50 mM HEPES 7.5, 500 mM NaCl, 0.1 % Tween). The clarified supernatant was incubated with 50 µL pre-equilibrated sepharose resins, washed twice with respective lysis buffer and eluted. His/TRX-tagged proteins were eluted with 1 M Imidazol and GST-tagged proteins with GST-lysis buffer containing 20 mM reduced Glutathion. Samples from cell pellet and elution were analysed with SDS PAGE gel electrophoresis.

2.3.2 Protein expression in *E. coli*

Large-scale protein expression in *E. coli* was performed with colonies from plates with freshly transformed bacteria. The pre-culture was set up with 50 mL LB medium supplemented with respective antibiotics and inoculated with several bacterial colonies. After incubation at 37 °C for 3-14 h with 130 rpm, preculture was added to 3 L pre-warmed LB medium supplemented with antibiotics. Cells were grown at 37 °C with 130 rpm until an OD_{600} of 0.4-0.6 was reached. Expression was induced with 0.3-0.5 mM IPTG. Then, protein was expressed at 18 °C for 17-20 h with 130 rpm or at 37 °C for 3 h with 130 rpm. For expression of pOPIN-M plasmid harboring bacteria 0.2 % (w/v) D(+)-glucose was added. List of *E. coli* expression strains can be found in **Table 11.**

Alternatively, autoinduction was performed according to the original protocol (Studier, 2005). Here, the pre-culture was added to 3 L pre-warmed 2XY 5052 autoinduction medium supplemented with antibiotics, 2 mM $MgSO_4$, 2x trace metal mix, 1x 5052 sugar mix and 1x M salt mix. After bacteria reached appropriate density of OD_{600} 0.4-0.6, lowering the temperature to 18 °C automatically induced protein expression. Protein was expressed for 12-20 h with 130 rpm.

Human TGS1 (hTGS1) harbouring pGEX vector containing bacteria grew in ampicillin containing 2XY medium supplemented with 2 % (w/v) D(+)-glucose. Expression was induced at OD_{600} 0.8 by adding 0.5 mM IPTG, 2 % (v/v) EtOH and 50 mM K_2HPO_4. Protein hTGS1 was expressed for 17-20 h at 16 °C. Expression protocol was developed by Dr. Thomas Monecke (Monecke et al., 2009b).

For crystallography, L-selenomethionine (SeMet)-containing protein was expressed using the methionine auxotrophic *E. coli* strain B834 (DE3). The preculture inoculated with bacteria

was set up with 300 mL SelenoMet™ base medium containing 5 mL steril filtrated SelenoMet™ Nutrient Mix and 400 µL SeMet (stock 10 mg/mL) as well as respective antibiotics. After incubation at 37 °C for 3-14 h with 130 rpm, preculture was added to 3 L SelenoMet™ Base medium complemented with 150 mL steril filtrated SelenoMet™ nutrient mix, 15 mL SeMet and respective antibiotics. Cells were grown at 37 °C until an OD_{600} of 0.5 was reached. After protein expression induction with 0.5 mM IPTG, temperature was lowered to 18 °C and protein was expressed for 12-20 h with 130 rpm.

2.3.3 Protein expression in insect cells

The Bac-to-Bac baculovirus expression system (Invitrogen) was employed for protein expression according to manufacturers instructions and based on work by Imre Berger (Berger et al., 2004). Parallely, for each construct pOPIN vector, Bac-to-Bac vector and MultiBac vector were compared in respect to expression and yield before proceeding with the best system for protein expression. Preparatory, Sf21 cells with a density of $0.4*10^6$ cells/mL in Sf-900 medium were seeded in 6-well plates and allowed to adhere for 30-45 min at 27.5 °C. For transfection with the FuGene HD transfection reagent 1.5 µg bacmid DNA (Bac-to-Bac, MultiBac) and 3 µL transfection reagent were preincubated for 30 min in 200 µL Sf-900 medium at RT, then added dropwise to the cells and incubated for 4 days at 27.5 °C. For transfection with Cellfectin™ II reagent 8 µg Cellfectin was diluted in 100 µL medium and 1-3 µg of DNA (pOPIN) was diluted in 100 µL medium. Both dilutions were mixed and incubated for 20 min at RT. Then, DNA-lipid mixture was dropwise added to cells and incubated for 4 days at 27.5 °C.

Supernatant of transfected cells from two 6-wells was used to infect 10 mL of Sf21 shaking cell culture at a density of $1.4*10^6$ cells/mL. After 3-4 days incubation at 27.5 °C with 85 rpm, insect cells were harvested by centrifugation for 10 min at 4 °C with 2000 rpm (Hettich centrifuge Rotina 420R). Virus-containing supernatant “P1” was steril-filtered using a 0.22 µm filter (Merck). To amplify the virus 1.5 mL “P1” was added to 250 mL of Sf21 shaking cell culture at a density of $0.4*10^6$ cells/mL. After another 3-4 days incubation at 27.5 °C with 85 rpm cells were harvested. The virus-containing supernatant “P2“ was sterile filtered and stored at 4°C. Protein was expressed in Hi5 insect cells by adding 20 mL of “P2“ to 500 mL shaking culture at a density of $1*10^6$ cells/mL. Proteins were expressed in Hi5 insect cells for 2-3 days at 27.5 °C with 85 rpm.

2.3.4 Cell lysis

Bacterial cells were harvested by centrifugation for 20 min at 4 °C with 5000 x *g*. Insect cells were harvested by centrifugation for 10 min at 4 °C with 2000 x *g*. Pellets were directly used for purification or flash-frozen and stored at -80 °C.

For cell lysis, pellet was resuspended in respective lysis buffer containing one tablet Pierce® Protease Inhibitor. Typically, per 3 L culture 25 mL lysis buffer was added. Respective lysis buffer for each protein is listed in **Table 13**. The resuspended bacterial cell pellet was sonified at 4 °C with a Branson sonifier 250 (Emerson) 3-4 times for 6 min with an amplitude of 40 % and output control of 5-7. Insect cells were lysed by either three times sonication for 2 min, with an amplitude of 40 % and output control of 5 or by douncing twenty times with a dounce homogenizer. Insoluble cellular debris was separated from soluble *E. coli* expressed proteins by centrifugation for 30 min at 4 °C with 20.000 x *g*. Insect cell suspension was clarified by two times centrifugation for 20 min at 4 °C with 16.000 x *g*. Before proceeding with further purification steps, supernatant was filtered with a 2.7 µm filter (Whatman).

Table 13 – Lysis buffer for purification of SUMO/TRX and GST-tagged proteins

SUMO/TRX-tagged protein (volume and expression strain)	**Lysis buffer**
hTRMT2A RBD (6 L Rosetta), *dm*TRMT2A RBD (6 L Rosetta)	500 mM NaCl, 50 mM HEPES 8.5, 20 mM Imidazole, 0.5 % Tween, 2 % Glycerol
hTRMT2A globular (6-18 L Rosetta)	500 mM NaCl, 50 mM HEPES pH 7.5, 0.1 % (v/v) Tween, 20 mM Imidazol, 1 mM DTT
hTRMT2A RBD-central1 (3 L pLysS)	500 mM NaCl, 50 mM HEPES pH 7.5, 0.1 % (v/v) Tween, 20 mM Imidazol
hTRMT2A FL (1 L Hi5) *dm*TRMT2A FL (1L Hi5)	500 mM NaCl, 50 mM HEPES pH 7.5, 0.1 % (v/v) Tween, 10 % Glycerol, 20 mM Imidazol
TRX-hTRMT2A central 1 (3-6 L pLysS)	500 mM NaCl, 50 mM HEPES pH 7.5, 0.1 % (v/v) Tween, 20 mM Imidazol, 10 % Glycerol, 100 mM Arginine
hTRMT2A central 2 (3 L pLysS) hTRMT2A fusion 1 (6 L pLysS)	500 mM NaCl, 50 mM HEPES pH 7.5, 0.1 % (v/v) Tween, 20 mM Imidazol, 10 % Glycerol
*dm*TRMT2A FL (3 L Rosetta), *dm*TRMT2A globular 1b (3 L Rosetta)	500 mM NaCl, 50 mM HEPES pH 7.5, 0.1 % (v/v) Tween, 20 mM Imidazol, 10 % Glycerol
*ct*Trm2 globular 1 (3 L Rosetta) *ct*Trm2 globular 2 (3 L Rosetta)	500 mM NaCl, 50 mM HEPES pH 7.5, 0.5 % (v/v) Tween 10 % Glycerol, 20 mM Imidazol
GST-tagged protein (volume and expression strain)	**Lysis buffer**
hTRMT2A globular (6-18 L Rosetta), *ct*Trm2 FL (3 L Rosetta)	50 mM HEPES pH 7.5, 500 mM NaCl, 0.1% (v/v) Tween
hTGS1 (6 L Rosetta)	50 mM Tris/HCl pH 7.5, 500 mM NaCl, 2 mM EDTA, 2 mM DTT

2.3.5 Purification of hTRMT2A RBD and *dm*TRMT2A RBD

Dr. Elena Davydova developed the purification protocol of the hTRMT2A N-terminal RBD (aa 69-147) for crystallization. Both native and SeMet labelled *dm*TRMT2A RBD (57-137) were purified accordingly. Protein with cleavable SUMO-tag was expressed and lysed as described in **2.3.4** with respective lysis buffer (**Table 13**). Composition of buffers used for purification is listed in **Table 14**. Clarified and filtered supernatant was loaded onto 5 mL

HisTrap FF column equilibrated with His-A buffer, pH 8.5. Then, protein was washed with 10 column volumes (CV) of His-A buffer, followed by washing with 10 CV of high salt containing His-B buffer, pH 8.5. SUMO-tagged protein was eluted with a 10 CV gradient of His-A buffer and His-C elution buffer, pH 8.5. For SUMO-tag cleavage, the eluate was supplemented with 100 µg of PreScission™ protease and dialyzed against Dialysis-A buffer, pH 7.5, in a 6.0 S tubing (ZelluTrans, Carl Roth) ON at 4 °C. The day after, cleaved protein was applied onto an equilibrated subtractive HisTrap FF column, and the protein-containing flowthrough was collected. This flowthrough was concentrated to 2 mL with a centrifugal filter (Amicon® Ultra, Merck, 3K cut-off) and loaded onto a size exclusion chromatography (SEC) Superdex 75, (S75, 10/300 GL) column equilibrated in SEC-A buffer, pH 7.5. The protein containing fractions were unified and concentrated to 8 mg/mL. Aliquots were flash frozen in liquid nitrogen and stored at -80 °C.

Table 14 – Buffers for purification of SUMO/TRX-tagged or GST-tagged proteins

Buffer name	Buffer composition
His-A	500 mM NaCl, 50 mM HEPES 7.5/8.5, 20 mM Imidazole
His-B	2000 mM NaCl, 50 mM HEPES 7.5/8.5, 20 mM Imidazole
His-C	500 mM NaCl, 50 mM HEPES 7.5/8.5, 500 mM Imidazole
Dialysis-A	500 mM NaCl, 50 mM HEPES pH 7.5, 1 mM DTT
Dialysis-B	150 mM NaCl, 50 mM HEPES pH 7.5, 1 mM DTT
SEC-A	500 mM NaCl, 50 mM HEPES pH 7.5
SEC-B	500 mM NaCl, 50 mM HEPES pH 7.5, 1 mM DTT
SEC-C	250 mM NaCl, 25 mM HEPES pH 7.5, 1 mM DTT
SEC-D	500 mM NaCl, 50 mM HEPES pH 7.5, 0.5 mM TCEP
SEC-E (hTGS1)	200 mM NaCl, 20 mM Tris/HCl pH 7.5, 2 mM DTT
HP-A	150 mM NaCl, 50 mM HEPES pH 7.5, 1 mM DTT
HP-B	1000 mM NaCl, 50 mM HEPES pH 7.5, 1 mM DTT
GST-A	500 mM NaCl, 50 mM HEPES pH 7.5
GST-B	2000 mM NaCl, 50 mM HEPES pH 7.5
GST-C	2000 mM NaCl, 50 mM HEPES pH 7.5, 10 mM reduced Glutathione
GST-D (hTGS1)	1000 mM NaCl, 50 mM Tris/HCl pH 7.5, 2 mM DTT

2.3.6 Purification of SUMO-tagged hTRMT2A, *dm*TRMT2A and *ct*Trm2 domains

From hTRMT2A, *dm*TRMT2A and respective *Chaetomium thermophilum* (*ct*) homolog *ct*Trm2 several domains were purified with a N-terminal SUMO-tag. In detail, SUMO-tagged hTRMT2A globular (166-593), central 2 (237-414), fusion 1 (166-240/413-590), hTRMT2A FL (1-625), *dm*TRMT2A globular 1b (57-581), globular 2 (160-579), *dm*TRMT2A FL (1-620), *ct*Trm2 globular 1 (91-544), globular 2 (54-544) and TRX-tagged hTRMT2A central 1 (148-390) domain were purified as described in this section and summarized in **Supplemental Table 1**. Lysis was performed as described in **2.3.4** with lysis buffer described in **Table 13.** In all buffers pH was kept 1 over or below the isoelectric point of the protein. Protein purification

buffer compositions are listed in **Table 14**. After lysis, the clarified protein supernatant was loaded onto a 5 mL HisTrap FF column equilibrated with His-A buffer. Next, column was washed with 5 CV His-A buffer and 10 CV high salt containing His-B buffer. After re-equilibration in His-A buffer, protein was eluted with a 10 CV gradient of His-A and His-C buffer. The peak fractions were supplemented with 50-100 µg PreScission™ protease to remove the SUMO-tag and dialyzed ON at 4 °C in a 15.0 S dialysis tubing (ZelluTrans, Carl Roth) against Dialysis-A buffer. The SUMO-tag of the hTRMT2A central 2 was not cleaved due to degradation of the untagged protein. Proteins like hTRMT2A central 2, for which the next purification step was a HiTrap affinity chromatography, were dialyzed ON at 4 °C against Dialysis-B buffer.

If protein precipitate was observed after ON dialysis, the protein was filtered with a 2.7 µm filter prior to further purification. For proteins whose second purification step was a subtractive HisTrap FF column the dialysed protein was loaded onto a pre-equilibrated HisTrap FF column as described in **2.3.5**. The protein-containing flowthrough was concentrated with a centrifugal filter using the appropriate molecular weight cut-off and proceeded to SEC.

For proteins whose second purification step was an affinity chromatography, the dialyzed protein was loaded onto a 5 mL HiTrap Heparin HP column equilibrated with HP-A buffer. Unbound protein was removed by washing with 5 CV HP-A buffer. Protein was eluted with either 3 CV of HP-B buffer or using a 5 CV gradient of HP-A and HP-B buffer. The peak fractions were unified, concentrated with a centrifugal filter to 2 mL or 5 mL and proceeded to SEC.

In case precipitation was observed during concentration, NaCl was added to reach a final concentration of 1 M NaCl. Chaperone-protein or RNA-protein binding visible as higher molecular weight contaminations were avoided by addition of 5-10 mM $MgCl_2$ and a small amount of ATP before the SEC run. To remove protein aggregates, the protein was either filtered with a 0.44 µm filter or centrifuged for 10 min at 4 °C with 13.000 x *g* prior to SEC run. Proteins above 40 kDa were purified using the Superdex 200 column (S200, 16/600) or S200 increase (10/300). Proteins below 40 kDa were purified using the Superdex 75 column (S75, 16/600). Columns were equilibrated in SEC-B buffer and SEC run performed with 1.1 CV SEC-B buffer. Proteins used for crystallization trials were eluted into SEC-3 buffer. hTRMT2A FL purified for crosslinking and mass spectrometry experiments was purified with SEC-D buffer, where DTT was exchanged by TCEP, which is more suitable for crosslinking experiments. Pooled protein peak fractions were concentrated to 2-5 mg/mL with a centrifugal filter, flash-frozen in liquid nitrogen and aliquots were stored at -80 °C.

2.3.7 Purification of GST-tagged hTRMT2A globular domain and *ct*Trm2 FL

GST-tagged hTRMT2A globular domain (166-593) and *ct*Trm2 FL (1-544) were purified as described in this section and **Supplemental Table 1**. Composition of lysis buffer and other buffers used for these purifications is listed in **Table 13** and **Table 14**. Clarified and filtered supernatant was loaded onto a pre-equilibrated 5 mL GSTrap FF column. Column was washed with 10 CV GST-A buffer and 5 CV high salt containing GST-B buffer. After re-equilibration in GST-A buffer, the protein was eluted with 30 mL GST-C buffer containing 10 mM reduced glutathione. The pooled peak fractions were proceeded to GST-tag cleavage with 50 µg of PreScission™ protease: *ct*Trm2 FL was dialyzed in presence of protease against Dialysis-B buffer using a 15.0 S tubing ON at 4 °C. Alike, hTRMT2A globular domain 1 was dialysed against Dialysis-A buffer.

Next, an affinity chromatography with a HiTrap Heparine column was performed for *ct*Trm2 FL as described in **2.3.6**. Thereafter, protein was concentrated to 5 mL and loaded on a S200 (16/600) column run in SEC-C buffer. If overlapping peaks were observed during SEC run, the unified protein from one peak was subjected to a second polishing SEC.

After dialysis ON, hTRMT2A globular 1 was concentrated to 5 mL and directly run on a S75 (16/600) column using SEC-A buffer. Pooled peak fractions were concentrated to 2-5 mg/mL with a centrifugal filter, flash-frozen in liquid nitrogen and aliquots stored at - 80 °C.

2.3.8 Purification of the catalytic domain of GST-tagged hTGS1

The catalytic domain of hTGS1 (aa 618-853) was expressed as described in **2.3.2**. Purification protocol was kindly shared by Dr. Thomas Monecke (University Ulm). The bacterial pellet was resuspended in respective lysis buffer (**Table 13**). Purification buffer composition is given in **Table 14**. The cleared and filtered supernatant was loaded onto a pre-equilibrated 5 mL GSTrap FF column. Unbound protein was removed with 10 CV lysis buffer and 5 CV high salt containing GST-D buffer. After re-equilibration in lysis buffer the protein was eluted with lysis buffer containing 25 mM reduced glutathione. For cleavage of GST–tag the protein was incubated with 50 µg of PreScission™ protease and dialyzed with 15.0 S tubing ON at 4 °C. Further, the protein was loaded onto a S75 (16/600) column equilibrated in SEC-4 buffer. After the run small amounts of contaminating GST-tag were removed from the pooled fractions by using GST sepharose resin. The pure protein was concentrated to 8 mg/mL using a centrifugal filter with molecular weight cut-off of 10 kDa. Aliquots were frozen in liquid nitrogen and stored at -80 °C.

2.4 Protein biochemistry

2.4.1 Determination of protein concentration

Protein concentration was either determined with a NanoDrop ND-1000 UV-Vis spectrophotometer (Peqlab) or by the infrared-based DirectDetect® spectrometer (Merck). For UV spectroscopy the extinction coefficient was calculated with the tool ProtParam of the ExPASy server. The A_{260nm}/A_{280nm} value was used to estimate the amount of nucleic acid contaminations with a nucleic acid-free base value of 0.5-0.6. The concentration of proteins with low molar extinction coefficients was evaluated with infrared spectroscopy. To do so, 1 µL protein solution was dispensed on the Direct Detect® assay-free cards (Merck), dried for 5 min and inserted into the machine for measurement.

2.4.2 Gel electrophoresis

To analyse purity and molecular weight of proteins, electrophoretic separation of proteins was performed. Depending on the molecular weight of the protein, 10-19 % polyacrylamide separating gels were prepared covered with 5 % polyacrylamide stacking gels. Proteins were denatured by adding 4x SDS loading dye and by heating the sample up to 98 °C for 5 min. Proteins were separated using an electrophoresis chamber (Invitrogen) run at a constant voltage of 200 V in 1x TGS buffer. Protein bands were visualized with Coomassie staining (GiottoBiotech). For this purpose gels were shortly heated in coomassie staining solution, incubated for 20 min at RT followed by destaining in MilliQ-H_2O for > 1 h. PageRuler low range protein ladder (3.4-100 kDa) and Pierce™ MW marker (14.4-166 kDa) were used to estimate correct protein band size.

To assess purity and integrity of RNA, denaturing 8 % polyacrylamide (25 %, Rotiphorese® sequencing gel concentrate) TBE-PAGE with urea was prepared. RNA samples were prepared by mixing equivolumes of 500 ng RNA with 2x formamide loading dye and incubating the sample at 98 °C for 1 min. RNA was separated by running gels at constant 80 V in 1x TBE buffer for 1-1.5 h.

To monitor homogenous RNA folding, native 8 % polyacrylamide (40 %, Rotiphorese® gel, 19:1) TBE-PAGE was prepared. For EMSAs, 4 % native TBE-PAGE was made. Prior to electrophoresis run, RNA was denatured at 98 °C for 5 min and refolded by snap cooling on ice or slowly cooling to RT. Then, samples were prepared by mixing equivolumes of 500 ng refolded RNA with 50 % glycerol. RNA was separated by running gel at constant 80 V in 1x TBE buffer for 1 h. Finally, both denaturing and native TBE-PAGE were stained in 1x TBE buffer supplemented with 1:10000 Roti® GelStain Red (Roth) for 5 min. Gels were rinsed with 1x TBE buffer to remove non-intercalated stain. Subsequently, stained RNA was visualized in the Fusion SL 4 device and respecitve software (Vilber Lourmat) using the UV

option. Single-stranded RNA (ssRNA) low range ladder (50-300 nt) was used as molecular size marker.

2.4.3 Analytical limited proteolysis

Limited proteolysis experiments were performed to identify a stable subdomain of *dm*TRMT2A for crystallization. For analytical limited proteolysis of *dm*TRMT2A FL, 0.6 mg/mL protein was incubated with different concentrations of proteases (0.1 mg/mL = 1:10, 0.01 mg/mL = 1:100, 0.001 mg/mL = 1:1000) in a final volume of 10 µL using SEC-B buffer for dilution. Samples were incubated on ice for 30 min. After addition of 4x SDS loading dye to stop the reaction, samples were separated with SDS gel electrophoresis. The proteases Trpysin, Chymotrypsin, Elastase, Subtilisin and Glu-C protease were used. After this initial experiment, the experiment was repeated with varying incubation times of 30 min, 1 h and 2 h.

2.4.4 Methyltransferase assay

The commercially available Methyltransferase assay MTase Glo™ from Promega was established to assess enzymatic properties of hTRMT2A FL and the inhibitory activity of selected compounds on hTRMT2A enzymatic function (Hsiao et al., 2016). The assay was performed according to manufacturers recommendations and experiments described in Hsiao et al., 2016. For the assay white-opaque OptiPlate™-384 (PerkinElmer) and the EnVision 2104 MultiLabel plate reader (PerkinElmer) were used. Final volume of all reactions was 20 µL. Concentration-series were pipetted in 96-well plates.

2.4.4.1 Saturation curves with increasing substrate concentration

Experiments to determine K_m values were performed with increasing substrate concentrations. The 4x reaction buffer 1 (80 mM Tris buffer pH 8.0, 200 mM NaCl, 4 mM EDTA, 12 mM $MgCl_2$, 0.4 mg/mL BSA, 4 mM DTT) was prepared and frozen in aliquots. The 2x substrate solution, a 2x tRNA concentration series of 0-12 µM PAGE-purified tRNA, was pre-pipetted using dilution buffer (1x reaction buffer 1, 40 µM SAM in DEPC-H_2O). Dilution buffer alone served as no-substrate control. Moreover, 2x enzyme solution was prepared (1x reaction buffer 1, 10 µM hTRMT2A FL). For the assay, 4 µL of 2x substrate solution was mixed with 4 µL of 2x enzyme solution in a 384-well plate, reaching a final concentration of 0-6 µM tRNA and 5 µM hTRMT2A FL. Next, plates were centrifuged for 1 min at 1000 rpm (56 x *g*) in a Hettich universal 320 centrifuge. Then, plates were sealed to avoid evaporation and shaken for 2-3 min on a horizontal plate shaker (Heidolph unimax 1010, speed 3). After an incubation period of 1 h at RT, the reaction was stopped by addition of 2 µL 0.5 % TFA diluted in MilliQ-H_2O. The stopped reaction was incubated for 5 min at RT, before 2 µL of a

6x MTase Glo™ reagent diluted in MilliQ-H_2O was added. Plates were centrifuged for 1 min at 1000 rpm, sealed, shaken for 2-3 min and then incubated for 30 min at RT. Thereafter, 12 µL (1 volume) of MTase Glo™ solution was added. Plates were centrifuged another time for 1 min at 1000 rpm, sealed and shaken for 2-3 min. An incubation period of 30 min at RT in the dark was followed by lumniscence-measurement. The substrate and enzyme concentrations given here apply to K_m curve results described in **3.3.2** and **3.4.1**, which were performed in triplicates. For initial refinement of the assay other substrate and protein concentrations were used, but otherwise experimental procedure remained the same.

2.4.4.2 Saturation curves with increasing protein concentrations

Saturation curves experiments to assess concentration-dependent effects of enzyme on enzymatic reaction were performed with constant substrate concentration and increasing amounts of enzyme. The same procedure as described in **2.4.4.1** was applied. However, the concentration series was prepared using the 2x enzyme solution, prepared with increasing protein concentrations in dilution buffer. The 2x substrate solution (with constant substrate concentration) was prepared in 1x reaction buffer. Downstream processing was performed as described above.

2.4.4.3 Inhibitors

Third, inhibitor experiments were performed to assess inhibitory activity of selected compounds on hTRMT2A enzymatic activity. The experiment was set up as described above with the exception that the number of pipetting steps was reduced to minimize error. Due to poor water solubility of some compounds, all compounds used in the assay were first diluted in DMSO. Overall, compounds were prepared 5x their final concentration in 1x reaction buffer 1 containing 2.5 % DMSO. A reaction with only 1x reaction buffer 1 containing 2.5 % DMSO was used as control to normalize for inhibitory effects of DMSO.

A 2.5x reaction solution containing 12.5 µM hTRMT2A FL, 0.625 µM $tRNA^{Phe}$ and 2.5x MTAse Glo™ reagent diluted in 1x reaction buffer 1 was prepared. For the assay, 4 µL of 2.5x reaction solution was incubated with 2 µL 5x compound solution for 5-10 min at RT. To start the reaction, 4 µL of 2.5 µM SAM diluted in 1x reaction buffer 1 was added. Plates were centrifuged for 1 min at 1000 rpm, sealed, shaken for 2-3 min and then incubated for 1 h at RT. Thereafter, 10 µL (1 volume) of MTAse Glo™ solution was added. Plates were centrifuged another time for 1 min at 1000 rpm, sealed and shaken for 2-3 min. An incubation period of 30 min at RT in the dark was followed by lumniscence-measurement. The final reaction consisted of 5 µM hTRMT2A FL, 0.25 µM $tRNA^{Phe}$, 1 µM SAM and 1 mM compound in 1x reaction buffer 1. The initial pilot assay was performed with dilutions of 50 µM and 6.25 mM inhibitor. Inhibitor experiments were performed in triplicates.

2.4.4.4 m^5U levels of tRNA and RNA

To indirectly measure TRMT2A-dependent m^5U levels of cellular RNA, the MTAse Glo™ assay was performed with purified total mouse RNA and tRNA, as well as purified total HEK RNA as described before (Thongdee et al., 2019). For these experiments the adapted 1x reaction buffer 2 (50 mM Tris-HCl pH 8.0, 5 mM $MgCl_2$, 50 mM KCl) was used. Per reaction 5 µM hTRMT2A FL, 50 µM SAM and 2.5 µg total mouse RNA or 0.5 µg purified mouse tRNA or 250 ng total HEK RNA were mixed in a volume of 9 µL using 1x reaction buffer 2. A reaction without RNA served as background control. After 30 min incubation at RT, 1 µL of 10x MTAse Glo™ reagent was added. Samples (9 µL) were transferred to the 384-well plate, centrifuged for 1 min at 1000 rpm, sealed and shaken for 2-3 min. After 30 min incubation period at RT, 9 µL MTAse Glo™ detection solution was added. Plates were centrifuged, sealed, shaken and then incubated for another 30 min at RT in the dark. Finally, luminiscence signal was measured. Mouse RNA and tRNA were obtained from the liver of two different animals per condition (wildtype, TRMT2A knockout) and measured in triplicates. Total HEK RNA was obtained from biological duplicates (two different passages) and measured as technical triplicates.

2.5 RNA work

During RNA handling special care was taken to work with gloves, treat surfaces with RNAse away and to use DEPC-treated H_2O. RNA sequences of *in vitro* transcribed RNA are listed in **Table 8**.

2.5.1 Small-scale *in vitro* transcription

For small-scale *in vitro* transcription of RNA the MEGAshort script T7 kit (Thermo) was used according to manufacturer's recommendations. RNA was *in vitro* transcribed from a forward primer that contained the T7 RNA polymerase promotor region and a reverse primer that consisted of the reverse complement DNA template and the T7 RNA polymerase promotor region (**Table 7**). To do so, a reaction mix was assembled with T7 polymerase, other kit components, the DNA oligonucleotide and the T7 promotor. The reaction was incubated for 3 h at 37 °C. From *in vitro* transcribed RNA the template DNA was removed by DNAse digestion (1.5 µL) at 37 °C for 15 min.

For purification of *in vitro* transcribed RNA, PCI precipitation was performed. The reaction was mixed with 115 µL DEPC-H_2O and 15 µL 3 M NaOAc. Next, 1 volume (150 µL) phenol-chloroform-isoamylacohol (25:24:1) was added. After centrifugation for 1 min at 16.100 x *g*, upper aquous phase was transferred to new tube and mixed with 1 volume chloroform to remove phenol. The recovered upper phase from this purification step was precipitated in presence of 0.5 µL RNA-grade glycogen and 2 volumes EtOH at -20 °C for > 20 min. RNA was pelleted at 4 °C for > 20 min with 16.100 x *g*. RNA pellet was air-dried and resuspended in 20 µL DEPC-H_2O. Conformational homogenity and product size of purified RNA was monitored by native/denaturing PAGE.

2.5.2 Large-scale *in vitro* transcription

For the methyltransferase MTase Glo™ assay higher amounts of RNA was needed, wherefore large-scale *in vitro* transcription was conducted. A HPLC purified forward primer, which contained the T7 RNA polymerase promoter region, was annealed with a PAGE purified reverse primer that consisted of the reverse complement DNA template and the T7 RNA polymerase promoter region. In brief, 4 µM forward primer, 3.3 µM reverse primer and 20 mM $MgCl_2$ were incubated for 5 min at 60 °C in a final volume of 1.2 mL, followed by cooling down to 20 °C. To the DNA template reaction, 4 mM of each NTP, 16 mM $MgCl_2$, 80 mg/mL PEG 800, 10x TRX buffer (40 mM Tris/HCl pH 8.0, 1 mM spermidine, 0.1 % Triton X-100, 5 mM DTT) and 0.5 mg/mL T7 RNA polymerase were added in a final volume of 5 mL. The optimal $MgCl_2$ concentration for successful *in vitro* transcription was pre-determined with a $MgCl_2$ screening from 0-60 mM $MgCl_2$. The transcription reaction was incubated for 3 h at 37 °C. Emerging precipitate was removed by centrifugation for 10 min at

4 °C with 14.000 x *g*. The RNA was precipitated with 0.1 volumes 3 M NaOAc and 3.5 volumes EtOH for > 30 min or over the weekend at -20 °C.

Precipitated RNA was pelleted by centrifugation for > 30 min at 4 °C with 14.000 x *g* and air-dried. Next, pellet was solubilized by adding 500 µL DEPC-H_2O and then mixed with 500 µL 2x formamide loading dye. Sample was seperated by 8 % denaturing TBE-PAGE gel run in 1x TBE running buffer ON at constant 300 V. Transcripts were visualized by UV-shadowing and correct product band was excised. To separate RNA from polyacrylamide gel, the excised gel piece was processed by electroelution in a Whatman Elutrap electroelution system (GE-Healthcare) at constant 200 V according to manufacturers recommendations. Every hour for > 8 h 1 mL of 1x TBE that contained eluted RNA was collected from the apparatus. Subsequently, unified RNA was dialyzed with a 3.5 S dialysis tubing (ZelluTans, Carl Roth) against 1 M NaCl at 4 °C ON. Moreover, RNA was twice dialyzed against DEPC-H_2O at 4 °C ON. Finally, RNA was lyophilized by vacuum centrifugation (Concentrator Plus, Eppendorf).

2.5.3 Mouse liver tRNA purification using ion-exchange chromatography

To purifiy tRNA from total RNA a protocol adapted with minor changes from Ponchon et al., 2017 was employed. In the laboratory of Dr. Aaron Voigt RNA was extracted from mouse liver using TRIzol reagent (Invitrogen) according to manufacturers instructions and purified total RNA dissolved in DEPC-H_2O. RNA was precipitated with 0.1 volume of 5 M NaCl and 2 volumes of EtOH. Next, RNA was pelleted for 30 min with 10.000 x *g* at 4 °C and then resuspended in RNA buffer A (40 mM Na_2HPO_4, pH 7.0). Sample was loaded with 0.5 mg/mL flow rate on a RNAse-free MonoQ 5/50 GL column (GE Healthcare) equilibrated with RNA buffer A. Next, the column was washed with 5 CV RNA buffer B (400 mM NaCl, 40 mM Na_2HPO_4, pH 7.0). Thereafter, RNA was eluted with a 20 CV linear gradient from RNA buffer B to RNA buffer C (700 mM NaCl, 40 mM Na_2HPO_4, pH 7.0). The fractions containing pure tRNA as monitored with 8 % denaturing PAGE were pooled and precipitated by adding 2 volumes of EtOH. tRNA was pelleted by centrifugation for 30 min with 10.000 x *g* at 4 °C and subsequently air-dried. Lastly, tRNA was resuspended in DEPC-H_2O and used for methyltransferase assays described in **2.4.4.4**.

2.5.4 Isotopic labeling of RNA

For electrophoretic mobility shift assays (EMSAs), RNA of interest was radioactively labelled with γ^{32}-P ATP. The 5'-end phosphate group of 13 pmol RNA was removed by FastAP™ thermosensitive alkaline phosphatase (Thermo). The reaction mixture was set up according to manufacturers recommendations and supplemented with 1 µL RiboLock RNAse inhibitor (Thermo). Next, a PCI extraction followed by isopropanol precipitation was

performed as described in **2.5.1**. Finally, purified RNA was dried and the pellet used for 5'-end phosphorylation with γ^{32}-P ATP (Hartmann Analytics) using the PKA kit (NEB) according to instructions. In short, RNA pellet was mixed with 2 µL 10x PKA buffer A, 2 µL T4 polynucleotide kinase and 3 µL y-^{32}P ATP in a final volume of 20 µL. Labelling was performed at 37 °C for 30 min and subsequently the enzyme was deactived at 75 °C for 10 min. With a NucAway™ spin column (Ambion) free nucleotides and radioactivity were separated from radiolabelled RNA according to manufacturers recommendations. Labelled RNA was diluted to a final concentration of 100 nM in DEPC-H_2O before usage and stored at -20 °C. To ensure proper RNA folding after each thawing cycle, RNA was denatured at 98 °C for 2 min and snap-cooled on ice prior to usage.

2.5.5 Electrophoretic mobility shift assay (EMSA)

EMSAs were performed to qualitatively assess complex formation and the affinity of protein to RNA. Complexes were formed in RNAse-free EMSA buffer (150 mM NaCl, 50 mM HEPES pH 7.5, 4 % (v/v) glycerol). PolyU (poly-uridine ssRNA, Sigma) competitor dilutions were prepared in EMSA buffer. Increasing protein concentrations (0-25 µM) were incubated with 100 nM γ^{32}-P-labelled RNA in the presence of 2.5 ng/µL polyU competitor in a final volume of 20 µL. This results in a final concentration of 5 nM labelled RNA and 0-1.25 µM protein per reaction. The mix was incubated at RT for 20 min. Meanwhile, 4 % native PAGE gels were freshly prepared. Samples were loaded into the pockets, inclusively an only RNA and only polyU competitor control. The protein-RNA complexes were resolved by running the native PAGE gel in 1x TBE running buffer at 70 V for 1 h. Gels were fixed by incubation in 30 % (v/v) methanol and 10 % (v/v) acetic acid solution for 10 min. Then, gels were dried in vacuum gel dryer (model 583, BioRad) for 2 h at 80 °C. For analysis phosphor imaging plates were exposed to the radioactive dried gels for > 20 min and scanned with a FLA-300 (Fujifilm) system. The program ImageQuantTL (version 8.1) was used to export image files. EMSAs were performed in triplicates.

2.5.6 3' end biotinylation of RNA

For surface plasmon resonance-based binding assays, RNA was 3' end biotinylated to immobilize it on a streptavidin coated surface chip. To do so, the Pierce™ RNA 3' end biotinylation kit (Thermo) was used according to manufacturer's recommendations. For a 30 µL biotinylation reaction 50 pmol PAGE-purified tRNA was used. Prior to assembly of reaction the highly structured tRNA was unfolded by heating to 85 °C for 5 min in the presence of 25 % DMSO. Labelled RNA was purified and precipitated with PCI extraction (see **2.5.1**) followed by isopropanol precipitation as described in **2.5.1**. RNA pellet was dissolved in 120 µL DEPC-H_2O and directly used in experiments outlined in **2.6.3**.

2.6 Biochemical/-physical experiments

2.6.1 Thermofluor assay

Thermofluor experiments were conducted to identify the protein's melting temperature T_m and thus the protein stability of selected hTRMT2A proteins, namely hTRMT2A FL, hTRMT2A RBD and hTRMT2A central 1. The sensitive SYPRO orange dye (Thermo, 5000 X in DMSO) was choosen for experiments (Boivin et al., 2013). Initially, conditions were optimized in a reaction volumne of 50 µL with 40 µL buffer of protein sample, 5 µL protein (1, 2 or 5 mg/mL) and 5 µL 100x, 50x, 10x SYPRO orange dye (final concentration: 10x, 5x, 1x). Experiments were run on a qPCR machine (Stratagene Mx3005P, Agilent Technologies) with 25-95 °C temperature gradient, incremental 0.5 °C steps per cycle and a cycle duration of 15 sec. Thermofluor assay was performed in triplicates for optimized conditions. T_m was calculated with an excel-script published by Boivin et al., 2013.

2.6.2 Right angle light scattering (RALS)

RALS was performed to determine experimentally the molecular weight of an hTRMT2A FL and to obtain information about its oligomerization status. Experiments were done with a 270 Dual Detector and a VE3580 RI Detector (Malvern) coupled to a Superdex 6 (5/150) column (GE Healthcare) at 4 °C. System was calibrated with 4 mg/mL BSA. Experiments were run with a flow rate of 0.4 mg/mL. The sample concentration of hTRMT2A FL for SLS runs was 1.1 mg/mL. Data were anlyzed with the OmniSEC 5.02 software (Malvern).

2.6.3 Surface plasmon resonance (SPR)

2.6.3.1 Protein-small molecule interactions

To assess protein-small molecule interactions, SPR was performed using a BIACORE 3000 system (GE Healthcare). hTRMT2A RBD was diluted in 10 mM HEPES, pH 7.5 for immobilization. Using coupling buffer (500 mM NaCl, 50 mM HEPES 7.5, 0.05 % Tween) the protein was amino coupled to a CM5 chip (GE-Healthcare) according to manufacturer's instructions reaching 3000 resonance units (RU). Protein-small molecule interactions were assessed at a flow rate of 30 µL/min in running buffer (150 mM NaCl, 50 mM HEPES 7.5, 0.05 % Tween). Analyte of interest was diluted in running buffer and injected for 2 min. To remove any residual attached compound, 2 min regeneration injections with 1 M NaCl were executed two times in between runs. The compound concentration series reached from 0.5 µM to 8 µM for the positive control spermine and for spermidine (compound 12) and from 0.5 µM to 32 µM for other compounds. Data were analysed with the BIAevaluation software (GE Healthcare). Obtained binding curves were double-referenced against the signal in the empty reference channel and a buffer run. At equilibrium of the binding curves the corresponding response was plotted against analyte concentration. The K_D was determined

by fitting this curve to a steady-state affinity model. All experiments were performed in triplicates.

2.6.3.1 RNA-protein interactions

To assess RNA-protein interactions, SPR was performed using a BIACORE 200 system (GE Healthcare). The biotinylated tRNA (120 µL) from **2.5.6** was immobilized on a streptavidin coated SA-chip (GE-Healthcare) according to manufacturer's instruction. Prior to immobliziation both the empty reference channels and the analyte channel were activated with three consecutive injections of 50 mM NaOH. Immbolization was performed in running buffer (150 mM NaCl, 50 mM HEPES pH 7.5, 0.05 % Tween) and a 10 µL/min flow rate. RNA-protein interactions were assessed at a flow rate of 30 µL/min. Analyte of interest was injected for 3 min and dissociated for 6 min. To remove any residual attached protein, 3 min regeneration injections with 0.5 M NaCl were performed for two times. The protein concentration series reached from 12.5 nM to 400 nM for hTRMT2A WT and from 15.6 nM to 1000 nM for the mutant TRMT2A IR. Curves were double referenced against signal from empty reference channel and buffer run. The K_D was calculated with the BIAevaluation software for the BIACORE 200 system. All experiments were performed in triplicates.

2.6.4 Western blot

Samples from BioID and Co-IP were subjected to Western blot experiments to check for enrichment and correct size of protein. Usually, 15 µL of sample mixed with 5 µL 4x SDS loading buffer were heated for 10 min to 95 °C or 10 min to 70 °C. Samples were loaded on a NuPAGE 4-12 % Bis-Tris gradient gels (Invitrogen) and run with 1x NuPAGE MOPS SDS running buffer for 1 h at 180 V. Prior to run 500 µL NuPAGE antioxidant (Invitrogen) was added to the front chamber. BlueStar Plus Prestained Protein Marker (Nippon Genetic) was co-run with samples.

To allow protein transfer from the SDS gel to a PVDF membrane (Thermo), the Western blot chamber from Invitrogen was assembled (bottom-sponge-whatman-gel-blotting membrane-whatman-songe-top). PVDF membrane was pre-activated for 1 min in MeOH. All botting components were soaked with 1x NuPAGE transfer buffer before assembly. Blotting module was assembled, the outer chambers filled with MilliQ-H_2O and the Westernblot run for 1.5 h at 30 V. Successful blotting was probed with Ponceau S staining. Thereafter, blots were rinsed with MilliQ-H_2O and blocked for 30 min using 1 % Casein in PBS-T (1 % Tween in PBS). All incubation steps were performed on a rotating wheel to ensure proper distribution of solution. After blocking, the solution was substituted by primary antibody diluted in 0.5 % Casein in PBS-T. Blots were either incubated ON at 4 °C or for 1 h at RT. Next, the blot was washed three times for 5 min in PBS-T. In case of anti HRP-Streptavidin

antibody the blot was washed five times for 5 min and therafter directly visualized. The other secondary antibodies diluted in PBS-T were added to washed blot and incubated for 1 h at RT. Three 5 min washing steps with PBS-T were performed before visualization of blots.

The chemoluminiscent substrate was activated by mixing solution A an B from the Pierce®ECL western blotting kit (Thermo) in a 1:1 ratio. The substrate was distributed over the whole blot. After incubation for 1 min, the blot was visualized with the Fusion SL 4 device and software (Vilber Lourmat) while residing in between two plastic sheets. chemoluminiscence and starlight options permitted simultaneous overlay of chemoluminiscent signal and molecular weight maker. All antibodies used in Western blot experiments and their dilutions are listed in **Table 15**.

Table 15 – Antibodies used for Western blots

Sample	Primary antibody/dilution	Secondary antibody/dilution
BioID samples	Streptavidin-HRP (Thermo, N100), 1:10.000	-
BioID and Co-IP samples (house keeping)	Anti-H3 (abcam, ab1791), polyclonal rat, 1:10.000	Goat-anti-rabbit-HRP (abcam6721), IgG H&L, polyclonal goat, 1:10.000
BioID samples (Input) and Co-IP samples	Anti-FLAG (*, IgG1), monoclonal rat, 1:10	Mouse-anti-rat-HRP (*, IgG1), polyclonal mouse, 1:1000

* Antibodies were kindly provided by the HMGU antibody core facility

2.6.5 Proximity-dependent biotinylation (BioID)

BioID experiments were conducted to identify the hTRMT2A proximity interactome in HEK cells as described (Roux et al., 2013). MP6, MW1 and MW2 HEK cells (**Table 11**) were plated on three 15 cm cell culture dishes with five replicates per condition. At 70 % cell confluency protein expression was induced by addition of doxycycline (1:1000). 6 h later 1 mL steril-filtered 20x DMEM/biotin was added to the cells to reach a final concentration of 50 µM biotin. Cells were incubated for 16-18 h. GFP-expression and thus successful induction was inspected with a fluorescence microscope (EVOS FL, Life Technologies). Prior to trypsination cells were washed with PBS. Detached cells were centrifuged for 5 min at 4 °C with 300 x *g*. Two additional wash steps of the cell pellet with PBS ensured complete biotin removal. Washed cell pellets were frozen in liquid nitrogen to align all sample time points.

Cell pellets were thawed and resuspended in 5 mL lysis buffer (50 mM Tris-HCl pH 7.4, 500 mM NaCl, 0.2 % SDS) freshly supplemented with 1:1000 benzonase (Thermo), 1 mM DTT and 1 tablet of Pierce® Protease Inhibitor (per 100 mL lysis buffer). Thereafter, cell suspension was incubated on a rotating wheel at 4 °C for 30 min. After 500 µL of 20 % Triton X-100 was added, the samples were sonicated for 1 min with 30 % duty cycle and the output level at mid position (Bandelin Sonopuls GM 70UV 70). Three sonication rounds were

performed, and the samples incubated on ice for 5 min in between them. Before the third sonication round, 4.5 mL pre-chilled 50 mM Tris-HCl pH 7.4 was added and mixed.

Sonicated samples were distributed on 2 mL eppendorf tubes and centrifuged for 10 min at 4 °C with 16.100 x *g*. During sample centrifugation, 500 µL Dynabeads MyOne Streptavidin T7 magnetic beads (Thermo) per condition were equilibrated in a 15 mL tube containing 1.5 mL lysis buffer and 1.5 mL 50 mM Tris-HCl, pH 7.4. Beads were placed in a magnetic stand (DYNAL®, Invitrogen) for 3 min. Then, supernatant was removed by pipetting and the protein-containing supernatant from the centrifugation step was added to the equilibrated beads. Solution and beads were incubated on a turning wheel ON at 4 °C. Before (input) and after incubation ON (supernatant) 80 µL of sample were pertained for Western blot analysis.

The supernatant was removed from the beads and substituted with 8 mL of wash buffer 1 (2 % SDS in MilliQ-H_2O), which was gently pipetted up and down. Beads were generally washed by incubating the beads for 8 min with wash buffer on a turning wheel at RT. Then, tubes were placed in a magnetic stand, incubated for 3 min and the solution was then substituted by the next wash buffer. The wash step with wash buffer 1 was repeated. Next, beads were washed once with wash buffer 2 (0.1 sodium deoxycholate, 1 % Triton X-100, 1 mM EDTA, 500 mM NaCl, 50 mM HEPES pH 7.5) and wash buffer 3 (0.5 % sodium deoxycholate, 0.5 % NP-40, 1 mM EDTA, 250 mM LiCl, 10 mM Tris-HCl pH 7.4). To remove detergent, beads were washed three times with wash buffer 4 (1 mM EDTA, 20 mM NaCl, 50 mM Tris-HCl pH 7.4). After each wash step 80 µL sample was collected for Western blot analysis.

Washed beads were resuspended in 1.5 mL of 50 mM Tris-HCl pH 7.4 and distributed on two tubes: 1.35 mL for mass spectrometry and 150 µL for Western blot analysis. Both tubes were put in magnetic stand to remove supernatant. For elution 50 µL 1x sample buffer (50 mM Tris-HCl pH 6.8, 12 % sucrose, 1 % SDS, 0.004 % bromophenol blue, 20 mM DTT) supplemented with 3 mM biotin was added to beads, mixed and incubated at 98 °C for 7 min. Subsequently, samples were placed in magnetic stand and supernatant transferred to a new tube for respective mass spectrometry analysis in the HMGU proteomics core facility (Dr. Stefanie Hauck) and analytical Western blot analysis (paragraph **2.6.4**).

2.6.6 Co-immunoprecipitation (Co-IP)

Co-IP experiments of hTRMT2A WT and IR were performed to identify the hTRMT2A proteome. MP3, MW3 and MW4 HEK cells (**Table 11**) were plated on a 15 cm cell culture dish. At 70 % cell confluence protein expression was induced with doycycline (1:1000). 16-18 h later GFP expression was inspected with fluorescence microscopy and cells were washed twice with PBS. For cell harvest, 10 mL ice-cold PBS was added and cells scraped

off the plate. Cell suspension was centrifuged for 5 min at 4 °C with 300 x *g*. Pellets were flash-frozen in liquid nitrogen to ensure equal sample time point.

Cell pellets were thawed and resuspended in 1 mL lysis buffer (50 mM Tris-HCl pH 7.8, 150 mM NaCl, 1 mM EDTA, 1 % Triton X-100) supplemented with one tablet Pierce® Protease Inhibitor (per 100 mL lysis buffer). Suspension was transferred to a new tube and centrifuged for 10 min at 4 °C with 16.100 x *g*. Meanwhile, 50 µL Anti-FLAG® M2 Magnetic Beads (Merck) were equilibrated two times with 900 µL TBS (50 mM Tris-HCl pH 7.8, 150 mM Nacl) and three times with 900 µL lysis buffer. In between wash steps the beads were incubated for 3 min on a magnetic stand (DynaMag 2, DYNAL®, Invitrogen). Then, 3.5 mg protein from the supernatant of the centrifugation step were added to the equlibrated beads. Protein concentration was measured with the Bradford assay solution (Roth) according to instructions. Beads were incubated for 1 h at 4 °C in the shaking mode on a rotator wheel. Therafter, unbound protein was removed by washing three times with 900 µL high salt wash buffer (50 mM Tris-HCl pH 7.8, 250 mM NaCl, 1 mM EDTA, 1x Triton X-100). The third wash step was incubated for 5 min at 4 °C in shaking mode on a rotator wheel. To remove detergent, beads were washed three times with 900 µL 50 mM Tris-HCl, pH 7.8. Beads were distributed to two tubes for elution: 900 µL for mass spectrometry and 100 µL for Western blot analysis. Elution was performed by addition of 20 µL 2x Laemmli buffer (4 % (w/v) SDS, 20 % glucose, 0.004 % bromophenol blue, 125 mM Tris-HCl pH 6.8) and incubation for 10 min at 98 °C. Finally, tubes were placed into the magnetic stand and the supernatant transfered to a new tube for respective mass spectrometry analysis and analytical Western blot analysis (**2.6.4**).

2.6.7 Mass spectrometry and crosslinking

For *in vitro* reconstitution, PAGE purified $tRNA^{Gln}$ (**2.5.2**) and purified hTMRT2A FL (**2.3.6**) were sent for analysis. For complex formation a 1:1 ratio of $tRNA^{Gln}$ and hTRMT2A FL was incubated on ice for 30 min. Then, complex was separated from single RNA and protein with SEC using a S6 (15/150) column. Denaturing PAGE and SDS PAGE analysis allowed to unify complex-containing elution fractions. The complex was concentrated, and flash frozen in liquid nitrogen for transport.

In vitro reconstituted and purified hTRMT2A FL-$tRNA^{Gln}$ complexes were crosslinked and analysed by mass spectrometry in the Hennig Urlaub laboratory by Luisa Welp and Dr. Monika Raabe (MPI Göttingen). For UV crosslinking, the complex was irradiated at 254 nm for 10 min on ice using an in-house built crosslinking apparatus as described previously (Kramer et al., 2014). For chemical crosslinking, mechlorethamine (NM, B1785, APExBIO Technology LLC) was added to a final concentration of 1 mM following incubation for 30 min at 37 °C. Crosslinked samples were precipitated using ethanol and further processed as

described in Kramer et al., 2014. In brief, 10 µg RNase A (EN0531, Thermo Fisher Scientific), 1 kU RNase T1 (EN0531, Thermo Fisher Scientific) and 250 U PierceTM universal nuclease (88700, Thermo Fisher Scientific) were used for tRNA digestion that was carried out for 2 h at 37 °C. Subsequently, proteins were digested using trypsin (V5111, Promega) at a 1:20 (enzyme to protein) mass ratio. After protein digestion, another 10 µg of RNase A and 1 kU of RNase T1 were added and the samples were incubated for 1 h at 37 °C. Free nucleotides and salts were removed using C18 columns (744601, Harvard Apparatus) and crosslinked peptides were enriched using in-house packed TiO_2 columns (Titansphere 5 µm; GL Sciences). Enriched peptides were dried and dissolved in 2 % (v/v) acetonitrile, 0.05 % (v/v) TFA. LS-MS/MS analyses were performed on a Thermo Scientific Orbitrap Exploris 480 mass spectrometer coupled to a nanoflow liquid chromatography system (Thermo Scientific Dionex Ultimate 3000). Peptide separation was performed over 58 min with a flow rate of 300 nl/min using a linear gradient and a buffer system consisting of 0.1 % (v/v) formic acid (buffer A) and 80 % (v/v) acetonitrile, 0.08 % (v/v) formic acid (buffer B). Peptide-nucleotide heteroconjugates were analysed in positive mode using a data-dependent top 30-acquisition method. MS1 and MS2 resolution were set to 120.000 and 30.000 FWHM, respectively. AGC targets were set to 10^6 (MS1) and 10^5 (MS2), normalized collision energy to 28, dynamic exclusion to 10 s, and maximal injection times to 60 ms (MS1) and 120 ms (MS2). Mass spectrometry data were analysed and manually validated using the OpenMS pipeline RNPxl and Open MS TOPPASViewer (Kramer et al., 2014).

2.7 Structural biology

2.7.1 Crystallization screens and optimization of crystals

Crystallization screens were performed at the HMGU X-ray Crystallography Platform run by Dr. Robert Janowski (Niessing laboratory). Before crystallization, protein samples were centrifuged at 4 °C for 10 min with 16.000 x *g* to remove precipitated protein. To identify the optimal protein concentration for crystallization, a PCT™ pre-crystallization test (Hampton Research) was performed according to manufacturers recommendations.

For initial crystallization condition screening, 200 nL protein was mixed with 200 nL reservoir solution from commercial crystallization screens in sitting-drop 96-well format using a Mosquito nandrop dispenser (SPT LabTech). Following commercial screens from Hampton Research were used: JSCG+, Nucleix, PACT, Natrix, AmSO4, MPD, Classics I, Classics II, PEG. Pipetted plates were stored at 20 °C or 4 °C and visually inspected with an Olympus SZX16 microscope. Polarized light and izit crystal dye were used in case of uncertainty about protein or salt nature of crystals. When crystal size was appropriate, crystals were mounted in a nylon fiber loop and cryoprotected with 25 % (v/v) ethylengylcol. Crystals were flash frozen in liquid nitrogen for storage.

If crystals were too small, they were manually optimized. Either reservoir solution was directly used from commercial crystallization screens or stock solutions were self-prepared and steril filtered with a 0.22 µm filter. Crystals were optimized with the hanging drop vapor diffusion method. Reservoirs of the VDX 24-well plates contained 1 mL of prepared reservoir solution. The crystallization drop was set up with 1 µL of protein and 1 µL of reservoir solution on an OptiClear Plus square cover slip. Either pH, salt or precipitant concentration of the reservoir solution was varied in incremental steps. Moreover, protein concentration was another variable changed during optimization. Grown crystals were mounted and frozen as described above.

For co-crystallization with the cofactor SAM/SAH or compounds, the protein and small molecule were mixed in a molar ratio of 1:2 to 1:5 protein:compound in the respective SEC buffer. Then, the mix was incubated for 30 min on ice and dispensed into crystallization screen plates as described above.

Initial crystals of hTRMT2A RBD (8 mg/mL) grew in 0.22 M Li_2SO_4, 0.1 M NaOAc (pH 4.5) and 26 % PEG 6000 (PEG screen). Dataset with higher resolution of 1.2 Å was obtained from a crystal grown in a condition with 0.2 M CsCl and 2.2 M $AmSO_4$ ($AmSO_4$ screen). *dm*TRMT2A RBD crystals (4-8 mg/mL) grew in 2 M $AmSO_4$ and 2 M NaCl ($AmSO_4$ screen). Non-reprodubile, small crystals of *dm*TMRT2A FL grew in 0.2 M $CaCl_2$ 0.1 M HEPES (pH 7.5) and 28 % PEG 400 (Classics I screen). All crystallization trials are summarized in **Supplemental Table 2.**

2.7.2 Crystal soaking

Small molecules can be soaked into appropriately sized crystals to provide information about localization of the small molecule in respect to the protein. hTRMT2A RBD crystals were soaked with compound 13, 15 and 17 designed in the laboratory of Prof. Dr. Giulia Rossetti (Forschungszentrum Jülich) by *in silico* screening. Compounds were diluted in reservoir solution and added to crystal containing drops in a final concentration of 2-6 mM.

Heavy atom containing compounds were soaked into *dm*TRMT2A RBD crystals in order to obtain a dataset for phase calculation and hence structure determination of the protein by single-wavelength anomalous dispersion (SAD). For soaking, 10 mM stock solution were added to the drop to reach a final concentration of 1-3 mM. For initial screening green Ta_6Br_{12}, NaBr and the derivatives Pt2 ($(NH_4)_2PtCl_4$) and Au3 ($NaAuCl_4$) from the heavy atom screen (Hampton Research) were used. Soaked crystals were frozen either directly or after 24 h equilibration. Datasets were successfully recorded for Pt2 and Au3 soaked crystals.

2.7.3 *In situ* proteolysis

In situ proteolysis and crystallization was employed to increase the chance of crystallization of the very pure *dm*TRMT2A (Wernimont and Edwards, 2009). As trypsin was identified as optimal protease for *dm*TRMT2A FL in limited proteolysis experiments (**2.4.3**), it was used in a concentration of 0.001 mg/mL and 0.0002 mg/mL for *in situ* proteolysis. Protein and trpysin were mixed in a 1:1 ratio with a final concentration of 6 mg/mL protein. After 30 min incubation on ice, initial crystallization trials were set up as described in **2.7.1** and pipetted plates were stored at 20 °C. Crystals emerged in a condition with 0.1 M HEPES (pH 7.5) and 1.4 M sodiumcitrate. However, these were salt crystals.

2.7.4 Data collection and solving X-ray structures

Diffraction data of frozen crystals were collected at -180 °C on the PXI beamline (DESY, Hamburg), PIII beamline (Swiss Light Source, SLS, Villigen) and MX1937 beamline (ESRF, Greoble). For all structures the diffraction data were indexed and integrated using XDS (Kabsch, 2010) and scaled using SCALA (Evans, 2006). Intensities were converted to structure-factor amplitudes using the program TRUNCATE (French and Wilson, 1978).

The structure of hTRMT2 RBD was solved at a resolution of 2.02 Å using the Auto-Rickshaw pipeline with protein sequence as input (Panjikar et al., 2005, 2009). For the molecular replacement step followed by several cycles of automated model building and refinement, the Auto-Rickshaw pipeline invoked the following X-ray crystallography software: BUCCANEER (Cowtan, 2006), MORDA (Vagin and Lebedev, 2015), SHELXE (Sheldrick, 2002), CCP4 (Winn et al., 2011), REFMAC5 (Murshudov et al., 2011), PHENIX (Adams et al., 2010) and RESOLVE (Terwilliger, 2002). Further model rebuilding was performed in

COOT (Emsley and Cowtan, 2004). Initial refinement was done with the 2.02 Å dataset, while follow-up refinement was done with another dataset having the higher resolution of 1.23 Å. The stereochemical analysis of the final model was done with Procheck (Laskowski et al., 1993), MolProbity (Chen et al., 2010) and the integrated validation programs of the protein data bank (PDB).

Heavy atoms (**2.7.3**) or SeMet containing crystals (**2.3.2**) were measured to obtain the structure of *dm*TRMT2A RBD. On the mounted crystal a fluorescence scanning was performed to identify the respective atom edge and thus to determine the X-ray energy needed for data collection. The structure was solved with SAD using the integrated SAD mode of Auto-Rickshaw pipeline. Further structure refinement was performed as described above and a final resolution of 1.6 Å was reached for a crystal soaked with Au3. Models were deposited in the protein data bank (https://www.rcsb.org) with following PDB-IDs: hTRMT2A RBD (2.02 Å) = 7NTN, hTRMT2A RBD (1.23 Å) = 7NTO, *dm*TRMT2A RBD (1.6 Å) = 7PV5. Refinement statistics of both hTMRT2A RBDs can be found in **Supplemental Table 3** and those of *dm*TRMT2A RBD in **Figure 15**.

2.7.5 Visualization of X-ray structures

Crystal structures and super positions of different molecules were visualized with PyMol (Schrodinger, https://pymol.org/2/, version 2.0.4.). RMSD was also calculated in PyMol.

2.8 Cell culture

2.8.1 Culturing of HEK cells and cryopreservation

Adherently growing HEK cells were used for cellular experiments. HEK cells were cultivated in complete medium at 37 °C in an incubator with 5 % CO_2. At 80 % confluency cells were propagated. Briefly, cells were washed with PBS, before 0.05 % Trpysin-EDTA was added to detach the cells. After incubation for 5 min at 37 °C, complete medium was added, and cell suspension centrifuged for 5 min with 300 x *g*. The supernatant was discarded, and the cell pellet resuspended in complete medium. For passaging the appropriate dilution was plated on 24-well, 6-well, 10 cm or 15 cm plates. Usually, a 1:10 dilution was optimal for HEK cell propagation. Cells were light microscopically inspected with an Olympus CKZ53 microscope.

For cryopreservation cells were trypsinated and pelleted. The pellet was resuspended in freezing medium, distributed in cryo vials and slowly frozen to -80 °C ON in a cool cell (Corning). Therafter, cells were transferred to liquid nitrogen for storage. Usually, material from a confluent 10 cm dish was distributed into four cryo vials.

Cells were thawed by adding warm complete medium to the frozen cells. The cell suspension was centrifuged for 5 min with 300 x *g*. Then, supernatant was aspirated, cells resuspended with the appropriate amount of fresh complete medium and plated in cell culture dishes.

2.8.2 Generation of stably transfected cell lines

For stable transfection of HEK cells a PiggyBac (PB) transposon plasmid was used. The PB system requires the gene of interest to be cloned into a PB vector with inverted terminal repeat sequences at each end. A representative plasmid map can be found in **Supplemental Figure 1**. Co-transfection with the PB helper plasmid (MP11), encoding for PiggyBac transposase, allows for stable insertion of the gene of interest into the chromosome. Protein expression can be induced by administration of doxycyline via the Tet-On/Off system (Li et al., 2013; Krendl et al., 2017). For transfection HEK cells were plated in a 6-well plate and grown to 80 % confluency. According to the Lipofectamine™ 3000 transfection kit manual (Invitrogen), two solutions were prepared. Solution 1 contained 7.5 µL Lipofectamine 3000 in 125 µL OptiMEM medium. Solution 2 contained 4 µL P3000™ reagent, 2.5 µg of PB plasmid with the gene of interest, 2.5 µg MP11 in 125 µL OptiMEM. Both solutions were mixed and incubated for 15 min at RT. HEK cells were washed two times with PBS and 2 mL fresh complete medium was added to the cells. After the incubation period of the lipofection solution, it was dropwise added to the cells and incubated for 3 days. For antibiotic selection complete medium supplemented with hygromycin B (0.7 mg/mL) was added and exchanged 2-3 times a week for stable integration of the PB plasmid into the genome.

2.8.3 Fluorescence-activated cell sorting (FACS)

For BioID and Co-IP experiment the same expression level of the protein of interest was achieved by fluorescence-activated cell sorting (FACS). Protein expression in cells was induced with doxycycline treatment (1:1000) 18 h before FACS experiment. For FACS the cells were detached with trpysin, washed twice with PBS for 5 min and resuspended in sterile FACS buffer (0.5 % BSA, 2 mM EDTA, 25 mM HEPES pH 7.5 in PBS). Directly prior to FACS experiment the cells were passed through a 35 µm cell strainer to prevent clocking of the FACS instrument. The Flow Cytometry Facility at the Biomedical Center in Munich performed FACS. First gating step substracted dead cells and aggregates. A second gate was set to sort the cell population with a low GFP signal into a 15 mL tube pre-filled with 2 mL complete medium. Of note, cells for the same experiment were sorted with the same gating profiles (**Supplemental Figure 2**). Sorted cells were plated in 6-well plates and propagated liked described in **2.8.1** with complete medium containing hygromycin-B.

2.8.4 Immunocytochemistry and fluorescence microscopy

Immunocytochemistry (ICC) experiments were performed to determine TRMT2A localization in HEK cells. Prior to the experiment, coverslips were poly-D-lysine (PDL) coated to prevent cell detachment. PDL solution was added to coverslips for 20 min at RT, two times washed with PBS and then dried for > 1 h at RT. Cells were cultivated on PDL coated coverslips in 12-well plates until a confluency of 60 %.

Following steps were performed at RT. Cells on coverslips were fixated for 7 min using 3.7 % fromaldehyde solution in PBS. After two PBS washing steps, cells were permeabilized for 5 min with 0.5 % Triton X-100 in PBS. Next, coverslips were transferred to a parafilm placed on top of a H_2O soaked Whatman paper to prevent evaporation of buffers from coverslips. Cells were blocked for 10 min with 200 µL blocking buffer (1 % donkey serum in PBS-T). Primary antibody diluted in blocking buffer was added for 1 h. After three washing steps with PBS-T, cells were incubated with secondary antibody diluted in blocking buffer for 1 h in the dark. Again, cells were washed three times with PBS-T. Therafter, cell nucleus was stained with DAPI at a concentration of 0.5 µg/mL DAPI (Thermo) in PBS for 5 min. This time coverslips were washed two times with PBS. Finally, coverslips were mounted cell-side down on a microscopic slide using the ProLong™ Diamond Antifade mountant (Invitrogen). Mounting medium was dried ON at RT in the dark, before imaging with the fluorescence microscope Axio.Observer.Z1 (Carl Zeiss) and the Zeiss imaging software. The instrument belonged to the Drukker laboratory (ISF, HMGU), which kindly provided access. The same exposure time was used for images of the same experiment. Images were analysed with the Fiji ImageJ software (Schindelin et al., 2012). All primary and secondary antibodies and their dilutions are listed in **Table 16**.

Table 16 – Antibodies used for Immunocytochemistry

Sample	Primary antibody/dilution	Secondary antibody/dilution
Co-IP cell line	Anti-FLAG (*, IgG1), monoclonal rat, undiluted	goat-anti-rat-Alexa647 (abcam, ab150167), polyclonal goat, 1:500
Co-IP cell line, background	Anti-IgG1, (*), monoclonal rat, 1:250	goat-anti-rat-Alexa647 (abcam, ab150167), polyclonal goat, 1:500

* Antibodies were kindly provided by the HMGU antibody core facility

2.9. Bioinformatics tools

Drosophila melanogaster DNA and protein sequences, as well as the *dm*TRMT2A containing plasmid were obtained from the FlyBase. *Chaetomium thermophilum* sequence information was retrieved from *Chaetomium thermophilum* genome resource of the Bork laboratory at EMBL (Bock et al., 2014). Two sequences were aligned with Blast from NCBI. Multiple sequence alignment was performed with ClustalO (Madeira et al., 2019) and visualized with ESPript 3 (Robert and Gouet, 2014). IUPred2A was used to predict unstructured regions within the protein (Mészáros et al., 2018). Based on protein sequence the ProtParam program of the ExPASy server calculated protein properties such as molecular weight, isoelectric point, and extinction coefficient. Secondary structure prediction of RNA was computed with the RNAfold web server (Hofacker, 2003). CATH domain analysis was performed using the CATH database (Knudsen and Wiuf, 2010).

Secondary structure of proteins was predicted with the Phyre2 (Kelley et al., 2015), SWISS-MODEL (Waterhouse et al., 2018) and the Robetta server (Kim et al., 2004). For the generation of hybrid tRNA-protein model the AlphaFold predicted homology model of hTRMT2A, ID Q8IZ69, was used (Jumper et al., 2021).

2.9.1 Statistical analysis with R

For various statistical tests custom R-scripts attached in **Supplemental Figure 8** were used. To check for normal distribution of data from inhibitor experiments the normality test function shapiro.test (), an R base function, was used. Significance of results from inhibitor treatment was calculated with the Wilcoxon rank sum test using the function wilcox.test () with default variables. Barplots were plotted with ggplot2.

2.9.2 Michaelis Menten fitting with R

Michaelis Menten fitting of K_M curves from MTAse Glo™ experiments was performed with custom R-script attached in **Supplemental Figure 9.** Briefly, the package ‚drc' and its function ‚drm' were used for Michaelis Menten fitting (Christian Ritz, Package ‚drc'). Curves and fitted models were plotted with ggplot2.

2.9.3 GO-term analysis

„Biological processes" (BP) and „cellular compartements" (CC) gene ontology (GO) term analysis was performed with data from BioID experiments using the GO enrichment analysis tool from gene ontology using the PANTHER databank (Ashburner et al., 2000; Mi et al., 2013; The Gene Ontology Consortium, 2021). UniProt protein names of significantly enriched hits from BioID experiments were used for GO enrichment analysis. Significance of GO-term enrichment was calculated as false discovery rate (FDR) with the Fisher's exact test. Using

the custom R-script found in **Supplemental Figure 10** a ggplot2 bubble diagram visualized enrichment for respective GO-term on x-axis, the significance of enrichment with color code and the counts per GO-term with node size.

2.9.4 Data processing for BioID and Co-IP mass spectrometry results

Raw spectra from mass spectrometry experiments were imported into Progenesis QI software (version 4.1). After feature alignment and normalization, spectra were exported as Mascot Generic files and were searched with Mascot (Matrix Science, version 2.6.2) against the human UniProt database (20,237 sequences). The following search parameters were used: 10 ppm peptide mass tolerance and 20 mmu fragment mass tolerance, one missed cleavage allowed, carbamidomethylation was set as fixed modification, methionine oxidation, and glutamine or asparagine deamidation were allowed as variable modifications. A Mascot-integrated decoy database search calculated the false discovery rate using searches with a mascot percolator score cut-off of 13 and appropriate significance threshold. Peptide assignments were imported into the Progenesis QI software, and the abundances of all unique peptides allocated to each protein were summed up. The resulting normalized abundances of the individual proteins were used for calculation of fold-changes of protein ratios between TRMT2A and BirA* backgroud as well as TRMT2A IR and TRMT2A WT. A ratio of at least two was considered differentially abundant. Statistical analysis was performed on log2 transformed normalized abundance values using the Student's t-test. Changes in protein expression between conditions were considered significant at $p < 0.001$. Using these data, volcanoplots were generated with the R-script adapted from Melina Klostermann (Zarnack laboratory) attached in **Supplemental Figure 11**. R-script for plotting the ratio of different conditions for example TRMT2A WT versus TRMT2A IR ratios can be found in **Supplemental Figure 12**.

3. Results

3.1 Structure determination of TRMT2A

Detailed understanding of the enzymatic mechanism of TRMT2A and a general understanding of its function requires structural information. Additionally, a three-dimensional structure is highly useful for structure-based drug discovery – an approach that was considered due to the drug target-like features of hTRMT2A outlined in section **1.4**. Hence, a major goal was to solve the structure either of TRMT2A full-length (FL) or subdomains of TRMT2A by X-ray crystallography, for which high amounts of pure and stable recombinant protein were required.

3.1.1 Expression and purification of hTRMT2A proteins

Human TRMT2A (hTRMT2A) consists of an N-terminal RBD and a C-terminal methyltransferase domain. Dr. Robert Janowski and Dr. Elena Davydova from our laboratory have already solved the structure of the RBD, spanning amino acids 67 to 147. According to structure homology models (Phyre2, SWISS-MODEL) and unstructured region predictors (IUPred2A), protein segments N- and C-terminal to the RBD are flexible. Additionally, hTRMT2A is predicted to exhibit a globular domain towards the C-terminus. As domains without flexible termini are more likely to crystallise (Gräslund et al., 2008), such a structured globular domain is supposedly the best starting point to pursue crystallography trials. Therefore, a set of SUMO-tagged globular domain fragments with different N-termini (aa 166, 178 and 198) and C-termini (aa 591 and 593) was generated.

CATH domain analysis allows for determination of domain borders based on evolutionary relationships of protein domains. Taking CATH information into account, the globular domain was further divided into a central domain 1 (aa 148-390), central domain 2 (aa 237-414), catalytic domain 1 (aa 391-625) and catalytic domain 2 (aa 414-590). Combinations of central-catalytic (aa 148-625) and RBD-central (aa 67-390) domains were generated too. According to homology models, the RBD and catalytic domain would interact and potentially stabilise each other. Thus, fusion fragments lacking the central domain were designed; fusion 1 (aa 69-240/413-590) and fusion 2 (aa 166-240/413-590). To determine the optimal *E. coli* expression strain and fusion tag, small-scale expression screens were performed as described in paragraph **2.3.1**. Only the well-soluble proteins listed in **Figure 10A** were selected for large-scale purification. For a full list of all protein fragments refer to **Supplemental Figure 3**.

The solubility of the globular domain reaching from aa 166 to 593 outperformed shorter fragments (aa 178-593, aa 198-593). During large-scale purification of this globular domain (aa 166-593) the major problem was heavy degradation, which could not be resolved by

addition of a C-terminal His-Tag. Moreover, protein solubility was not optimal and low yield was obtained. Both issues could not be resolved by exchange of the SUMO-tag to a GST-tag, known to increase protein solubility, and purification of 18 L *E. coli* culture.

In contrast, subdomains of the globular domain, central domain 1 and 2, were well expressed and soluble in the *E. coli* strain pLyS. This *E. coli* strain is specifically designed for the expression of toxic proteins by encoding for T7 lysozyme, which suppresses basal expression of toxic protein of interest. During purification of central domain 1, impurities remained, which largely derived from co-elution of the tag and central domain 1 itself. Thus, SUMO-tag was exchanged by a thioredoxin (TRX)-tag. TRX-tagged protein enrichment and subsequent purification resulted in > 95 % pure and stable protein in sufficient amounts for crystallization. The purification protocol included a primary HisTrap FF column, after PreScission™ protease cleavage a subtractive HisTrap FF column to remove the TRX-tag and a final SEC step using a S75 (16/600) column (**Figure 10B**). Despite a positive pre-crystallization test, no crystals grew in any of the crystallization conditions.

To increase the likelihood of crystallization, the domain borders of SUMO-tagged central domain 2 were readjusted. This fragment showed increased degradation after tag-cleavage. Therefore, the SUMO-tag remained uncleaved in the final purification protocol, which resulted in > 95 % pure SUMO-tagged protein. The protocol started with protein enrichment using a HisTrap FF column and dialysis overnight without tag cleavage. Due to the presence of SUMO-tag, the subtractive HisTrap FF column step was exchanged by affinity chromatography using a HiTrap heparin column, followed by a final SEC step with a S75 (16/600) column (**Figure 10C**). Despite these adjustments, crystallization trials were unsuccessful.

Purification of the SUMO-tagged fusion protein 1 yielded < 80 % pure protein, which is insufficient for crystallization trials (**Figure 10D**). The protein was expressed in *E. coli* pLysS and purification protocol resembled the protocol for central domain 1 purification (**Figure 10D**). Despite major efforts, the main issue remained protein degradation.

Detailed purification strategies are summarized in **Supplemental Table 1** and all crystallization trials in **Supplemental Table 2**. The observed poor protein stability and solubility likely has the following reason. Mammalian posttranslational modifications increase protein stability and are not available during *E. coli* expression. To address this problem, firstly the full-length (FL) protein was expressed in insect cells, whose posttranslational-modification machinery is closer to the mammalian one as described in paragraph **3.1.2**. Secondly, two other hTRMT2A homologs – from *Drosophila melanogaster* (paragraph **3.1.3**) and *Chaetomium thermophilum* (paragraph **3.1.4**) were employed to increase the likelihood of crystallization and if successful to guide structure determination of the hTRMT2A.

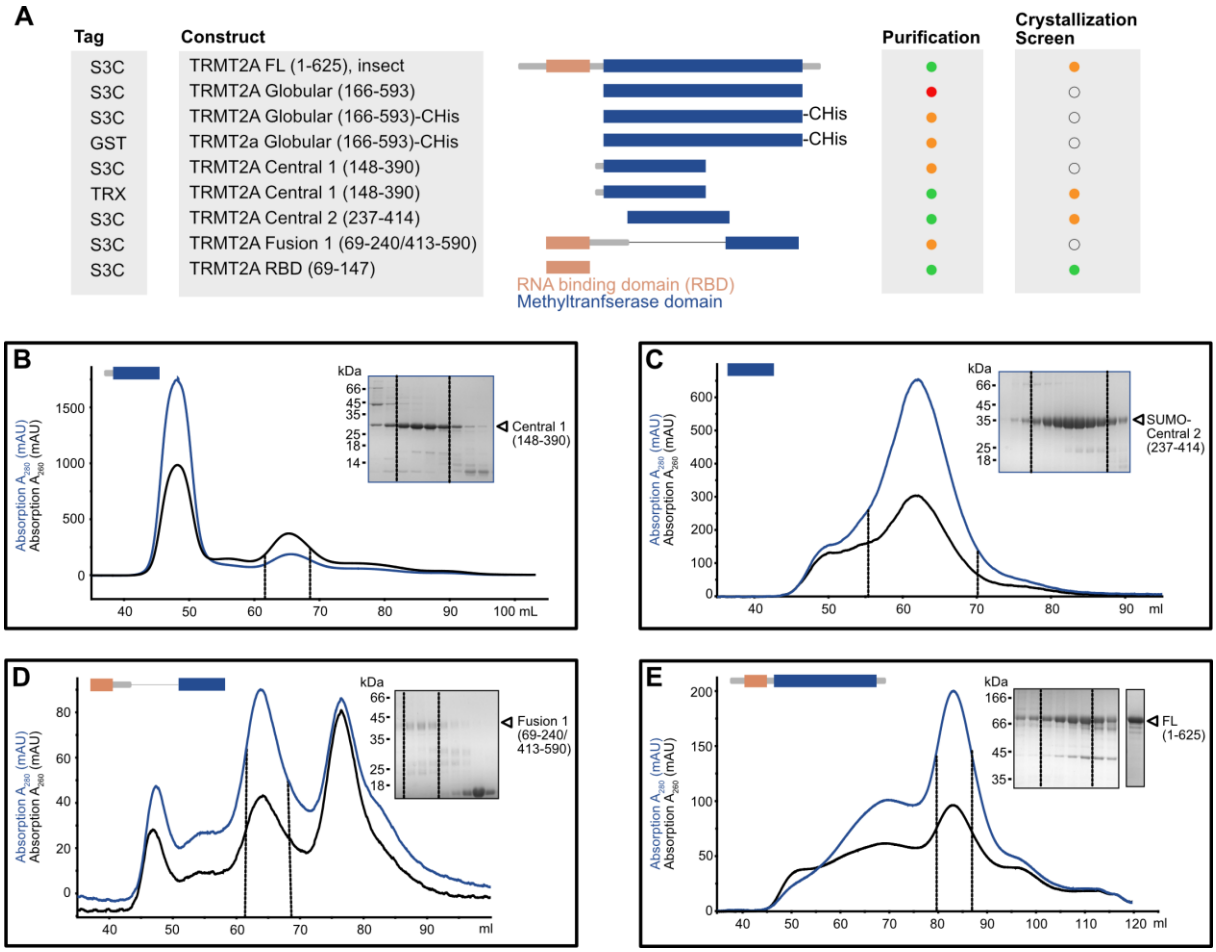

Figure 10 – hTRMT2A domains and protein purifications.
A The listed protein fragments with respective tag were used in this thesis. Middle panel shows the domain organization of hTRMT2A fragments. Success in purification and crystallization is indicated in green for successful, orange for moderately successful and red not successful. Only for hTRMT2A RBD a crystal structure was obtained. **B** SEC elution profile and respective SDS PAGE from last purification step of central domain 1 with 27.7 kDa. **C** SUMO-tagged central domain 2 with 33.2 kDa. **D** Fusion protein 1 with 39.4 kDa. **E** hTRMT2A FL with 68.9 kDa was expressed in insect cells. After SEC of hTRMT2A FL, a final subtractive GST column was performed to remove GST-tagged PreScission™ protease. Protein of interest is indicated with an arrow. Lines show fractions pooled for further experiments.

3.1.2 Expression and purification of hTRMT2A FL from insect cells

To produce well-expressed and purifiable recombinant hTRMT2A FL (aa 1-625), SUMO-tagged hTRMT2A FL was cloned into pFastBac plasmid, a vector for the Bac-to-Bac insect cell expression system. The protein was well expressed in Hi5 insect cells. Purification resulted in > 90 % pure and stable protein with moderate yield (around 1 mg from 1 L culture), which is a clear improvement to unsuccessful expression attempts of hTRMT2A FL in *E. coli*. SUMO-tagged protein was enriched with a HisTrap FF column. Subsequently, the tag was cleaved with PreScission™ protease and finally a SEC run was performed. Unfortunately, the concentration of the protein to 1 mL prior SEC caused heavy protein aggregation. Thus, larger injection volumes (5 mL) and a S200 (16/600) column instead of a S75 (16/600) were favoured to successfully resolve this issue. The SEC-purified protein co-eluted with the GST-tagged PreScission™ protease (dimerized form, 45 kDa). To separate

protease and protein a final purification step with GSTrap FF column was performed (**Figure 10E**). During crystallization trials of hTRMT2A FL, no crystals emerged, which is likely due to nucleic acid contaminations ($A_{260/280} > 0.6$). Any attempt to remove nucleic acids caused heavy protein degradation. Nevertheless, protein was purified in sufficient amounts and homogeneity for a variety of biochemical assays reported in chapter **3.2** and **3.3**.

According to right angle static light scattering experiments (RALS), hTRMT2A FL exists as monomeric species in solution with a measured molecular weight of 72.2 kDa, which is in line with computationally calculated molecular weight of 68.9 kDa (**Figure 11A/B**). BSA was employed for initial calibration run (**Figure 11C/D**).

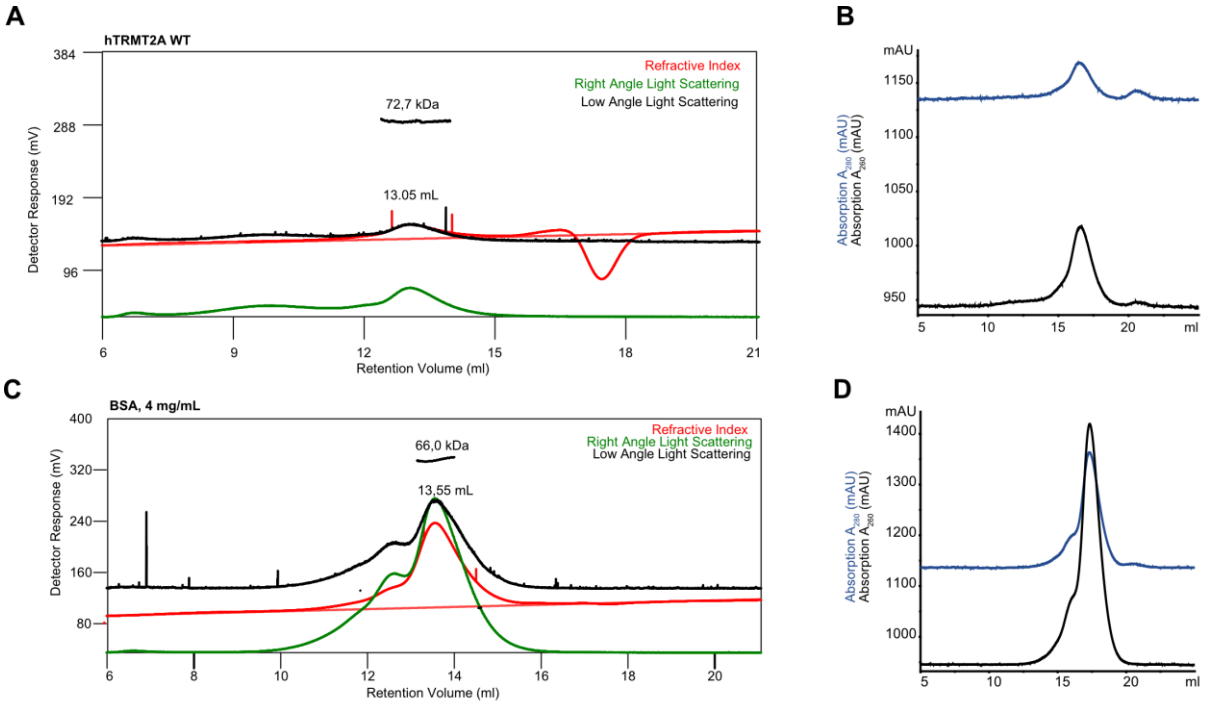

Figure 11 – RALS of hTRMT2A FL.
A Right-angle light scattering (RALS) run of 1.2 mg/mL hTRMT2A FL showed a light scattering peak at an elution volume of 13.05 mL corresponding to a calculated molecular weight of 72.2 kDa. Thus, hTRMT2A is monomeric in solution. **B** RALS was coupled to a SEC run using a S6 (15/150) column and the 3 mL delayed elution profile is shown. **C** RALS calibration run of 4 mg/mL BSA with elution volume of 13.55 mL and calculated molecular weight of 66.0 kDa in line with known molecular weight of BSA. **D** SEC run with BSA. Representative runs from duplicate measurements are shown.

3.1.3 Expression and purification of *dm*TRMT2A proteins

Except for the RBD, none of the hTRMT2A subdomains was suitable for crystallization purposes. Therefore, we switched to the *Drosophila melanogaster* (*dm*) ortholog of hTRMT2A. *dm*TRMT2A exhibits a 33.8 % sequence identity and a 49.0 % sequence similarity with hTRMT2A (ClustalO). Moreover, the domain organization of *dm*TRMT2A is predicted to be similar to hTRMT2A (**Figure 10A**), consisting of an N-terminal RBD and a C-terminal globular domain. Similarly, homology models were employed to design the fragments that are listed in **Figure 12A**. Additionally, sequence alignment with hTRMT2A

allowed for mapping the precise RBD borders of *dm*TRMT2A (**Supplemental Figure 4A**) and successful purification of > 95 % pure *dm*TRMT2A RBD protein. Expression and purification of *dm*TRMT2A RBD (aa 57-137) started with a HisTrap FF column step and tag cleavage. Subsequently, a subtractive HisTrap FF column removed the cleaved SUMO-tag and a final SEC step using a S75 (16/600) column was performed (**Figure 12B**). This protein was successfully crystallised as described in paragraph **3.1.6**.

To also obtain the crystal structure of the C-terminal part of *dm*TRMT2A, globular domain 1 (aa 57-579) and 1b (aa 57-581), which both include the RBD, as well as globular domain 2 lacking the RBD (aa 160-579) and *dm*TRMT2A FL (aa 1-620) were generated. All four SUMO-tagged proteins were well expressed and soluble in the *E. coli* Rosetta strain. Despite high protein purity of > 95 % during the purification of *dm*TRMT2A FL, nucleic acid contaminations were observed. Several techniques were employed to remove contaminating nucleic acids such as combined $AmSO_4$ and PEI precipitation, as well as slow denaturing and refolding with a urea gradient. However, nucleic acids were only successfully removed with a HiTrap Heparin FF column. Briefly, the final purification protocol of *dm*TRMT2A FL was performed with an initial HisTrap FF column, followed by PreScission™ protease-mediated tag cleavage, a HiTrap Heparin FF and a final SEC step with a S200 (16/600) column (**Figure 12C**). Despite a positive pre-crystallization test, only non-reproducible small needles occurred in one condition of the crystallization screen. Previously it was reported that with the aid of the co-factor SAM and its reaction product SAH, SAM-dependent methyltransferases were successfully crystallised (Alian et al., 2008; Jiang et al., 2017). However, in case of *dm*TRMT2A, co-crystallization with co-factors SAM or SAH and change of crystallization temperature to 4 °C did not improve the crystallization outcome. Purification and crystallization of *dm*TRMT2A FL expressed in insect cells did also not result in purer protein or protein crystals.

Generally, flexible N- and C-termini are one reported reason for unsuccessful crystallization (Gräslund et al., 2008). Thus, the globular domains 1 and 1b devoid of flexible termini were purified using the same purification protocol as described above for *dm*TRMT2A FL purification, which yielded > 90 % pure and stable protein in case of globular domain 1b (**Figure 12D**). The shorter globular domain 1, lacking three additional amino acid, degraded heavily during purification and hence was not suitable for crystallization trials (**Supplemental Figure 4B**). Crystallization of the globular domain 1b or co-crystallization with SAM or SAH or change of crystallization temperature was also not successful. Due to impurities, globular domain 2 (aa 160-579) was not suitable for crystallization trials either (**Supplemental Figure 4C**).

At last, limited proteolysis was employed to identify a minimal protein fragment lacking flexible regions and loops that prohibit crystallization (Wernimont, 2009). Optimal proteolysis conditions were identified and a stable *dm*TRMT2A subfragment (~50 kDa) generated by incubation with the trypsin protease (**Figure 12E**, left image). Other proteases such as elastase or chymotrypsin did not generate a suitable subfragment. Co-crystallization of *dm*TRMT2A FL with trypsin in identified conditions produced no protein crystals. Reasons for this failure could be that contaminations with partially trypsinated or FL protein might have interfered with crystallization. Hence, the trypsinated subfragments were separated from the rest of the protein with SEC using a S75 (16/600) column. However, SEC could not dissociate trypsin effectively, wherefore continued proteolysis was observed (**Figure 12E**, right image), which prevented further crystallization trials.

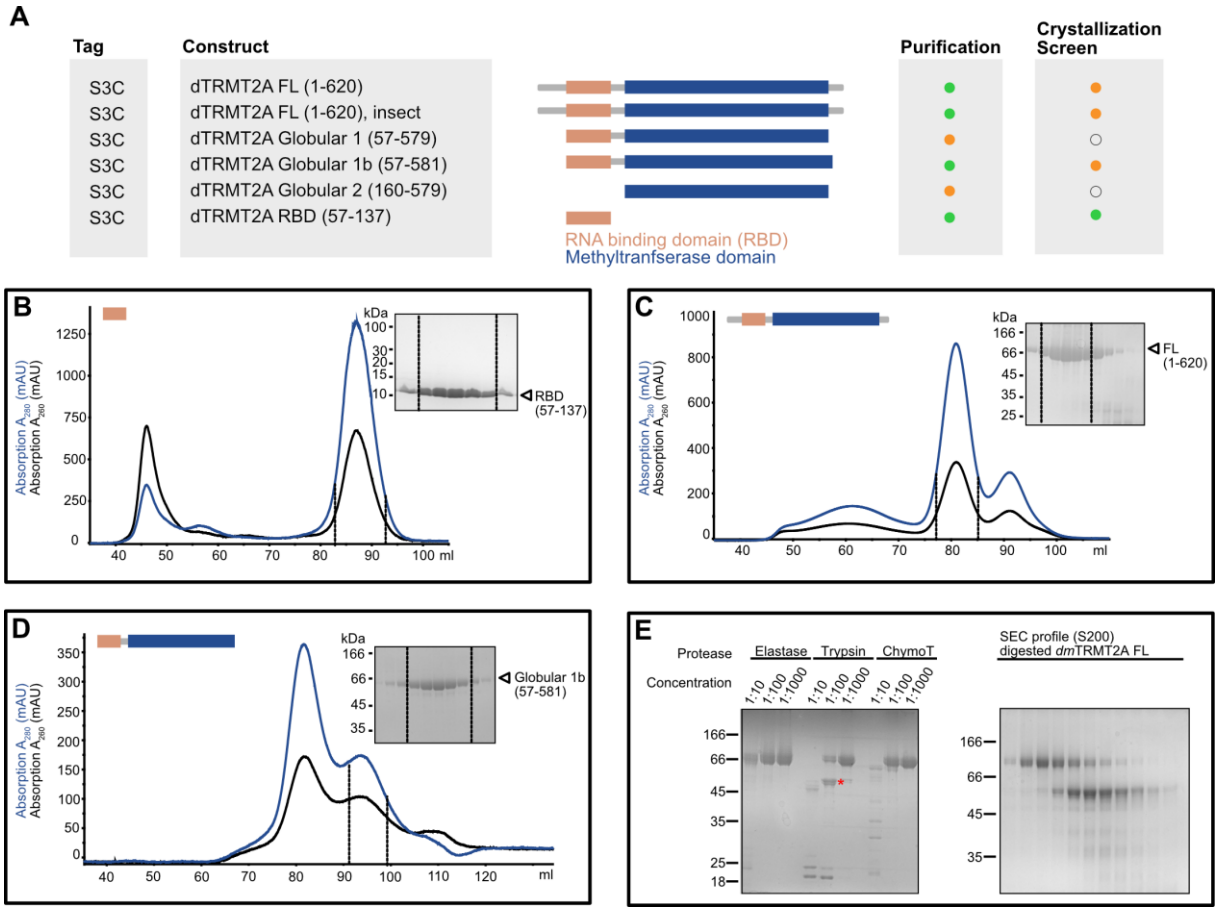

Figure 12 – *dm*TRMT2A domains and protein purifications.
A List of protein fragments with respective tags that were used in this thesis. Middle panel shows domain organization on *dm*TRMT2A. Purification and crystallization attempts are indicated in green as successful, orange as modestly successful and red as not successful. Only for *dm*TRMT2A RBD a crystal structure was obtained. **B** SEC elution profile and respective SDS PAGE from last purification step of RBD with 9.8 kDa. **C** Globular domains 1b with 65.3 kDa. **D** SEC profile of *dm*TRMT2A FL with 68.7 kDa. Protein of interest is indicated with an arrow on SDS-PAGE. Lines show fractions unified for further experiments. **E** Limited proteolysis experiments with *dm*TMRT2A FL. The left gel shows protein digestion with three selected proteases (elastase, trypsin, chymotrypsin) at different concentrations, 0.1 mg/mL (1:10), 0.01 mg/mL (1:100) and 0.001 mg/mL (1:1000). Stable subfragment emerged at around 50 kDa after incubation with 0.01 mg/mL trypsin (red asterisk). Right gel shows elution fractions from SEC run using a S75 (16/600) column to separate undigested and trypsin digested *dm*TRMT2A. Continued degradation and unsuccessful separation prevented crystallization of the 50 kDa subfragment.

3.1.4 Expression and purification *ct*Trm2 proteins

The termophilic fungus *Chaetomium thermophilum* exhibits an optimal growth temperature of 55-60 °C. Since *ct* proteins evolved to be more thermostable, they are better suited for structural biology campaigns (Bock et al., 2014). Hence, crystallization of the less conserved hTRMT2A homolog, *ct*Trm2, was pursued. Codon optimized GST-tagged *ct*Trm2 FL was synthesized by a commercial supplier. To generate C-terminal domain fragments, SUMO-tagged globular domain 1b (aa 54-544) and globular domain 2 (aa 91-544, without RBD), both devoid of flexible N- and C-termini, were cloned. Protein fragments used for successful purification are listed in **Figure 13A**. All proteins were well expressed and soluble in *E. coli* Rosetta. *ct*Trm2 FL purification protocol consisted of an initial GSTrap FF column, followed by tag-cleavage with PreScission™ protease. Heparin affinity chromatography was used to separate nucleic acid contaminations, followed by a SEC step. The SEC elution profile displayed an overlapping double peak indicative of dimer formation or aggregation. With a second SEC step, the peaks were separated, and the > 95 % pure protein could be subjected to crystallization trials (**Figure 13B**). None of the crystallization trials set up at different temperatures (RT, 4 °C) and with SAM/SAH cofactors were successful.

A Robetta-generated homology model of *ct*Trm2 showed four cysteines – C171, C177, C180, and C274 – in correct proximity to coordinate a metal ion, as it was already observed for the structurally related *E. coli* methyltransferase RlmD, which coordinates an iron ion (PDB: 3UWV, **Figure 13C**). Of note, the purified protein solution displayed a brown colour, which might derive from process-related impurities or indeed metal ions (Witkowska and Rowińska-Żyrek, 2019).

For purification of globular domain 1b and 2 an initial HisTrap FF column was coupled to a subtractive HisTrap FF column to remove the SUMO-tag. After the final SEC step globular domain 2 showed a purity of > 80 % (**Figure 13D**) and globular domain 1 (**Figure 13E**) a purity of > 90 %. However, crystallization trials remained unsuccessful. Like *ct*Trm2 FL, both globular domains displayed overlapping peaks during SEC. Cross contaminations from the other overlapping peaks could have prevented crystallization.

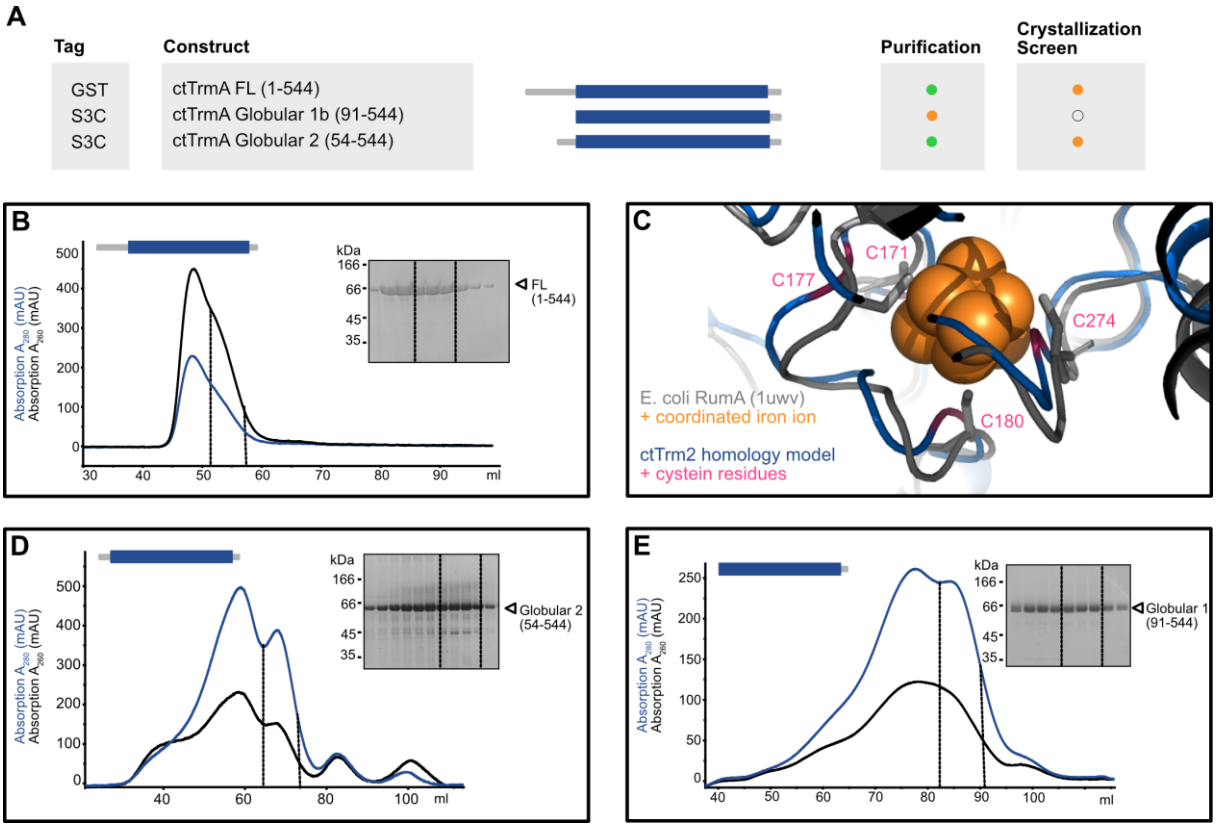

Figure 13 – *ct*Trm2 domains and protein purifications.
A List of protein fragments with respective fusion tag that were used in this thesis. Middle panel shows domain organization of *ct*Trm2. Success in purification and crystallization is indicated in green for successful, orange for medium successful and red not successful. No crystal structure of *ct*Trm2 was solved. **B** SEC elution profile and SDS PAGE from last purification step of *ct*Trm2 FL with 60.1 kDa. **C** Overlay of *E. coli* RlmD structure (3UWV, grey) and *ct*Trm2 Robetta-generated homology model (dark blue) with conserved RlmD cysteines (grey, stick visualization), respective *ct*Trm2 cysteines (pink) and RlmD coordinated iron ion (orange). **D** Final SEC of globular domain 1 with 54.5 kDa. **E** Final SEC of globular domain 2 with 50 kDa. Protein of interest is indicated with an arrow on SDS-PAGE. Lines show fractions unified for further experiments.

3.1.5 Crystal structure of hTRMT2A RBD

As mentioned above the crystal structure of hTRMT2A RBD (aa 67-147) has already been solved by Dr. Robert Janowski and Dr. Elena Davydova at a resolution of 2.02 Å (PDB: 7NTN). However, further crystallization trials were set up by me with purified, > 95 % pure hTRMT2A RBD (**Figure 14A**) to achieve a higher resolution structure. The optimal crystallization condition was found to be 0.2 M CsCl and 2.2 M $AmSO_4$, which was different from previously used conditions (paragraph **2.7.1**). The structure was solved using molecular replacement with the initial hTRMT2A RBD structure as search model. Processing statistics of the initial and newly solved structure are listed in **Supplemental Table 3** (PDB: 7NTO). As result, the resolution could be improved from 2.02 Å of the previous structure to 1.26 Å. Furthermore, the structure was solved in a different space group (C2 instead of F432) (**Figure 14B**). Overall, more amino acids at the termini and a more detailed water-network could be resolved. Refinement statistics that allow assessing the quality of the structure were improved such as the Ramachandran outliers (amino acids with non-favourable dihedral

angles). Different space group of this structure in comparison to the initial one explains the structural deviation evident as root mean square deviation of its C_α atoms (R.M.S.D) of 1.12 Å. Structural deviations between both structures are visible in the ribbon overlay image (**Figure 14C**).

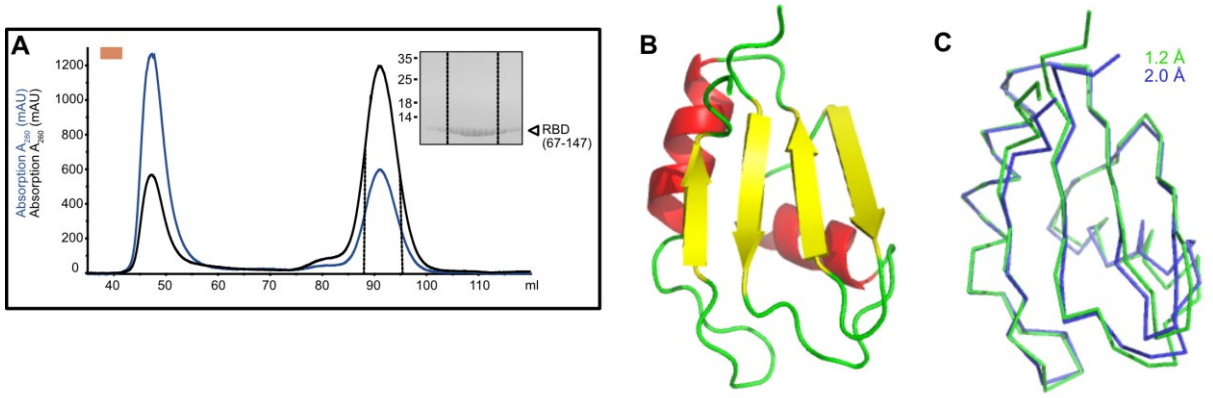

Figure 14 – Structure of hTRMT2A RBD shows typical RBD fold.
A SEC elution profile and SDS PAGE from last purification step of hTRMT2A RBD with 9.6 kDa. Protein indicated with arrow and lines was concentrated and subjected successfully to crystallography. **B** Structure of hTRMT2A RBD at 1.26 Å resolution with R_{work}/R_{free}-factors of 12.71 and 17.15 %, respectively (PDB: 7NTO). Secondary structure elements are highlighted in red for α-helixes, green for loops and yellow for ß-sheets. **C** Overlay with initial hTRMT2A RBD structure (2.0 Å) shows a root mean square deviation (R.M.S.D.) of 1.12 Å. Overaly is presented in green (1.2 Å) and blue (2.0 Å) ribbon visualization. Structures are generated with PyMol.

3.1.6 Crystal structure of *dm*TRMT2A RBD

Crystallization trials of *dm*TRMT2A RBD (aa 37-137) resulted in large needle crystals in one condition after one day (2 M NaCl, 2 M $AmSO_4$; **Figure 15B**). These crystals diffracted to 2.1 Å resolution and native datasets were collected at the Swiss Light Source synchrotron. However, the structure could not be solved using molecular replacement with hTRMT2A RBD as search model. Thus, anomalous data for phasing were collected from a crystal soaked with the gold atom-containing molecule $NaAuCl_4$ (paragraph **2.7.2**). The structure was solved by single-wavelength anomalous dispersion (SAD) using the AutoRickshaw pipeline. Processing statistics are listed in **Figure 15A** and methods for solving and refining the structure described in methods paragraph **2.7.4**. The crystal contained two *dm*TRMT2A RBD molecules per asymmetrical unit. The structure was resolved to 1.6 Å resolution, had R_{work}/R_{free}-factors of 14.1 % and 19.9 %, respectively, and displayed favorable stereo-chemical statistics. As shown in **Figure 15C**, the molecule adopts the typical RNA-binding domain β1-α1-β2-β3-α2-β4 topology as already reported for hTRMT2A RBD (Margreiter et al., 2021, bioRxiv) and other RBDs (Cléry et al., 2008). The structural conservation of *dm*TRMT2A and hTRMT2A RBD manifests with a low R.M.S.D. of 1.7 Å. This indicates that despite a sequence identity of only 33.8 % between hTRMT2A and *dm*TRMT2A FL, their structure is highly conserved. The soaked gold atom-containing derivative was found to be covalently bound to cysteine 111 (**Figure 15C**, orange).

Previous analysis of RBDs identified conserved consensus regions on the two central, adjacent ß-sheets that interact with RNA nucleotides and are termed ribonucleoprotein 1 (RNP) and RNP 2 (Loerch and Kielkopf, 2015). In case of *dm*TRMT2A RBD, RNP 1 consists of **K97**/R-G-**F99**/Y-G/**A100**-**F101**/Y-**V102**/I/L-X-**F104**/Y (bold = *dm*TRMT2A residues, normal = RNP consensus). *dm*TRMT2A RNP 2 consists of I/**V63**/L-F/Y-I/**V65**/L-X-**N67**-L. Conclusively, for *dm*TRMT2A RBD, both RNP 1 and 2 constitute a partially conserved RNA binding platform with solvent exposed amino acids such as F101 and F104.

To summarize, hTRMT2A FL, its subdomains and orthologs largely resisted crystallization attempts except for the determination of the *dm*TRMT2A RBD structure. Moreover, a better resolution structure for hTRMT2A RBD was generated. Additionally, purified protein subdomains described here were used for biochemical experiments in chapter **3.2** and **3.3**.

A

Processing Statistics - Refinement

Resolution (Å)	1.60
No. Reflections	22079
Rwork / Rfree	14.1/19.9
No. Atoms	1552
Protein	1341
Water	146
Other atoms	66
B-factor overall	21.5
R.m.s. deviations	
Bond lengths (Å)	0.02
Bond angles (°)	1.94
Ramachandran plot	
Most favored (%)	100
Additional allowed (%)	0

B

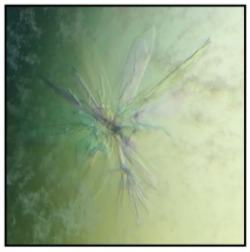

C

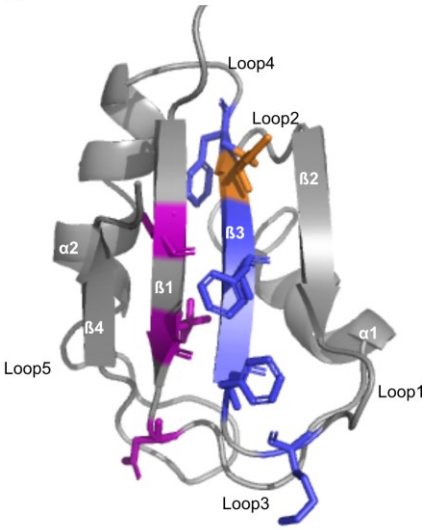

Figure 15 – Structure of *dm*TRMT2A RBD shows typical RBD fold.
A The *dm*TRMT2A RBD (aa 57-137) crystal was soaked with a gold heavy atom derivative to allow for SAD measurements. Processing statistics of anisotropic refinement with Refmac (CCP4 suite) are listed. Final resolution of the structure is 1.6 Å and R_{work}/R_{free}-factors are 14.1 % and 19.9 %, respectively. **B** Image of the *dm*TRMT2A RBD crystals. **C** Structure of *dm*TRMT2A RBD displays the typical fold of an RBD (PDB: 7PV5). The gold atom derivative is covalently bound to cysteine 111 (orange). Certain residues, known to bind RNA, are highlighted in stick visualization, and located to the conserved RNP1 (blue) and RNP2 (violet) patches on the ß-sheet surface. PyMol was used for visualization.

3.1.7 Stability of hTRMT2A proteins

One indicator for success in crystallization trials is the protein's stability, which can be approximated with the protein melting temperature (T_m). To determine the protein melting temperature and thus stability of hTRMT2A RBD, FL and central domain 1, a thermofluor assay was employed. In a qPCR instrument the protein was heated gradually (25-95 °C, 0.5 °C steps) in presence of the fluorophore SYPRO orange. The fluorophore emits a fluorescence signal when it binds to hydrophobic patches of the protein. Those are only accessible when the protein unfolds. At half peak height of the melting curve, the T_m can be derived (Boivin et al., 2013). It is apparent from **Figure 16A** that TRMT2A FL and central

domain 1 unfold at lower temperatures than TRMT2A RBD. Together with clearly lower calculated T_m of 36.8 ± 1.7 °C for hTRMT2A FL and 34.72 ± 0.5 °C for hTRMT2A central domain 1 compared to the higher T_m of hTRMT2A RBD (70.7 ± 0.8 °C), both FL and central domain 1 seem to exhibit high protein instability that might have hindered crystallization (**Figure 16B**).

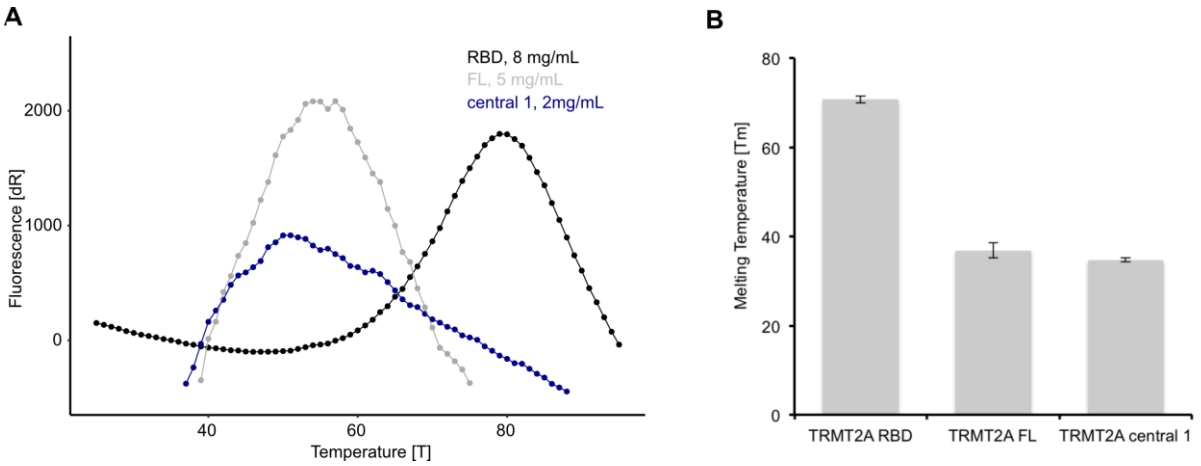

Figure 16 hTRMT2A FL and central domain 1 are less stable than hTRMT2A RBD.
A Melting curves from thermofluor assay measurements show a curve shift to lower temperatures for hTRMT2A FL and central domain 1 compared to hTRMT2A RBD. **B** hTRMT2A RBD possesses a 30 °C higher T_m than hTRMT2A FL and central domain 1 indicating higher protein stability of hTRMT2A RBD. For calculation of the T_m at half peak height, the melting curve was fitted with an Excel program sheet described earlier (Boivin et al., 2013). Data are mean ± SD. Values were derived from triplicate measurements. Thermofluor assays were conducted on a qPCR instrument with a 25-95 °C gradient and 0.5 °C steps. Based on initial pre-screening 8 mg/mL hTRMT2A RBD, 2 mg/mL hTRMT2A central domain 1 and 5 mg/mL hTRMT2A FL were incubated with 10x SYPRO orange.

3.2 Identification of small inhibitory molecules of hTRMT2A

As described in paragraph **1.4**, hTRMT2A fulfils all important requirements to be considered as potential drug target for polyQ diseases. Several approaches could be undertaken to identify pharmacological inhibitors of hTRMT2A. One approach is *in silico* drug screening for which we teamed up with the laboratory of Prof. Dr. Giulia Rossetti that is specialized in chemoinformatics (Forschungszentrum Jülich). Their informatics workflow to identify hTRMT2A binding compounds contained a structure-based screening against the hTRMT2A RBD structure (**Figure 14**) and a pharmacophore-based screening against the catalytic domain. In summary, 7.5 million compounds were *in silico* screened and 25 compounds selected for further *in vitro* and cell-based validation. Details about the workflow and applied algorithms are described in the bioRxiv preprint Margreiter et al., 2021. Computational work was done by Dr. Michael Margreiter from the Rossetti group and the cell-based validation by Yasmine Wasser from the Voigt group. Compound 13, 15 and 17 (**Figure 17A**) reduced cell death or polyQ protein aggregation (**Table 17**) or both. Due to these results, the potential of several selected compounds to inhibit the enzymatic activity of hTRMT2A FL was tested *in vitro*.

3.2.1 Co-crystallization and soaking of hTRMT2A RBD with small molecules

In silico modelling and molecular dynamics simulation allowed for the identification of a potential small molecule binding pocket in the hTRMT2A RBD structure (**Figure 17B**). To check for binding of compounds to hTRMT2A RBD and to confirm the predicted binding pocket, X-ray crystallography was the method of choice. Compounds 13, 15 and 17 (**Figure 17A**) were either soaked into hTRMT2A RBD crystals or co-crystallized with purified hTRMT2A RBD to obtain a co-structure. For soaking, highly concentrated compound solutions (2-6 mM) were incubated for 3- or 24-hours with crystals of the appropriate size before flash freezing as described in paragraph **2.7.2**. Co-crystallization was performed manually or with robot-assisted crystallization trials. Subsequently, two new crystallization

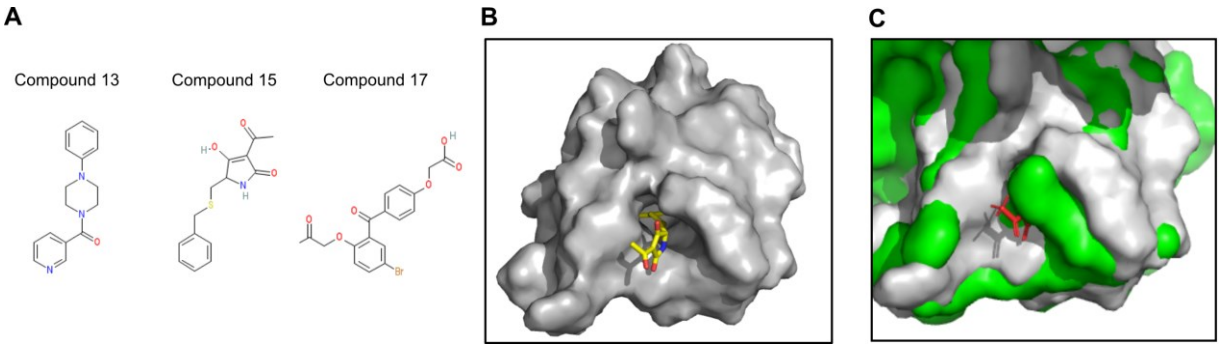

Figure 17 – Selected compounds of *in silico* screening and the predicted hTRMT2A RBD binding pocket. **A** Chemical structure of compound 13, 15 and 17. **B** *In silico* model of compound 15 (yellow) bound to the cryptic binding pocket of hTRMT2A RBD (grey), which was discovered with molecular dynamics simulations. **C** Overlay of *in silico* model (grey; compound red) and one representative hTRMT2A RBD crystal structure soaked with compound 15 (green) shows the absence of compound density and absence of the predicted cryptic binding pocket. Figures were generated with PyMol.

conditions were discovered, in which hTRMT2A RBD crystals emerged. In summary, 135 hTRMT2A RBD crystals were frozen, and 41 datasets were recorded. The resolution of the datasets ranged between 1.5 and 3.5 Å. However, inspection of all datasets did not reveal any additional electron density in the predicted binding pocket or elsewhere on the protein surface. Moreover, the predicted cryptic binding pocket itself was not observed in any of the 41 solved hTRMT2A RBD structures (**Figure 17C**).

3.2.2 Small molecules bind to TRMT2A RBD

Since binding of compounds to hTRMT2A RBD could not be confirmed with co-crystallization, direct binding of selected compounds (ID: 12 = spermidine, 13, 15, 17, 24, 25) was tested with SPR (paragraph **2.6.3.1**) This technique was chosen due to its high sensitivity and ability to detect low affinity, as well as transient binding events. hTRMT2A RBD was amine-coupled to a CM5 sensor chip surface. Size difference of compounds (< 0.2 kDa) and hTRMT2A RBD (9.8 kDa) was considered by coupling high protein densities (3000 response units = RU). Otherwise, binding signals from low molecular weight compounds would be below detection limit. An empty flow channel served as control flow cell. The polyamine Putrescine, which is a reported regulator of tRNA methyltransferases, and the polyamine spermine were used as positive binding controls (Mach et al., 1982). Sinefungin is a well-known pan-methyltransferase inhibitor that binds to the catalytic center of methyltransferases (McCammon and Parks, 1981; Cai et al., 2016). As sinefungin was not reported to bind to RBDs, it was used as negative binding control. Concentration series of 0.5-8 µM for controls and spermidine and 0.5-32 µM for other compounds were injected with a continuous flow rate of 30 µL/min. The positive control spermine showed a robust response as illustrated by its double referenced binding curves (**Figure 18A**, spermine). A plot of RU against concentration at the binding curve equilibrium was fitted with a steady state affinity model, which allowed for calculation of a K_D of 1.3 ± 0.17 µM. Only compound 12 = spermidine showed binding responses similar to the positive control spermine with a K_D of 2.28 ± 0.69 µM (**Figure 18A**, spermidine). None of the other tested compounds could demonstrate responses above the buffer control reference level (**Figure 18B**, compound 13, 15, 17). Equally, compound 24 and 25, which were improved derivatives of the *in silico* screening campaign, were tested with no detectable responses. Conclusively, binding of selected compounds to hTRMT2A RBD could not be observed. Serendipitously, spermidine binds hTRMT2A RBD, although it was pre-selected based on the pharmacophore approach against the catalytic domain. Thus, spermidine was not supposed to bind to the RBD.

Due to the even lower detection limit of small molecule interactions with larger proteins, no SPR study was performed with hTRMT2A FL protein or together with the RNA substrate. Moreover, SPR can analyse whether selected compounds are binding to hTRMT2A RBD,

but cannot inform whether these compounds inhibit hTRMT2A function as well. Therefore, an enzymatic assay was established.

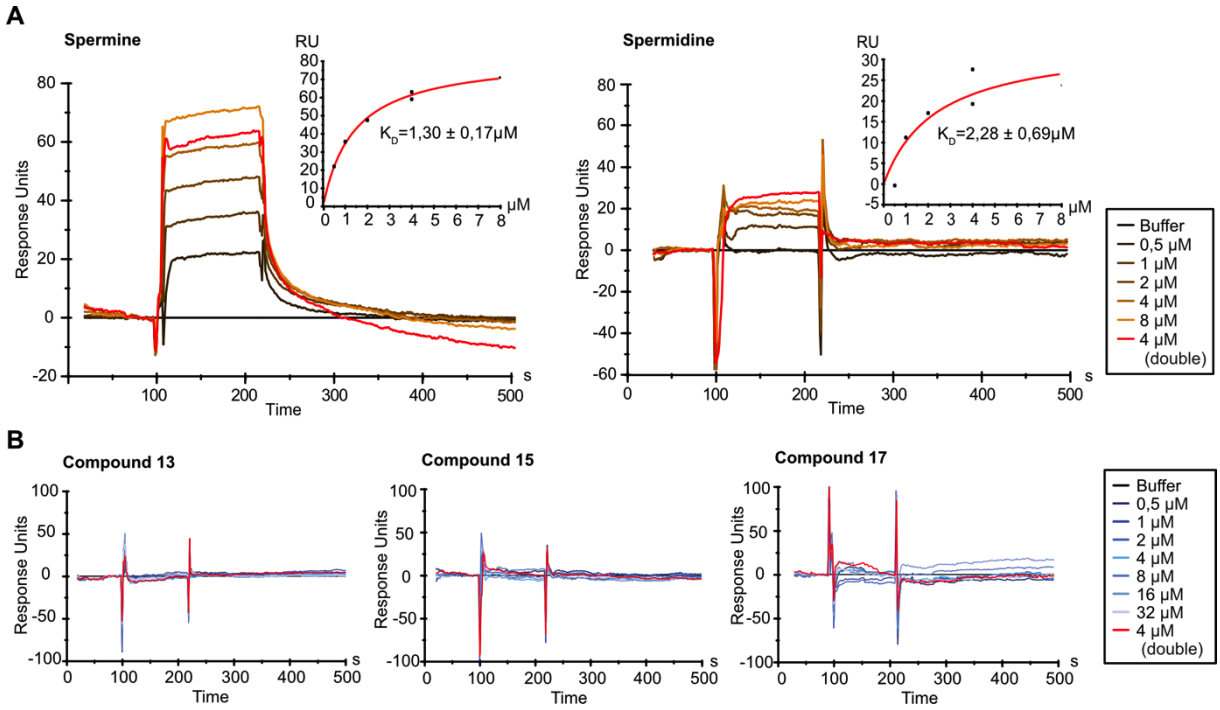

Figure 18 – SPR experiments with selected small molecules confirm spermidine binding to hTRMT2A RBD. **A** Spermine and spermidine (compound 12) curves confirm binding to the coupled hTRMT2A RBD. Injection series of 0-8 µM spermine and spermidine resulted in illustrated, representative double referenced binding curves. Steady state model was fitted at binding curve equilibrium and allowed for calculation of shown K_D values. Given values derived from triplicate measurements. **B** Compound 13, 15 and 17 do not show binding to coupled hTRMT2A RBD. 0-32 µM of compounds were injected. The control measurement of 4 µM compound at the end of each concentration series is shown as red curve. hTRMT2A RBD diluted in 10 mM HEPES pH 7.5 was amine-coupled to a CM5 chip with 3000 RU for SPR experiments. Representative binding curves of triplicate measurements are shown.

3.2.3 Establishment of an assay to determine hTRMT2A FL inhibition

To determine TRMT2A inhibition by selected compounds from *in silico* screening, the commercially available MTase Glo™ assay from Promega was chosen. The principle of this assay is based on the TRMT2A-mediated methyl group transfer from the methyldonor SAM onto the tRNA substrate. The reaction product is SAH. In successive steps, SAH levels are coupled to a bioluminescent signal by SAH conversion to ADP and ATP (**Figure 19A**). Via a luciferin luciferase reaction, the ATP production is read out as luminescence signal. Pharmacological inhibition of TRMT2A enzymatic activity by selected compounds should result in a decrease of SAH levels and thus luminescence values (Hsiao et al., 2016).

Initial assay establishment for hTRMT2A and its tRNA substrate was required. Firstly, linear correlation of SAH and luminescence signal was confirmed (correlation coefficient R' = 0.99), which also allows for back conversion of Relative Luminescence Units (RLU) to SAH concentration (**Figure 19B**). Backconversion was performed for all experiments in this thesis.

As positive control, the catalytic domain of trimethylguanosine synthase (hTGS1, aa 618-853) was purified (paragraph **2.3.8**). Human TGS1 is a methyltransferase with known

minimal substrate (m^7GTP) and enzymatic activity as tested by mass spectrometry (Monecke et al., 2009). Hence, it also served as reference to establish the assay under saturating conditions. Experiments with either constant protein and varying substrate concentration or vice versa can help to identify concentrations where the signal over background is well distinguishable, which is crucial for experiments with inhibitors. An experiment with constant m^7GTP concentration (100 µM) and variable hTGS1 concentrations (0-10 µM) was performed and showed that saturation was already reached with 1 µM hTGS1 (**Figure 19C**). Thus, for an experiment with constant hTGS1 concentration and variable m^7GTP concentrations, 0.5 µM hTGS1 and lower substrate concentrations (0-200 nM) were used (**Figure 19D**). Conclusively, optimal concentrations for a saturated reaction were 0.5 µM Tgs1 and 200 nM m^7GTP. The previously reported high affinity of hTGS1 to m^7GTP (Monecke et al., 2009a) was confirmed with a calculated K_m of 66.7 nM (**Figure 19D**). In conclusion, the assay works optimal with the well-studied catalytic domain of human methyltransferase hTGS1.

Subsequently, similar experiments with hTRMT2A FL and $tRNA^{Phe}$ (**Figure 19E**) were performed, to identify assay conditions for a saturated reaction and for a sufficient signal over background ratio. First, constant 500 nM $tRNA^{Phe}$ was incubated with increasing concentrations of hTRMT2A FL (0-25 µM) and saturation occurred at 15 µM protein. Contrary to hTGS1, higher hTRMT2A FL concentrations were required to reach saturation and overall, less signal was observed, which is characteristic for a slower or less active enzyme. A lower concentration of hTRMT2A FL (5 µM) was selected to perform an assay with increasing $tRNA^{Phe}$ concentrations (0-400 nM). Since the reaction was saturated with 250 nM $tRNA^{Phe}$ and 5 µM hTRMT2A FL (**Figure 19F**), this concentration pair was selected to validate an appropriate signal to background ratio.

The Z'-factor has been reported to be the optimal statistical measure to decide whether an assay has appropriate robustness and signal to background ratio for inhibitor experiments (Sui and Wu, 2007). For the Z'-factor experiment a reaction with and without enzyme was set up. The assay proved to be robust with a Z'-factor of 0.73 as shown in **Figure 19G** (Z'-factor > 0.5).

Lastly, crowding effects were sampled using PEG 400, which correlates with 400 Da sized compound. Such an experiment can exclude whether high concentrations of any 400 Da sized compound would inhibit hTRMT2A activity. In an assay with established conditions no reduction of hTRMT2A activity in presence of up to 4 mM PEG 400 was observed, although treatment with the same amount of the pan-methyltransferase inhibitor sinefungin reduced hTRMT2A activity around 30 % (**Figure 19H**).

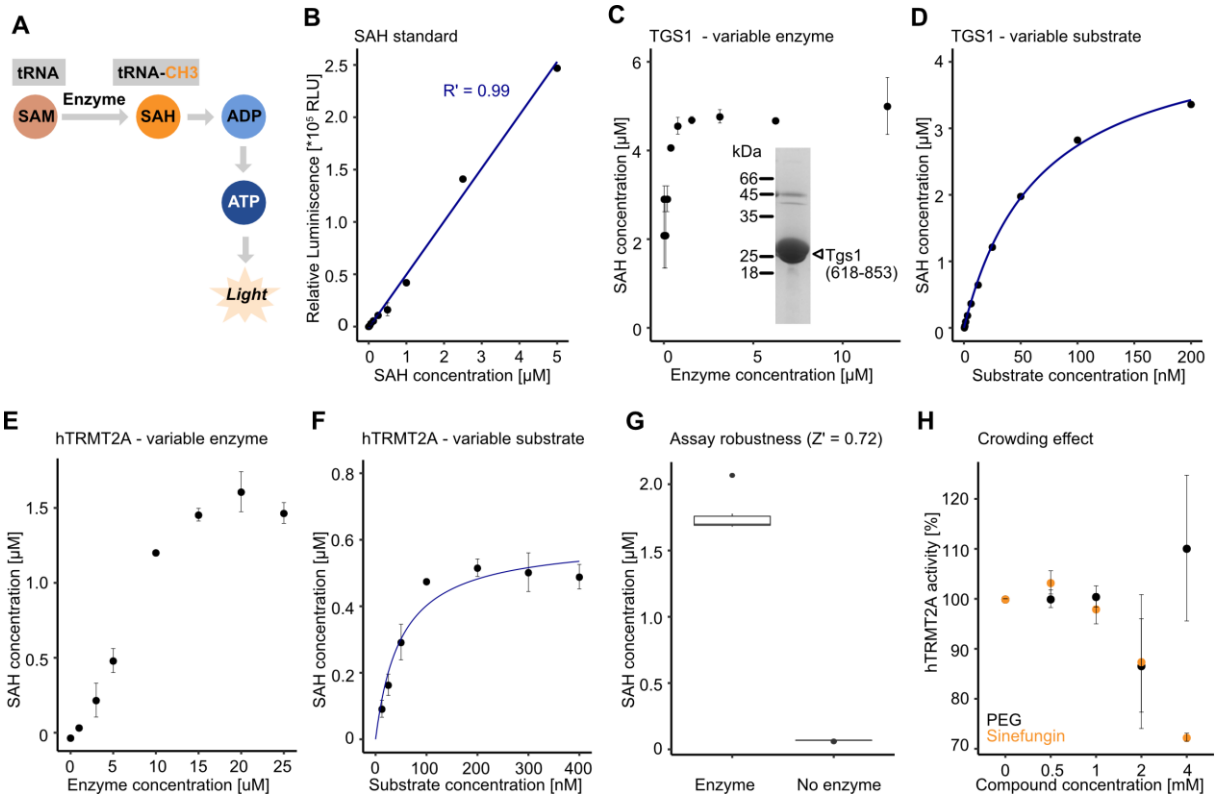

Figure 19 – Successful establishment of the MTase Glo™ assay for testing of hTRMT2A FL inhibitors.
A The principle of the luminescence based MTse Glo™ assay from Promega, where methylation of tRNA substrate by hTRMT2A FL is coupled to a luminescence signal via SAH conversion to ATP. **B** SAH concentration (0-5 µM) and RLU values correlate linearly indicated with a correlation coefficient R' of 0.99 (N=2). All RLU values were back converted to SAH concentration. **C** Assay conducted with 0-12.5 µM hTGS1 (purity depicted on SDS-PAGE) and constant 100 µM minimal substrate m^7GTP (N=2) shows saturation with 1 µM hTGS1. **D** Pilot assay performed with 0-200 nM m^7GTP and constant 0.5 µM hTGS1 reaches saturation with 200 nM m^7GTP (Pilot; N=1). Michaelis Menten fit results in an estimated K_m of 66.7 nM. **E** Assay with 0-25 µM recombinantly purified hTRMT2A FL and constant 0.5 µM $tRNA^{Phe}$ shows saturation with 15 µM protein (N=2). **F** Assay with 0-400 nM $tRNA^{Phe}$ and constant 5 µM hTRMT2A FL reaches saturation with 250 nM $tRNA^{Phe}$ (N=3). For assays with variable enzyme concentration a no enzyme control reaction was included and for assays with variable substrate concentration a no substrate control reaction. **G** Assay robustness as calculated by the Z'-factor formula with data from enzyme (5 µM hTRMT2A FL, 250 nM $tRNA^{Phe}$) and no enzyme experiments shows high robustness with a Z'-factor of 0.72 (robust > 0.5; N=6). **H** Increasing concentration of 0-4 mM PEG and sinefungin in a reaction with 5 µM hTRMT2A FL and 250 nM $tRNA^{Phe}$ shows no effect of PEG on hTRMT2A activity and a 30 % activity reduction upon sinefungin treatment (N=3). Buffer control was set to 100 % and data were normalized. All data are mean ± SD.

3.2.4 Small molecules reduce catalytic activity of hTRMT2A *in vitro*

The established enzymatic assay was used to test the inhibitory effects of selected compounds (ID: 12 = spermidine, compound 13, 15, 17) on hTRMT2A FL activity using its substrate $tRNA^{Phe}$. To determine the optimal inhibitor and its concentration, experiments with different concentrations of spermidine, spermine, sinefungin were performed (50 µM, 1 mM and 6.25 mM). A reaction without tRNA served as background subtraction control and values from this control experiment were subtracted from the final data. Then, data were normalized against the value from the only buffer reaction. An inhibitor concentration of 50 µM was insufficient to result in hTRMT2A inhibition, whereas treatment with 1 mM inhibitor caused robustly reduced enzymatic activity (**Figure 20A**). Treatment with spermine caused an extreme reduction of hTRMT2A activity with values close to the background. Of note,

treatment with every inhibitor using a concentration of 6.25 mM decreased hTRMT2A activity but was not further used in order to keep inhibitor concentration as low as possible. Consequently, spermidine and sinefungin at a concentration of 1 mM were selected for further inhibition experiments.

An additional experiment with assay components/buffers and selected compounds was performed prior to the main experiment (without tRNA or enzyme). This control was necessary to exclude that possibility that compounds inhibit the assay components itself. However, this was not the case.

For the inhibition experiments, compounds 12 = spermidine, 12, 13, 15 and 17 were tested. Sinefungin was employed as positive control. A reaction with the same buffer the compounds were diluted in was employed as negative control. The assay was performed as described in paragraph **2.4.4.3**. A reaction without tRNA served as background subtraction control and values from this control experiment were subtracted from the final data. Then, data were normalized against the value from the only buffer reaction (**Figure 20B**). To apply the Student's t-test for significance testing, values need to be normally distributed. This does not apply to data from inhibitor experiment in **Figure 20** (Shapiro's tests for normal distribution). Instead, significance was computed with the Wilcoxon rank sum test, a non-parametric statistical test fit for low sample size. According to these calculations, treatment with 1 mM spermidine (compound 12) and sinefungin significantly decreased hTRMT2A

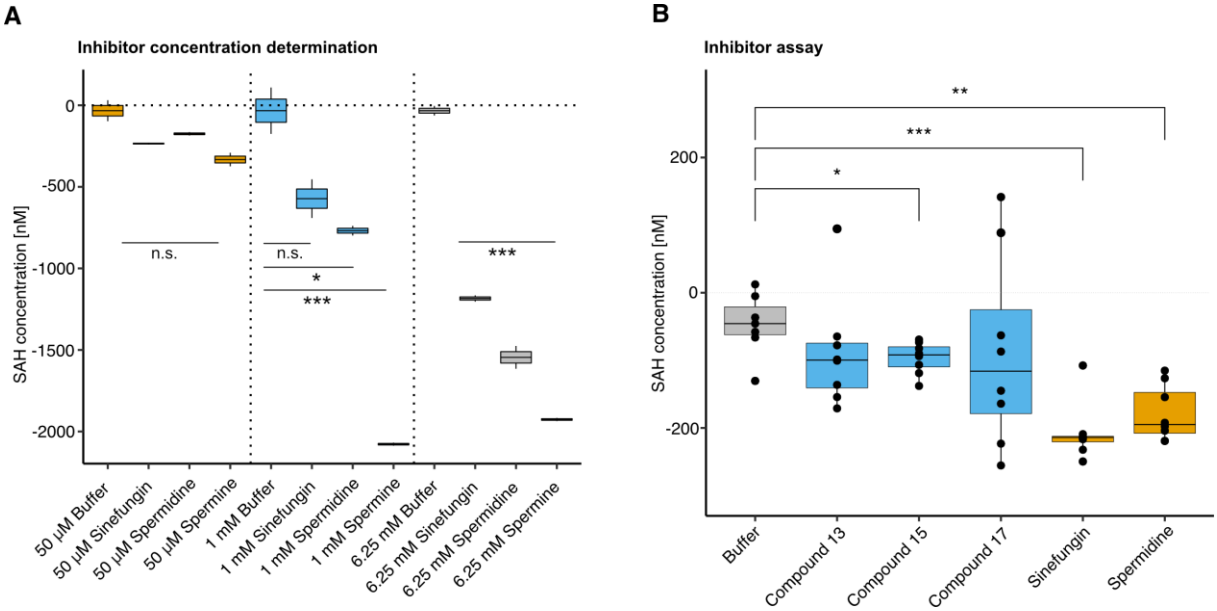

Figure 20 – Methylation assay with hTRMT2A FL and selected small molecules confirms spermidine as hTRMT2A FL inhibitor.
A Pilot methylation assay with Promegas MTase Glo™ to determine the optimal inhibitor amongst spermidine, spermine and sinefungin, as well as the optimal inhibitor concentration using 5 µM hTRMT2A and 250 nM $tRNA^{Phe}$. Data were normalized to buffer control. RLU values were back converted to SAH concentration. Data show optimal buffer concentration to be 1 mM sinefungin and spermidine. Data are mean ± SD (N=3). Significance testing with Student's t-test. **B** Inhibitor assay with 1 mM compound 12 = spermidine, compound 13, 15, 17, the positive control sinefungin and negative buffer control. Data were normalized to buffer control and back converted to SAH concentration. Treatment with spermidine, sinefungin and compound 15 caused significant reduction of hTRMT2A activity. Data are mean ± SD (N=8). Non-parametric Wilcoxon sum rank test for non-normally distributed data was used for significance testing. Significance levels are $p \geq 0.05$ (n.s.), $p < 0.05$ (*), $p < 0.01$ (**), $p < 0.001$ (***).

activity. Compound 15 only mildly affected enzymatic activity, whereas compound 13 and 17 treatment did not cause any hTRMT2A inhibition.

3.2.5 A small molecule hTRMT2A inhibitor reduces polyQ aggregation in cells

Cellular assays that assess reduced aggregation and improved cell viability upon inhibitor treatment were conducted in the laboratory of Dr. Aaron Voigt (RWTH Aachen). Results from my *in vitro* (**3.2.2** and **3.2.4**) and the cellular assays did not correlate. The only exception was spermidine, which bound to hTRMT2A RBD, inhibited hTRMT2A FL activity, reduced cell death and polyQ aggregation. Therefore, spermidine was chosen for further follow up studies, which will be conducted after this thesis will have been submitted. An experimental summary of performed experiments is listed in **Table 17**.

Table 17 – Experimental summary of inhibitor experiments
Summary of results from binding assay (chapter **3.2.2**), inhibition assay (chapter 3.2.4), as well as in cell polyQ aggregation and cell death assays (Margreiter et al., 2021, bioRxiv) are summarized with red = negative result, green = positive result, orange = no definite result.

	In vitro		***Cellular***		
ID	**Binding Assay**	**Inhibition Assay**	**Reduced aggregation**	**Reduced cell death**	**Internal name**
13					87013
15					118840
17					106084
24		-			1
25		-			2
-		-	-	-	3
12			-	-	Putrescine
13	2.28 µM				Spermidine
-	1.3 µM		-	-	Spermine
-			-	-	Sinefungin

3.2.6 Indirect testing of m^5U levels from different cellular sources

Previously, the MTase Glo™ assay was used to assess methylation levels of tRNA at position G46. RNA was isolated from a WT *E. coli* strain and a mutant strain, which lacked TrmB-mediated RNA G46 methylation activity (Thongdee et al., 2019). Methylation experiments were performed with recombinantly purified TrmB and RNA isolated from TrmB mutant strain, which supposedly possess lower G46 tRNA methylation levels. In this experiment higher methylation activities were observed for RNA isolated from TrmB mutant background compared to RNA isolated from WT strains. This indicates that RNA from a TrmB mutant background indeed harbored lower TrmB accessible G46 methylation levels.

Inspired by this experiment, it was anticipated that an assay with recombinantly purified hTRMT2A FL could indirectly measure the methylation levels of U54. To detect methylation levels of total RNA isolated from hTRMT2A WT and hTRMT2A KD HEK cells, purified hTRMT2A FL and isolated RNA were incubated in presence of SAM. Downstream processing was performed as described in paragraph **2.4.4.4**. A reaction without enzyme was used as control for background subtraction. RNA from TRMT2A KD cells showed significantly higher methylation levels than RNA from TRMT2A WT cells, which is in line with lower cellular RNA methylation in a TRMT2A KD background (**Figure 21A**).

To confirm whether this assay is robust enough to translate to closely related species and to other biological samples such as tissue, this experiment was repeated with RNA extracted from liver of TMRT2A WT and KO mice. Assay experiments with purified hTRMT2A FL and isolated RNA in presence of SAM confirmed that total RNA from TRMT2A KO mice is significantly more methylated *in vitro* than total RNA from TRMT2A WT mice (**Figure 21B**). Thus, TRMT2A KO mice RNA displays lower TRMT2A-dependent methylation levels.

To corroborate whether the observed effect derives predominantly from tRNA and not from other RNA species as observed earlier (Cheng et al., 2020; Dai et al., 2021), tRNA was isolated from total RNA according to the protocol described in (Ponchon et al., 2009). Briefly, RNA was separated with a NaCl gradient on a MonoQ column and respective tRNA fractions unified for the experiment (paragraph **2.5.3**). Native PAGE of total RNA and tRNA confirmed successful isolation of tRNA (**Figure 21C**). The methylation assay was conducted with purified tRNA and purified hTRMT2A FL. Correspondingly, tRNA from TRMT2A KO mice displayed significantly higher methylation levels than tRNA from TRMT2A WT mice (**Figure 21D**). Consequently, TRMT2A KO mice tRNA displays lower m^5U54 methylation levels.

In conclusion, the MTase Glo™ assay allows for an indirect measurement of TRMT2A dependent methylation levels of tRNA and total RNA isolated from immortalized cell lines and mice liver. Moreover, these results suggest that TRMT2A KD HEK cells and TRMT2A KO mice display lower methylation levels than the respective WT condition. Interestingly, hTRMT2A methylated both human and mouse derived RNA similarly well, suggesting a cross-species conservation of TRMT2A function.

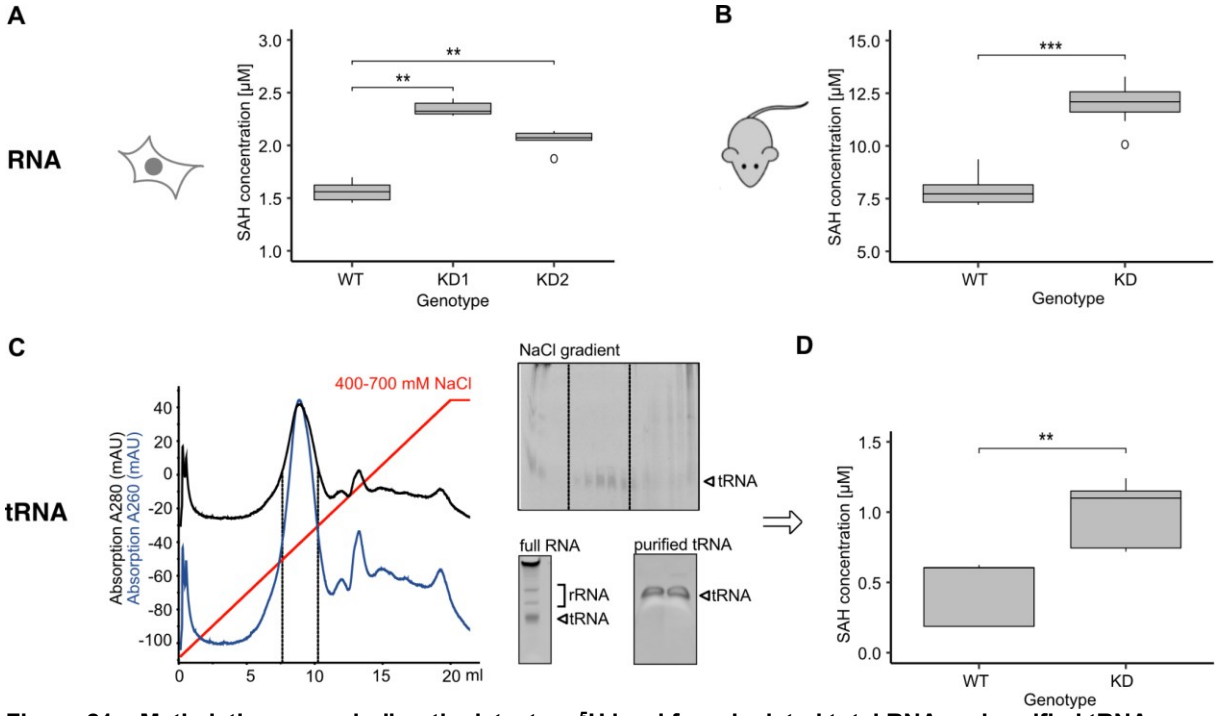

Figure 21 – Methylation assay indirectly detects m^{5}U level from isolated total RNA and purified tRNA.
A For experiments with HEK cell RNA, 5 µM purified hTRMT2A FL and 200 ng isolated RNA from hTRMT2A WT and KD HEK were used. RNA from the hTRMT2A KD HEK cell line displayed significantly higher methylation levels *in vitro* (N=3). **B** For experiments with mouse liver RNA, 5 µM purified hTRMT2A FL and 5 µg isolated RNA from TRMT2A WT and KO mice liver were used. RNA from TRMT2A KO mice displayed significantly higher methylation levels *in vitro* (N=3). **C** tRNA purification was performed with a MonoQ column using a 400-700 mM NaCl gradient. The unified RNA fractions are highlighted with dotted lines on the elution profile and the denaturing 8 % PAGE. Comparison of total RNA and purified RNA on 8 % denaturing PAGE shows enrichment of tRNA after purification. **D** For experiments with mouse liver tRNA, 5 µM purified hTRMT2A FL and 5 µg purified tRNA from TRMT2A WT and KO mice liver were used showing significantly increased methylation levels of TRMT2A KO tRNA *in vitro* (N=3). All methylation assays were performed with Promega MTase Glo™ assay according to a protocol published by Thongdee et al., 2019. Data were normalized to a no-enzyme control and back converted to SAH concentration. Data are mean ± SD. Student's t-test was used for significance testing with $p \geq 0.05$ (n.s.), $p < 0.05$ (*), $p < 0.01$ (**), $p < 0.001$ (***).

3.3 RNA binding and methylation by hTRMT2A

To study the specificity of tRNA methylation by hTRMT2A, it is imperative to assess both RNA binding and catalytic activity of hTRMT2A. Recent high-throughput cellular analyses with hTRMT2A already suggested that RNA binding correlates well with RNA methylation, but does not necessarily cause methylation (Carter et al., 2019). In this chapter, the dissection of hTRMT2A substrate requirements based on several previously identified hTRMT2A RNA targets is described. Additionally, hTRMT2A domains and residues that are required for RNA binding are reported. Based on these results, a three-dimensional model of the hTRMT2A-tRNA complex and its interaction interface could be built for the first time.

3.3.1 RNA binding by hTRMT2A

For the *in vitro* characterization of hTRMT2A binding preferences, recombinant hTRMT2A FL (**Figure 10E**) and different *in vitro* transcribed RNA (**Figure 22F**) were used. Binding was assessed with EMSAs, where ^{32}P-labelled RNA (5 nM) was preincubated with increasing concentrations of hTRMT2A FL (0-1.25 µM) and poly-uridine ssRNA (polyU) as competitor to preclude non-specific binding. To explore the importance of uridine in position 54 of a given tRNA for binding, three tRNA with U54 (tRNA^{Gln}, tRNA^{Phe}, tRNA^{Asn}) and two tRNA lacking U54 were included. The latter consisted of tRNA^{Ala} with A54 and a mutant version of tRNA^{Gln}, where U54 had been changed into G (tRNA$^{Gln\ U54G}$). Additionally, radiolabelled polyU alone was used as negative control, as it supposed to bind hTRMT2A unspecifically in line with its usage as competitor. hTRMT2A bound all tRNA with apparent equilibrium dissociation constants (K_D) in a low nanomolar range (**Figure 22A**). A slightly stronger binding was observed for tRNA^{Gln}, where a shifted band was already observed at a protein concentration of 60 nM. Of note, for all tRNA except for tRNA^{Phe}, supershifts were observed, which imply that multiple hTRMT2A enzymes bind to one RNA molecule. However, since these supershifts only occurred at higher, micro-molar protein concentrations, they represent assumably unspecific oligomerization without physiological importance.

To dissect the structural requirements for hTRMT2A binding, EMSAs with only the T-loop portion of tRNA^{Gln} and tRNA^{Lys} were performed, the latter with natural-occurring adenine at the respective position 54. In experiments with *E. coli* TrmA, the tRNA T-loop was reported to be sufficient for binding (Urbonavičius et al., 2007). Moreover, two structured fragments derived from mRNA were selected: a fragment of the KCND2 mRNA, which consists of the previously reported stem-loop target of hTRMT2A (Carter et al., 2019) and the unrelated E3 stem-loop of the *S. cerevisiae ASH1* E3 mRNA (Edelmann et al., 2017). *ASH1* E3 is supposed to display a similar structure than the known hTRMT2A target KCND2 and thus constitutes a suitable negative control. To further expand the structure space, also tmRNA was selected, which is an *E. coli* TrmA target resembling the tRNA structure without the D-

Loop. In binding experiments, both $tRNA^{Gln}$ T-loop and $tRNA^{Lys}$ T-loop irrespective of the presence of U54 showed a weaker band shift with most of the RNA remaining in its free form. The latter suggests the formation of complexes with lower stability (**Figure 22C**). The stem-loop containing KCND2 and tmRNA displayed binding, however in the micromolar K_D range (**Figure 22B/D**), which indicates much lower affinity than observed with tRNA. Surprisingly, the unrelated *ASH1* E3 stem-loop was bound almost as good as tRNA with binding in the higher nanomolar K_D range (**Figure 22D**). As expected polyU alone did not cause any band shifts in EMSAs (**Figure 22E**).

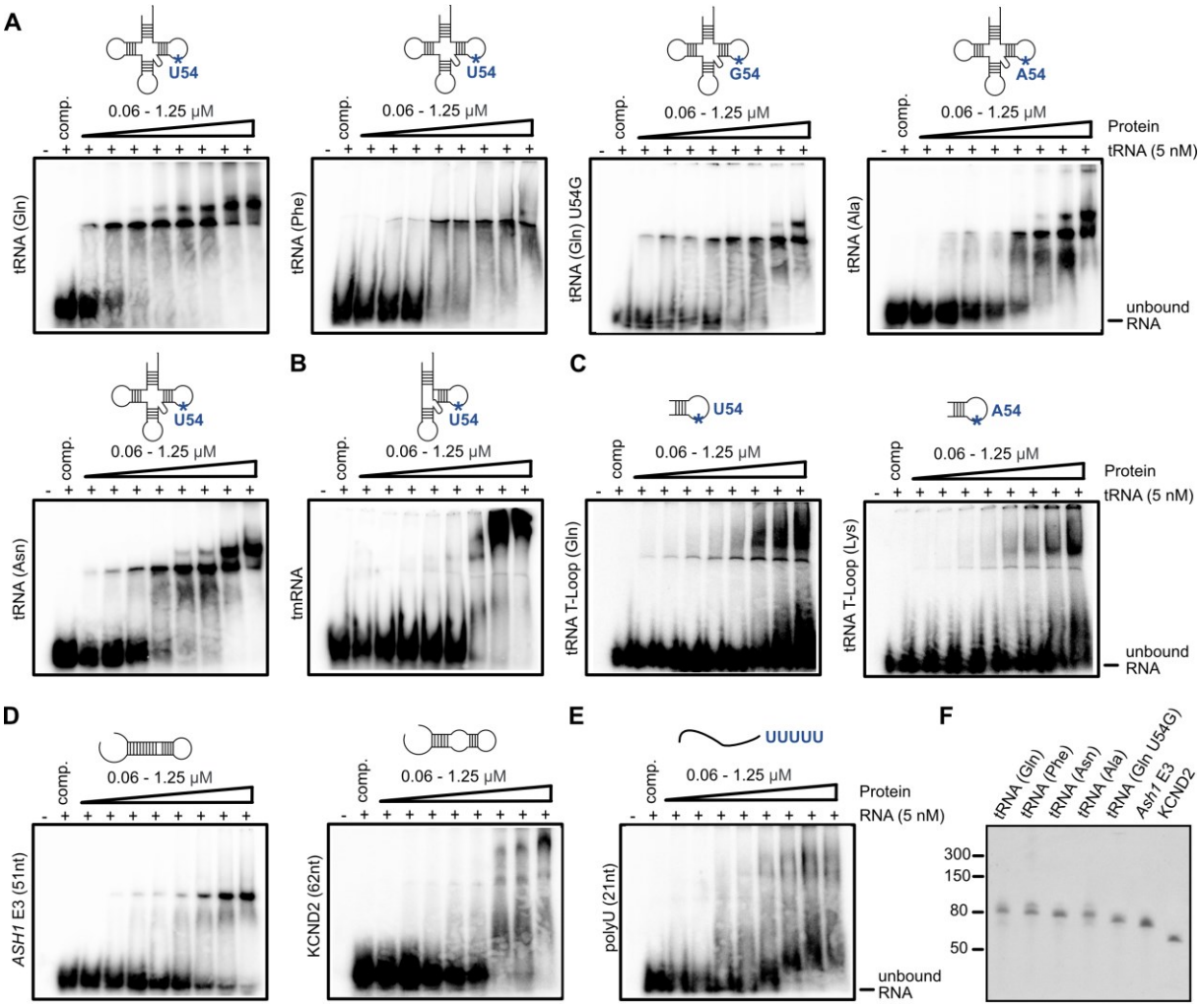

Figure 22 – EMSAs with hTRMT2A FL and different RNA confirms tRNA as major binding target.
A EMSAs of tRNA with differing nucleotides at position 54 shows for all tRNA high affinity binding in low nanomolar K_D range. **B** EMSA of tmRNA, a tRNA structure devoid of the D-loop, shows low affinity binding in micromolar K_D range. **C** EMSAs of truncated $tRNA^{Gln}$ T-loop and $tRNA^{Lys}$ T-Loop display unspecific binding with unbound RNA at high protein concentrations. **D** EMSA with mRNA derived from *S. cerevisiae ASH1* E3 element (1771-1821; 51nt) shows binding in nanomolar K_D range. EMSA with mRNA derived from human KCND2 (chr7: 366813-366875; 62nt) shows binding in micromolar K_D range. **E** Control polyU (21nt) does not show binding. **F** *In vitro* transcribed, PAGE purified RNA separated on an 8 % denaturing PAGE shows high purity and was used for EMSAs. Binding assays were performed with ^{32}P labelled RNA. For experiments 2.5 ng/µL polyU competitor and 5 nM labelled RNA were pre-incubated with increasing concentrations of recombinant hTRMT2A FL (0-12.5 µM) for 20 min. Reaction without protein served as control. Free RNA and RNA-protein complex were separated on 4 % native PAGE for 1 h at 80 V. Each experiment was performed in triplicates and representative plots are shown.

In summary, these results suggest that hTRMT2A binding to tRNA is independent of the presence of the potential methylation site U54 and that the enzyme binds tRNA with a higher affinity than differently structured RNA. While binding affinities are in the expected range, binding specificity of hTRMT2A for its physiological methylation targets appear to be low exemplified by binding of the unrelated *ASH1* E3 mRNA.

3.3.2 Enzymatic activity of hTRMT2A

To check whether tRNA binding correlates with tRNA methylation, the methyltransferase activity of hTRMT2A was tested on selected RNA using the luminescence based MTase Glo™ assay described in chapter 2. hTRMT2A FL was incubated with increasing RNA concentrations (0-6 µM) in presence of SAM with a reaction lacking RNA as background control. Hereafter, downstream processing was performed as described in paragraph **2.4.4.1**. Michaelis Menten fitting was performed on triplicate measurements to calculate the K_m value. As shown in **Figure 23A**, hTRMT2A methylates $tRNA^{Gln}$ and $tRNA^{Phe}$ with a K_m of 1.52 ± 0.05 µM and 0.72 ± 0.06 µM, respectively, which is rather high but in the range of previously reported K_m values for methyltransferases (Swinehart et al., 2013). In contrast, the two tRNA lacking U54 ($tRNA^{Ala}$, $tRNA^{Gln\ U54G}$) were methylated orders of magnitude less efficiently (K_m > 4 µM). On the other hand, the reaction of the hTRMT2A with $tRNA^{Asn}$, which possesses a uridine at position 54, was not saturated even at a concentration of 6 µM (K_m = n.d.). Thus, non-physiologically high $tRNA^{Asn}$ concentration was required for quantitative methylation. Conclusively, binding assays and enzymatic assays indicate that specificity of target-tRNA methylation is mainly mediated by a uridine residue in the right position and not by the affinity to these tRNA in general.

Additionally, methylation of mRNA derived stem-loops was probed with the MTase Glo™ assay. In agreement with binding experiments, KCND2 mRNA stem-loop was required in non-physiologically high concentrations for quantitative methylation (K_M = n.d.). Surprisingly, the heterologous *ASH1* E3 mRNA stem-loop from *S. cerevisiae* was methylated as efficiently as natural tRNA substrates with a K_m of 0.78 ± 0.15 µM (**Figure 23B**). These data indicate that hTRMT2A cannot only methylate substrate tRNA efficiently, but also other structured RNA such as the *ASH1* E3 element. Of note, a possible target uridine was located to the loop part of both mRNA stem-loops as visualized in **Supplemental Figure 6** and discussed further in paragraph **4.3.2**. In summary, the combined binding and enzymatic-activity data indicate a clear, but not exclusive, preference for tRNA.

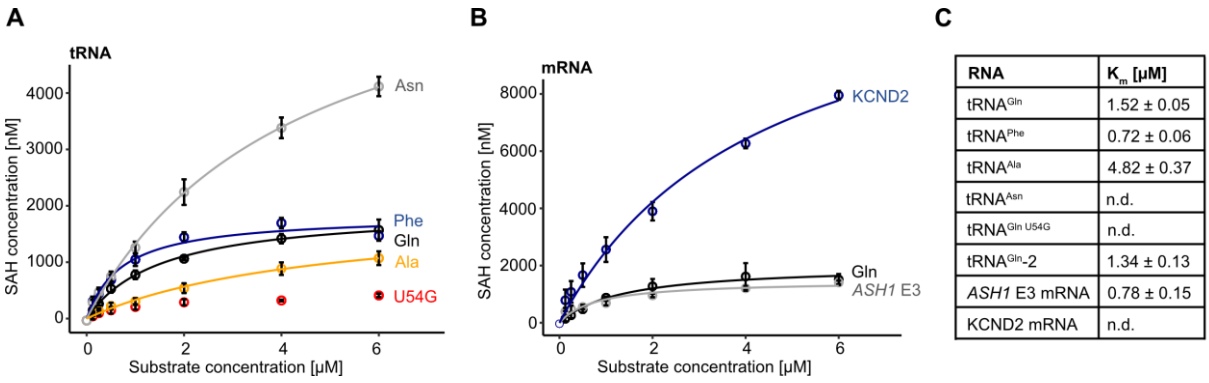

RNA	K_m [µM]
$tRNA^{Gln}$	1.52 ± 0.05
$tRNA^{Phe}$	0.72 ± 0.06
$tRNA^{Ala}$	4.82 ± 0.37
$tRNA^{Asn}$	n.d.
$tRNA^{Gln\ U54G}$	n.d.
$tRNA^{Gln}$-2	1.34 ± 0.13
ASH1 E3 mRNA	0.78 ± 0.15
KCND2 mRNA	n.d.

Figure 23 – Methylation assays with hTRMT2A FL and different RNA confirms U54 as major methylation parameter.
A Results of tRNA methylation experiments show efficient methylation for $tRNA^{Gln}$ (black) and $tRNA^{Phe}$ (blue) harboring an U54 and less efficient methylation for $tRNA^{Asn}$ (grey), $tRNA^{Ala}$ (yellow) and $tRNA^{Gln\ U54G}$ (red) with the two last tRNA lacking U54. **B** Results of mRNA methylation experiments indicate that the *ASH1* E3 mRNA (grey) stem-loop is similarly well methylated than $tRNA^{Gln}$ (black) The KCND2 mRNA stem-loop (blue) is not efficiently methylated. Promega's MTase Glo™ assay was used for methylation experiments. 5 µM purified hTRMT2A was preincubated with 0-6 µM *in vitro* transcribed RNA in the presence of SAM. Reaction without RNA served as control. All data represent mean ± SD (N=3). Curves were fitted with Michaelis Menten equation illustrated as lines using custom R scripts and calculated K_m values are listed on the right.

3.3.3 tRNA binding by hTRMT2A involves multiple domains

Based on the previously performed binding and methylation experiments, $tRNA^{Gln}$ was chosen to further investigate which hTRMT2A domains interact with the substrate tRNA. hTRMT2A FL (aa 1-625), RBD (aa 69-147), central domain 1 (aa 148-390), central domain 2 (aa 237-414) and fusion 1 (aa 69-240/413-590) were selected for binding assays, because together they span the complete enzyme except for the flexible N- and C-termini (**Figure 24A**). Proteins were purified as described in results paragraph **3.1.1** and methods paragraph **2.3.6**. Purity of proteins is shown in **Figure 24B**. For EMSAs, ^{32}P-labelled RNA was preincubated with increasing protein concentrations (0-1.25 µM) in the presence of the polyU competitor. For experiments with SUMO-tagged central domain 2, purified SUMO tag was used as control to exclude SUMO-tag binding to RNA. In comparison to high affinity binding of hTRMT2A FL and $tRNA^{Gln}$ (**Figure 24C**), all fragments showed mobility shifts only in the micromolar K_D range and hence much weaker binding (**Figure 24D**). Amongst the subdomains, RBD and central domain 1 show the clearest band shifts and decrease of free unbound RNA in line with a higher intrinsic capability to bind $tRNA^{Gln}$. However, none of the individual domains was sufficient for physiologic $tRNA^{Gln}$ binding. Thus, all domains might have to interact cooperatively for full binding affinity.

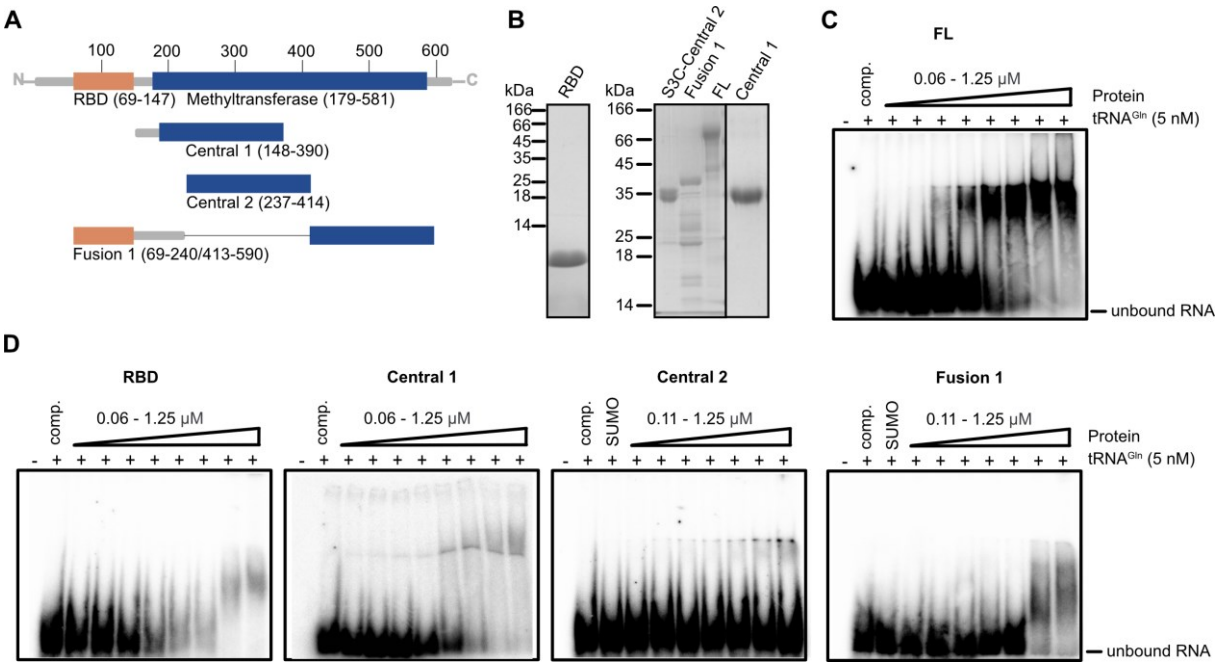

Figure 24 – EMSAs with different hTRMT2A subdomains and tRNA^{Gln} suggest cooperative binding of tRNA^{Gln} by all domains.
A Cartoon depicting purified domains of hTRMT2A used for EMSAs. **B** Recombinantly purified proteins separated on 19 % and 12 % SDS PAGE. **C** EMSA with hTRMT2A FL shows high affinity binding in nanomolar K_D range. **D** EMSA with hTRMT2A RBD, central domain 1, central domain 2 and fusion 1 displays only low affinity binding in micromolar K_D range. Because SUMO-tagged central domain 2 was used, a SUMO-tag control was included. EMSAs were performed using 5 nM ^{32}P labelled tRNA^{Gln} and increasing concentration of protein (0-1.25 µM) in presence of polyU competitor (2.5 ng/µL). Incubation time was 20 minutes. Reaction without protein served as control. Free RNA and RNA-protein complexes were separated on 4 % native PAGE for 1 h. Experiments were conducted in triplicates and representative EMSAs are shown.

3.3.4 tRNA binding by hTRMT2A involves amino acids from all domains

To map the TRMT2A-tRNA^{Gln} interaction surface with single amino acid resolution, nitrogen mustard (NM) and UV induced crosslinking of the TRMT2A-tRNA^{Gln} complex followed by mass spectrometry was performed in collaboration with Prof. Dr. Henning Urlaub, Luisa Welp and Dr. Monika Raabe (MPI Biochemistry, Göttingen). Experiments were conducted with the *in vitro* reconstituted protein-RNA complex (**Figure 25B**) and with the co-purified, stable complex (**Figure 25A**) generated as described in **2.6.7**. To confirm that hTRMT2A FL creates a stable complex with tRNA^{Gln}, SEC with tRNA^{Gln} and hTRMT2A FL alone, as well as with the tRNA^{Gln}-TRMT2A complex (1:1 ratio) was performed. Stable complex formation was apparent as a shift of the elution peak to smaller elution volumes (from 17.41 mL to 15.46 mL), corresponding to a higher molecular weight. The *in vitro* reconstituted and co-purified samples were cross-linked, trypsin- and RNase-digested, and analysed by mass spectrometry. Out of the four collected datasets (UV, NM, *in vitro* reconstituted, purified complex) in at least three of them the following amino acids were consistently found to be cross-linked to tRNA (**Figure 25C,** bold letters; **Figure 25F** dark blue): C270 to cytosine, C463 to adenine or uridine, H386 to uridine/cytosine or guanidine. In addition, both C111 and H83 cross-linked to all four RNA nucleotides. When crosslinked amino acids C111 and H83 were mapped onto the X-ray structure of hTRMT2A RBD

(paragraph **3.1.5**), it became apparent that C111 positions onto the ß-sheet surface and H83 is located to one of the flexible loops (**Figure 25D**). For RBDs, the ß-sheet surface has been identified as the major RNA binding platform, although also loop-mediated RBD-RNA interactions have been reported (Cléry et al., 2008; Cléry et al., 2013). Electrostatic surface representation illustrates that C111 and H83 are both part of a positively charged surface pre-dispositioned to bind RNA (**Figure 25E**). The crosslinked amino acids C270, H386 and C463 are distributed across the methyltransferase domain. According to sequence alignment with *E. coli* TrmA (**Supplemental Figure 5**), C463 of hTRMT2A corresponds to A241 of *E. coli* TrmA. In the *E. coli* TrmA RNA co-structure (PDB: 3BT7), residue A241 is close to the catalytic center and in proximity (below 10 Å) to the stem of the T-loop. Proximal to the crosslinked residue C270 lies G263, which corresponds to R51 of *E. coli* TrmA, a residue shown to contribute to tRNA binding (Keffer-Wilkes et al., 2020).

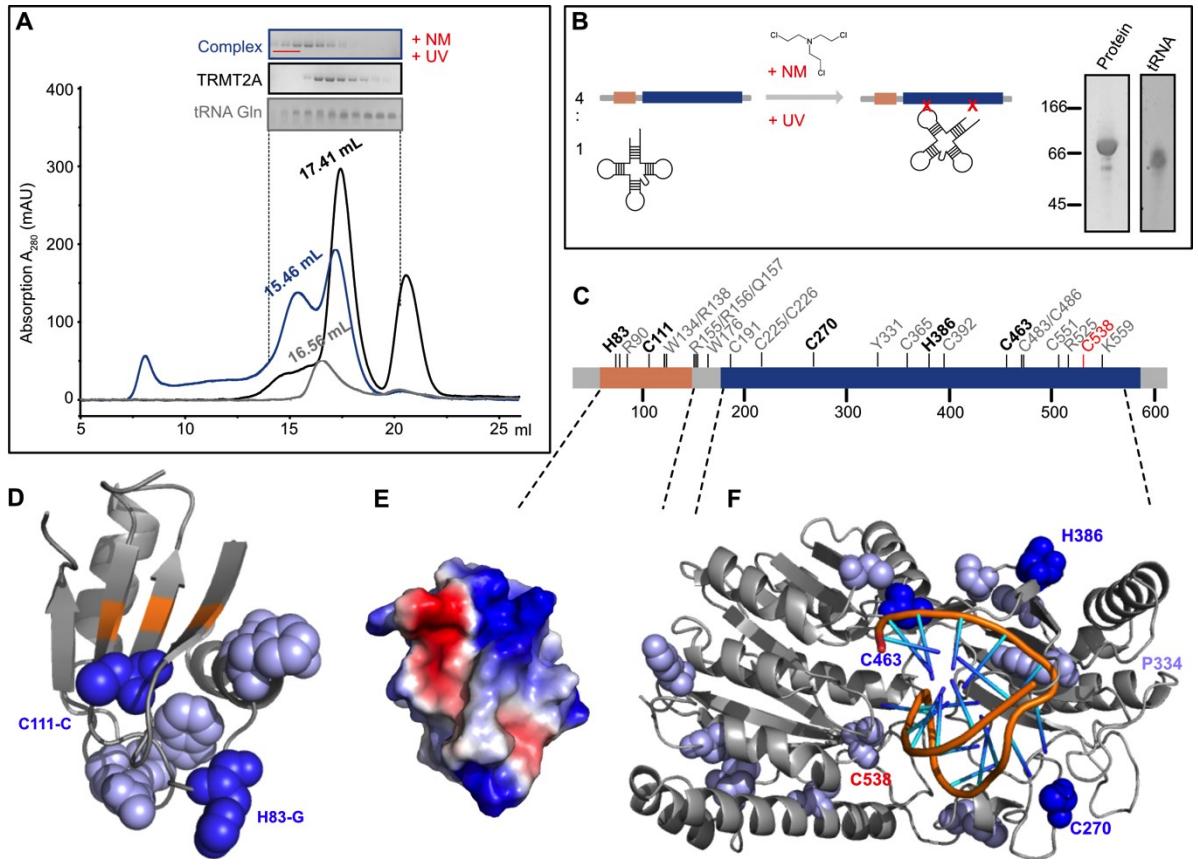

Figure 25 – Crosslinking and mass spectrometry of hTRMT2A FL and tRNA^{Gln} identifies several RNA-interacting residues
A SEC profile from a S6 (15/150) column run with hTRMT2A FL and tRNA^{Gln}, as well as the stable protein-RNA 1:1 complex. SDS-PAGE and denaturing PAGE of protein, RNA and complex are shown. Pooled fractions for crosslinking experiments are highlighted in red. **B** Scheme of *in vitro* reconstitution experiment with purified hTRMT2A and *in vitro* transcribed tRNA^{Gln}, both shown on denaturing PAGE. **C** Crosslinked amino acids are mapped on a linear representation of hTRMT2A and those consistently found in 3 or 4 of 4 datasets highlighted in bold letters. Catalytic cysteine C538 is labelled red. **D** Crosslinked amino acids are mapped on the hTRMT2A RBD structure. Consistently found crosslinked amino acids (3 or 4 of 4 datasets) are colored in dark blue, less consistently found amino acids (less than 3 of 4 datasets) in bright blue. Predicted RNA binding surface is colored orange. **E** Electrostatic surface representation of hTRMT2A RBD shows crosslinked amino acids being located to a positively charged patch. **F** hTRMT2A AlphaFold homology model (grey) overlayed with T-loop from *E. coli* TrmA structure (PDB: 3BT7; orange). Consistently (blue) and less consistently (bright blue) found crosslinked amino acids were mapped onto the model. Structure and model were generated with PyMol.

In two of four datasets (**Figure 25C**, grey; **Figure 25D/F**, bright blue), 17 additional cross-linked residues were identified. Most notably, amongst them is the catalytic cysteine C538 cross-linked to uridine. C538 is known to covalently bind the tRNA at position U54 (Carter et al., 2019). Hence, it constitutes an internal control for correctly crosslinked amino acids. For a complete list of crosslinked amino acids, refer to **Supplemental Table 4**. Taken together, these results support the previous observation from EMSAs that multiple domains are required for tRNA binding. Furthermore, the crosslinking experiments extend these findings to single amino acid resolution.

3.3.5 A model of hTRMT2A and $tRNA^{Gln}$ binding

In order to generate a cross-validated hTRMT2A-tRNA model the recently released AlphaFold homology model of hTRMT2a was used (ID: Q8IZ69, https://alphafold.ebi.ac.uk/entry/Q8IZ69). AlphaFold predictions have been proven to be more accurate than models generated by other algorithms (Jumper et al., 2021). An overlay of this homology model with the crystal structure of *E. coli* TrmA bound to a tRNA T-Loop (PDB: 3BT7) allowed to model a full tRNA (PDB: 4TRA) by superposition to the tRNA T-loop and th tRNA. Protein stretches with low confidence scores were removed from the model (< 70 PLDDT). RNA-protein crosslinks identified by mass spectrometry were subsequently mapped onto the model (**Figure 26**, dark blue = 3/4 of 4 datasets, bright blue = 2 of 4 datasets). In this hybrid model, all three hTRMT2A domains are in proximity to the tRNA.

Most notable is the localization of the crosslinked amino acids around the catalytic center, into which the T-loop is inserted for methylation. The crosslinked amino acid C463 is near the modeled T-loop stem. Additionally, the crosslinked C270 would be placed in between T-loop and D-loop and could interrupt tertiary interactions and hence render U54 accessible for methylation (**Figure 26A**). Several other crosslinked residues can be explained with our hybrid model such as Y331, W176 and C486.

In rare cases the nucleotide sequence crosslinked to the amino acid is not digested down to single nucleotides, but instead a dinucleotide remains. If the sequence is unique, this allows for narrowing down to the exact part of the tRNA, which is bound to a certain residue. In my data, double uridine (UU) is such as case, as it only occurs three times in the $tRNA^{Gln}$. UU occurs in the D-Loop (U19/20), the T-Loop (U54/55) and the Anticodon-Loop itself (U33/34). In mass spectrometry raw data C538, C270 and C463 residues were crosslinked to UU. Considering the structural model described here, the crosslinked C270 is ideally placed to bind to U19/20 of the D-Loop (**Figure 26A**, zoom in green). The already observed crosslink of the catalytic C538 to a single U is further corroborated by the UU, which agrees with U54/55 of the T-Loop. In the model, C463 is close to the T-Loop as well, wherefore the

observed UU crosslink is suggested to be U54/55 (**Figure 26A**, zoom in red), and not D-Loop or Anticodon-Loop UU. However, no other unique di- or trinucleotides were found.

According to this hybrid model, the RBD is placed to the tRNA four-way junction and is called RBD placement 1 (**Figure 26B**). To minimize clashes between RNA and protein, the RBD was manually readjusted and placed near the D-Loop on the opposite side of the anticodon stem. This is called RBD placement 2 and visualized in **Figure 26B** (zoom in beige). Both placements would partially explain the crosslinked amino acids C111 and H83 (dark blue), as well as R90 and R137 (bright blue). Especially for RBD placement 2, the consistently crosslinked C111 and H83 are proximal to the RNA.

In summary, the co-complex model is consistent with experimental crosslinking data and therefore is likely to be of high accuracy.

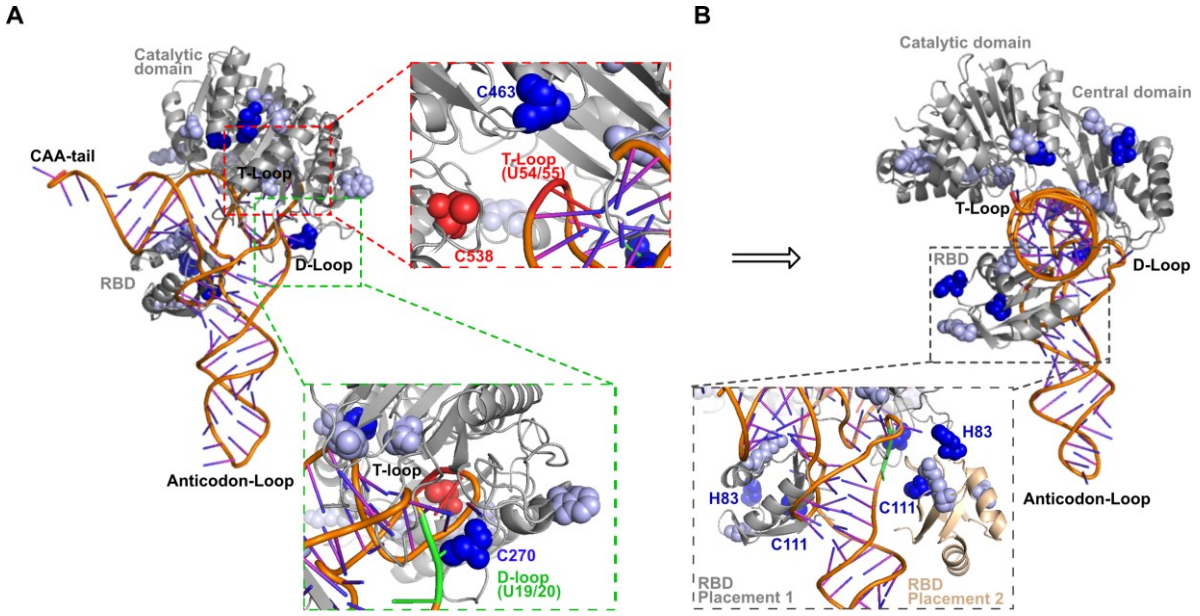

Figure 26 – Hybrid model of hTRMT2A-tRNA binding.
A Hybrid model consisting of the hTRMT2A AlphaFold homology model (grey) and overlayed experimental tRNA structure (PDB: 4TRA) based on the *E. coli* TrmA T-loop co-structure (PDB: 3BT7). Crosslinked amino acids from mass spectrometry experiments are highlighted blue (3/4 of 4 datasets) or bright blue (2 of 4 datasets) and mapped onto the hybrid model. Areas of interest for unique UU are zoomed in. In green is zoom in on D-Loop with U19/20 proximal to C270. In red is zoom in on T-Loop with U54/55 proximal to C538 and C463. **B** 90 ° turned hybrid model illustrates zoom in on RBD placement 1 (grey) and RBD placement 2 (beige). Latter brings H83 and C111 in proximity to RNA.

3.4 Interactome of hTRMT2A

Although a transcriptome-wide map of hTRMT2A RNA interactions has been produced recently (Carter et al., 2019), hTRMT2A function has not been studied in a proteome-wide approach, yet. To fill this gap, the hTRMT2A proteome was identified with two complementary techniques – proximity-dependent biotinylation and co-immunoprecipitation. For RNA-binding proteins such as hTRMT2A, a proteomics experiment can ideally be also used to differentiate between RNA-dependent and RNA-independent interactions.

3.4.1 Impaired RNA binding hTRMT2A mutant

Before hTRMT2A interactome studies were started, the aim was to generate a mutant version of hTRMT2A that lacks RNA binding as control for cellular studies. In line with results described in paragraphs **3.3.3** and **3.3.4**, an impaired RNA binding hTRMT2A mutant supposedly requires mutations in both the RBD and across the methyltransferase domain. Based on sequence conservation and the reported impact of mutations on RNA binding in *E. coli* TrmA (Urbonavičius et al., 2007), three amino acids on the ß-sheet surface of the RBD (E76A, K104E, F113A) and five across the methyltransferase domain were selected for mutation (K242A, F409A, Q411A, D510A, C538A). This hTRMT2A mutant was termed impaired RNA binding mutant (IR). hTRMT2A IR was used in comparative RNA-binding assays with hTRMT2A WT, the previously reported catalytic base mutant E581A (CBM), and the catalytic nucleophile mutant C538A (CNM) (Carter et al., 2019). All proteins were expressed and purified as outlined in paragraph **2.3.6** (**Figure 10E**). For EMSAs, ^{32}P-labelled tRNA^{Gln} was incubated with increasing concentrations of WT and mutant proteins (0-1.25 µM). The CBM and CNM mutants showed slightly less binding to tRNA^{Gln} than WT protein when comparing their fractions of unbound RNA at higher protein concentrations. In contrast, the IR mutant displayed similar binding as WT, but an increase in supershifted binding events (**Figure 27A**).

To characterize similar binding affinities of hTRMT2A WT and IR in a quantitative manner, analyses with SPR were performed. Biotinylated tRNA^{Gln} was surface-coupled to a streptavidin-coated SA sensor chip. An empty channel activated with NaOH served as reference flow channel. Protein concentration series from 12.5-400 nM (WT) and 15.6-1000 nM (IR) were injected with a constant flow rate of 30 µL/min. A long dissociation phase of 6 min and two successive regeneration steps with 500 mM NaCl were performed to ensure effective release of bound protein after each measurement. In agreement with EMSAs, hTRMT2A WT exhibited a high binding affinity with a K_D of 56 ± 16 nM (**Figure 27B**). Observed slow on- and off-rates are characteristic of stable complexes. In contrast, hTRMT2A IR showed a 5-6 times lower affinity (K_D of 304 ± 62 nM) and fast on- and off-rates indicative of more transient RNA binding. Of note, the regeneration procedure did not

completely prevent protein accumulation on the chip, as observed with shifted control measurements (**Figure 27B,** red curve). However, differences of hTRMT2A WT and IR binding affinities should remain largely unaffected by this observation.

Analogous to enzymatic assays presented in paragraph **3.3.2**, the MTase Glo™ assay was performed with purified hTRMT2A WT, CBM, CNM and IR mutants and increasing $tRNA^{Gln}$ concentrations (0-6 µM). Consistent with much weaker RNA binding capabilities of hTRMT2A IR, its enzymatic activity was abolished (**Figure 27C,** red curve). In contrast to hTRMT2A WT, the hTRMT2A CBM mediated methylation reaction saturated at lower RNA

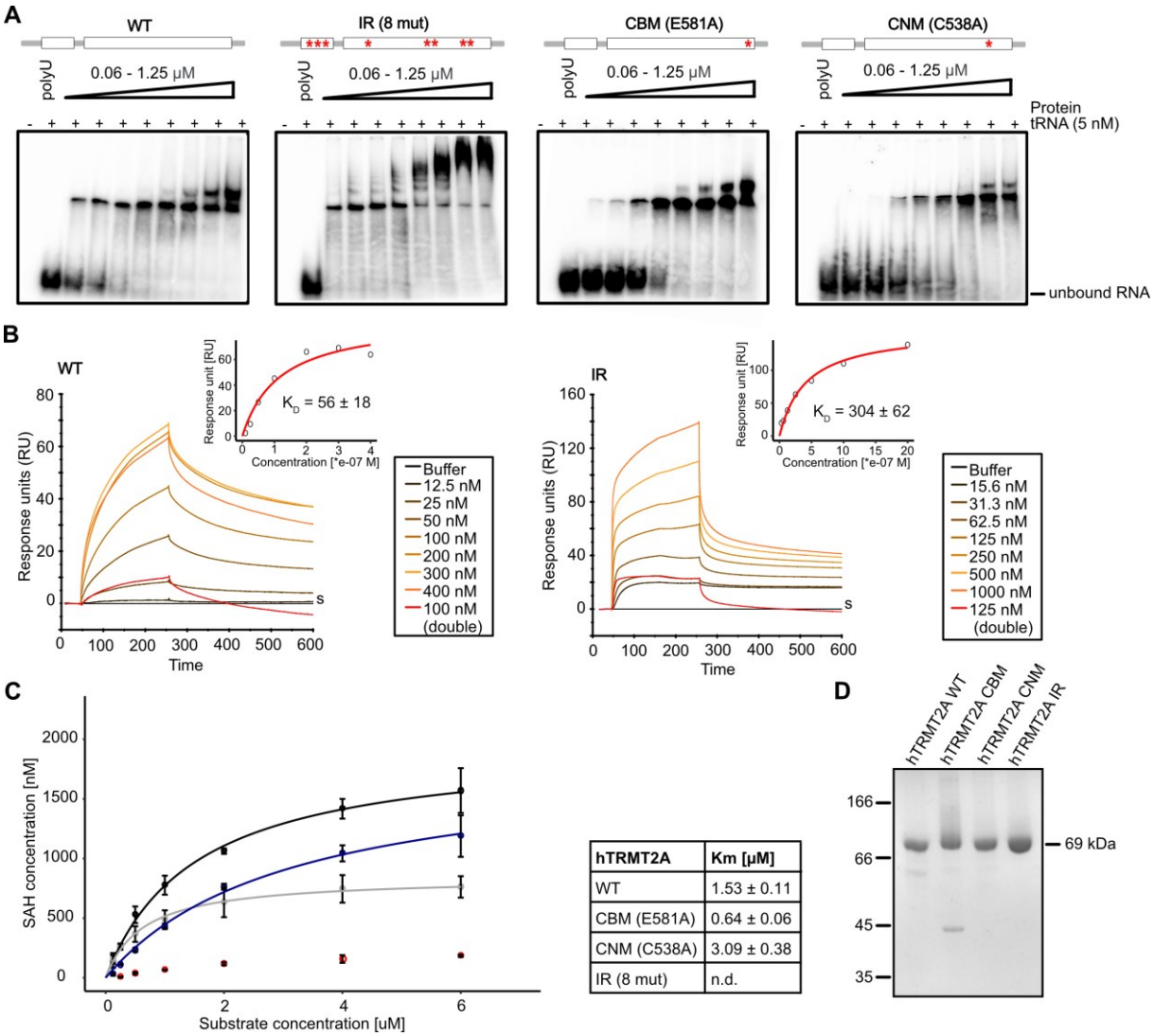

hTRMT2A	Km [µM]
WT	1.53 ± 0.11
CBM (E581A)	0.64 ± 0.06
CNM (C538A)	3.09 ± 0.38
IR (8 mut)	n.d.

Figure 27 – Validation of hTRMT2A mutant with impaired RNA binding (IR).
A EMSAs show that RNA binding was similar for hTRMT2A WT and mutants. For these binding assays 5 nM ^{32}P-labelled RNA was incubated with increasing concentration of hTRMT2A WT, CBM, CNM, IR (0-1.25 µM) in presence of polyU competitor (2.5 ng/µL) for 20 min. Reaction without protein served as control. Complexes were separated on 4 % native PAGE. **B** SPR experiments with biotinylated $tRNA^{Gln}$ coupled to streptavidin-coated surface of a SA-chip. Injection series of 12.5-400 nM (WT) and 15.6-1000 nM (IR) resulted in illustrated, representative double referenced binding curves. Steady state model was fitted at binding curve equilibrium and allowed computation of K_D values, which show a 5-6 times higher affinity binding for hTRMT2A WT than for hTRMT2A IR. K_D values were derived from triplicate measurements. **C** Promega's MTase Glo™ assay was performed with 5 µM protein and increasing concentrations of $tRNA^{Gln}$ (0-6 µM). Enzymatic activity of hTRMT2A IR mutant was completely abolished (red), whereas CBM and CNM mutants showed only changed enzymatic activity. Reaction without RNA served as control. Data represent mean ± SD (N=3). Curves were fitted with Michaelis Menten equation illustrated as lines using R and calculated K_m values are listed. **D** Purity of hTRMT2A WT and mutants is shown on SDS PAGE.

concentrations and a slightly lower K_M of 0.64 ± 0.06 µM (**Figure 27C**, grey curve). This agrees with irreversible trapping of RNA and therefore blockade of the catalytic center. The hTRMT2A CNM displayed a three times higher K_m, which indicates less efficient methylation (**Figure 27C**, blue curve). Conclusively, only hTRMT2A IR reduced $tRNA^{Gln}$ binding and abolished methylation and thus was selected as validated control for cellular studies.

3.4.2 BioID identifies the hTRMT2A proximity interactome

For unbiased assessment of the protein interactome of hTRMT2A and hence its cellular functions, proximity-dependent biotinylation was employed (Roux et al., 2013). This approach detects proximal proteins (**Figure 28A**), as the promiscuous biotin ligase BirA* fused to hTRMT2A biotinylates proteins in proximity of up to 10 nM. For the assay, BirA* was fused to the N-terminus of hTRMT2A WT and IR and stably overexpressed in HEK cells using the doxycycline-inducible PB transposon system (Li et al., 2013; Krendl et al., 2017). As control, BirA* alone was expressed. HEK cells were incubated with biotin and subsequently lysed. Biotinylated proteins were captured by streptavidin-coated beads and analysed by mass spectrometry done in collaboration with the proteomics core facility of the Helmholtz Center Munich (Dr. Stefanie Hauck). BirA* biotinylated many cellular proteins as detected by streptavidin Western blotting (**Figure 28B**). Experiments were conducted in quintuplicates and principal component analysis of mass spectrometry results confirmed significant differences between samples from the different cell lines (**Supplemental Figure 7A**) Significance values of data comparison between WT/BirA*, IR/BirA* and IR/WT were computed with the Progenesis QI software (version 4.1). Data were visualized as volcanoplots with a R-script adapted from Melina Klostermann (Zarnack laboratory, Frankfurt University). The ratios of WT/BirA* and IR/BirA* were plotted against significance values with cut-offs for ratio as fold change > 2 or < 0.5 and for p-value < 0.001 (**Figure 28C/D**)**.** Proteins from a previously published frequent false discovery list for BioID experiments (Roux et al., 2013; Go et al., 2021) were subtracted from significant hits prior to further analysis. 222 (orange) and 177 (blue) proteins were enriched in WT and IR samples over BirA* background control, respectively (**Supplemental Table 5**). Both datasets shared a subset of 115 proteins. Since hTRMT2A IR is impaired in RNA binding, these 115 proteins constitute candidates for potential RNA-independent interactions.

GO-term analyses were performed with the GO enrichment analysis tool from the gene ontology server using the PANTHER databank (Ashburner et al., 2000; Mi et al., 2013; The Gene Ontology Consortium, 2021). Data were visualized with custom R-scripts (**Supplemental Figure 10**). The GO-terms “biological processes” and “cellular compartments” revealed an enrichment of rRNA processing and ribosome biogenesis and a primary localization to the nucleolus in WT/BirA* and IR/BirA* datasets (**Figure 28C/D**). In

agreement with this observation, amongst the top 15 most significantly enriched factors are proteins involved in rRNA processing and proteins localized to the nucleus. One such hit is PDCD11, which is involved in the maturation of 16S rRNA, and the transcription factors

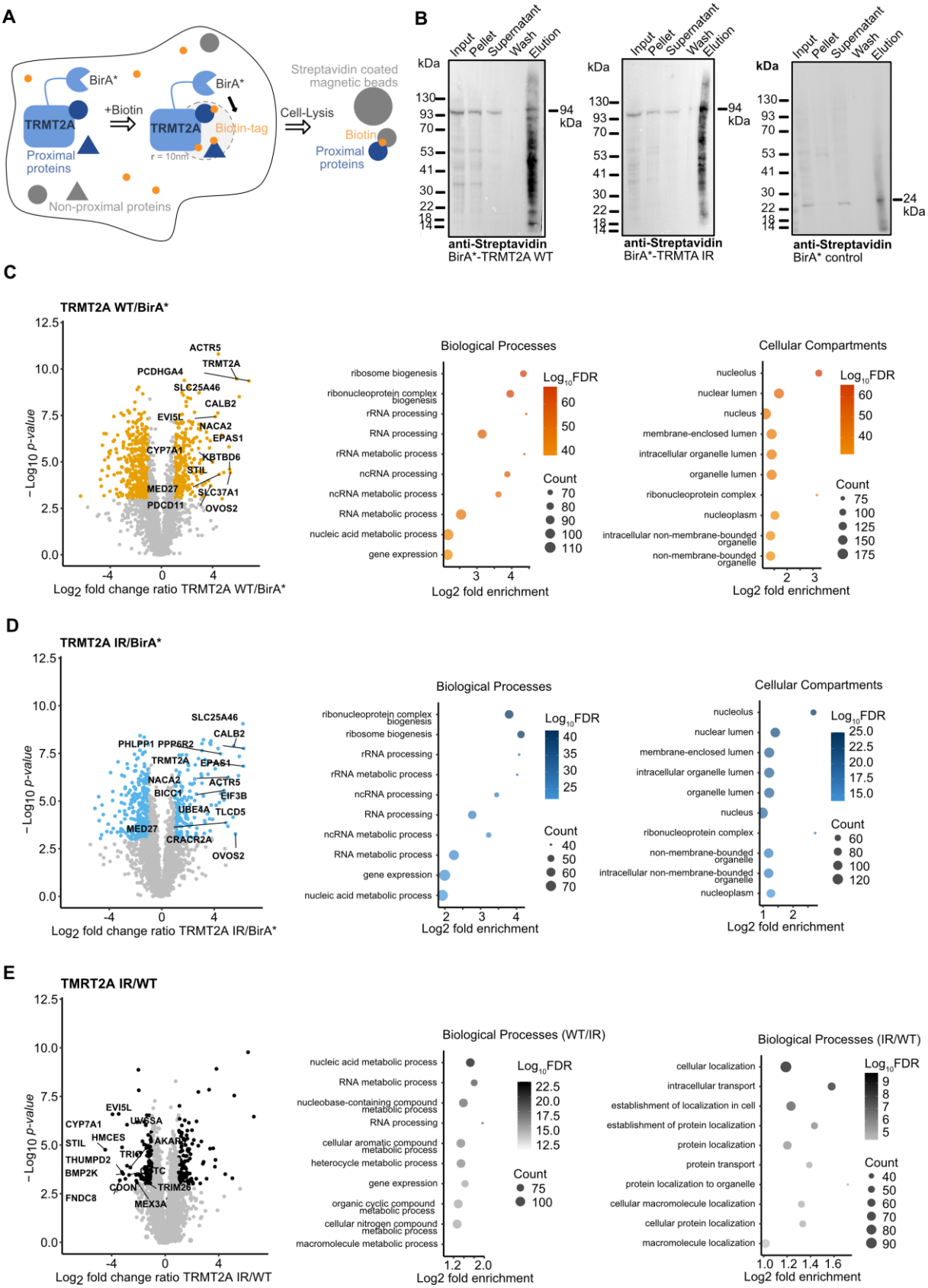

Figure 28 – Results of BioID experiments with hTRMT2A WT and IR.
A Cartoon of BioID experiment, where BirA* fused to hTRMT2A biotinylates all proximal proteins. Biotinylated proteins are enriched with streptavidin coated magnetic beads and subjected to mass spectrometry. **B** Streptavidin Western blots of samples from hTRMT2A WT, hTRMT2A IR and BirA* control BioID experiments shows elution of a wide range of biotinylated proteins. Respective electrophoretic run length of pulled-down protein of interest is indicated with an arrow. **C** Volcanoplot of BioID experiment (N=5) with hTRMT2A WT. Log_2 fold change ratio of hTRMT2A WT/BirA* was plotted against $-Log_{10}$ p-value. Ratio cut-offs were > 2 and < 0.05 and significance cut-off was a p-value < 0.001. Hits in agreement with these thresholds are highlighted (yellow). Top 15 hits are labelled with protein names. Top 10 most enriched GO-terms for biological processes (BP) and cellular compartments (CC) were retrieved from the PANTHER GO-term databank and ranked according to false discovery rate (FDR) as computed with the fisher's exact test. GO-terms were visualized in R. Graphs illustrate GO-terms plotted against Log_2 fold enrichment. Node color represents Log_{10}FDR. Node size represents counts per GO-term. **D** Volcanoplot of hTRMT2A IR BioID experiment (N=5) with significant hits in blue. BP and CC GO-terms. **E** Volcanoplot, for which hTRMT2A IR/WT ratio is plotted against significance values, with significant hits in black. GO terms of BP from hTRMT2A WT/IR and hTRMT2A IR/WT comparisons indicate loss of RNA-related processes in the hTRMT2A IR mutant.

MED27 or EPAS1 both localized to the nucleus.

Moreover, the difference in the interactome of hTRMT2A WT and IR was compared by plotting the ratio of IR/WT against significance values (**Figure 28E**). Overall, 95 proteins were enriched in the WT over the IR dataset and constitute potential RNA-dependent interaction partners. Notably, these hTRMT2A WT enriched proteins are associated with RNA and nucleic acid-related processes (GO-term analysis; **Figure 28E**). For example, amongst the top 15 enriched proteins were RNA-binding proteins like MEX3A or the 5-hydroxymethylcytosine binding protein HMCES. This demonstrates that hTRMT2A IR interacting-proteins were depleted in nucleic acid associated functions. Hence, RNA binding deficiency of the hTRMT2A IR mutant was not only confirmed *in vitro*, but also with cellular experiments.

3.4.3 Co-IP identifies hTRMT2A interacting proteins

To cross-validate the interaction partners identified by BioID with a second proteome-wide approach, co-immunoprecipitation experiments were performed (**Figure 29A**). Fusion proteins consisting of a FLAG peptide and hTRMT2A WT or hTRMT2A IR or the FLAG peptide alone were stably overexpressed in HEK cells using the doxycycline-inducible PB transposon system. After cell lysis, interacting proteins were indirectly captured with FLAG antibody-coated beads and analysed with mass spectrometry. Successful elution of FLAG-hTRMT2A, FLAG alone and its interacting proteins from beads was confirmed in Western blot experiments (**Figure 29B**). Co-IP experiments were conducted in quintuplicates and principal component analysis showed differences between samples from different cell lines (**Supplemental Figure 7B**). A plot of WT/FLAG and IR/FLAG ratios against significance values (cut-offs for ratio were fold change > 2 or < 0.5 and for p-value < 0.001) revealed enrichment of 74 and 72 proteins in hTRMT2A WT and IR samples over FLAG background control, respectively (**Figure 29C/D** and **Supplemental Table 6**).

Both datasets shared a subset of 39 proteins that constitute possible RNA-independent interacting proteins. Moreover, differences in the interactome of hTRMT2A WT and IR were

compared by plotting the ratio of hTRMT2A IR/WT against significance values. Overall, 19 proteins were enriched in hTRMT2A WT/IR and constitute potential RNA-dependent

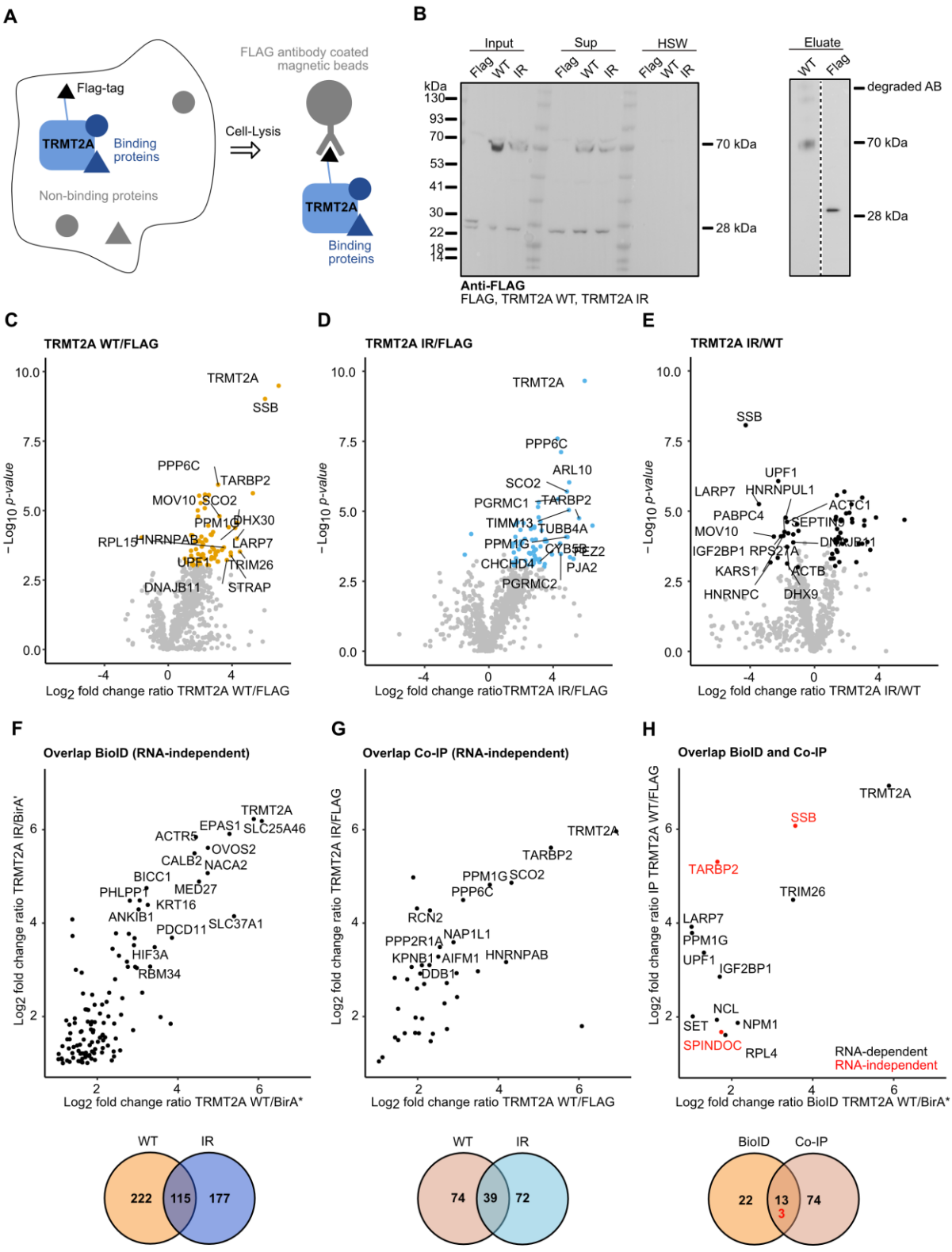

Figure 29 – Result of Co-IP experiments with hTRMT2A WT and IR.
A Cartoon of Co-IP principle. FLAG-tag fused to hTRMT2A allows for enrichment of hTRMT2A and bound proteins with FLAG antibody-coated magnetic beads. **B** Anti-FLAG Western blots of samples from Co-IP experiment with hTRMT2A WT, hTRMT2A IR and FLAG control confirm successful enrichment of hTRMT2A using magnetic beads. Respective height of pulled-down protein of interest is indicated with an arrow. **C** Volcanoplot of Co-IP experiment (N=5) with hTRMT2A WT. Log_2 fold change ratio of hTRMT2A WT/FLAG was plotted against $-Log_{10}$ p-value. Ratio cut-offs were > 2 and < 0.05 and significance cut-off was a p-value < 0.001. Hits in agreement with these thresholds are highlighted (yellow). Top 10 hits are labelled with protein names. **D** Volcanoplot of Co-IP experiment (N=5) with hTRMT2A IR. Significant hits are colored blue. **E** Volcanoplot of hTRMT2A IR/WT ratios plotted against significant values. Significant hits are colored black. **F** Overlap of significant hits from BioID datasets. Number of enriched proteins (222/177) is illustrated in a Venn diagram below with an overlap of 115 proteins. **G** Overlap of significant hits from Co-IP with number of enriched proteins in Venn diagram (74/72) and an overlap of 39 proteins. **H** Overlap of significant hits from BioID and Co-IP hTRMT2A WT datasets shows 13 co-occurring RNA-dependent protein interaction partners. In an additional comparison with hTRMT2A IR datasets three RNA-independent protein interaction partners were extracted and are highlighted in red.

interaction partners (**Figure 29E**). Several proteins with RNA binding function were enriched in this hTRMT2A WT/IR comparison, which validates again the hTRMT2A IR mutant. Amongst the top 15 most enriched proteins in the WT over IR data were the RNA binding proteins LARP7, which processes snRNA, and the tRNA maturation chaperone SSB. These are highlighted, because they both associate with small non-coding RNA processing pathways, tRNA and snRNA maturation. These processes seem to be depleted in the hTRMT2A IR mutant.

For a close-up look on RNA-independent interaction partners, the ratios of significantly enriched proteins from hTRMT2A WT and IR datasets were plotted against each other (BioID: **Figure 29F,** Co-IP: **Figure 29G**)**.** Strikingly, in the case of Co-IP experiments several protein phosphatases (PPP6C, PPM1G, PPP2R1A) were enriched, which are expected to act RNA-independently and might represent phosphatases that modify hTRMT2A post-translationally.

To identify high confidence hTRMT2A interacting proteins BioID and Co-IP datasets were compared. The ratios of significant hTRMT2A WT hits from BioID and Co-IP datasets were plotted against each other. This resulted in 13 common proteins, three of them previously identified with a different high-throughput approach (Huttlin et al., 2017; Huttlin et al., 2021): SSB, TARBP2 and PPM1G (**Figure 29H**). Of note, three of the 13 common proteins participate in mitosis; NPM1 in centrosome duplication, NCL in chromatin decondensation and SET in nucleosome assembly. This constitutes an interesting link to the known feature of hTRMT2A to be cell-cycle regulated (Guarguaglini et al., 1997). Furthermore, several ribosome related proteins were identified, such as LARP7, NCL, NPM1 and RPL4.

Ratios of significant hits from BioID and Co-IP hTRMT2A IR data were added to the comparison. The three proteins labelled in red in **Figure 29H** were found in all datasets and thus comprise the most likely RNA-independent protein interaction partners. Firstly, human Lupus La protein (SSB), which is part of the pre-tRNA processing pathway. Secondly, the RISC complex subunit TARBP2 involved in the miRNA pathway and thirdly the

transcriptional regulator SPINDOC. Follow-up studies will be required to validate interaction partners and establish functional relevance.

3.4.4 hTRMT2A localizes to the nucleus

The list of GO-terms shown in **Figure 28** suggested a primary hTRMT2A localization to the nucleus and nucleoplasm. To verify subcellular localization, ICC of the FLAG-fused hTRMT2A WT and IR overexpression HEK cell lines with an anti-FLAG antibody were performed as outlined in paragraph **2.8.4**. DAPI (blue) served as nuclear stain and GFP (green) as positive control for successful dox-induction of protein expression (**Figure 30**). Additionally, cells were stained with an IgG control antibody to estimate unspecific background staining. To prevent bleaching effects from the GFP channel, Alexa-648 (red) was used as secondary antibody. Images confirm clearly that hTRMT2A WT and IR were localized predominantly to the nucleus, although also faint cytoplasmic staining was visible. Conclusively, these immunostainings are consistent with the GO-terms for cellular compartments “nucleoplasm”, “nucleus” and “cytosol”. Furthermore, the here observed hTRMT2A localization is in line with previously reported hTRMT2A localization in the Human Protein Atlas (https://www.proteinatlas.org) (Uhlén et al., 2015) and a previous study (Chang et al., 2018).

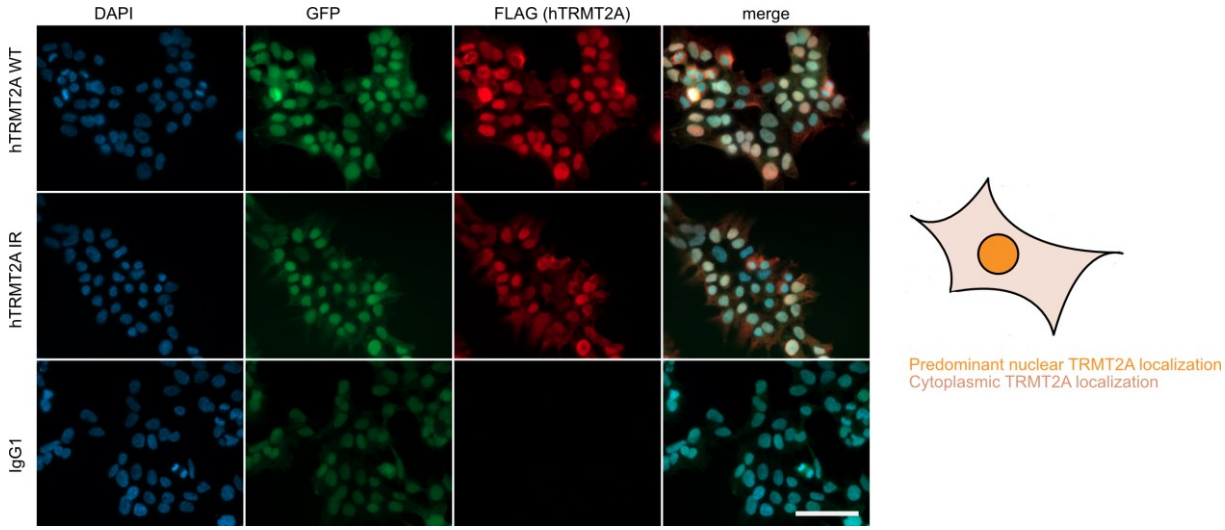

Figure 30 – IHC of overexpressed hTRMT2A WT and IR confirms nuclear localization in HEK cells.
Cartoon on the right indicates the localization of hTRMT2A in HEK cells with primary localization to the nucleus. Images on the left show a primarily localization of FLAG-fused hTRMT2A WT and IR to the nucleus. FLAG-fused hTRMT2A WT and IR HEK cells, which were grown on poly-D-Lysine coated coverslips, were immunostained. 18 h prior to staining the protein expression was induced with 1:1000 doxycycline. Incubation with primary antibody dilutions (rat-FLAG = undiluted, rat-IgG1 = 1:250) was followed by incubation with secondary antibody dilutions (goat-α-rat-Alexa647, 1:500). Coverslides were analysed with fluorescence microscopy and a magnification of 63x. Exposure times were for GFP = 134 ms, DAPI = 5 ms and Alexa 647 = 146 ms. Images were analysed with Fiji. Marker (white bar) correlates with 100 µm.

4. Discussion

A variety of hTRMT2A domains from different homologs were successfully purified and either used for crystallization trials or biochemical assays. In addition, a methyltransferase assay was established that allows for measuring the inhibitory effect of potential compounds on hTRMT2A activity. Combined with compound binding assays an *in vitro* validation pipeline for potential hTRMT2A inhibitors was set up.

Mechanistically, determinants of hTRMT2A substrate binding and methylation were characterized, as well as amino acids/domains involved in tRNA binding. Finally, the hTRMT2A-interactome was identified. To my knowledge, this thesis provides the most detailed structural and functional characterization of hTRMT2A so far. My work will hopefully contribute to an understanding of the underexplored m^5U RNA modification enzyme hTRMT2A and its importance in different cellular processes.

4.1 Purification and crystallization of hTRMT2A and its homologs

A TRMT2A X-ray structure would support structure-based drug discovery and reveal underlying catalytic and RNA binding mechanisms of the enzyme. Therefore, purification of hTRMT2A, *dm*TRMT2A and *ct*Trm2, as well as purification of their subdomains was performed to obtain material for biochemical assays and crystallization trials.

4.1.1 Predicted RNA recognition mode of hTRMT2A RBD and *dm*TRMT2A RBD

Crystallization trials with several proteins (**Supplemental Table 2**) resulted finally in the structures of N-terminal hTRMT2A RBD at 1.2 Å and *dm*TRMT2A RBD at 1.6 Å. Both RBD structures adopt the typical ß1-α1-ß2-ß3-α2-ß4 topology as depicted in **Figure 31A**, which is the most abundant RBD fold in higher vertebrates (Venter et al., 2001). Two conserved regions on the two middle ß-strands called RNP1 and RNP2 are responsible for canonical single stranded RNA binding via solvent exposed aromatic residues. Comparison of previous RBD-RNA co-structures showed that the RNA 5' and 3' ends base stack with the aromatic ring in ß1 (position 2 of RNP2) and ß3 (position 5 of RNP1). A third aromatic ring on ß3 (position 3 of RNP1) is usually inserted between the two sugar rings of this RNA dinucleotide.

In **Figure 31B** the conserved sequence of RNP1 and RNP2 and its agreement with hTRMT2A and *dm*TRMT2A RBD is shown. Conclusively, two residues on TRMT2A RNP1 (*dm*TRMT2A: F98, F101; hTRMT2A: C111, F113) mostly agree with conserved RNP binding residues, except for hTRMT2A C111, and are solvent exposed. However, no aromatic residue is found on position 2 of RNP 2. Consequently, the TRMT2A RBD-RNA interaction is classified as non-canonical and other structural elements likely contribute to RNA binding.

Candidate regions for such an alternative RNA binding platform are α-helix α1, loops 1-5 or unstructured N- and C-termini of the RBD (Cléry et al., 2013). RBDs that bind RNA only with the α-helix α1 are called pseudo-RBDs and possess a conserved sequence motif that is not present in the TRMT2A RBD structures. RBDs that bind RNA only with loop 3 and loop 5 are termed quasi-RBDs and also harbour a conserved sequence motif that is not found in TRMT2A RBD structures (Dominguez and Allain, 2006). Interestingly, the most consistently found crosslinks of hTRMT2A RBD with $tRNA^{Gln}$, as outlined in paragraph **3.3.4**, are located on the conserved RNP1 position 3 (C111) and to loop 3 (H83). Another less consistent crosslink (R137) is found in loop 5. Thus, it is hypothesized that TRMT2A RBDs bind RNA with residues on the ß-sheet and additionally extend the RNA binding interface beyond the canonical ß-sheet to loop residues. A similar interaction was reported for the splicing factor Fox1, where ß-sheet, loop 3 and loop 5 participated in RNA binding of an U-G-C-A-U-G element as shown in **Figure 31C** (Auweter et al., 2006). Respective positively charged patch on the hTRMT2A RBD surface pre-dispositioned to bind RNA and visualized in **Figure 25E**, support this hypothesis**.** To sum up, both hTRMT2A and *dm*TRMT2A are neither quasi-RBDs, nor canonical RBDs nor pseudo-RBDs, but both are conserved in their predicted RNA-binding features. Thus, they most likely recognize RNA in a similar way. The RNA binding mode remains to be proven for example with a co-structure of TRMT2A RBD and a 4-8 nucleotide RNA or mutational studies of the proposed RNA binding residues.

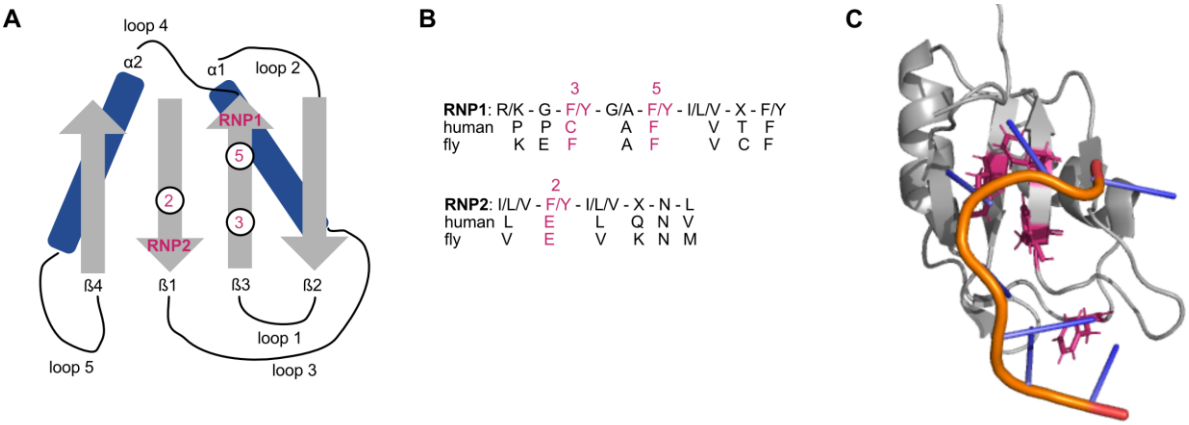

Figure 31 – RBD topology and conserved RNA binding residues.
A Typical fold of an RBD. Conserved RNA binding residues of RNP1 (position 3 and 5, pink) and RNP 2 (position 2, pink) are indicated. **B** Conserved sequence of RNP1 and RNP2 in comparison to respective elements of hTRMT2A and *dm*TRMT2A shows partial conservation. **C** Structure of splicing factor Fox1 with UGCAUG RNA shows an RBD that binds its target RNA with ß-sheet surface and an additional loop (loop 3). RNA binding residues are indicated in pink. Structure was visualized with the program PyMol (PDB: 2ERR).

4.1.2 Future directions for solving the TRMT2A structure

hTRMT2A, *dm*TRMT2A and *ct*Trm2 FL, as well as their subdomains resisted crystallization, although high protein purity was achieved. Until now, however, no experiments with recombinantly purified hTRMT2A, *dm*TRMT2A or *ct*Trm2 were reported. Hence, these trials constitute a source of valuable information to inform future TRMT2A

structural-biology campaigns and provide material for biochemical experiments. In the following paragraph reasons for limited success in crystallography trials and potential ways to overcome these obstacles are given.

Firstly, the segment between RBD and central domain is predicted to be unstructured, which provides the enzyme with the required flexibility for structural rearrangements upon RNA binding (yellow; **Figure 32B**). This was also reported for the evolutionary related *E. coli* m^5U RNA methyltransferase RlmD, introduced in section **1.2.1** (Lee et al., 2004). The flexibility of this part might also prevent crystallization. Additionally, thermofluor experiments indicated low protein stability of hTRMT2A FL (**Figure 16**). Co-crystallization with the cognate RNA substrate, either as tRNA T-loop or the complete tRNA, might help to order TRMT2A properly and hence allow for crystallization. Of note, an RNA-trapping mutant and a fluorinated uridine-containing RNA were required previously to generate a stable enzyme-RNA complex for crystallographic studies (Alian et al., 2008; Carter et al., 2019). Secondly, during hTRMT2A and *dm*TRMT2A purification trials, removal of endogenous bound RNA rendered the proteins less stable. Thus, co-expression and co-purification of a TRMT2A-RNA complex is advised, which could be achieved with a previously published protein-RNA co-expression system (Ponchon et al., 2013). Thirdly, another way to remove flexible loops and termini to foster crystallization is limited or *in situ* proteolysis. Although first attempts in this direction with *dm*TRMT2A remained unsuccessful (**Figure 12E**), further trials with *dm*TRMT2A and *ct*Trm2 FL using different proteases and conditions might improve the outcome (Gräslund et al., 2008; Wernimont and Edwards, 2009).

For the *ct*Trm2 FL protein I predicted a metal-ion sulphur cluster as visualized in **Figure 13C**. To determine the importance of co-factors like metal ions for protein stability, a thermofluor-based stability screen has been suggested in the past (Boivin et al., 2013). In case of *ct*Trm2 FL a thermofluor assay and successive purification with identified metal ion and a sulphur-containing molecule (for example NH_4SO_4) might render the protein accessible for crystallization. Basis for this assumption is the purification of the structurally related m^5U methyltransferase RlmD, where four cysteines (C81, C87, C90, C162) coordinate an iron-sulphur cluster crucial for maintaining the protein fold (Lee et al., 2004). Like *ct*Trm2 FL protein, the purified RlmD protein showed a yellow colour. If confirmed, such a *ct*Trm2 metal-ion sulphur cluster would constitute a heat adaptation and protein-stabilization mechanism of the thermophilic fungus *Chaetomium thermophilum*.

Lastly, also other structural biology methods could be employed to solve TRMT2A structures if crystallography remains unsuccessful. Recent advancements in cryo-EM, allowed for the structure determination of an 82 kDa sized protein with conventional cryo-EM equipment (Herzik et al., 2019). Thus, the approximately 90 kDa complex of TRMT2A-tRNA might also be accessible for cryo-EM studies in the future.

4.1.3 The AlphaFold homology model of hTRMT2A

Routinely, domain borders are predicted with homology models generated by algorithms such as SWISS-MODEL and Phyre2. This algorithms are based on sequence and structural homology to previously solved structures. In 2020, a significantly improved artificial intelligence-based protein structure prediction software was released called AlphaFold. It outperformed all previous algorithms in terms of prediction accuracy of folded protein domains (Jumper et al., 2021). Hence, based on the new AlphaFold homology model of hTRMT2A (ID: Q8IZ69), the chosen hTRMT2A domain borders were re-evaluated (**Figure 32B**).

The AlphaFold model correlates well in central and catalytic domain predictions with previous models. Therefore, no major re-adjustments of domain borders are proposed. However, a slightly shortened C-terminus from N593 to E590 and a shorter central domain (aa 237-390 instead of aa 237-414) might be worth considering. Noteworthy, AlphaFold was able to predict the RBD fold, which other algorithms like Phyre2 failed to predict.

Conserved structural elements of m^5U methyltransferases have been discussed in paragraph **1.2.1.** The AlphaFold homology model of hTRMT2A recapitulates all these typical elements: RBD, central domain and catalytic domain containing a Rossmann fold with conserved motifs I, II, IV, VI and VII, catalytic cysteine C538 and proton abstracting base E581 (**Figure 32A**). Additionally, the long, selectivity-mediating loop of *S. pneumoniae* RlmCD (Jiang et al., 2017) is also present in the hTRMT2A homology model (**Figure 32B**, red arrow).

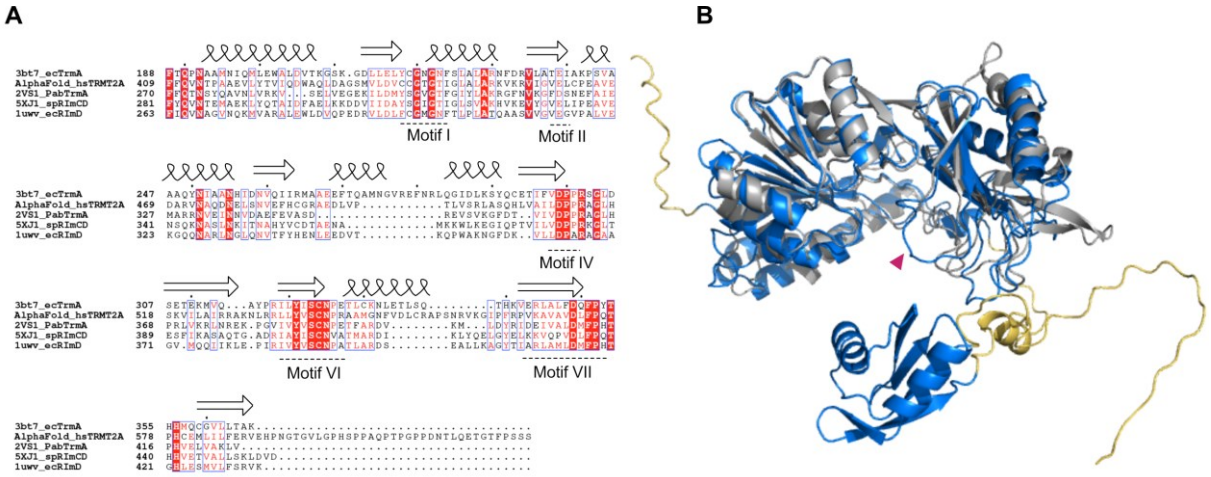

Figure 32 – AlphFold generated homology model of hTRMT2A.
A Sequence alignment of hTRMT2A and other m^5U methyltransferases confirms presence of Rossmann fold and conserved motifs. **B** AlphaFold model (blue) overlayed with the model generated using the the Phyre2 algorithm shows lack of the RBD prediction in the Phyre model. Yellow colored parts of AlphaFold model have a low prediction score of < 70 pLDDT and include N- and C-terminus of the RBD, as well as the C-terminus of the FL protein. The arrow indicates a AlphaFold newly predicted long loop. possibly mediating selectivity. AlphaFold-ID: Q8IZ69. Figures was generated with PyMol.

4.2 Hybrid model of hTRMT2A and tRNA gives insights into RNA recognition

The technology of crosslinking followed by mass spectrometry in combination with the RNP^{xl} analysis pipeline was developed in the laboratory of Prof. Dr. Henning Urlaub (MPI Biochemistry, Göttingen). It is a powerful approach to identify RNA-protein binding sites to single amino acid resolution and is comparable to recently developed RNA-protein binding experiments like PAR-CLIP (Kramer et al., 2014) on an individual RNP scale. Moreover, the approach is not biased to known RNA-binding domains in comparison to computational predictions. Results from these experiments shown in **Figure 25** are the up to date most detailed description of the tRNA-hTRMT2A interface including non-conventional RNA-binding residues such as H83 in the RBD loop.

4.2.1 Crosslinking and mass spectrometry reveals the hTRMT2A-tRNA^{Gln} binding interface to single amino acid resolution

Based on my approach to find unique RNA-peptide crosslinks outlined in paragraph **3.3.5**, interaction events between C270 and U19/U20, as well as C463 and U54/U55 of the tRNA are proposed and visualized in **Figure 26A**. The information I derived from undigested RNA dinucleotides (UU) allowed for identification of unique crosslinks. A similar approach was followed up in a previous study and thus constitutes a valid procedure to gain more information from crosslinking data (Luo et al., 2008; Kramer et al., 2014).

Previously, the crosslinking and massspectrometry technique predominantly identified crosslinked amino acids in RBDs such as RRM motifs and KH domains. However, crosslinked amino acids were also reported to occur within the Rossmann fold (Kramer et al., 2014), which is in line with our data. Specifically, crosslinked amino acids C486 and C538 in our data are part of hTRMT2A's Rossmann motif (**Figure 25**).

Interestingly, in the past a proteome-wide approach for the identification of mRNA-binding proteins based on a different mass spectrometry pipeline has been undertaken (Castello et al., 2016). Amongst those hits was also hTRMT2A, which interacted with mRNA by using part of its Rossmann fold. The same part of the Rossmann fold is also found to crosslink to RNA in our data. The agreement is remarkable because Castello et al., 2016 studied mRNA binding, not tRNA interactions. Thus, hTRMT2A might also bind mRNA using a similar binding interface as for tRNA.

Certain limitations must be kept in mind when discussing the results from these experiments. For two reasons crosslinking followed by mass spectrometry is restricted in respect to the exact identification of the interacting amino acid. Firstly, each crosslinking method has a bias for specific residues such as cysteine or histidine. Usage of two crosslinking methods – UV and NM mediated crosslinking – partially resolved this problem

for our experiments. Secondly, for the *in vitro* reconstituted complex, crosslinked residues can also be identified for potential transient intermediates with different binding modes and not only for the final complex. Indeed, samples from the *in vitro* reconstituted complex resulted in more crosslinked residues than samples from the purified complex (**Supplemental Table 4**). This might also explain less consistently crosslinked residues (in less than 3 of 4 datasets) far away from expected RNA binding interface for example C191, C224/225, K559 or C551.

4.2.2 The hybrid model

Despite a missing experimental structure, a hybrid model for the hTRMT2A-tRNA complex was proposed based on the AlphaFold homology model, the T-loop RNA placement in the *E. coli* TrmA structure (Alian et al., 2008) and experimental tRNA-hTRMT2A crosslinking data outlined in paragraph **3.3.4**. Previously, also for other protein-RNA complexes, including *E. coli* TrmA T-Loop complex (PDB: 3BT7), binding models had been generated where the RNA placement was suggested based on crosslinking data (Keffer-Wilkes et al., 2020; Blersch et al., 2021). Nevertheless, it must be kept in mind that our hybrid model is based on a homology model and not an experimental X-ray structure. That being said, **Figure 26** visualizes placement of a complete tRNA in respect to hTRMT2A, which agrees well with various crosslinked amino acids. Firstly, the model gives insights into possible T-/D-Loop intercalating residues that are important for the catalytic mechanism and discussed in paragraph **4.2.3**. Moreover, superpositioning of the TrmA-tRNA complex structure allowed me to place the tRNA very well in respect to the catalytic center of hTRMT2A. However, this approach also caused many clashes between RBD and the tRNA anticodon stem. A manual readjustment of the RBD allowed for another possible RBD placement right of the anticodon stem proximal to the D-Loop as shown in **Figure 26B**. The linker between RBD and central domain allows for flexibility in readjusting the RBD location. In both models highly validated crosslinked amino acids of the RBD are in proximity to the RNA, although RBD placement 2 agrees better with consistently crosslinked amino acids H83 and C111. Future experiments, such as NMR measurements with tRNA and domain-selective, isotope-labelled hTRMT2A RBD in a hTRMT2A FL context as described earlier (Aizu et al., 2020), might be required to shed light on binding and dynamics of the RBD in respect to the tRNA.

The superposition approach used to create the hTRMT2A-tRNA hybrid model (**Figure 26**) does not allow for direct inclusion of constraints from crosslinking data. Thus, the docking algorithm Haddock was employed to include constraints U19-C270 and U54-C538 (Yan et al., 2017). Unfortunately, docking resulted in suboptimal predictions, where the tRNA T-Loop was not inserted into the catalytic center. For this lack of conclusive results, the outcome of the Haddock docking was not shown in this thesis. Generally, docking might perform better

with an experimental X-ray structure or additional computational modelling like molecular dynamic simulations.

4.2.3 hTRMT2A is potentially a tRNA chaperone

In previous work, *E. coli* TrmA residues F106 and H125 were predicted to interrupt tertiary interactions of D-Loop and T-Loop making U54 accessible for methylation. Mutation of these residues decreased tRNA binding affinity fifty times and tRNA methylation up to 23-fold. Moreover, in a bacterial fitness assay *E. coli* TrmA H125E and F106E mutants were overgrown by *E. coli* WT cells after four days. Both results confirm these D-/T-Loop interrupting TrmA residues to be important for tRNA binding (Keffer-Wilkes et al., 2020). According to the structural alignment of *E. coli* TrmA and the hybrid model, F106 and H125 would correspond to K114 and H333. These are bulky positively charged amino acid that would be perfectly placed to intercalate between D- and T-Loop and interrupt tertiary interactions. However, in my experiments none of these residues was crosslinked to tRNA. Instead P334 adjacent to H333 was crosslinked to RNA in two datasets. Moreover, another consistently crosslinked amino acid, C270, was inserted between D- and T-Loop in the hybrid model (**Figure 26A**). Recent evidence proposed that *E. coli* tRNA modification enzymes that must interrupt tertiary interactions between D- and T-Loop to reach their target nucleotide (m^5U54, ψ55, m^1A58), also execute a secondary tRNA chaperone function. This mechanism forces misfolded tRNA to fold into their functionally important L-shaped conformer (Hoang and Ferré-D'Amaré, 2001; Keffer-Wilkes et al., 2016; Wolin, 2016). For human tRNA modification enzymes no such chaperone function has been reported yet but based on the hTRMT2A hybrid model and crosslinking data could indeed exist for hTRMT2A. A straightforward experiment would be a tRNA aminoacylation assay in presence of catalytically inactive hTRMT2A. A proxy for proper tRNA folding is efficient aminoacylation. In case presence of catalytically inactive hTRMT2A would facilitate efficient aminoacylation, hence tRNA folding, the hTRMT2A tRNA chaperoning function independent of the m^5U catalysis function would be confirmed (Keffer-Wilkes et al., 2020).

4.3 hTRMT2A is potentially a multi-substrate RNA methyltransferase

Previously, it has been shown by transcriptome-wide iCLIP experiments that hTRMT2A binds to the sequence motif G-U-U-C-G/A-A in human cells (Carter et al., 2019), which suggests a clear sequence preference of hTRMT2A *in vivo*. Interestingly, these data contained also hits that lacked the consensus motif. Although most RNA targets were tRNA (87 %), also other coding and non-coding RNA such as mRNA and rRNA were bound (**Figure 33A**)**.** In the same study, no further dissection of structural requirements, orthogonal assays or mutational studies of the sequence motif were performed. Thus, we chose positive hits from these experiments to complement available data with our orthogonal *in vitro* binding assays described in paragraph **3.3.1** and summarized in **Figure 33B**.

4.3.1 hTRMT2A FL binds preferentially tRNA

My main finding was high hTRMT2A binding affinities for tRNA. In contrast, hTRMT2A binding to the T-Loop was much weaker, showing a large proportion of unbound RNA and an RNA smear in EMSAs (**Figure 22C**). Both indicate a less strong and specific interaction. Although it has been previously shown that only the T-Loop is a sufficient substrate for *E. coli* TrmA, additional structural elements might be required to form a stable high-affinity hTRMT2A complex (Gu and Santi, 1991).

The bacterial tmRNA, basically resembling a tRNA without D-Loop, was reported to be bound by *E. coli* TrmA (Ranaei-Siadat et al., 2013). In binding assays tmRNA interacted only weakly with hTRMT2A. Either the bacterial target is not recognized by hTRMT2A, or the D-Loop is required for high affinity binding (**Figure 22B**).

The mRNA target from the iCLIP study, KCND2, was bound in my experiments with very low affinity (**Figure 22D**). Potential reasons include inaccurate *in vitro* RNA folding, missing co-factors for recognition, but also the inherently higher error rates that high-throughput experiments are burdened with. Of note, only a degenerate hTRMT2A binding motif is present in KCND2, where the downstream nucleotides of the target uridine are computationally predicted to be paired instead of located to the loop region as shown in **Supplemental Figure 6B**. Sequence-wise a C-U-U-C-U-G instead of G-U-U-C-G/A-A is found around the iCLIP crosslink. Further experiments are required to find out whether KCND2 binding is indeed a physiological event. Interestingly, an unrelated control mRNA, the E3 localization element of the *S. cerevisiae ASH1* mRNA, was bound similarly well as the target tRNA (**Figure 22D**). After closer inspection of the stem loop containing *ASH1* E3 RNA, a partial hTRMT2A binding motif was identified in the *ASH1* E3 loop (U-U-U-C-A-A), wherefore both sequence and structure would make *ASH1* E3 mRNA an hTRMT2A target (**Supplemental Figure 6C**). In conclusion, the *in vitro* results indicate that the complete tRNA structure or certain stem-loop structures are the preferred target for hTRMT2A binding.

A

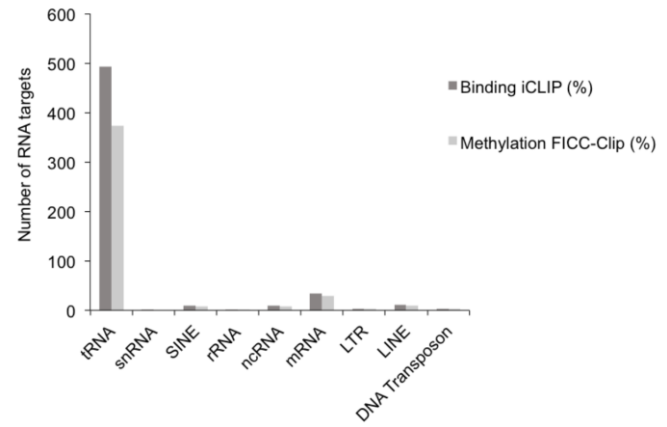

B

***In vitro* hTRMT2A targets (thesis)**

RNA	Binding [nM]	Methylation K_m [µM]
$tRNA^{Gln}$	60	1.52
$tRNA^{Phe}$	60	0.72
$tRNA^{Asn}$	60	n.d.
$tRNA^{Ala}$	60	-
$tRNA^{Gln\ U54G}$	60	n.d
$tRNA^{Gln}$ T-loop	110	-
$tRNA^{Lys}$ T-loop	165	-
tmRNA	555	-
KCND2	555	n.d
ASH1 E3	110	0.78

Figure 33 – hTRMT2A RNA targets.
A Number of different hTRMT2A bound and methylated RNA targets in HEK and HAPI cells as retrieved from FICC-CLIP and iCLIP data (Carter et al., 2019). The majority of hTRMT2A targets are tRNA, followed by mRNA. Binding correlates well with methylation of these targets. **B** Summary of my results from *in vitro* binding and methylation assays with hTRMT2A and different RNA. Binding data are from EMSA experiments and shown in **Figure 22**. Methylation data are from MTase Glo™ experiments and shown in **Figure 23.**

4.3.2 U54 in tRNA is the major parameter for methylation by hTRMT2A FL

Moreover, Carter et al., 2019 differentiated between hTRMT2A-mediated binding and methylation of RNA using two high-throughput methods. It was apparent that most but not all bound RNA substrates were also methylated. For *in vitro* methylation experiments in this thesis, the MTAse Glo™ assay was used. Observations from the assay agree well with the notion that tRNA binding correlates well with tRNA methylation (**Figure 33B**). However, tRNA binding does not necessarily mediate methylation as shown for $tRNA^{Gln\ U54G}$ and $tRNA^{Ala}$, the two tRNA that lacked U54 (**Figure 23A**). In line with the here proposed identification as hTRMT2A binding target, the *ASH1* E3 element was similarly well methylated to tRNA, although it folds into a stem-loop structure only remotely resembling a tRNA fold. Possibly, the presence of a uridine in the loop region allowed for methylation. Hence, the major parameter for efficient tRNA methylation seems to be the presence of U54 in tRNA or more general the presence of uridine in the loop region of a stem-loop. However, participation of other conserved hTRMT2A binding motif nucleotides in methylation has not been addressed here and still can play an important role (Gu et al., 1996). As mentioned previously, tRNA binding without tRNA methylation points to a different, m^5U catalysis-independent function of hTRMT2A like tRNA chaperoning.

4.3.3 Multisubstrate recognition by hTRMT2A

Data from hTRMT2A transcriptome mapping and my *in vitro* experiments (**Figure 22** and **Figure 23**) suggest that hTRMT2A predominantly targets tRNA, but can also bind and methylate non-tRNA substrates (Carter et al., 2019). The hybrid model of the hTRMT2A-

tRNA complex can explain hTMRT2A binding to other RNA such as rRNA and mRNA: large regions of the tRNA such as the anticodon or acceptor loop are not bound by hTRMT2A and deviations in these structural tRNA elements might be tolerated in terms of binding and methylation. With *ASH1* E3 mRNA it was proven that a stem-loop mRNA structure with certain length can be bound and methylated by hTRMT2A as well (**Figure 22** and **Figure 23**). Additionally, structural conservation of tRNA and rRNA methyltransferases such us *E. coli* TrmA and *S. pneumoniae* RlmCD conservation indicate an inherent multi-substrate specificity of these tRNA modification enzymes towards rRNA substrates. This is further underlined by dual specificity of the paralog hTRMT2B for tRNA and 23S mt-rRNA (Powell and Minczuk, 2020).

This multi-substrate specificity has been observed for other human tRNA modification enzymes as outlined in paragraph **1.1.2.3**. Moreover, it has been speculated that methyltransferases throughout evolution retained high promiscuity to other RNA substrates as "evolutionary playground" (Wiener and Schwartz, 2021) every now and then leading to actual new functionality. m^1A conversion of mitochondrial ND5 mRNA by the tRNA methyltransferase TRMT6/TRMT61, for example, is crucial for development (Safra et al., 2017b). Thus, non-tRNA hTRMT2A targets could have functional importance, although orthogonal studies are necessary to confirm this.

4.3.4 RNA binding ability of hTRMT2A FL is robust towards mutations

Methylation experiments with mutated hTRMT2A confirm the important role of C538 and E581 in tRNA methylation but were not sufficient to abolish catalytic activity (**Figure 27C**). In case of the CNM mutant (C538A), the catalytic constant K_m was only decreased, but enzymatic activity was still observed. In line with RNA trapping by the CBM mutant (E581A), earlier saturation of the enzymatic reaction was apparent. In addition, the CNM and CBM hTRMT2A only exhibited slightly reduced RNA binding (**Figure 27A/B**). These observations were unexpected, as the same mutants of *E. coli* TrmA showed completely abolished enzymatic activity and highly reduced RNA binding (Urbonavičius et al., 2007; Keffer-Wilkes et al., 2020).

Leftover catalytic activity of the CNM C538A mutant can be explained by an environment in the catalytic center that is sufficient to render target uridine reactive enough for methylation by SAM. Possibly, mutation to A538 was not enough to abolish the activity of the main catalytic residue. A similar observation was previously made for a RNA pseudouridine synthase, which retained catalytic activity upon mutation of catalytic cysteine to alanine (Zhao and Horne, 1997). For determination of the exact catalytic mechanism, an X-ray structure of hTRMT2A-RNA complex would be insightful.

To generate a mutant that possesses abolished or decreased RNA binding and catalytic activity, eight residues were rationally selected for mutation. These mutations destroyed for example further contacts with target U54 and the predicted SAM binding pocket. The resulting hTRMT2A IR mutant formed a less stable complex and revealed abolished enzymatic activity (**Figure 27**).

4.3.5 Oligomerization status of hTRMT2A FL

Previously, RNA modification enzymes have been shown to act on their RNA targets as standalone enzymes or enzymatic complexes. Regarding the enzymatic complexes, the enzyme can interact as homodimer, heterodimer or even with several other cofactors. Representative is the heterodimer of TRMT6/TRMT61A, which installs m^1A on RNA, whereas its homolog TRMT61B installs m^1A as homodimer (Chujo and Suzuki, 2012). The modular design of RNA modification enzymes was suggested to contribute to RNA selectivity as reviewed in paragraph **1.1.1**.

In my BioID an Co-IP data no obvious protein binding partner of hTRMT2A FL to build a heterdimeric complex was identified. Moreover, hTRMT2A FL can methylate its RNA targets without additional protein binding partners as shown in **Figure 23**. Therefore, the questions remains whether hTRMT2A FL acts as homodimer on its RNA targets. Results from RALS experiments displayed in **Figure 11**, suggest hTRMT2A FL to be monomeric in solution. Finally, the AlphaFold hTRMT2A FL homology model predicts a catalytic center with all necessary residues for catalytic activity present in one molecule (**Figure 32B**). Conclusively, I suggest hTRMT2A FL to act as monomer on its RNA targets. This remains to be proven for example with a X-ray structure and in cells with FRET analysis as done previously (Gautier et al., 2001).

4.4 The hTRMT2A interactome suggests different functions

4.4.1 Strengths and limitations of BioID and Co-IP

By using BioID and Co-IP, we combined the strengths of both methods to analyse the human TRMT2A interactome. BioID is superior in recapitulating transient and weak interactions because cell lysis or washing steps occur after in-cell biotinylation. However, BioID picks not only up on direct interacting but also proximal proteins in a 10 nm-radius, which makes proper controls essential. As biotinylation of proteins occurs within intact cells, the endogenous protein localization can be captured (Roux et al., 2013). Co-IP confidently identifies direct interactions and RNA/protein mediated interactions but bears the risk to also detect unphysiological interactions that occur after cell lysis and to lose transient interaction partners. For unspecific RNA binding proteins in particular the risk of false-positive results is high when using Co-IP. As consequence of these different technical limitations, Co-IP and BioID are expected to show differences in the identified interactomes. Indeed, although hTRMT2A lacks a mitochondrial localization sequence (Powell and Minczuk, 2020), mitochondrial rRNA binding proteins are amongst the hTRMT2A Co-IP hits (MRSP2, MRSP25, MRPS7, MRPS27), but not amongst BioID hits. Such interactions could have occurred physiologically after breakdown of cellular compartments during cell lysis.

We used hTRMT2A IR, which is the reduced RNA binding mutant (**Figure 27**), as additional control to distinguish between RNA-dependent and independent interacting partners. Depletion of RNA-related processes in experiments with the hTRMT2A IR mutant implies that its reduced RNA binding is sufficient to distinguish between RNA-dependent and independent interactions (**Figure 28E**). From a statistical point of view, BioID hits were compared with a list of frequent false positive hits from previous BioID experiments (Go et al., 2021). 4.3 % of the hTRMT2A BioID hits (10/232) were classified as frequent false positive hits and excluded from further analysis. Moreover, the strictest significance threshold was selected for hit identification ($p < 0.005$) to further decrease selection of false positive hits. An often-reported limitation of BioID experiments is cellular mislocalization of BirA*-tagged protein of interest (Sears et al., 2019). Staining against the FLAG epitope fused to hTRMT2A indicated a predominant localization to the nucleus, but also faint staining in the cytosol. Together with GO-term analysis for cellular compartments in **Figure 28C-E,** which imply localization to nucleus and cytosol, this suggests that the possibility of mislocalization is rather unlikely. Lastly, it must be kept in mind that data were obtained from HEK cells, an immortalized cell line, using an overexpression system. HEK cells were preferred for BioID experiments, due to their easy maintenance and high transfection efficacy, which contributes to high data reproducibility. However, this model system requires caution in interpreting the physiological relevance of interaction partners. To improve BioID results, a second cell line such as HAP1 cells and endogenous levels of hTRMT2A might be employed in the future.

4.4.2 High confidence protein interaction partners of hTRMT2A

With these limitations in mind and controls in place it was anticipated that most confident candidates for protein interactions can be identified by overlapping Co-IP and BioID data. A total of thirteen proteins were found both in BioID and Co-IP datasets from hTRMT2A WT conditions, thus constituting the most confident RNA-dependent interaction partners: NCL, TRIM26, hTRMT2A, SSB, TARBP2, LARP7, PPM1G, UPF1, IGF2BP1, NPM1, SET, SPINDOC and RPL4. Proteins found in BioID and Co-IP from both hTRMT2A WT and IR cell lines constitute the most confident RNA-independent protein interaction partners: SSB, TARBP2 and SPINDOC. Candidates from BioID and Co-IP data superposition, as well as certain top candidates were selected for following discussion. Associated biological pathways are suggested thereafter and summarized in **Table 18** and **Figure 34.**

Table 18 – RNA-dependent and -independent BioID and Co-IP hits with high significance
Blue indicates association of respective protein from BioID/Co-IP experiments in designated biological process. *Previously reported hTRMT2A interaction partners are indicated with a green checkmark.

Protein	rRNA and Ribosome	tRNA maturation	miRNA processing	Chromatin-context	snoRNA processing	Previously reported *
Highly confident RNA-independent interaction partners (BioID, Co-IP, WT, IR)						
SSB						✓
TARBP2						✓
SPINDOC						×
Highly confident RNA-dependent interaction partners (BioID, Co-IP, WT)						
NCL						×
NPM1						×
TRIM26						×
LARP7						×
UPF1						×
IGF2BP1						×
SET						×
PPM1G						×
RPL4						×
Significant RNA-independent interactions partners from BioID experiments (WT, IR)						
NOP56						×
RPL8/12/15						×
PDCD11						×
Significant RNA-dependent interaction partners from BioID experiments (WT)						
NSUN2						×
WDR43						×
NOP2						×
NOL11						×
ACTR5						×
Significant RNA-independent interactions partners from Co-IP experiments (WT, IR)						
RPL10A/P0						×
PPP2AR1/2A						×
PPP6C						✓
NAP1L						×
Significant RNA-dependent interactions partners from Co-IP experiments (WT)						
MOV10						×

Several BioID hits corresponded to previously reported hTRMT2A interactors, namely the SSB and the RISC-loading complex subunit TARBP2 (Huttlin et al., 2017). Also, several Co-IP hits corresponded to previously described hTRMT2A interactors namely the protein phosphatase 6 subunit C PPP6C (Huttlin et al., 2021), SSB and TARBP2. These overlaps with independent studies may serve as positive controls and indicate that our combinatory interactome study is robust and reliable enough to identify previously published interactors.

4.4.2.1 hTRMT2A participates in tRNA maturation

Several confident hTRMT2A interactors showed up both in BioID and Co-IP data. One of them was the human La protein, SSB. SSB acts as 3' poly(U) terminus dependent transcription factor of RNA polymerase III-dependent transcripts by facilitating proper folding and maturation of target RNA. Binding of SSB to precursor RNA protects RNA from exonucleolytic cleavage. Amongst the RNA targets that are stabilized and protected by SSB are pre-tRNA, 5S pre-rRNA, pre-miRNA, snRNA and certain species of mRNA (Wolin and Cedervall, 2002; Liang et al., 2013). The best-studied function of SSB is its association with the pre-tRNA 3' trailer, which supports proper endonucleolytic cleavage. In yeast, early tRNA modifications like m^1A58 or m^5U54 occurred while the pre-tRNA was still associated with the *S. cerevisiae* homolog of SSB, Lhp1 (Etcheverry et al., 1979; Maraia and Intine, 2002), hence suggesting a functional link.

Along this line, not much is known about hTRMT2A and SSB in human cells. Our BioID and Co-IP hTRMT2A data show SBB as one of the RNA-independent interaction partners suggesting a close interplay between both proteins (**Figure 28** and **Figure 29**). Moreover, SSB and hTRMT2A both localize to the nucleolus, and thus are enabled to physically interact and/or act on the same RNA targets (Human Protein Atlas, **Figure 30**). Moreover, another early tRNA maturation enzyme, NSUN2, was found in my BioID data from the hTRMT2A WT condition, thus I suggest that it is possibly acting on the same tRNA as hTRMT2A. Of note, NSUN2 was also reported to be associated with the SSB-tRNA complex (Maraia and Intine, 2002; Van Haute et al., 2019).

As hTRMT2A interacts with early tRNA maturation-associated proteins like SSB and NSUN2, I propose hTRMT2A to be an early tRNA maturation enzyme. Moreover, based on my Co-IP and BioID data, SSB is suggested as direct protein interaction partner.

4.4.2.2 hTRMT2A associates with miRNA processing

MicroRNA (miRNA) is a class of regulatory, non-coding RNA that induce for instance mRNA degradation or translational repression. Pre-miRNA matures in several steps into miRNA. The last biogenesis step requires the RISC loading complex (RCL), which consists of the RNase Dicer and the RNA binding protein TARBP2. RCL mediates the last pre-miRNA

processing step and then loads the mature miRNA together with the RNase Argonaute 2 (AGO2) into the RNA-induced silencing complex (RISC) for miRNA mediated gene silencing (Chendrimada et al., 2005).

The RCL constituent TARBP2 itself was identified as an RNA-independent hTRMT2A interaction partner in both my BioID and Co-IP data (**Figure 29H**). This suggests a role of hTRMT2A in the miRNA biogenesis pathway. Next to the fact the TARBP2 is enriched in both WT and the RNA binding mutant data, two additional studies indicate that hTRMT2A-TARBP2 is a miRNA-independent interaction. Firstly, hTRMT2A iCLIP data does not contain miRNA (Carter 2019). Secondly, hTRMT2A was not reported as pre-miRNA binding partner before (Treiber 2017). Interestingly, the earlier discussed SSB has two functions in miRNA processing: It protects pre-miRNA and prevents mischanneling of tRNA fragments into the miRNA pathway, which might establish a link between hTRMT2A, SSB and TARBP2 (Liang et al., 2013; Hasler et al., 2016).

During miRNA mediated gene silencing, FMR1 and the RNA helicase MOV10 together regulate translational repression by AGO2 (Kenny et al., 2014). MOV10 is significantly enriched in Co-IP data in an RNA-dependent fashion (only found in hTRMT2A WT datasets, **Figure 29C/E**), thus indicating MOV10 and hTRMT2A to bind the same RNA targets. MOV10 might not be enriched in BioID data because the commonly bound RNA transcript length is above the BirA* labelling radius of 10 nm. Therefore, these joint MOV10/hTRMT2A targets might not be the short miRNA, but longer MOV-10 bound RNA targets, such as 3' UTR of mRNA or long interspersed elements (LINE) (Gregersen et al., 2014; Warkocki et al., 2018). Of note, the highly confident RNA-dependent hTRMT2A interaction partner UPF1 (**Figure 29H**) interacts as well with MOV10 to contribute to mRNA degradation (Gregersen et al., 2014), which establishes a possible link between UPF1, MOV10 and hTRMT2A.

4.4.2.3 hTRMT2A associates with rRNA processing

The ribosome is the cellular protein synthesis machinery. It consists of a small (40S) and large (60S) subunit. The 40S subunit contains 18S rRNA and the 60S subunit 5.8S, 28S and 5S rRNA. Ribosome biogenesis encompasses different maturation steps, starting with processing and modification of pre-rRNA. Assembly of pre-40S and pre-60S subunits in the nucleolus with a variety of ribosomal proteins is followed by export of both subunits and assembly into the mature ribosome in the cytoplasm (Lafontaine, 2015).

Both "rRNA processing" and "ribosome biogenesis" were revealed as most significantly enriched GO-terms in BioID data by GO-term analysis (**Figure 28C/D**). Therefore, significantly enriched interaction partners in association with this GO-terms were inspected more closely. The already discussed hTRMT2A interaction partner SSB not only chaperones pre-tRNA, but also 5S pre-rRNA. Additionally, other RNA-dependent interaction partners

enriched in both BioID and Co-IP data are involved in these processes (**Figure 29H**): firstly, the nucleolar protein nucleolin (NCL) plays a role in pre-rRNA transcription and processing (Cong et al., 2012; Turi et al., 2019). Secondly, the nucleolar protein nucleophosmin (NPM2) is involved in ribosome biogenesis, specifically in ribosome export to the cytosol (Maggi et al., 2008). Thirdly, the 60S ribosomal protein L4 (RPL4) is associated with rRNA processing (Pöll et al., 2009). More RNA-independent and -dependent interaction partners involved in rRNA processing are only found in the BioID data, thus being possibly transient interaction partners in the < 10 nm vicinity of hTRMT2A (**Figure 28C-E**). Examples are the nucleolar protein 56 (NOP56), which participates in the early 60S ribosomal subunit and snoRNA biogenesis (Hayano et al., 2003; Watkins et al., 2004), the ribosomal RNA processing proteins 15, 12 and 8 (RRP12, RRP8, RRP15), the 18S pre-rRNA processing factors PDCD11, WDR43 and NOL11, as well as the 28S rRNA m^5C methyltransferase NOP2 to name a few (Prieto and McStay, 2007; Freed et al., 2012; Sloan et al., 2013). Upon closer inspection of Co-IP data, it became apparent that other ribosome biogenesis factors were enriched, namely those that are localized to cytoplasm instead of nucleoplasm (**Figure 29C-E**). Examples for such cytoplasmic ribosome associated proteins are the 60S ribosomal proteins L10A, L15 and P0 (RPL10, 15 and P0). Differences in the ribosome associated interactome might derive from experimental differences initially mentioned in this chapter. Of note, hTRMT2A did not associate with polysomes or mature 60S and 40S subunit, as shown in a previous polysome profiling study (Imami et al., 2018). Thus, hTRMT2A most likely does not associate with mature ribosomes or polysomes, but rather participates in ribosome biogenesis steps.

4.4.2.4 hTRMT2A might methylate rRNA

As discussed, a large amount of RNA-dependent or -independent interaction partners of hTRMT2A participate in rRNA processing and ribosome biogenesis pathways. Functionally, hTRMT2A is either a binding partner of ribosomal factors or directly methylates rRNA. Several indications from literature support the latter theory. Firstly, two methylated uridines are found in rRNA: specifically, on position U814 of the 18S rRNA and position U4083 of the 28S rRNA. Until to date, no dedicated methyltransferases for this m^5U conversions have been identified (Natchiar et al., 2017). Secondly, the homolog of hTRMT2A, TRMT2B methylates both 12S-rRNA and tRNA in mitochondria by recognizing an A-U-U-A-G-A motif (Powell and Minczuk, 2020). The same motif is also found around position U814 of cytosolic rRNA. Lastly, the small subunit rRNA is amongst the hTRMT2A RNA targets from the iCLIP study (Carter et al., 2019). All together, these indications are convincing enough that currently experiments are planned to assess the m^5U status of cytosolic rRNA isolated from

hTRMT2A WT and KD HEK cells. If true, this would confirm cytosolic rRNA as hTRMT2A target, with potential biological implications in ribosomes-related processes.

4.4.2.5 hTRMT2A associates with chromatin related transcriptional processes

Chromatin regulation plays a well-known role in gene expression. Amongst chromatin regulators are a variety of DNA modification enzymes such as histone methyltransferases. During the last years, several studies highlighted an additional connection between RNA modification enzymes and chromatin-associated regulators. An example is the m^6A methyltransferase METTL3, which co-localizes with other modifiers to UV-induced DNA-damage sites to facilitate DNA repair (Tzelepis et al., 2019).

These very recent observations agree well with findings from my interactome data, which indicate chromatin association of hTRMT2A binding partners. SPINDOC is one of the RNA-independent interactors found in both BioID and Co-IP data (**Figure 29H**). It regulates transcriptional activity via inhibition of histone binding proteins (Bae et al., 2017). In BioID and Co-IP data, also RNA-dependent binding partners were associated with chromatin function: next to its already discussed role in rRNA processing, NPM1 participates in centrosome duplication and histone assembly processes (Swaminathan et al., 2005; Wang et al., 2011). As discussed in **1.2.4.2**, hTRMT2A has been previously reported to be tightly cell cycle regulated with a peak during S-phase, when centrosome duplication occurs (Guarguaglini et al., 1997; Hicks et al., 2010). Next, NCL can induce chromatin decondensation by binding to histone 1. More chromatin-associated factors were identified in only BioID data (**Figure 28C-E**), such as the RNA-independent, highly enriched actin related protein 5 (ACTR5), which is part of the chromatin remodelling complex involved in DNA repair (Jiang et al., 2010). Other proteins involved in chromatin-related processes like DNA repair or mitosis were only enriched in Co-IP data, wherefore they could be associated with the same complex as hTRMT2A, but likely in a distance of more than 10 nm (**Figure 29C-E**): amongst them are the nucleosome assembly factor NAP1L1, which aids several DNA repair mechanism and facilitates chromosome remodelling (Lee et al., 2017), and the serine/threonine protein phosphatase 2A that is required for chromosome segregation (Tang et al., 2006). It remains to be examined how hTRMT2A might be associated with chromatin in processes like DNA repair or mitosis or whether above-mentioned factors are interconnected. For a first insight whether hTRMT2A plays a role in DNA-repair or cell-cycle progression, I would suggest confocal microscopy experiments. Co-staining of hTRMT2A and histones with or without stress stimuli like UV-radiation will inform about hTRMT2A association with chromatin (Xiang et al., 2017). Follow-up experiments will then show the regulatory potential of hTRMT2A and m^5U on a chromatin level.

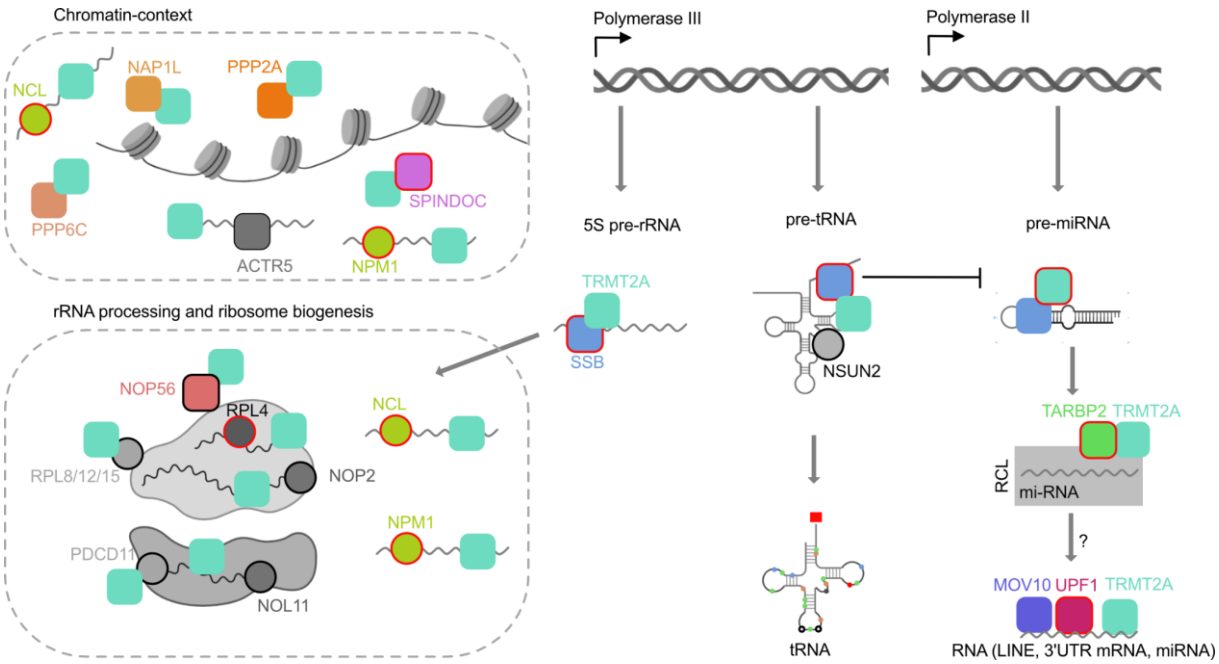

Figure 34 – hTRMT2A associated pathways in the nucleus.
Selected RNA dependent and independent interaction partners and their associated pathways are shown with a focus on rRNA processing, ribosome biogenesis, tRNA maturation, pre-miRNA processing and chromatin context. Interaction partners enriched in both BioID and Co-IP data are encircled in red. Interaction partners that are only enriched in BioID data are encircled in black. MOV10, NAP1L, PPP2A, PPP6C and NAP1L are only enriched in Co-IP data. RNA-independent protein interaction partners are shown to bind to each other. RNA-dependent interaction partners, binding to the same RNA transcript, are indicated as well and potential RNA transcript species are suggested for MOV10, UPF1 and NSUN2.

4.4.2.6 Nuclear import mechansims for hTRMT2A

Human TRMT2A is shuttled back into the nucleus, as indicated with hTRMT2A nuclear staining shown in this thesis (**Figure 30**), my GO-data analysis (**Figure 28**) and in the Human Protein Atlas. This raises the question which nuclear import mechanisms are engaged to transport hTRMT2A from cytosol to nucleus. Towards its N-terminus, hTRMT2A is predicted to possess a nuclear localization signal (NLS) (Nguyen Ba et al., 2009). Thus, it most likely shuttles to the nucleus via the transport protein family of importins. Importin α connects the NLS signal via an Importin ß family member to the nuclear pore to facilitate import (Kimura and Imamoto, 2014). Importin subunit α-2 (KPNA2) and importin subunit ß-1 (KPNB1) were enriched in my Co-IP data and importin-7 and importin-9 (IPO7/9), were enriched in the BioID data. Consequently, a heterodimer of KPNB1-KPNA2, KPNB1-IPO7, both reported previously (Percipalle et al., 1997; Jäkel et al., 1999), or a heterodimer of KPNB1-IPO9 or standalone importins are proposed as hTRMT2A importer complexes. However, biochemical assay such as pulldowns with recombinantly purified proteins will have to prove whether these proteins interact directly. Additional cellular experiments will be needed to identify which of the above-mentioned molecules transport hTRMT2A most efficiently into the nucleus.

4.4.3 hTRMT2A associates with several nuclear processes

To sum up, hTRMT2A interaction partners, RNA-dependent and independent, shed light on several associated processes such as tRNA maturation, rRNA processing and chromatin-related processes. The most prominent nuclear processes suggested by my interactome studies are visualized in **Figure 34**. These processes align well with the predominant hTRMT2A localization to the nucleus shown with BioID GO-terms in **Figure 28C-E**, staining in **Figure 30** and stainings from the Human Protein Atlas. However, hTRMT2A localizes to the cytosol too as indicated with the above-mentioned stainings and BioID GO-terms. In the cytosol hTRMT2A might be associated with different functions such as later cytosolic instalment of tRNA m^5U54 modification or later steps of miRNA processing. Other RNA modification enzymes like pseudouridine synthases change their subcellular localization upon environmental stimuli like heat stress (Schwartz et al., 2014). It would be interesting to find out whether a subcellular re-localization upon stress stimuli can be observed for hTRMT2A. In such a context, hTRMT2A might execute different functions in cytosol and nucleus. For clarification exact localization studies will be needed.

4.5 hTRMT2A associates with polyQ disease pathology

Human TRMT2A RNAi silencing reduced polyQ protein associated toxicity and aggregation without an negative impact on actual cell survival (Voßfeldt et al., 2012). This hTRMT2A phenotype is resembled in *S. cerevisiae* or *M. musculus*, where Trm2p/TRMT2A deletion has been shown to be non-lethal (Johansson and Byström, 2002). Hereafter, a hypothesis for the described phenotype with inclusion of the results presented in this thesis is introduced.

4.5.1 Hypothesis for hTRMT2A silencing phenotype in a polyQ disease model

Knockdown of human TRMT2A in HEK cells was shown by me to reduce methylation of RNA (**Figure 21**). Previous *in vitro* work indicated that tRNA without m^5U54 modification causes an increased rate of amino acid misincorporation from 3 in 10000 to 3 in 1000 (Kersten et al., 1981). Such a mistranslation mechanism in our polyQ disease model would facilitate the incorporation of other amino acids than glutamine into the polyQ tract. It has been shown that polyQ tract interruptions slow polyQ aggregation *in vitro* and correlate with later age of onset in SCA patients (Menon et al., 2013). Consequently, the mistranslation hypothesis would explain decreased polyQ aggregation in hTRMT2A-silenced cells (**Figure 9**). To underline this point, mammalian cells were shown to tolerate decreased translational fidelity under stress conditions (Wang and Pan, 2016; Mohler and Ibba, 2017). This feature could explain why the hTRMT2A KD, exhibiting possibly reduced translational fidelity, was not disadvantageous for the HEK cells. Currently, a mistranslation assay is established in our laboratory to study translational fidelity in hTRMT2A WT and KD cells. On a molecular level, several mechanisms could be the cause for mistranslation.

First, mistranslation might be caused by decreased affinity to the ribosome as proposed earlier (Kersten et al., 1981). The impaired three-dimensional structure of m^5U54 hypomodified tRNA could impair tRNA binding to the initiation factor or the ribosomal binding sites. Second, causative for mistranslation might be incorrect aminoacylation of tRNA upon m^5U54 hypmodification. Until now, cellular stress or anticodon hypomodification, but not T-loop hypomodification, were reported to associate with tRNA misacylation and resulting translational infidelity in a cellular model (Pan, 2013; Ou et al., 2019). Employing isoacceptor specific aminoacylation profiling (ISAP), a method that uses isolated tRNA species to identify the respective charged amino acids, would contribute to a better understanding of this mechanism and its importance in a hTRMT2A KD background (Mohler et al., 2017). Third, the suggested role of hTRMT2A in rRNA processing and ribosome biogenesis from my BioID data (**Figure 28**) could result in a ribosome machinery with intrinsically higher translational error rates via yet to determined processes. In this context, one m^5U modified rRNA stretch is an expansion segment that is responsible for strengthening the inter-subunit bridge

between large and small subunit, thus stabilizing the ribosome assembly (Ramesh and Woolford, 2016). Fourth, tRNA m^5U54 hypomodification has been shown to induce a stress response in cells and cause production of tRFs by tRNA cleavage (Pereira et al., 2021). This general stress response could increase the translational error rate via other mechanisms and co-factors as reviewed earlier (Pan, 2013). Analysis whether our hTRMT2A KD cells exhibit transcriptional rewiring towards stress response will be needed to confirm or exclude this mode of action.

4.5.2 hTRMT2A as potential drug

Due to reasons mentioned in paragraph **1.4**, hTRMT2A was considered as valid drug target for treatment of polyQ diseases. With my hTRMT2A interactome data in hand (**Figure 28** and **Figure 29**) the question can be addressed, whether hTRMT2A acts upstream of other polyQ disease modifiers or indeed is itself as polyQ-disease modifier. Comparison of the BioID and Co-IP hitlists with previously reported polyQ-disease modifiers from two *Drosophila* screens did not reveal any matches (Zhang et al., 2010; Voßfeldt et al., 2012). This allows me to conclude that no other polyQ-disease modifier regulated by hTRMT2A, is likely to mediate the observed hTRMT2A silencing phenotype. Moreover, hTRMT2A is not amongst the 350 interaction partners of wildtype and mutant Htt protein derived from two proteomics studies (Culver et al., 2012; Shirasaki et al., 2012). Hence, a direct effect of hTRMT2A on Htt can be largely excluded too.

4.5.3 hTRMT2A drug discovery campaign using *in silico* methods

To pharmacologically “silence” hTRMT2A with novel and specific compounds, a structure-based drug discovery campaign was started with the X-ray structure of the hTRMT2A RBD generated in our laboratory. Concretely, hTRMT2A RBD was analysed using molecular dynamics simulation, which resulted in the identification of a cryptic binding site. By definition, cryptic binding pockets are not visible in X-ray structures, but become available upon binding of a ligand. Thereafter, small molecules were designed that stabilize the cryptic pocket. In cell-culture experiments some of these small molecules decreased cell death and aggregation. Nonetheless, these small molecules did not directly bind to recombinantly purified RBD or inhibited methylation of tRNA by hTRMT2A FL as shown with SPR and enzymatic assays *in vitro*, respectively (**Figure 18** and **Figure 20**).

Several possibilities for this result must be mentioned. First, binding experiments were performed with the isolated recombinantly purified hTRMT2A RBD instead of the hTRMT2A FL protein and without the tRNA substrate, whose allosteric effects might be needed to allow for binding or methylation. Second, differences of *in vivo* and *in vitro* experiments might derive from off-target effects of small molecules on other cellular targets such as kinases

(identified with SwissTargetPrediction, Margreiter et al., 2021, bioRxiv). Third, small molecule design is based on an unvalidated *in silico* model. Experimental validation of the cryptic binding pocket could help to understand these results. Fourth, the RNA-binding mode of hTRMT2A RBD that is proposed by me in paragraph **4.1.1**, includes residues R137 and H83. Based on the *in silico* prediction R137 is, however, also part of the cryptic binding pocket. In case RNA is indeed bound to H83 and R137 it would sterically hinder the small molecule (compound 13, 15 and 17) to bind to the cryptic binding pocket and/or inhibit hTRMT2A FL. Of note, spermidine, which bound to hTRMT2A RBD, was not chosen due to its *in silico* binding profile to the cryptic pocket, but based on a pharamacophore approach against the catalytic domain (Mach et al., 1982).

As shown in **Figure 18** and **Figure 20**, the only compound that bound to the RBD and inhibited enzymatic activity of hTRMT2A FL was spermidine, which was previously reported as modulator of tRNA methyltransferases (Mach et al., 1982). This inhibitory effect could be indirect due to sequestering of negatively charged tRNA by positively charged spermidine as previously reported (Lightfoot and Hall, 2014). However, spermidine also binds to the hTRMT2A RBD without tRNA as shown in **Figure 18**. A co-crystal structure of spermidine and the hTRMT2A RBD would aid in understanding this interaction, its relevance for hTRMT2A inhibitor discovery, and might serve as new scaffold to design more potent inhibitors.

Based on rather discouraging results from *in silico* studies, alternative drug screening approaches for hTRMT2A inhibitors were considered. As the MTase Glo™ assay from Promega allowed me to detect hTRMT2A inhibition by spermidine and sinefungin (**Figure 19** and **Figure 20**), it is proposed as High throughput screening (HTS) method for hTRMT2A inhibitor screening. Indeed, several bacterial RNA-methyltransferase inhibitors were identified already with an MTAse Glo™-based screening approach (Coussens et al., 2018; Zhong et al., 2019). Before embarking on such a campaign it will be crucial to determine assay robustness via the Z'-factor, which was suggested as best statistical parameter to assess HTS results (Sui and Wu, 2007). Moreover, protein, tRNA and SAM concentrations require optimization for an optimal signal to background ratio before a large screening campaign can be commenced.

4.6 Conclusion

Although the predominant cellular role of hTRMT2A appears to be tRNA binding and methylation, not much is known about hTRMT2A functionality in health and disease. Here, for the first time hTRMT2A was comprehensively characterized biochemically, which confirmed RNA-target specificity for tRNA and more general stem-looped RNA. Moreover, the hTRMT2A protein interactome was mapped with two orthogonal techniques. Interactome results opened new avenues to understand the full biological function of hTRMT2A in human cells. Presented results will help to exploit hTRMT2A for biotechnological and therapeutical applications. In this context, structural information was gathered and an enzymatic assay for hTRMT2A inhibition was established. This aids the identification of novel drug candidates for polyQ diseases. Initial work in finding a specific hTRMT2A inhibitor gave insights into the catalytic mechanism of hTRMT2A and cellular effects upon hTRMT2A silencing. In the future, a specific hTRMT2A inhibitor that can exploit the potential of hTRMT2A as drug target, will potentially open a therapeutic window to treat polyQ disease patients preventively and thus reduce the burden of this group of devastating neurodegenerative diseases.

5. Supplementary Data

Supplementary Figures

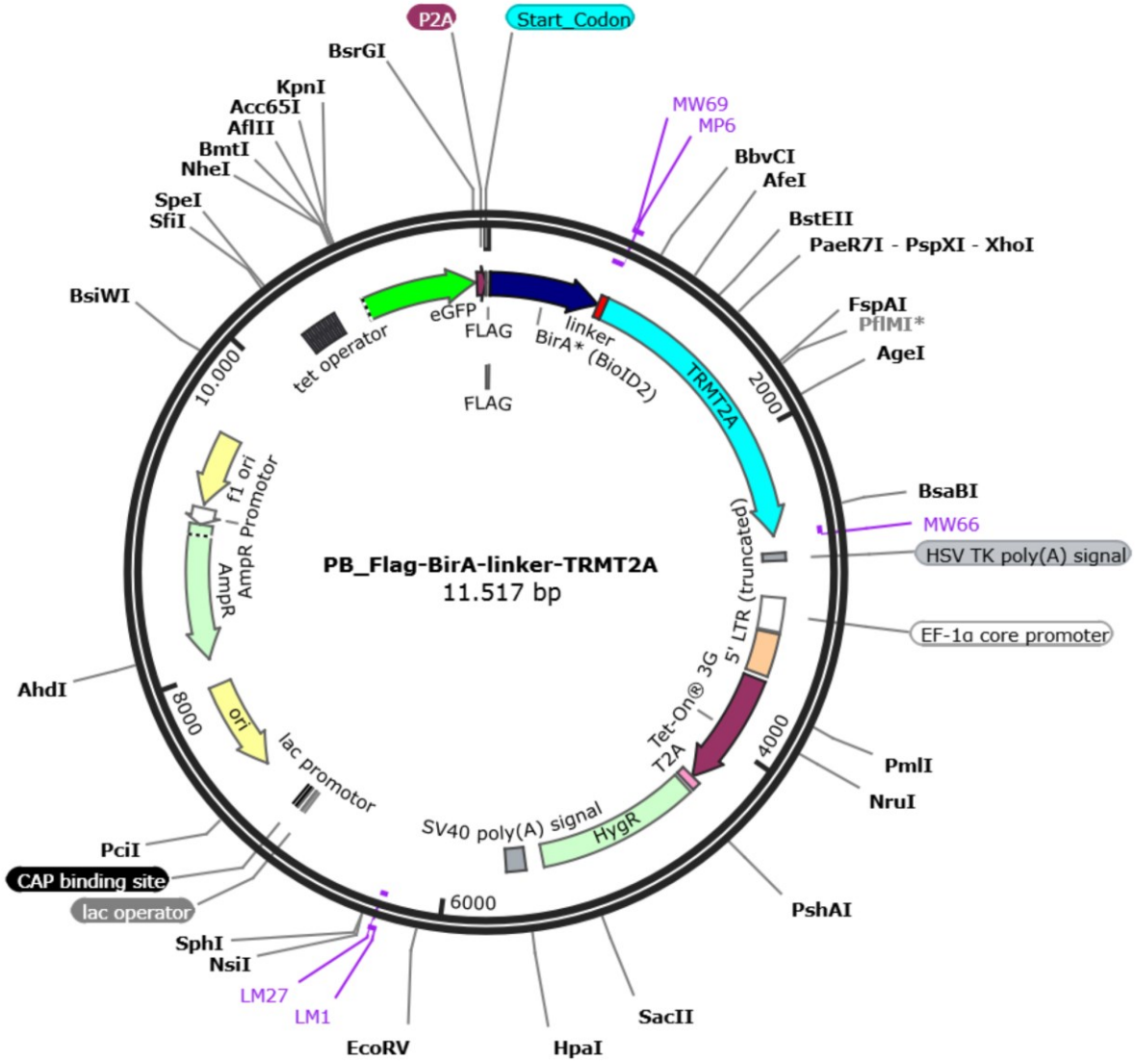

Supplemental Figure 1 – Map of plasmid used to generate PB-Flag-BirA*-TRMT2A WT (MW1) cell line.
This plasmid map is representative for all PB plamids used for BioID and Co-IP experiments. Plasmids for the Co-IP cell lines differed in BirA* and linker part. Plasmid map was generated with Snapgene.

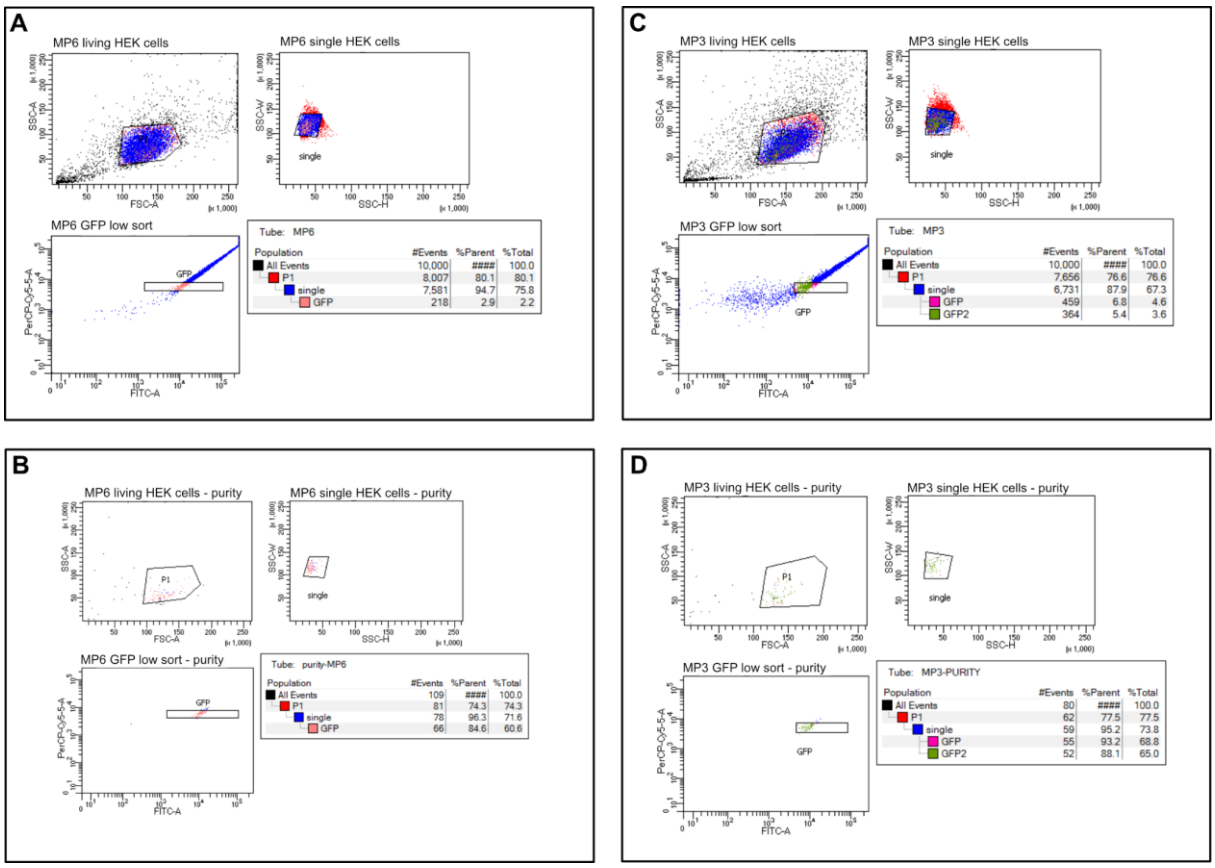

Supplemental Figure 2 – FACS sorting reports of control BioID and Co-IP cell lines.
A Representative sort for cell lines used in BioID experiment. Shown is the FACS-report of BirA* control HEK cell line (MP6) first gated for living cells (left), then for single cells (right) and finally for a cell population with low GFP signal (bottom). **B** Re-analysis of sorted cell with a small amount of cell-suspension showed high purity of MP6 sort. **C** Representative sort for cell lines used in Co-IP experiment. Shown is the FACS-report of FLAG control HEK cell line (MP3) with same gating profile than for BioID cell lines. **D** Re-analysis of sorted cell showed high purity of MP3 sort.

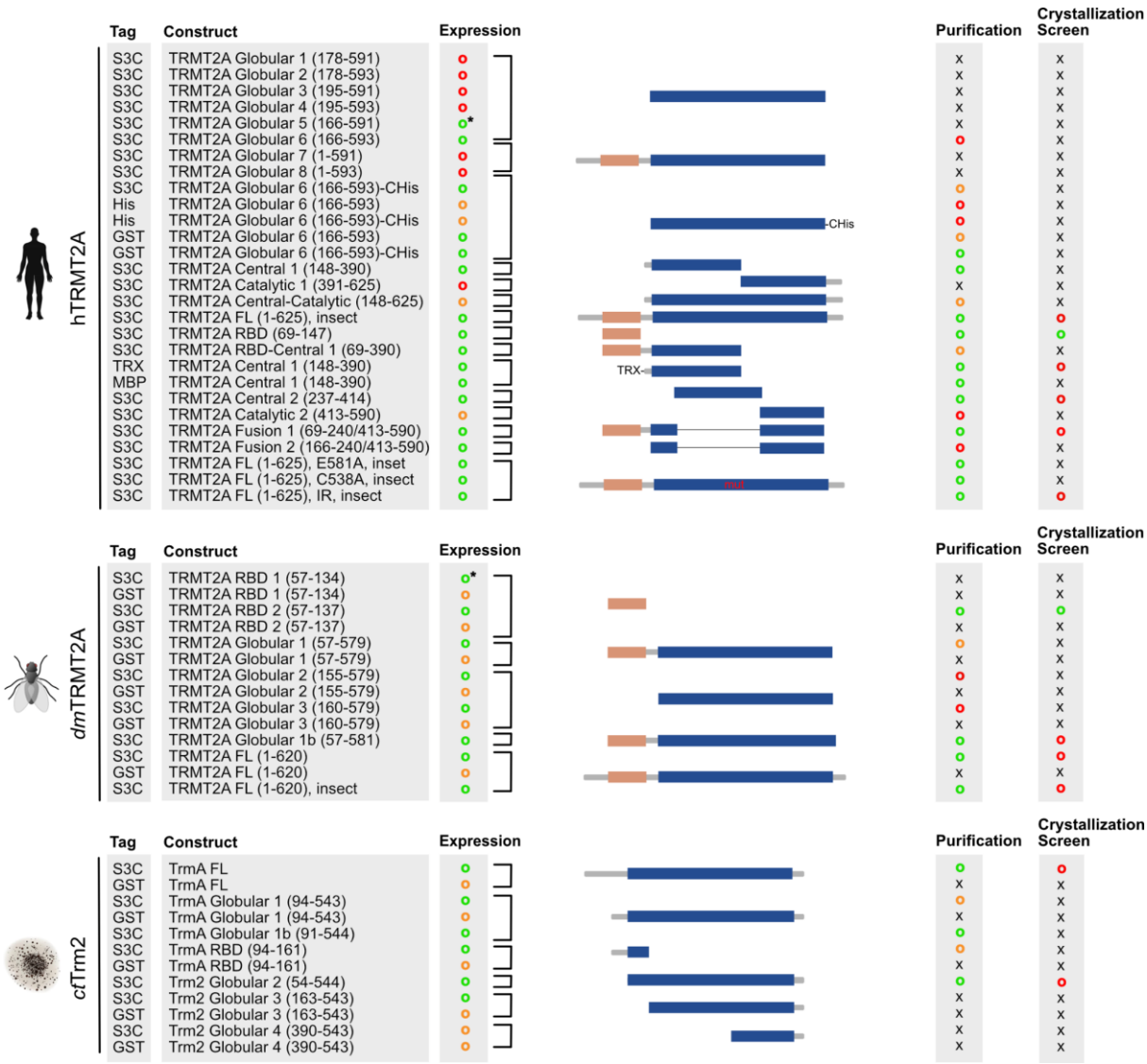

Supplemental Figure 3 – List of all purified hTRMT2A, *dm*TRMT2A and *cf*Trm2 proteins.
N-terminal tag, protein fragment, success in protein expression, protein purification and crystallization trials, as well as domain organization are visualized. Success is indicated as green circle, moderate success as orange circle and no success as red circle. Black x shows that this experiment was not performed. Asterisk indicates a protein whose expression was good, but not proceeded with for further experiments. Regarding domain organization, orange denotes the predicted RBD and blue the predicted methyltransferase domain.

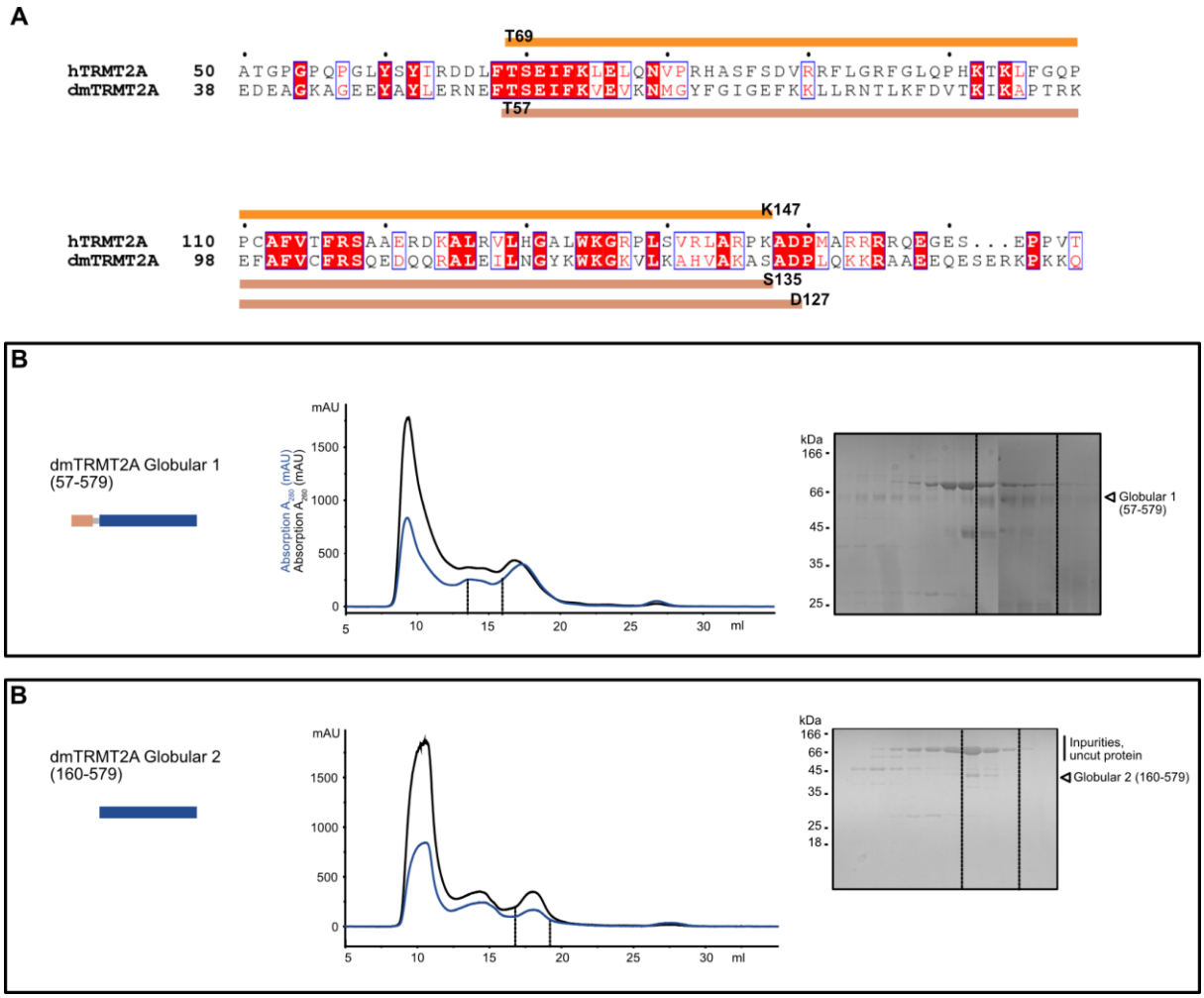

Supplemental Figure 4 – *dm*TRMT2A sequence alignment and unsucessfull domain purification.
A Sequence alignment of hTRMT2A (aa 50-166) and *dm*TRMT2A (38-157) was performed with ClustalO and visualized with ESPript 3. Red underlined residues are highly conserved. Bright orange on top shows domain borders of hTRMT2A RBD and dark orange below the derived domain borders of *dm*TRMT2A RBD. **B** SEC elution profile and respective SDS PAGE from last purification step (S200, 16/600) of *dm*TRMT2A globular domain 1 (aa 57-579) with 65.3 kDa. Protein was not stable enough for further experiments. **C** SEC elution profile and SDS PAGE from last purification step (S200, 16/600) of *dm*TRMT2A globular domain 2 (aa 160-579) with 47.1 kDa. Inpurities after final SEC step as visible on the SDS PAGE prevented further experiments. Protein of interest is indicated with an arrow. Lines show fractions containing protein of interest.

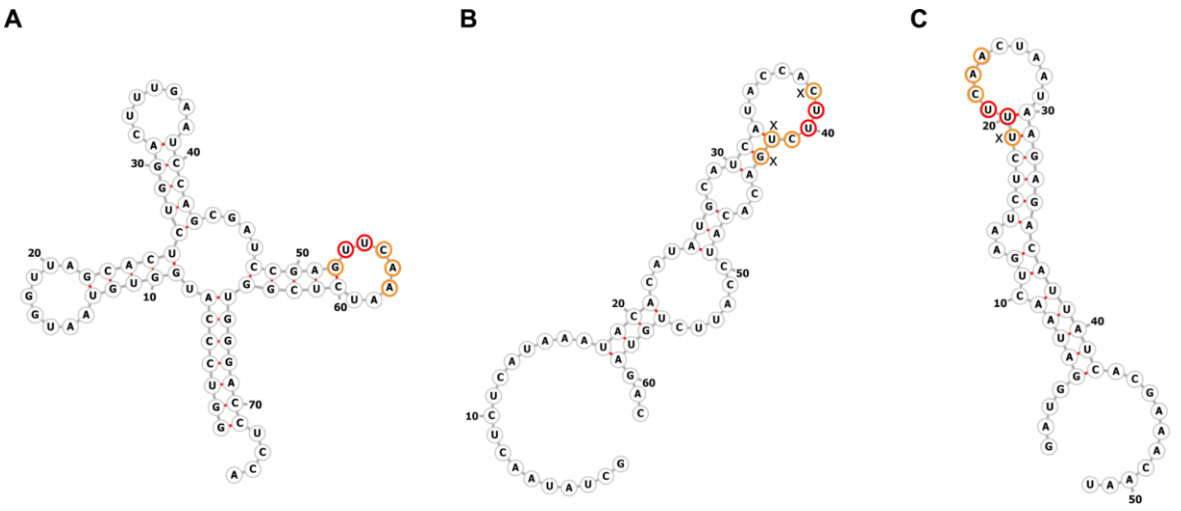

Supplemental Figure 6 – Predicted RNA structures.
A Predicted RNA fold of complete $tRNA^{Gln}$ (75 nt). **B** Predicted RNA fold of KCND2 mRNA, a potential hTRMT2A RNA target (62 nt). **C** Predicted RNA fold of the *E3* element of *S. cerevisiae ASH1* E3 (51 nt). Target uridine and adjacent uridine are highlighted in red. Other residues, which are supposed to be part of the hTRMT2A RNA sequence motif are highlighted in orange. RNA folds were predicted with the RNAfold Webserver (Hofacker, 2003).

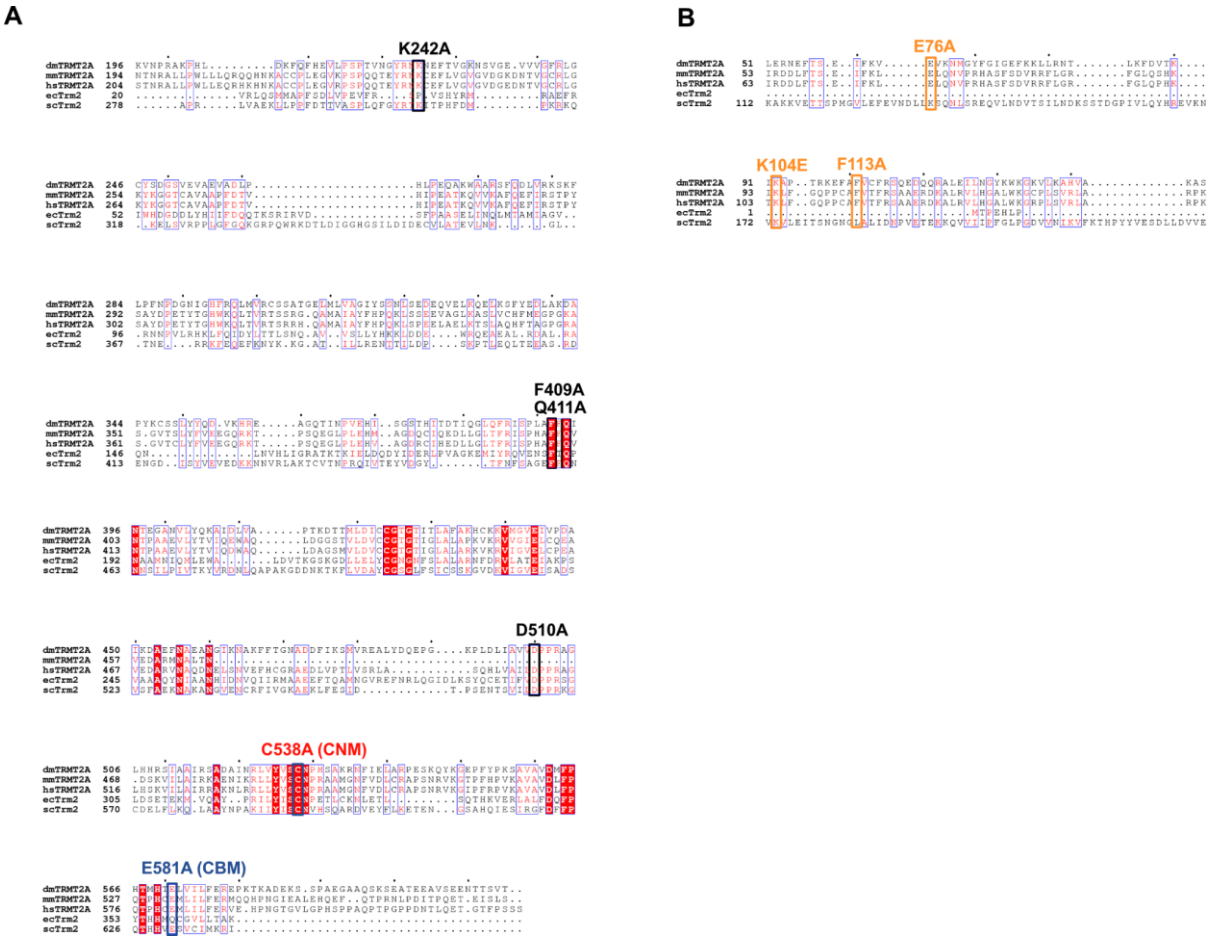

Supplemental Figure 5 – Sequence alignment of hTRMT2A homologs.
Sequence alignment of homologs of human TRMT2A from *D. melanogaster* (*dm*TRMT2A), *M. musculus* (*mm*TRMT2A), *E. coli* (*ec*TrmA) and *S. cerevisiae* (*sc*Trm2). Highly conserved residues are underlined in red. **A** methyltransferase domain with CBM (blue) and CNM (red) mutations, as well as IR (black) mutations. **B** TRMT2A RBD with IR (yellow) mutations. Protein sequences were aligned with ClustalO and visualized with ESPript 3.

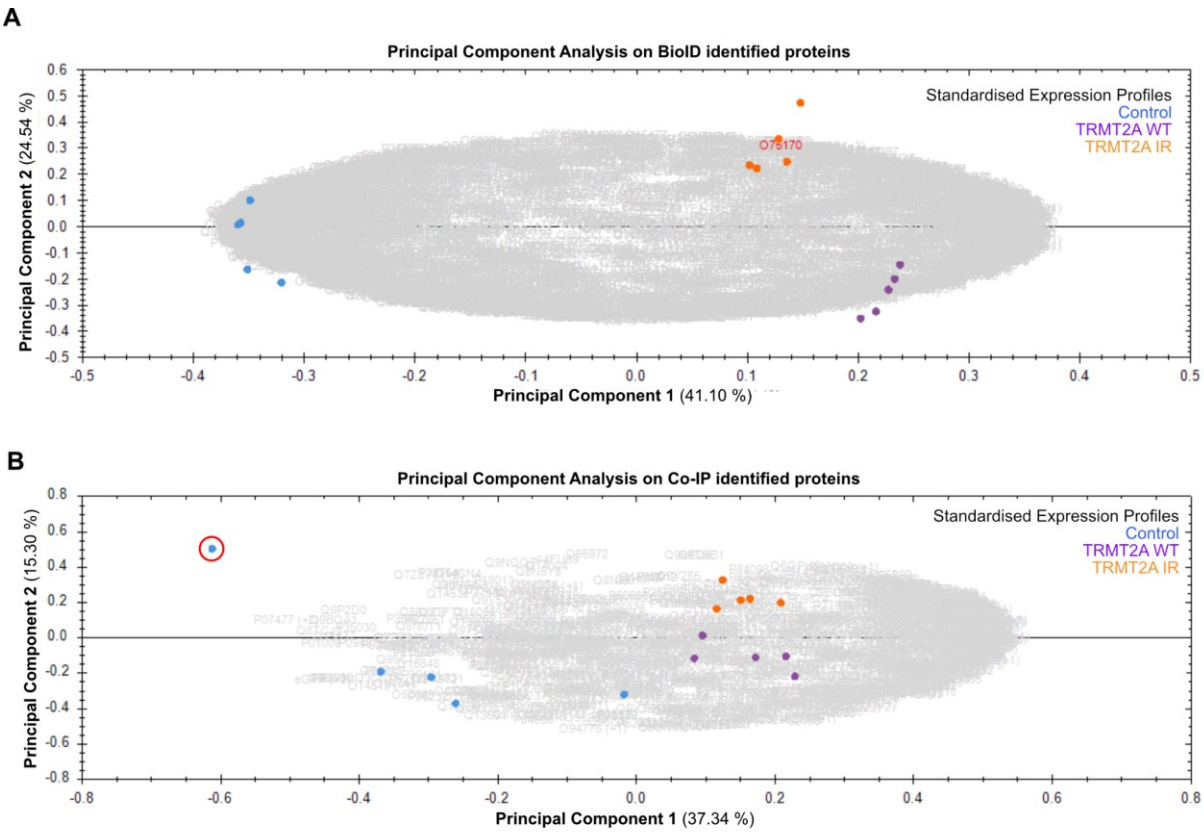

Supplemental Figure 7 – Principal Component Analysis (PCA) on BioID and Co-IP identified proteins.
A PCA on BioID identified proteins with quintuplicates of BirA* control (blue), BirA*-hTRMT2A WT (violet) and BirA*-hTRMT2A IR (orange) shows significant differences between samples from different conditions. **B** PCA on Co-IP identified proteins with quintuplicates of FLAG control (blue), FLAG-hTRMT2A WT (violet) and FLAG-hTRMT2A IR (orange) shows significant differences between samples from different conditions. Outlier from control samples is encircled in red. Taking this outlier out of the analysis did not change the significantly enriched proteins in hTRMT2A WT and IR conditions. PCA analysis was performed with Progenesis QI software in the HMGU proteomics core facility and uses feature abundance levels across runs to determine the principal axis of abundance variation.

```
library(ggplot2)
library(dplyr)
library(readxl)
library(openxlsx)
library(scales)
library(drc)
library(knitr)
library(matrixStats)
library(ggsignif)

##INPUT
#read in data from excel
Inhibitors <- read_excel("THESIS_Inhibitors.xlsx", sheet=2)
Inhibitors

# put in data frame for ggplot
dfInhibitor <- data.frame(Inhibitor = Inhibitors$Inhibitor,
                RLU = Inhibitors$RLU,
                SAH = Inhibitors$SAH,
                SAH2 = Inhibitors$SAH2
)
dfInhibitor


##STATISTIC and DATA PREPARATION
# Put in vectors for comparison
Inhibitor_Buffer <- dfInhibitor %>% slice(1:8)
Inhibitor_Spermidine <- dfInhibitor %>% slice(9:16)
Inhibitor_Sinefungin <- dfInhibitor %>% slice(17:24)
Inhibitor_13 <- dfInhibitor %>% slice(25:32)
Inhibitor_15 <- dfInhibitor %>% slice(33:40)
Inhibitor_17 <- dfInhibitor %>% slice(41:58)

#bind to matrix for wilcoxon test
dfInhibitor2 <- rbind(Inhibitor_Buffer, Inhibitor_Spermidine)
dfInhibitor3 <- rbind(Inhibitor_Buffer, Inhibitor_Sinefungin)
dfInhibitor4 <- rbind(Inhibitor_Buffer, Inhibitor_13)
dfInhibitor5 <- rbind(Inhibitor_Buffer, Inhibitor_15)
dfInhibitor6 <- rbind(Inhibitor_Buffer, Inhibitor_17)

# Shapiro test for normal distribution of data
shapiro.test(Inhibitor_Buffer$RLU)
shapiro.test(Inhibitor_Spermidine$RLU)
shapiro.test(Inhibitor_Sinefungin$RLU)
shapiro.test(Inhibitor_13$RLU)
shapiro.test(Inhibitor_15$RLU)
shapiro.test(Inhibitor_17$RLU)

#Wilcoxon testm because of non-normal distributed values
wilcox.test(dfInhibitor2$RLU ~ dfInhibitor2$Inhibitor) #s, 0,0006 = ***, Spermidine
wilcox.test(dfInhibitor3$RLU ~ dfInhibitor3$Inhibitor) #s, 0,0003 = ***, Sinefungin
wilcox.test(dfInhibitor4$RLU ~ dfInhibitor4$Inhibitor) #ns, 0,38 = ns, #13
wilcox.test(dfInhibitor5$RLU ~ dfInhibitor5$Inhibitor) #s, 0,007 = *, #15
wilcox.test(dfInhibitor6$RLU ~ dfInhibitor6$Inhibitor) #ns, 0,13 = ns, #17


##GGPLOT-Inhibitors
Inhibitor = ggplot(dfInhibitor, aes(x=Inhibitor, y = SAH2)) +
  geom_boxplot(color = "black", size = 0.5, outlier.color="black", outlier.shape=1, fill=colors2) +
  xlab(expression("Inhibitor 1 mM")) +
  ylab(expression("SAH concentration [nM]")) +
  geom_point(col="black") +
  geom_signif(comparisons = list(c("Buffer", "Cmp 15")), map_signif_level = TRUE, y_position = c(75)) +
  geom_signif(comparisons = list(c("Buffer", "Sinefungin")), map_signif_level = TRUE, y_position = c(135)) +
  geom_signif(comparisons = list(c("Buffer", "Spermidine")), map_signif_level = TRUE, y_position = c(195)) +
  geom_hline(yintercept = 0, col = "grey", linetype = "dotted") +
  theme_classic() +
  theme(axis.text.x = element_text(angle=45, hjust=1))
Inhibitor
```

Supplemental Figure 8 – R-code for statistical analysis.
Inhibitor experiments were analysed with the R inbuild shapiro.test and wilcox.test function.

```
library(ggplot2)
library(dplyr)
library(readxl)
library(openxlsx)
library(scales)
library(drc)
library(knitr)
library(png)
library(matrixStats)
library(ggsignif)

##INPUT
#read in data from excel
tRNA <- read_excel("THESIS_MTAseGlo-tRNA.xlsx", sheet=1)
tRNA

dftRNA<-data.frame(tRNA = tRNA$RNA,
                   Concentration = tRNA$Concentration,
                   SAH_1 = tRNA$LSAH_1,
                   SAH_2 = tRNA$LSAH_2,
                   SAH_3 = tRNA$LSAH_3
)
dftRNA

# Subset into different tRNA values
tRNA_Gln <- dftRNA %>% slice(1:8)

#Calcuate mean and SD of SAH values
mean_Gln <- rowMeans(cbind(tRNA_Gln$SAH_1, tRNA_Gln$SAH_2, tRNA_Gln$SAH_3))
sds_Gln <-  rowSds(cbind(tRNA_Gln$SAH_1, tRNA_Gln$SAH_2, tRNA_Gln$SAH_3))

#Dataframe with concentration and mean, SAH values
dfAlltRNA <- data.frame(concentration=tRNA$Concentration,
                        mean_Gln,
)

##Michaelis-Menten fitting with ‚drc'-package, SAH values, gives Km values
model.drm1 <- drm(mean_Gln ~ concentration, data =dfAlltRNA, fct = MM.2())
model1 <- data.frame(concentration = seq(0, max(dfAlltRNA$concentration), length.out = 100))
model1$mean_Gln <- predict(model.drm1, newdata = model1)
summary(model.drm1)
coef(model.drm1)
plot(model.drm1, log = '', pch = 17, main = "Fitted MM Gln curve")

##GGPLOT – tRNAGln, SAH values
gg1 = ggplot(dftAllRNA, aes(x = concentration, y = mean_Gln)) +
  geom_point(color="black", size=2, stroke=1, shape=21, fill="white") +
  theme_classic() +
  ggtitle("tRNA") +
  xlab(expression("Substrate Concentration [uM]")) +
  ylab(expression("SAH concentration [nM]")) +
  geom_errorbar(aes(ymin=mean_Gln-sds_Gln, ymax = mean_Gln+sds_Gln), width=0.1) +
  geom_line(data = model1, aes(x = concentration, y = mean_Gln), color = "black", size=0.5) +
  scale_x_continuous(limits = c(0,7))
gg1
```

Supplemental Figure 9 – R-code for Michaelis Menten fitting.
Exemplary code for $tRNA^{Gln}$ and SAH values from K_m curve experiments. Analogous other RNA and RLU values can be used for computation of K_m values and Michaelis Menten fitting. 'Drc' package with 'drm' function was used for fitting.

```
library(ggplot2)
library(dplyr)
library(readxl)
library(openxlsx)
library(scales)
library(drc)
library(knitr)
library(matrixStats)
library(ggsignif)

##INPUT
#read in data from excel
BioID_WT_BP <- read_excel("BioID_GO.xlsx", sheet=2)

## WT/Ctr, upregulated GO-terms for Biological Processes
#put data in dataframe
dfBioID_WT_BP <-data.frame(GO = BioID_WT_BP$`GO biological process complete`,
                Enrichment = BioID_WT_BP$`Log2(FoldEnrichment)`,
                Log10FDR = BioID_WT_BP$`Log10(FDR)`,
                Count = BioID_WT_BP$count
)
dfBioID_WT_BP

#sort according to FDR & top 15
dfBioID_WT_BP2 <- dfBioID_WT_BP[order(dfBioID_WT_BP$Log10FDR, decreasing = FALSE),]
dfBioID_WT_BP2$GO <- factor(dfBioID_WT_BP2$GO, levels=dfBioID_WT_BP2$GO)
dfBioID_WT_BP2_subset <- tail(dfBioID_WT_BP2, 10)

##GGPLOT – figure GO-term BioID WT, biological processes
fig <- ggplot(dfBioID_WT_BP2_subset, aes(x=Enrichment, y=GO, size = Count, color=Log10FDR)) +
  geom_point(alpha=0.7) +
  theme_classic() +
  xlab(expression(Log2FoldEnrichment)) +
  ylab(expression(GOterms)) +
  scale_color_gradient(low = "#EE8900", high = "#D23600")
```

Supplemental Figure 10 – R-code for GO-term analysis.
Exemplary code for BioID experiment derived hTRMT2A WT/BirA* significant hits and GO-term 'Biological Processes' (BP). Analogous, significant hits from hTRMT2A IR/BirA* and hTRMT2A IR/WT can be used for GO-term analysis of 'Biological Processes' (BP), 'Cellular Compartements' (CC) and 'Molecular Function' (MF). GO-term analysis data were derived from gene ontology enrichment analysis tool (http://geneontology.org, PANTHER) described earlier (Ashburner et al., 2000; Mi et al., 2013; The Gene Ontology Consortium, 2021)

```
library(ggplot2)
library(ggrepel) #Avoid overlapping labels
library(dplyr)
library(readxl)
library(openxlsx)

##INPUT
BioID_WT <- read_excel("BioID_WTvsCtr.xlsx", sheet=1)
flyers <- read_excel("frequent_flyers.xlsx", sheet=1)

dfWT<-data.frame(Genes = BioID_WT$Gene,
                Ratios = BioID_WT$Ratio,
                Pvalues = BioID_WT$pValue
)

#subtracting frequent flyers from dataframes of WT
dfflyers<-data.frame(Genes <- flyers$Genes)
dfflyersWT <- dfWT[!dfWT$Genes %in% dfflyers$Genes,]
dfflyersMut <- dfMut[!dfMut$Genes %in% dfflyers$Genes,]
dfflyersMW <- dfMW[!dfMW$Genes %in% dfflyers$Genes,]

# make columns-log10(p-value) and log2(ratio)
dfflyersWT <- mutate(dfflyersWT, min_log_10_pvalue = -log10(Pvalues))
dfflyersWT <- mutate(dfflyersWT, log2_ratio = log2(Ratios))
dfflyersWT
```

```
##ORDERING
# order -log10(p-value) and log2(ratio)
WT_order_log2 <- dfflyersWT[order(dfflyersWT$log2_ratio), ]
head(WT_order_log2)
WT_order_log10_pval <- dfflyersWT[order(dfflyersWT$min_log_10_pvalue), ]
head(WT_order_log10_pval)

# set minimum for -log10(p-value) and log2(ratio)
minimum_log10pvalue <- 3
minimum_log2Ratio <- 1

# in case log2ratio in both direction -2 or +2 are interesintg (abS)
WT_interesting_ones <- dfflyersWT[dfflyersWT$min_log_10_pvalue>minimum_log10pvalue & abs(dfflyersWT$log2_ratio)>
minimum_log2Ratio,]
WT_interesting_ones

# differentiate in interesting and not interesting
dfflyersWT$interesting <- FALSE # new column
idx_interesting1 <- match(WT_interesting_ones$Genes, dfflyersWT$Genes) # indexing
dfflyersWT$interesting[idx_interesting1] <- TRUE # TRUE or FALSE
WT_interesting_ones <- dfflyersWT[dfflyersWT$min_log_10_pvalue>minimum_log10pvalue & abs(dfflyersWT$log2_ratio)>
minimum_log2Ratio & dfflyersWT$interesting == TRUE,]
WT_interesting_ones

#Ordering for positive WT
WT_order_interesting_ones<-WT_interesting_ones[order(WT_interesting_ones$log2_ratio, decreasing =TRUE),]
WT_order_interesting_ones

##VOLCANO PLOT
#TRMT2A WT/BirA*
volc1 = ggplot(dfflyersWT, aes(log2(Ratios), -log10(Pvalues)))+
  geom_point(aes(col=interesting)) +
  scale_color_manual(values=c("grey", "#E69F00"), labels= c("p-value>0,001 ", "p-value<0,001 & Log2 fold Change >2")) +
  xlab(expression(Log[2]*~fold~change~ratio~TRMT2A~WT/Ctr)) +
  ylab(expression(-Log[10]~italic("p-value"))) +
  labs(color='TRMT2aWt/Ctr')+
  geom_text_repel(data=head(WT_order_interesting_ones, 15), aes(label=Genes), size = 5.5, fontface="bold", colour="black",
segment.colour="black", segment.size = 1)

volc1_1 = volc1 + theme_bw() + theme_classic() +
  theme(legend.position = "none", axis.title.x = element_text(face="bold", size = 19),
        axis.title.y = element_text(face="bold", size = 19),
        axis.text = element_text(size = 14, face="bold"),
        axis.line = element_line(colour = "black", size = 1, linetype = "solid")) +
  scale_x_continuous(limits=c(-7, 7)) +
  scale_y_continuous(limits=c(0, 12))
```

Supplemental Figure 11 – R-code for Volcanoplots of BioID and Co-IP mass spectrometry data.
Code for BioID derived hTRMT2A WT/BirA* significant hits. Frequent false positive proteins were subtracted and significant hits colored (p-value > 0.001, ratio > 2). Top 15 hits were labelled with names. Code was kindly provided by Melina Klostermann (Zarnack laboratory) and adapted. Analogous other BioID experiments and Co-IP experiments were visualized.

```
library(ggplot2)
library(ggrepel)
library(dplyr)
library(readxl)
library(ggplot2)

# read in data from excel
TRMT2a_WT_BioID <- read_excel("Top-BioID_WTvsCtr.xlsx", sheet = 1)
TRMT2a_WT_BioID
TRMT2a_Mut_BioID <- read_excel("Top-BioID_MutvsCtr.xlsx", sheet = 1)
TRMT2a_Mut_BioID

#Create dataframe for GGPlot
dfTRMT2a_WT_BioID <- as.data.frame(TRMT2a_WT_BioID)
dfTRMT2a_Mut_BioID <- as.data.frame(TRMT2a_Mut_BioID)

#Select Gene names & find overlapping one
WT_Genes_BioID <- dfTRMT2a_WT_BioID$Genes
WT_Genes_BioID
Mut_Genes_BioID <- dfTRMT2a_Mut_BioID$Genes
Mut_Genes_BioID
both_datasets_BioID <- intersect(WT_Genes_BioID, Mut_Genes_BioID)
both_datasets_BioID

#Put ovlerapping gene names in data frame & merge dataframe for ggplot BioID Wt&Mut
dfWT_intersect_BioID <- dfTRMT2a_WT_BioID %>% filter(`Genes` %in% both_datasets) %>% unique.data.frame()
dfMut_intersect_BioID <- dfTRMT2a_Mut_BioID %>% filter(`Genes` %in% both_datasets)%>% unique.data.frame()
dfmerge_BioID <- merge(dfWT_intersect_BioID, dfMut_intersect_BioID, by = "Genes")
dfmerge_BioID
tail(dfmerge_BioID)

##GGPLOT
#select what to label for BioID
dfmerge_BioID$label <- NA
dfmerge_BioID[dfmerge_BioID$`negLOG(P-value).x`>3 & dfmerge_BioID$`negLOG(P-value).y`>3 &
dfmerge_BioID$Difference.x > 3 & dfmerge_BioID$Difference.y > 3, ]$label <-
  dfmerge_BioID[dfmerge_BioID$`negLOG(P-value).x`>3 & dfmerge_BioID$`negLOG(P-value).y`>3 &
dfmerge_BioID$Difference.x > 3 & dfmerge_BioID$Difference.y > 3, ]$`Genes`
dfmerge_BioID

#'GGPLOT of overlap WT & Mut BioID
gg1 <- ggplot(data = dfmerge_BioID,
              mapping = aes(x = Difference.x, y = Difference.y, label = label)) +
  geom_point(colour="black")+
  geom_text_repel()+
  ggtitle("Overlap BioID - WT and Mut")+
  xlab(expression(Log[2]*~fold~change~ratio~TRMT2aWT/Ctr)) +
  ylab(expression(Log[2]*~fold~change~ratio~TRMT2aMut/Ctr)) +
  scale_x_continuous(limits=c(1, 7)) +
  scale_y_continuous(limits=c(1, 7)) +
  theme_bw() +
  theme_classic()
gg1
```

Supplemental Figure 12 – R-code for overlap of BioID results
Code for overlap of hTRMT2A WT and hTRMT2A IR (mut) significant hits from BioID experiment. Genes that possess respective cut-offs were labelled with the protein name (p-value > 0.001, ratio > 2). Analogous other BioID experiments and Co-IP experiments were visualized. R-code was kindly provided by Dr. Lena Molitor and adapted accordingly.

Supplementary Tables

Supplemental Table 1 – Purification strategies of TRMT2A subdomains and orthologs

Name	Protein	Expression Vector / *E. coli* strain	Purification
hTRMT2A RBD	hTRMT2A (aa 67-147)	pOPINS3C, Rosetta	HisTrap FF column, 3C cleavage, subtractive HisTrap FF column, SEC with S75 (16/600)
hTRMT2A globular	hTRMT2A (aa 166-593)-CHis	pOPINJ, Rosetta	HisTrap FF column, 3C cleavage, subtractive HisTrap FF column, SEC with S75 (16/600)
hTRMT2A central 1	hTRMT2A (aa 148-390)	pOPINTRX, pLyS	HisTrap FF column, 3C cleavage, subtractive HisTrap FF column, SEC with S75 (16/600)
hTRMT2A central 2	hTRMT2A (aa 237-414)	pOPINS3C, pLyS	HisTrap FF column, HiTrap Heparin, SEC with S75 (16/600)
hTRMT2A RBD-central	hTRMT2A (aa 67-390)	pOPINS3C, pLysS	HisTrap FF column, subtractive HisTrap FF column, SEC with S75 (16/600)
hTRMT2A fusion 1	hTRMT2A (aa 67-237/414-590)	pOPINS3C, pLyS	HisTrap FF column, 3C cleavage, subtractive HisTrap FF column, SEC with S75 (16/600)
hTRMT2A FL	hTRMT2A (aa 1-625)	pFastBacS3C, H5 insect cells	HisTrap FF column, 3C cleavage, SEC with S200 (16/600), GSTrap FF
*dm*TRMT2A RBD	dmTRMT2A (57-137)	pOPINS3C, Rosetta	HisTrap FF column, 3C cleavage, subtractive HisTrap FF column, SEC with S75 (16/600)
*dm*TRMT2A globular 1b	dmTRMT2A (57-581)	pOPINS3C, Rosetta	HisTrap FF column, 3C cleavage, HiTrap Heparin, subtractive HisTrap FF column, SEC with S200 (16/600)
*dm*TRMT2A FL	dmTRMT2A (1-620)	pOPINS3C, Rosetta	HisTrap FF column, 3C cleavage, HiTrap Heparin, SEC with S200 (16/600)
*ct*Trm2 globular 1	*ct*Trm2 (53-544)	pOPINS3C, Rosetta	HisTrap FF column, 3C cleavage, subtractive HisTrap FF column, HiTrap Heparin, SEC with S200 (16/600)
*ct*Trm2 globular 2	*ct*Trm2 (91-544)	pOPINS3C, Rosetta	HisTrap FF column, 3C cleavage, subtractive HisTrap FF column, HiTrap Heparin, SEC with S200 (16/600)
*ct*Trm2 FL	*ct*Trm2 (1-620)	pGEX, Rosetta	GSTrap FF, 3C cleavage, HiTrap Heparin, SEC with S200 (16/600)

Supplemental Table 2 – Crystallization trials

Protein	Concentration in mg/mL ($A_{260/280}$)	Screens	Volume/°C	Success
hTRMT2A FL (1-625), insect	1.57, 5.17	Classics I+II, AmSO4, Natrix1+2, Nucleix, PEG, PACT, JCSG+	200 uL / RT	No
hTRMT2A central1 (148-390)	1.2 (0.61), 4.4 (0.58)	Classics I+II, AmSO4, MPD, Nucleix, PEG, PACT, JCSG+	200 uL / RT	No
hTRMT2A central1 (148-390)	4.32, 7.29	Classics I+II, AmSO4, Natrix1+2, Nucleix, PEG, PACT, JCSG+	100 nL / RT	No
*dm*TRMT2A RBD (57-137)	8.00, 4.08	Classics I+II, AmSO4, Natrix1+2, MPD, PEG, PACT, JCSG+	200 nL / RT	Yes, $AmSO_4$ screen condition H1(2M NaCl, 2M $AmSO_4$)
*dm*TRMT2A RBD (57-137)	8.95, 15.22	Classics I+II, AmSO4, Natrix1+2, Nucleix, MPD, PEG, PACT	200 nL / RT	Yes, $AmSO_4$ screen condition H1
*dm*TRMT2A FL (1-620)	4.00, 10.2	Classics I+II, AmSO4, Natrix1+2, MPD, PEG, PACT, JSCG+	200 nL / RT	No, after 2 days small needles in Classics I screen condition G2 (0.2M $CaCl_2$, 0.1M HEPES 7.5, 28% PEG 400), not reproducible
*dm*TRMT2A FL (1-620)	3.00, 8.9	Classics I+II, AmSO4, Natrix1+2, MPD, PEG, PACT, JSCG+	200 nL / RT	No
SUMO-hTRMT2A central 2 (237-414)	0.92, 1.51	Classics I, AmSO4, Natrix1+2, MPD, PEG, PACT, JSCG+	200 nL / RT	No
SUMO-hTRMT2A central 2 (237-414)	1.1, 4.4	Classics I+II, AmSO4, Natrix1+2, MPD, PEG, PACT, JSCG+	200 nL / 4°C + RT	No
dmTRMT2A FL (1-620) + SAM (1:2, 1:5)	4.8 (0.56)	Classics 1+2, Natrix1+2, PEG, PACT, JSCG+	200 nL / RT	No
dmTRMT2A FL (1-620) + SAH (1:2, 1:5)	4.8 (0.56)	Classics 1+2, Natrix1+2, PEG, PACT, JSCG+	200 nL / RT	No
SUMO-hTRMT2A central 2 (237-414)	1.5 (0.6)	Classics 1+2, Natrix1+2, PEG, PACT, JSCG+	200 nL / RT	No
hTRMT2A Fusion 1 (67-237/414-590)	3.23 (0.87)	Classics 1+2, Natrix1+2, PEG, PACT, JSCG+	200 nL / RT	No, Classics I screen condition D9, JSCG+ screen condition F9, salt
*dm*TRMT2A FL (1-620) + 1:1000/1:5000 Trypsin	6.0 (0.56)	Classics 1+2, Natrix1+2, PEG, PACT, MPD, AmSO4, JSCG+	200 nL / RT	No, Classics I screen condition D8 + Classics II screen condition B8, salt
*ct*Trm2 FL (1-544)	2.54, 6.32	Classics I+II, Natrix1+2, PACT, PEG, JSCG+	200 nL / RT + 4°C	No

dmTRMT2A FL (1-620) from insect	8.9 (0.57)	JBS, PACT, JSCG+, Natrix 1+2, AmSO4, PEG, MPD	200 nL / RT	No
ctTrm2 FL (1-544)	13.3 (0.55)	JBS, PACT, JSCG+, Natrix 1+2, AmSO4, PEG, MPD	200 nL	No
hTRMT2A IR mutant (1-625)	1.2, 5.6 (0.61)	JSB, PEG, PACT, Natrix1+2, AmSO4, JSG+	200 nL / RT	No
*ct*Trm2 Globular 1 (53-544)	5.45, 2.14 (0.53)	JBS, Natrix 1+2, JSCG+	200 nL / RT	No

Supplemental Table 3 – Processing statistics of 2.0 and 1.2 hTRMT2A RBD structures

Data collection	**Initial model**	**Refined structure**
PDB ID	7NTN	7NTO
Beamline	DESY P11	SLS III
Wavelength	1.009300	1.000033
Space group	*F432*	*C2*
Cell dimensions *a*, *b*, *c* (Å)	131.28, 131.28, 131.28	52.88, 36.30, 39.10
No. of molecules per asymmetric unit	1	1
Resolution (Å)	50.00-2.02 (2.02-2.07)	50.00–1.23 (1.23-1.26)
R_{merge}	5.800 (110.100)	4.4 (105.8)
$I / \sigma I$	36.42 (3.85)	18.2 (1.95)
CC (1/2)	100.0 (92.000)	100.0 (61.4)
Completeness (%)	100.0 (100.0)	97.0 (94.4)
Redundancy	29.45 (31.92)	6.62 (6.60)
Refinement		
Resolution (Å)	2.02	1.23
No. reflections	6872	17,520
R_{work} / R_{free}	20.51 / 25.14	12.71 / 17.15
No. atoms		
Protein	648	708
Water	31	81
Other atoms	29	34
B-factor overall	41.66	18.83
R.m.s. deviations		
Bond lengths (Å)	0.01	0.018
Bond angles (°)	0.98	2.13
Ramachandran plot		
Most favored (%)	98.67	100
Additional allowed (%)	1.33	0

*Values in parentheses are for highest-resolution shell.

Supplemental Table 4 – Results from crosslinking and mass spectrometry experiments

XL type UV, complex, replicate 1			XL type NM, complex, replicate 1		
sequence	**cross-linked residue**	**adduct**	**sequence**	**cross-linked residue**	**adduct**
AAMGNFVDLCR	C551	U/C	GGTCAVAAPFDTVHIPEATK	C270	C
ACCPLEGVRPSPQQTEYR	C225, C226	U/C	HASFSDVR	H83	G
ASGVTCLYFVEEGQR	C365	U/C	LFGQPPCAFVTFR	C111	C
CIHEDLLGLTFR	C392	U/C	VIGVELCPEAVEDAR	C463	A
EGAGAATGPGPQPGLYSYIR	S61, Y62	U/C	VIGVELCPEAVEDAR	C463	U
GGTCAVAAPFDTVHIPEATK	C270	U/C			
GRPLSVR	R137	U/C			
HASFSDVR	F86	U/C			
HASFSDVRR	R90	U/C			
HQAMAIAYFHPQK	Y331	U/C			
KQLECEQVLQK	C191	U/C			
KTPSQEGLPLEHVAGDR	KC375	U/C			
LFGQPPCAFVTFR	C111	U/C			
LLYVSCNPR	C538	U/C			
QLECEQVLQK	C191	U/C			
RLLYVSCNPR	C538	U/C			
RQEGESEPPVTR	R156, Q157	U/C			
RRQEGESEPPVTR	R155, R156, Q157	U/C			
TPSQEGLPLEHVAGDR	H386	U/C			
VADVVTPLWTVPYAEQLER	W176	U/C			
VIGVELCPEAVEDAR	C463	U/C			
VILAIRR	R525	U/C			
VKGIPFRPVK	K559	U/C			
VLHGALWK	W134	U/C			
VNAQDNELSNVEFHCGR	C486	U/C			
YKGGTCAVAAPFDTVHIPEATK	C270	U/C			
XL type UV, complex, replicate 2			**XL type NM, complex, replicate 1**		
sequence	**cross-linked residue**	**adduct**	**sequence**	**cross-linked residue**	**adduct**
AAMGNFVDLCR	C551	U/C	GGTCAVAAPFDTVHIPEATK	C270	C
ACCPLEGVRPSPQQTEYR	C225, C226	U/C	HASFSDVR	H83	G
ASGVTCLYFVEEGQR	C365	U/C	LFGQPPCAFVTFR	C111	C
CIHEDLLGLTFR	C392	U/C	VIGVELCPEAVEDAR	C463	A
EGAGAATGPGPQPGL	S61, Y62	U/C	VIGVELCPEAVEDAR	C463	U

YSYIR					
GGTCAVAAPFDTVHIP EATK	C270	U/C			
GRPLSVR	R137	U/C			
HASFSDVR	F86	U/C			
HASFSDVRR	R90	U/C			
HQAMAIAYFHPQK	Y331	U/C			
KQLECEQVLQK	C191	U/C			
KTPSQEGLPLEHVAGD R	KC375	U/C			
LFGQPPCAFVTFR	C111	U/C			
LLYVSCNPR	C538	U/C			
QLECEQVLQK	C191	U/C			
RLLYVSCNPR	C538	U/C			
RQEGESEPPVTR	R156, Q157	U/C			
RRQEGESEPPVTR	R155, R156, Q157	U/C			
TPSQEGLPLEHVAGDR	H386	U/C			
VADVVTPLWTVPYAEQ LER	W176	U/C			
VIGVELCPEAVEDAR	C463	U/C			
VILAIRR	R525	U/C			
VKGIPFRPVK	K559	U/C			
VLHGALWK	W134	U/C			
VNAQDNELSNVEFHC GR	C486	U/C			
YKGGTCAVAAPFDTVH IPEATK	C270	U/C			
XL type UV, reconstituted, replicate 1			**XL type NM, reconstituted, replicate 1**		
sequence	**cross-linked residue**	**adduct**	**sequence**	**cross-linked residue**	**adduct**
AAMGNFVDLCR	C551	U/C	FGLQPHK	H101	G
ACCPLEGVRPSPQQTE YR	C225, C226	U/C	GGTCAVAAPFDTVHIP EATK	C270	C
ALLPWLLEQR	W213	U/C	HASFSDVR	H83	G
ALLPWLLEQRHKHNK	W213	U/C	HASFSDVR	H83	A
ASGVTCLYFVEEGQR	C365	U/C	HQAMAIAYFHPQK	H324	A
CIHEDLLGLTFR	C392	U/C	HQAMAIAYFHPQK	H333	G
DDLFTSEIFK	F68	U/C	LFGQPPCAFVTFR	C111	C
EIGSTNRALLPWLLEQ R	R207	U/C	LFGQPPCAFVTFR	C111	A
GGTCAVAAPFDTVHIP EATK	C270	U/C	LFGQPPCAFVTFR	C111	G
GIPFRPVK	F563	U/C	RHQAMAIAYFHPQK	H324	G
GRPLSVR	R138	U/C	STPYSAYDPETYTGH WK	H312	G
GRPLSVRLAR	R138	U/C	TPSQEGLPLEHVAGD R	H386	G
HASFSDVR	H83	U/C	TSLAQHFTAGPGR	H352	G

HASFSDVRR	R90	U/C	VEHPNGTGVLGPHSP PAQPTPGPPDNTLQE TGTFPSS	F622	A
HQAMAIAYFHPQK	Y331	U/C	VIGVELCPEAVEDAR	C463	A
KQLECEQVLQK	C463	U/C	VKGIPFRPVK	V558	G
LAKEIGSTNR	K200	U/C	VLHGALWK	H130	G
LFGQPPCAFVTFR	C111	U/C			
LLYVSCNPR	C538	U/C			
PKADPMAR	K147	U/C			
QLECEQVLQK	C191	U/C			
RHQAMAIAYFHPQK	H324	U/C			
RLLYVSCNPR	C538	U/C			
RQEGESEPPVTR	R156, Q157	U/C			
RRQEGESEPPVTR	R155, R156, Q157	U/C			
STPYSAYDPETYTGHW K	Y309	U/C			
TPSQEGLPLEHVAGDR	H386	U/C			
VADVVTPLWTVPYAEQ LER	W176	U/C			
VEHPNGTGVLGPHSPP AQPTPGPPDNTLQETG TFPSS	F622	U/C			
VIGVELCPEAVEDAR	C463	U/C			
VKGIPFRPVK	K559	U/C			
VLHGALWK	W134	U/C			
VNAQDNELSNVEFHC GR	C486	U/C			
YKGGTCAVAAPFDTVH IPEATK	C270	U/C			
XL type UV, reconstituted, replicate 2			**XL type UV, reconstituted, replicate 2**		
sequence	**cross-linked residue**	**adduct**	**sequence**	**cross-linked residue**	**adduct**
AAMGNFVDLCR	C551	U/C	FGLQPHK	H101	G
ACCPLEGVRPSPQQTE YR	C225, C226	U/C	GGTCAVAAPFDTVHIP EATK	C270	C
ALLPWLLEQR	W213	U/C	HASFSDVR	H83	G
ALLPWLLEQRHKHNK	W213	U/C	HASFSDVR	H83	A
ASGVTCLYFVEEGQR	C365	U/C	HQAMAIAYFHPQK	H324	A
CIHEDLLGLTFR	C392	U/C	HQAMAIAYFHPQK	H333	G
DDLFTSEIFK	F68	U/C	LFGQPPCAFVTFR	C111	C
EIGSTNRALLPWLLEQ R	R207	U/C	LFGQPPCAFVTFR	C111	A
GGTCAVAAPFDTVHIP EATK	C270	U/C	LFGQPPCAFVTFR	C111	G
GIPFRPVK	F563	U/C	RHQAMAIAYFHPQK	H324	G
GRPLSVR	R138	U/C	STPYSAYDPETYTGH WK	H312	G
GRPLSVRLAR	R138	U/C	TPSQEGLPLEHVAGD R	H386	G

HASFSDVR	H83	U/C	TSLAQHFTAGPGR	H352	G
HASFSDVRR	R90	U/C	VEHPNGTGVLGPHSP PAQPTPGPPDNTLQE TGTFPSS	F622	A
HQAMAIAYFHPQK	Y331	U/C	VIGVELCPEAVEDAR	C463	A
KQLECEQVLQK	C463	U/C	VKGIPFRPVK	V558	G
LAKEIGSTNR	K200	U/C	VLHGALWK	H130	G
LFGQPPCAFVTFR	C111	U/C			
LLYVSCNPR	C538	U/C			
PKADPMAR	K147	U/C			
QLECEQVLQK	C191	U/C			
RHQAMAIAYFHPQK	H324	U/C			
RLLYVSCNPR	C538	U/C			
RQEGESEPPVTR	R156, Q157	U/C			
RRQEGESEPPVTR	R155, R156, Q157	U/C			
STPYSAYDPETYTGHW K	Y309	U/C			
TPSQEGLPLEHVAGDR	H386	U/C			
VADVVTPLWTVPYAEQ LER	W176	U/C			
VEHPNGTGVLGPHSPP AQPTPGPPDNTLQETG TFPSS	F622	U/C			
VIGVELCPEAVEDAR	C463	U/C			
VKGIPFRPVK	K559	U/C			
VLHGALWK	W134	U/C			
VNAQDNELSNVEFHC GR	C486	U/C			
YKGGTCAVAAPFDTVH IPEATK	C270	U/C			
XL type UV, reconstituted, replicate 3			**XL type NM, reconstituted, replicate 3**		
sequence	**cross-linked residue**	**adduct**	**sequence**	**cross-linked residue**	**adduct**
AAMGNFVDLCR	C551	U/C	FGLQPHK	H101	G
ACCPLEGVRPSPQQTE YR	C225, C226	U/C	GGTCAVAAPFDTVHIP EATK	C270	C
ALLPWLLEQR	W213	U/C	HASFSDVR	H83	G
ALLPWLLEQRHKHNK	W213	U/C	HASFSDVR	H83	A
ASGVTCLYFVEEGQR	C365	U/C	HQAMAIAYFHPQK	H324	A
CIHEDLLGLTFR	C392	U/C	HQAMAIAYFHPQK	H333	G
DDLFTSEIFK	F68	U/C	LFGQPPCAFVTFR	C111	C
EIGSTNRALLPWLLEQ R	R207	U/C	LFGQPPCAFVTFR	C111	A
GGTCAVAAPFDTVHIP EATK	C270	U/C	LFGQPPCAFVTFR	C111	G
GIPFRPVK	F563	U/C	RHQAMAIAYFHPQK	H324	G
GRPLSVR	R138	U/C	STPYSAYDPETYTGH WK	H312	G
GRPLSVRLAR	R138	U/C	TPSQEGLPLEHVAGD	H386	G

			R		
HASFSDVR	H83	U/C	TSLAQHFTAGPGR	H352	G
HASFSDVRR	R90	U/C	VEHPNGTGVLGPHSPPAQPTPGPPDNTLQETGTFPSS	F622	A
HQAMAIAYFHPQK	Y331	U/C	VIGVELCPEAVEDAR	C463	A
KQLECEQVLQK	C463	U/C	VKGIPFRPVK	V558	G
LAKEIGSTNR	K200	U/C	VLHGALWK	H130	G
LFGQPPCAFVTFR	C111	U/C			
LLYVSCNPR	C538	U/C			
PKADPMAR	K147	U/C			
QLECEQVLQK	C191	U/C			
RHQAMAIAYFHPQK	H324	U/C			
RLLYVSCNPR	C538	U/C			
RQEGESEPPVTR	R156, Q157	U/C			
RRQEGESEPPVTR	R155, R156, Q157	U/C			
STPYSAYDPETYTGHWK	Y309	U/C			
TPSQEGLPLEHVAGDR	H386	U/C			
VADVVTPLWTVPYAEQLER	W176	U/C			
VEHPNGTGVLGPHSPPAQPTPGPPDNTLQETGTFPSS	F622	U/C			
VIGVELCPEAVEDAR	C463	U/C			
VKGIPFRPVK	K559	U/C			
VLHGALWK	W134	U/C			
VNAQDNELSNVEFHCGR	C486	U/C			
YKGGTCAVAAPFDTVHIPEATK	C270	U/C			

Supplemental Table 5 – Proteins significantly enriched/depleted in BioID data
Ratio column shows the log2 of the ratio between WT/BirA*, IR/BirA* (enriched: ratio > 1) or IR/WT (depleted: ratio < -1). P-value column is the -log10 of p-value with significance threshold > 3 (< 0.001).

WT/BirA* (enriched)			IR/BirA* (enriched)			IR/WT (depleted)		
Gene	Log2 Ratio	-Log10 pValue	Gene	Log2 Ratio	-Log10 pValue	Gene	Log2 Ratio	-Log10 pValue
PCDHGA4	6.85	9.36	PPP6R2	6.24	7.76	CWC25	-1.01	4.05
SLC25A46	6.08	8.51	TRMT2A	6.23	6.83	DDX52	-1.01	9.77
TRMT2A	5.88	9.46	SLC25A46	6.19	9.06	NCOA3	-1.02	7.54
SLC37A1	5.39	4.43	EPAS1	5.91	7.35	DBR1	-1.03	3.29
KBTBD6	5.34	4.59	ACTR5	5.84	6.33	CDK12	-1.03	3.51
EPAS1	5.28	5.81	OVOS2	5.61	3.28	MLLT1	-1.03	8.92
STIL	4.87	4.43	CALB2	5.50	7.89	COIL	-1.04	4.24
OVOS2	4.75	3.02	TLCD5	5.44	4.15	CUSTOS	-1.04	3.89
NACA2	4.74	6.44	NACA2	5.07	6.25	HNRNPUL1	-1.04	4.83
MED27	4.52	4.33	CRACR2A	5.04	3.68	SAMHD1	-1.05	4.81
ACTR5	4.45	10.80	EIF3B	5.03	5.31	GSTM3	-1.06	7.85
CALB2	4.41	7.63	MED27	4.89	3.87	PRB3	-1.06	3.27
EVI5L	4.22	7.43	BICC1	4.75	5.56	GTF2B	-1.07	4.14
CYP7A1	4.01	4.98	UBE4A	4.74	5.05	ELAC2	-1.07	4.04
PDCD11	3.85	3.72	PHLPP1	4.48	7.48	CMSS1	-1.08	5.19
MAK16	3.82	6.13	IPO9	4.48	5.40	RAD51AP1	-1.10	3.03
THUMPD2	3.76	5.75	GPC6	4.43	5.83	ZMAT2	-1.10	7.73
CIR1	3.68	3.99	KRT16	4.39	4.93	NOSIP	-1.11	4.97
SSB	3.57	6.27	ANKIB1	4.29	7.76	SART1	-1.12	6.22
TRIM26	3.51	6.60	SLC37A1	4.15	4.78	R3HDM2	-1.12	3.27
HIF3A	3.42	3.86	KEAP1	4.08	6.69	RADX	-1.13	5.26
RBM34	3.31	6.98	HIVEP1	3.87	4.04	SUGP2	-1.14	3.04
KRT16	3.25	4.57	PPIL2	3.78	3.04	FAM32A	-1.14	3.01
BICC1	3.22	3.75	RPL29	3.77	4.79	USP39	-1.16	5.06
SGCB	3.21	3.15	KLHDC4	3.74	8.15	TBL3	-1.16	3.13
RIBC1	3.20	5.11	TOMM20	3.72	7.97	ATAD5	-1.17	5.76
NGDN	3.19	3.21	PDCD11	3.69	3.44	RNMT	-1.17	3.27
YBX3	3.12	4.37	NOP56	3.68	8.04	CSTF3	-1.18	3.25
C11orf98	3.07	5.11	PTPN2	3.65	4.07	RRP8	-1.18	4.53
PHLPP1	3.05	6.72	VPS41	3.53	6.41	C2orf49	-1.18	4.31
ANKIB1	3.02	6.10	HIF3A	3.48	4.33	CACUL1	-1.19	3.54
NACA	2.98	4.93	PLAU	3.45	6.91	PRC1	-1.19	3.13
PUS7L	2.94	8.71	TXNL1	3.30	7.17	RBBP8	-1.19	4.79
NOP56	2.92	7.02	TOPBP1	3.30	3.85	ANGEL2	-1.20	6.15
VPS41	2.91	5.73	PDZRN4	3.27	3.97	NSUN2	-1.20	3.01
RRP8	2.89	6.79	WRN	3.24	3.31	IGHV4-4	-1.20	4.67
GNL3L	2.87	4.49	PROM2	3.18	8.22	CWF19L1	-1.22	3.52
IPO9	2.81	4.03	RIOK2	3.17	5.26	ALYREF	-1.22	4.80
RPL29	2.78	3.68	RPS9	3.16	5.31	WDR72	-1.23	4.20

PSD2	2.76	6.33	**RBM34**	3.07	7.65	**ASCC2**	-1.23	3.19
RIOK2	2.74	4.23	**PSD2**	3.06	5.94	**FTSJ3**	-1.23	4.72
RBM4B	2.62	3.15	**PUS7L**	3.06	8.01	**DAPK1**	-1.24	5.33
NOM1	2.59	7.67	**NACA**	3.04	6.30	**WDR12**	-1.25	5.74
THUMPD1	2.58	5.17	**PITRM1**	3.00	6.43	**NOL7**	-1.26	3.60
GNL2	2.57	6.26	**GANAB**	2.94	4.70	**RBM19**	-1.27	3.47
TXNL1	2.54	5.13	**TBC1D22B**	2.80	7.23	**GNL2**	-1.29	4.44
DDX55	2.53	4.39	**TACC1**	2.68	3.58	**SEMA3G**	-1.30	5.51
PPIL2	2.46	6.04	**IPO8**	2.64	5.37	**UBN1**	-1.30	3.10
NOL11	2.46	6.15	**TTC9C**	2.62	3.31	**SGO2**	-1.34	3.37
CAMK2B	2.46	4.71	**KIFBP**	2.61	3.21	**PIR**	-1.36	3.78
TBC1D22B	2.44	7.14	**GEMIN5**	2.55	6.90	**PCDHA3**	-1.37	4.43
WDR43	2.43	3.38	**YBX3**	2.51	5.03	**SPTY2D1**	-1.37	5.00
PPTC7	2.42	4.68	**RIOK1**	2.51	6.16	**UNG**	-1.38	3.85
RBM19	2.41	7.02	**TARBP2**	2.49	4.13	**ZFPM2**	-1.40	3.53
PWP2	2.41	3.80	**LAS1L**	2.47	5.94	**CCDC82**	-1.41	3.08
PLAU	2.38	5.64	**RBM4B**	2.39	3.05	**VGLL4**	-1.42	5.25
SEMA3G	2.36	4.95	**RFX1**	2.32	5.88	**NKTR**	-1.42	4.18
RIOK1	2.30	6.80	**PITX2**	2.25	3.82	**WDR36**	-1.44	6.27
DDX21	2.28	8.41	**PQBP1**	2.25	5.18	**CCDC59**	-1.44	3.43
ZCCHC3	2.27	3.26	**ABCF2**	2.24	3.77	**GNL3L**	-1.45	3.83
PUM3	2.26	7.15	**POLR3C**	2.21	3.11	**ZC3H8**	-1.48	3.32
ERICH1	2.24	3.56	**SF3A3**	2.15	4.82	**FBL**	-1.48	3.82
RFX1	2.23	6.08	**SPINDOC**	2.15	5.91	**ARHGAP11A**	-1.51	4.12
FTSJ3	2.20	5.20	**TSR1**	2.14	5.52	**NGDN**	-1.53	3.42
IPO7	2.20	5.87	**WRNIP1**	2.10	3.67	**NUP43**	-1.54	3.92
TEX10	2.16	3.64	**RPL6**	2.06	5.20	**METTL14**	-1.55	3.53
NPM1	2.15	7.19	**NOM1**	2.04	6.86	**SSB**	-1.58	5.33
EHBP1L1	2.14	5.42	**DDX21**	2.00	6.95	**RNF8**	-1.58	3.30
MYBBP1A	2.14	9.03	**MIS18BP1**	1.99	4.06	**CIR1**	-1.61	4.11
DDX10	2.12	6.20	**SSB**	1.99	6.63	**ZNF589**	-1.70	4.46
PITX2	2.12	3.75	**SCAF4**	1.97	3.35	**JADE3**	-1.73	4.00
RRP12	2.12	4.08	**BTF3L4**	1.96	3.76	**NUSAP1**	-1.80	3.56
RPL6	2.07	4.20	**PSAT1**	1.93	3.18	**MLLT6**	-1.82	3.21
NOP2	2.07	8.45	**HSPA5**	1.93	3.39	**CAMK2B**	-1.82	3.52
NSUN2	2.06	3.61	**SRP54**	1.92	5.05	**SYTL1**	-1.95	3.89
ZC3H10	2.06	3.48	**H2BU1**	1.89	4.20	**MAK16**	-1.98	4.71
WDR36	2.05	4.74	**TUT7**	1.89	4.56	**DDX55**	-2.00	3.47
RRP15	2.01	5.89	**SOX5**	1.88	4.17	**SH3RF3**	-2.10	4.71
KRI1	1.96	3.56	**ETS2**	1.88	7.42	**ZSCAN26**	-2.10	4.72
UVSSA	1.95	4.86	**TEX10**	1.86	4.09	**SP1**	-2.13	3.95
NIFK	1.95	8.00	**RPS15**	1.86	4.56	**MEX3A**	-2.16	6.01
FAM207A	1.94	6.76	**FKBP5**	1.86	4.19	**TRIM26**	-2.17	3.31
ETS2	1.94	8.24	**NECTIN3**	1.85	4.19	**AKAP8**	-2.60	3.29

PQBP1	1.93	8.24	**PPTC7**	1.85	4.09	**CUTC**	-2.70	4.07
MAPKAPK2	1.92	6.26	**MAK16**	1.84	4.34	**TRIO**	-2.85	4.95
ABT1	1.90	4.25	**ACACA**	1.83	4.29	**UVSSA**	-2.85	3.76
IGF2BP3	1.89	4.33	**MCCC1**	1.83	4.15	**CDON**	-2.98	5.65
LAS1L	1.87	5.08	**DNAJC7**	1.81	3.82	**BMP2K**	-3.14	5.58
AATF	1.87	5.33	**STK26**	1.78	4.41	**HMCES**	-3.22	3.16
PES1	1.87	5.06	**RPL4**	1.72	5.22	**THUMPD2**	-3.24	3.41
TUT7	1.86	6.57	**RRP8**	1.71	5.17	**FNDC8**	-3.39	3.28
PIP	1.86	3.96	**ABT1**	1.71	4.38	**EVI5L**	-3.47	4.89
SURF6	1.85	6.45	**ISG20L2**	1.68	3.85	**CYP7A1**	-3.94	5.46
RPL4	1.84	5.19	**FAM120A**	1.67	4.84	**STIL**	-4.48	3.57
ACACA	1.84	3.76	**CACYBP**	1.67	7.09	**PCDHGA4**	-7.33	4.24
CCDC82	1.83	4.56	**IGF2BP3**	1.66	3.86			
GNL3	1.81	3.67	**BTF3**	1.64	4.73			
POP4	1.81	4.77	**EHBP1L1**	1.61	4.80			
CEBPZ	1.81	6.11	**DDX10**	1.59	5.74			
BMS1	1.80	4.04	**SSR4**	1.56	3.07			
NOL8	1.79	9.39	**IPO7**	1.55	5.03			
PNO1	1.78	3.60	**NOP2**	1.55	7.42			
TSR1	1.78	3.81	**DHX29**	1.54	3.95			
CCDC59	1.77	4.98	**NOL11**	1.53	5.55			
H2BU1	1.76	3.92	**STAU2**	1.51	5.11			
NOP53	1.75	5.83	**CXorf58**	1.51	3.66			
STRBP	1.75	6.09	**DDX27**	1.51	3.29			
SPINDOC	1.74	6.28	**NPM1**	1.49	5.78			
DDX50	1.74	5.93	**PSMC1**	1.48	3.10			
UBN1	1.73	5.74	**FMR1**	1.48	3.41			
EBNA1BP2	1.72	8.59	**RRP15**	1.46	5.45			
NOP16	1.71	5.56	**CDC27**	1.46	3.13			
SF3A3	1.71	4.05	**PES1**	1.45	4.08			
IGF2BP1	1.70	7.12	**SRCAP**	1.44	4.03			
TENT4B	1.68	4.42	**ZNF534**	1.42	3.34			
ZCCHC17	1.68	3.56	**DCAF5**	1.40	3.68			
L1RE1	1.67	4.22	**POP4**	1.39	4.12			
DDX27	1.66	3.80	**CDC73**	1.38	5.98			
ZFP64	1.66	3.43	**PUM3**	1.38	5.47			
NOC3L	1.65	3.99	**UPF3B**	1.36	6.51			
TARBP2	1.65	3.74	**DVL2**	1.35	4.87			
C18orf25	1.63	7.56	**RBM4**	1.35	4.63			
NCL	1.63	5.13	**FKBP4**	1.34	4.86			
NPM3	1.63	5.11	**SRPK1**	1.33	3.97			
UTP14A	1.63	6.57	**MYBBP1A**	1.33	7.41			
ESF1	1.63	7.08	**NOL9**	1.32	4.32			
GANAB	1.61	3.20	**ARID4B**	1.32	4.57			

ISG20L2	1.61	3.40	**RPL26L1**	1.31	3.30
DDX52	1.61	3.69	**NIFK**	1.30	6.34
BYSL	1.60	8.73	**PDLIM3**	1.28	4.75
RSL1D1	1.60	5.24	**GNL2**	1.27	5.04
FAM120A	1.59	4.19	**DDX18**	1.27	4.92
LTV1	1.58	4.09	**PWP2**	1.25	3.15
ZKSCAN3	1.58	5.04	**AATF**	1.25	4.23
TBL3	1.58	3.30	**MAGED2**	1.24	4.68
RSL24D1	1.58	4.93	**RRP12**	1.23	3.38
RRP1B	1.58	6.27	**EBNA1BP2**	1.23	3.95
DCAF5	1.57	4.05	**CNBP**	1.22	3.27
LSM14B	1.56	5.62	**MAPKAPK2**	1.21	3.08
SUGP2	1.55	3.32	**SPATS2**	1.21	5.11
CMSS1	1.54	5.25	**RSL1D1**	1.21	4.00
DDX18	1.53	5.15	**NOC3L**	1.21	3.91
IWS1	1.53	3.62	**LTV1**	1.20	3.20
FAM32A	1.53	3.91	**RPL19**	1.20	3.69
GZF1	1.53	4.05	**CEBPZ**	1.17	4.44
YBX1	1.52	3.06	**NOP16**	1.17	4.35
THUMPD3	1.51	3.08	**PFAS**	1.17	3.18
HEXB	1.51	5.05	**NOL8**	1.16	4.35
DDX17	1.50	3.69	**RBM19**	1.15	5.48
NOL10	1.50	3.37	**EIF5B**	1.14	3.26
CDC73	1.50	4.80	**SIRT1**	1.13	3.78
LYAR	1.50	6.31	**IGF2BP1**	1.13	4.64
DNTTIP2	1.49	7.12	**POGZ**	1.13	4.82
MPHOSPH10	1.48	4.67	**RPL17**	1.12	3.84
ING2	1.47	4.96	**PFKFB3**	1.11	4.40
PITRM1	1.47	4.19	**PRSS1**	1.11	3.13
TLK2	1.45	3.35	**PC**	1.11	3.52
RPP38	1.45	7.52	**SPATS2L**	1.10	4.13
KRR1	1.44	5.36	**SURF6**	1.10	6.61
BTF3L4	1.44	5.40	**UTP14A**	1.10	5.33
RPS15	1.44	3.98	**RPL24**	1.09	3.31
PRDM1	1.44	3.32	**MRPS28**	1.09	3.71
SRFBP1	1.44	6.37	**CASC3**	1.09	3.72
NOP14	1.42	3.56	**YWHAZ**	1.08	3.60
RBM4	1.41	4.60	**YTHDF2**	1.08	5.79
PFKFB3	1.40	4.07	**FAM207A**	1.07	4.65
DNAH9	1.40	4.23	**SEMA3G**	1.06	3.16
TOMM20	1.39	4.58	**FAM193A**	1.06	4.15
CNBP	1.38	4.25	**HAT1**	1.06	4.07
KEAP1	1.38	7.05	**CNOT1**	1.06	3.09
EMG1	1.37	3.55	**IWS1**	1.05	3.16

RBIS	1.37	6.83	**RSL24D1**	1.04	3.01
PHF23	1.36	4.55	**PIK3C3**	1.04	3.33
KNOP1	1.36	5.86	**UPF1**	1.03	3.95
H1-10	1.35	3.10	**ABCF1**	1.03	3.76
FXR2	1.34	3.31	**ESF1**	1.02	4.91
BTF3	1.33	5.37	**YARS1**	1.02	3.07
BLM	1.33	6.39	**C18orf25**	1.02	5.87
KLKB1	1.33	5.22	**CCDC9**	1.02	3.78
STAU2	1.31	5.63	**NOP53**	1.01	5.17
UPF1	1.31	4.14	**NAT10**	1.00	4.43
CUSTOS	1.31	4.88	**CCDC6**	1.00	3.08
UTP3	1.31	3.83			
GPATCH4	1.31	6.86			
MCCC1	1.31	3.37			
CCDC86	1.29	3.29			
ARID4B	1.29	4.18			
YTHDF1	1.29	3.63			
CLSPN	1.27	3.99			
ILF3	1.27	4.08			
CXorf58	1.26	3.18			
GRIPAP1	1.25	4.74			
HAT1	1.25	4.58			
CASP8AP2	1.24	3.33			
SRP54	1.23	3.71			
ZNF589	1.23	5.21			
SART3	1.22	4.87			
MFAP1	1.22	6.47			
RBM28	1.20	5.84			
RRS1	1.20	4.34			
SYF2	1.19	3.52			
ELOA	1.18	7.09			
PARN	1.18	6.23			
ZFR	1.17	7.24			
ZNF106	1.17	5.58			
ZC3H8	1.17	3.78			
CWF19L2	1.17	6.37			
SPTY2D1	1.16	3.26			
HTATSF1	1.16	4.41			
DDX24	1.15	4.81			
EXOSC9	1.15	6.48			
NAT10	1.15	4.99			
UPF3B	1.14	5.83			
CHCHD3	1.13	4.23			
YTHDF2	1.13	5.91			

SPATS2L	1.11	6.04
PINX1	1.11	5.24
RPS17	1.11	3.32
ADAR	1.10	4.52
NVL	1.09	3.03
USP36	1.07	3.31
HEXIM1	1.06	5.04
GTF2B	1.05	4.96
GTPBP4	1.05	4.05
RPL19	1.04	3.41
SYNCRIP	1.04	3.82
SET	1.04	4.72
CASC3	1.04	3.08
PPM1G	1.02	4.71
FXR1	1.02	3.64
LARP7	1.01	5.78
SRSF5	1.01	3.90

Supplemental Table 6 – Proteins significantly enriched/depleted in Co-IP data
Ratio column shows the log2 of the ratio between WT/FLAG, IR/FLAG (enriched: ratio > 1) or IR/WT (depleted: ratio < -1). P-value column is the -log10 of p-value with significance threshold > 3 (< 0.001).

WT/FLAG (enriched)			IR/FLAG (enriched)			IR/WT (depleted)		
Gene	Log2 ratio	-Log10 pValue	Gene	Log2 ratio	-Log10 pValue	Gene	Log2 ratio	-Log10 pValue
TRMT2A	6.93	9.49	TIMM8B	8.34	3.50	NPM1	-1.00	4.30
SSB	6.07	9.02	TUBB4A	6.45	4.49	MYH9	-1.04	3.01
TARBP2	5.31	5.62	TRMT2A	5.97	9.66	SRP68	-1.08	4.54
TRIM26	4.50	3.52	TARBP2	5.61	4.75	YBX1	-1.32	4.17
SCO2	4.33	4.56	PJA2	5.27	3.30	DNAJB11	-1.32	3.89
DHX30	4.30	3.99	CYB5B	5.05	3.36	SEPTIN9	-1.64	4.21
HNRNPAB	4.19	4.38	ARL10	5.00	6.03	DHX9	-1.71	3.13
STRAP	3.93	3.38	TIMM13	4.98	5.04	ACTC1	-1.71	4.62
LARP7	3.92	3.49	FEZ2	4.90	4.08	ACTB	-1.71	3.73
PPM1G	3.79	4.40	SCO2	4.86	5.70	HNRNPUL1	-1.79	4.77
DNAJB11	3.67	3.22	PPM1G	4.82	4.08	PABPC4	-1.87	4.26
RPL15	3.49	3.67	PPP6C	4.49	7.11	KARS1	-1.94	4.12
UPF1	3.37	3.58	PGRMC2	4.48	3.48	IGF2BP1	-2.09	4.10
MOV10	3.21	4.80	CHCHD4	4.43	3.85	UPF1	-2.26	6.08
PPP6C	3.13	5.93	PGRMC1	4.31	5.43	RPS27A	-2.29	3.34
MRPS2	3.13	3.17	RCN2	4.27	7.60	MOV10	-2.53	4.09
KPNA2	3.11	3.53	XPOT	3.93	3.46	HNRNPC	-2.74	3.17
MRPS25	3.09	3.17	NAP1L1	3.59	3.92	LARP7	-3.46	5.25
RPL10A	2.98	3.40	HAT1	3.51	4.00	SSB	-4.28	8.07
DDOST	2.97	3.46	PPP2R1A	3.49	3.93			
NAP1L1	2.89	3.28	TIMM50	3.48	3.11			
RPL34	2.87	3.60	OLA1	3.45	3.02			
IGF2BP1	2.86	3.30	AIFM1	3.28	4.31			
PABPC4	2.81	4.23	SDF4	3.21	3.74			
HNRNPUL1	2.76	3.68	GPRASP2	3.21	4.63			
MLLT11	2.73	4.12	HNRNPAB	3.17	3.29			
HNRNPF	2.72	3.32	ANKHD1	3.16	3.19			
PABPC1	2.69	3.25	DICER1	3.14	3.19			
RPLP0	2.67	4.14	DDB1	3.10	5.32			
RPL8	2.62	3.52	KPNB1	3.10	4.78			
IMPDH2	2.56	3.02	CALU	3.06	5.15			
PPP2R1A	2.55	5.56	RPL15	2.97	3.29			
AIFM1	2.51	4.45	DDOST	2.93	3.63			
RPL18A	2.44	3.05	PPP2R2A	2.92	3.99			
RPL3	2.38	3.92	ATP2A2	2.90	3.33			
RPL21	2.38	3.92	PCNA	2.84	3.42			
MRPS7	2.33	3.96	DNAJA3	2.83	4.45			
RPL10	2.32	5.37	TUBB6	2.83	4.41			
RCN2	2.30	5.58	RCN1	2.81	3.57			

DDB1	2.29	5.09	**TUFM**	2.80	3.23
MRPS27	2.28	3.26	**MAGED1**	2.79	3.15
RPL5	2.22	3.30	**FKBP10**	2.75	3.72
RPL12	2.19	3.41	**HNRNPF**	2.72	3.08
SRSF1	2.19	3.79	**ATP1A1**	2.71	3.25
MCM3	2.16	3.43	**MCM3**	2.70	3.98
YWHAE	2.11	3.86	**DNAJA1**	2.61	4.37
KPNB1	2.10	3.70	**MMS19**	2.60	3.50
RPS6	2.08	4.06	**CPVL**	2.58	3.48
PPP2R2A	2.06	3.38	**TUBB**	2.51	3.51
RPLP1	2.03	5.27	**RPL10A**	2.42	3.07
SET	2.01	3.08	**RPLP0**	2.28	3.24
MMS19	1.98	3.08	**PRPS1**	2.24	4.02
PGRMC1	1.98	3.10	**DNAJA2**	2.17	4.57
TNPO1	1.95	3.24	**IPO4**	2.07	3.87
NCL	1.94	5.54	**TNPO1**	1.98	3.92
HSPA5	1.93	3.92	**SLC25A10**	1.97	4.33
TIMM13	1.89	3.89	**YWHAE**	1.96	3.79
MRPS22	1.87	3.44	**IRS4**	1.86	3.64
NPM1	1.87	4.79	**SSB**	1.79	4.60
CALU	1.85	5.00	**MLLT11**	1.73	3.19
KHSRP	1.80	3.02	**YWHAQ**	1.69	3.32
TUFM	1.74	3.61	**NCL**	1.65	4.09
SPINDOC	1.68	3.89	**SPINDOC**	1.64	3.88
RPL4	1.61	3.25	**RPLP1**	1.64	4.53
HSPH1	1.59	3.05	**RPL21**	1.63	3.19
HSPA1A	1.52	3.11	**RBBP7**	1.56	3.06
DNAJA2	1.51	4.11	**NAP1L4**	1.55	3.53
RPL18	1.50	3.09	**HSPA1A**	1.50	3.17
EEF1A1P5	1.49	3.02	**HSPD1**	1.47	3.84
RPL26	1.44	4.12	**RPL10**	1.47	3.74
NAP1L4	1.44	3.37			
TUBB6	1.43	3.56			
RPS3	1.13	3.13			
RPS15A	1.04	3.27			

6. Appendix

List of Abbreviations

Abbreviation	Name	Abbreviation	Name
aa	amino acid	**nm**	nanometer
APS	ammonium persulphate	**nM**	nanomolar
ATP	adenosin triphosphat	**NP-40**	nonidet-40
BSA	bovine serum albumin	**NTP**	nucleoside triphosphate
CTP	cytidine triphosphat	**OE**	over expression
DAPI	4′,6-diamidin-2-phenylindol	**ON**	over night
DEPC	diethyldicarbonat	**PBS**	phosphate buffered saline
DMEM	dulbecco′s modified eagle′s medium	**PCI**	phenol chloroform isoamyl alcohol
DOC	sodium deoxycholate	**PEI**	polyethylenimine
DTT	dithiothreitol	**PFA**	paraformaldehyd
EDTA	ethylenediaminetetraacetic acid	**PEG**	polyethylenglycol
FBS	fetal bovine serum	**pmol**	picomol
FL	full-length	**polyU**	poly uridine
GTP	guanosin triphosphate	**rpm**	rounds per minute
HEPES	4-(2-hydroxyethyl)-1-piperazineethanesulfonic acid	**RT**	room temperature
h	hour	**SAH**	S-adenosylhomocysteine
IPTG	isopropyl-ß-D-thiogalactopyranosid	**SAM**	S-adenosylmethionine
KD	knockdown	**SDS**	sodium dodecyl sulfate
KO	knockout	**sec**	second
LB	lysogeny broth	**SOB**	super optimal broth
L	liter	**SOC**	Super optimal broth with catabolite repression (+glucose)
m7GTP	7-methylguanosine 5‘-triphosphate	**NaOAc**	sodium acetate
µm	mikroliter	**TCEP**	tris(2-carboxylethyl) phosphine hydrochloride
µM	mikrometer	**TEMED**	tetramethylethylenediamine
mL	mikromolar	**TFA**	trifluoroacetic acid
mM	milliliter	**TRIS**	tris(hydroxymethyl)aminomethane
ms	millimolar	**UTP**	uridine triphosphate
min	millisecond	**UV**	ultra violet
M	molar	**V**	volt
MTA	5'-deoxy-5'-methylthioadenosine	**WT**	wildtype
nL	nanomolar		

Figure Index

Figure 1 – RNA modifications. 5
Figure 2 – tRNA biogenesis pathway. 6
Figure 3 – Evolutionary tree of m^5U RNA methyltransferases. 9
Figure 4 – Structures and common aspects of selected m^5U methyltransferases. 10
Figure 5 – Catalytic mechanism of m^5U formation by *E. coli* TrmA. 12
Figure 6 – Domain organization of wildtype huntingtin. 17
Figure 7 – Pathobiology of HD. 18
Figure 8 – Selected treatment strategies for HD in preclinical trials. 20
Figure 9 – TRMT2A silencing in fly and HEK cells reduces cell death and polyQ protein aggregation. 21
Figure 10 – hTRMT2A domains and protein purifications. 73
Figure 11 – RALS of hTRMT2A FL. 74
Figure 12 – *dm*TRMT2A domains and protein purifications. 76
Figure 13 – *ct*Trm2 domains and protein purifications. 78
Figure 14 – Structure of hTRMT2A RBD shows typical RBD fold. 79
Figure 15 – Structure of *dm*TRMT2A RBD shows typical RBD fold. 80
Figure 16 hTRMT2A FL and central domain 1 are less stable than hTRMT2A RBD. 81
Figure 17 – Selected compounds of *in silico* screening and the predicted hTRMT2A RBD binding pocket. 82
Figure 18 – SPR experiments with selected small molecules confirm spermidine binding to hTRMT2A RBD. 84
Figure 19 – Successful establishment of the MTase Glo™ assay for testing of hTRMT2A FL inhibitors. 86
Figure 20 – Methylation assay with hTRMT2A FL and selected small molecules confirms spermidine as hTRMT2A FL inhibitor. 87
Figure 21 – Methylation assay indirectly detects m^5U level from isolated total RNA and purified tRNA. 90
Figure 22 – EMSAs with hTRMT2A FL and different RNA confirms tRNA as major binding target. 92
Figure 23 – Methylation assays with hTRMT2A FL and different RNA confirms U54 as major methylation parameter. 94
Figure 24 – EMSAs with different hTRMT2A subdomains and $tRNA^{Gln}$ suggest cooperative binding of $tRNA^{Gln}$ by all domains. 95
Figure 25 – Crosslinking and mass spectrometry of hTRMT2A FL and $tRNA^{Gln}$ identifies several RNA-interacting residues 96
Figure 26 – Hybrid model of hTRMT2A-tRNA binding. 98
Figure 27 – Validation of hTRMT2A mutant with impaired RNA binding (IR). 100
Figure 28 – Results of BioID experiments with hTRMT2A WT and IR. 103
Figure 29 – Result of Co-IP experiments with hTRMT2A WT and IR. 106
Figure 30 – IHC of overexpressed hTRMT2A WT and IR confirms nuclear localization in HEK cells. 107

Figure 31 – RBD topology and conserved RNA binding residues. 109
Figure 32 – AlphFold generated homology model of hTRMT2A. 111
Figure 33 – hTRMT2A RNA targets. 116
Figure 34 – hTRMT2A associated pathways in the nucleus. 125

Supplemental Figure 1 – Map of plasmid used to generate PB-Flag-BirA*-TRMT2A WT (MW1) cell line. 132
Supplemental Figure 2 – FACS sorting reports of control BioID and Co-IP cell lines. 133
Supplemental Figure 3 – List of all purified hTRMT2A, *dm*TRMT2A and *ct*Trm2 proteins. 134
Supplemental Figure 4 – *dm*TRMT2A sequence alignment and unsucessfull domain purification. .. 135
Supplemental Figure 5 – Sequence alignment of hTRMT2A homologs. 136
Supplemental Figure 6 – Predicted RNA structures. 136
Supplemental Figure 7 – Principal Component Analysis (PCA) on BioID and Co-IP identified proteins. 137
Supplemental Figure 8 – R-code for statistical analysis. 138
Supplemental Figure 9 – R-code for Michaelis Menten fitting. 139
Supplemental Figure 10 – R-code for GO-term analysis. 140
Supplemental Figure 11 – R-code for Volcanoplots of BioID and Co-IP mass spectrometry data. ... 141
Supplemental Figure 12 – R-code for overlap of BioID results 142

Table Index

Table 1 – List of chemicals 25
Table 2 – Stock solutions and loading dyes 27
Table 3 – Enzymes and enzyme-based kits 28
Table 4 – Kits 28
Table 5 – Media, antibiotics and supplements used for *E. coli* and insect cell culture 29
Table 6 – Media, antibiotics and supplements used for mammalian (HEK) cell culture 30
Table 7 – Oligonucleotides for cloning, mutagenesis, and *in vitro* transcription 30
Table 8 – RNA sequences produced by *in vitro* transcription 34
Table 9 – Plasmids obtained and generated in this thesis 35
Table 10 – Plasmids generated during this thesis 36
Table 11 – List of *E. coli* strains and mammalian cell lines 38
Table 12 – Parameters of Phusion and Clone Amp HiFi PCR 42
Table 13 – Lysis buffer for purification of SUMO/TRX and GST-tagged proteins 45
Table 14 – Buffers for purification of SUMO/TRX-tagged or GST-tagged proteins 46
Table 15 – Antibodies used for Western blots 58
Table 16 – Antibodies used for Immunocytochemistry 67
Table 17 – Experimental summary of inhibitor experiments 88
Table 18 – RNA-dependent and -independent BioID and Co-IP hits with high significance 120

Supplemental Table 1 – Purification strategies of TRMT2A subdomains and orthologs 143
Supplemental Table 2 – Crystallization trials 144
Supplemental Table 3 – Processing statistics of 2.0 and 1.2 hTRMT2A RBD structures 145
Supplemental Table 4 – Results from crosslinking and mass spectrometry experiments 146
Supplemental Table 5 – Proteins significantly enriched/depleted in BioID data 151
Supplemental Table 6 – Proteins significantly enriched/depleted in Co-IP data 157

7. References

Adams, P.D., Afonine, P.V., Bunkóczi, G., Chen, V.B., Davis, I.W., Echols, N., Headd, J.J., Hung, L.-W., Kapral, G.J., and Grosse-Kunstleve, R.W., et al. (2010). PHENIX: a comprehensive Python-based system for macromolecular structure solution. Acta Crystallographica Section D *66*, 213-221. https://doi.org/10.1107/S0907444909052925.

Aizu, T., Suzuki, T., Kido, A., Nagai, K., Kobayashi, A., Sugiura, R., Ito, Y., and Mishima, M. (2020). Domain selective labeling for NMR studies of multidomain proteins by domain ligation using highly active sortase A. Biochimica et Biophysica Acta (BBA) - General Subjects *1864*, 129419. https://doi.org/10.1016/j.bbagen.2019.129419.

Alexandrov, A., Chernyakov, I., Gu, W., Hiley, S.L., Hughes, T.R., Grayhack, E.J., and Phizicky, E.M. (2006). Rapid tRNA Decay Can Result from Lack of Nonessential Modifications. Molecular Cell *21*, 87-96. https://doi.org/10.1016/j.molcel.2005.10.036.

Alexandrov, A., Martzen, M.R., and Phizicky, E.M. (2002). Two proteins that form a complex are required for 7-methylguanosine modification of yeast tRNA. RNA *8*, 1253-1266. https://doi.org/10.1017/s1355838202024019.

Alian, A., Lee, T.T., Griner, S.L., Stroud, R.M., and Finer-Moore, J. (2008). Structure of a TrmA–RNA complex: A consensus RNA fold contributes to substrate selectivity and catalysis in m5U methyltransferases. Proceedings of the National Academy of Sciences *105*, 6876-6881. https://doi.org/10.1073/pnas.0802247105.

Ashburner, M., Ball, C.A., Blake, J.A., Botstein, D., Butler, H., Cherry, J.M., Davis, A.P., Dolinski, K., Dwight, S.S., and Eppig, J.T., et al. (2000). Gene Ontology: tool for the unification of biology. Nature Genetics *25*, 25-29. https://doi.org/10.1038/75556.

Auweter, S.D., Fasan, R., Reymond, L., Underwood, J.G., Black, D.L., Pitsch, S., and Allain, F.H.T. (2006). Molecular basis of RNA recognition by the human alternative splicing factor Fox-1. EMBO Journal *25*, 163-173. https://doi.org/10.1038/sj.emboj.7600918.

Bae, N., Gao, M., Li, X., Premkumar, T., Sbardella, G., Chen, J., and Bedford, M.T. (2017). A transcriptional coregulator, SPINDOC, attenuates the coactivator activity of Spindlin1. Journal of Biological Chemistry *292*, 20808-20817. https://doi.org/10.1074/jbc.M117.814913.

Barbieri, I., Tzelepis, K., Pandolfini, L., Shi, J., Millán-Zambrano, G., Robson, S.C., Aspris, D., Migliori, V., Bannister, A.J., and Han, N., et al. (2017). Promoter-bound METTL3 maintains myeloid leukaemia by m6A-dependent translation control. Nature *552*, 126-131. https://doi.org/10.1038/nature24678.

Barraud, P., Gato, A., Heiss, M., Catala, M., Kellner, S., and Tisné, C. (2019). Time-resolved NMR monitoring of tRNA maturation. Nature Communications *10*, 3373. https://doi.org/10.1038/s41467-019-11356-w.

Bauer, P.O., and Nukina, N. (2009). The pathogenic mechanisms of polyglutamine diseases and current therapeutic strategies. Journal of Neurochemistry *110*, 1737-1765. https://doi.org/10.1111/j.1471-4159.2009.06302.x.

Benn, C.L., Landles, C., Li, H., Strand, A.D., Woodman, B., Sathasivam, K., Li, S.-H., Ghazi-Noori, S., Hockly, E., and Faruque, S.M., et al. (2005). Contribution of nuclear and extranuclear polyQ to neurological phenotypes in mouse models of Huntington's disease. Human Molecular Genetics *14*, 3065-3078. https://doi.org/10.1093/hmg/ddi340.

Bennett, E.J., Shaler, T.A., Woodman, B., Ryu, K.-Y., Zaitseva, T.S., Becker, C.H., Bates, G.P., Schulman, H., and Kopito, R.R. (2007). Global changes to the ubiquitin system in Huntington's disease. Nature *448*, 704. https://doi.org/10.1038/nature06022.

Berendzen, K.M., Durieux, J., Shao, L.-W., Tian, Y., Kim, H., Wolff, S., Liu, Y., and Dillin, A. (2016). Neuroendocrine Coordination of Mitochondrial Stress Signaling and Proteostasis. Cell *166*, 1553-1563.e10. https://doi.org/10.1016/j.cell.2016.08.042.

Berger, I., Fitzgerald, D.J., and Richmond, T.J. (2004). Baculovirus expression system for heterologous multiprotein complexes. Nature Biotechnology *22*, 1583-1587. https://doi.org/10.1038/nbt1036.

Blersch, K.F., Burchert, J.-P., August, S.-C., Welp, L., Neumann, P., Köster, S., Urlaub, H., and Ficner, R. (2021). Structural model of the M7G46 Methyltransferase TrmB in complex with tRNA. RNA Biology, 1-14. https://doi.org/10.1080/15476286.2021.1925477.

Boccaletto, P., Machnicka, M.A., Purta, E., Piatkowski, P., Baginski, B., Wirecki, T.K., Crécy-Lagard, V. de, Ross, R., Limbach, P.A., and Kotter, A., et al. (2018). MODOMICS: a database of RNA modification pathways. 2017 update. Nucleic Acids Research *46*, D303-D307. https://doi.org/10.1093/nar/gkx1030.

Bock, T., Chen, W.-H., Ori, A., Malik, N., Silva-Martin, N., Huerta-Cepas, J., Powell, S.T., Kastritis, P.L., Smyshlyaev, G., and Vonkova, I., et al. (2014). An integrated approach for genome annotation of the eukaryotic thermophile Chaetomium thermophilum. Nucleic Acids Research *42*, 13525-13533. https://doi.org/10.1093/nar/gku1147.

Bohanna, I., Georgiou-Karistianis, N., and Egan, G.F. (2011). Connectivity-based segmentation of the striatum in Huntington's disease: Vulnerability of motor pathways. Neurobiology of Disease *42*, 475-481. https://doi.org/10.1016/j.nbd.2011.02.010.

Bohnsack, K.E., Höbartner, C., and Bohnsack, M.T. (2019). Eukaryotic 5-methylcytosine (m^5C) RNA Methyltransferases: Mechanisms, Cellular Functions, and Links to Disease. Genes *10*, 102. https://doi.org/10.3390/genes10020102.

Boivin, S., Kozak, S., and Meijers, R. (2013). Optimization of protein purification and characterization using Thermofluor screens. Protein Expression and Purification *91*, 192-206. https://doi.org/10.1016/j.pep.2013.08.002.

Boo, S.H., and Kim, Y.K. (2020). The emerging role of RNA modifications in the regulation of mRNA stability. Experimental and Molecular Medicine *52*, 400-408. https://doi.org/10.1038/s12276-020-0407-z.

Bykhovskaya, Y., Casas, K., Mengesha, E., Inbal, A., and Fischel-Ghodsian, N. (2004). Missense mutation in pseudouridine synthase 1 (PUS1) causes mitochondrial myopathy and sideroblastic anemia (MLASA). American Journal of Human Genetics *74*, 1303-1308. https://doi.org/10.1086/421530.

Cai, X.C., Kapilashrami, K., and Luo, M. (2016). Synthesis and Assays of Inhibitors of Methytransferases. Methods in Enzymology, 245-308.

Carlile, T.M., Rojas-Duran, M.F., Zinshteyn, B., Shin, H., Bartoli, K.M., and Gilbert, W.V. (2014). Pseudouridine profiling reveals regulated mRNA pseudouridylation in yeast and human cells. Nature *515*, 143-146. https://doi.org/10.1038/nature13802.

Caron, N.S., Dorsey, E.R., and Hayden, M.R. (2018). Therapeutic approaches to Huntington disease: from the bench to the clinic. Nature Reviews Drug Discovery *17*, 729. https://doi.org/10.1038/nrd.2018.133.

Carter, J.-M., Emmett, W., Mozos, I.R., Kotter, A., Helm, M., Ule, J., and Hussain, S. (2019). FICC-Seq: a method for enzyme-specified profiling of methyl-5-uridine in cellular RNA. Nucleic Acids Research. https://doi.org/10.1093/nar/gkz658.

Castello, A., Fischer, B., Frese, C.K., Horos, R., Alleaume, A.-M., Foehr, S., Curk, T., Krijgsveld, J., and Hentze, M.W. (2016). Comprehensive Identification of RNA-Binding Domains in Human Cells. Molecular Cell *63*, 696-710. https://doi.org/10.1016/j.molcel.2016.06.029.

Chan, C.T.Y., Pang, Y.L.J., Deng, W., Babu, I.R., Dyavaiah, M., Begley, T.J., and Dedon, P.C. (2012). Reprogramming of tRNA modifications controls the oxidative stress response by codon-biased translation of proteins. Nature Communications *3*, 937. https://doi.org/10.1038/ncomms1938.

Chan, P.P., and Lowe, T.M. (2009). GtRNAdb: a database of transfer RNA genes detected in genomic sequence. Nucleic Acids Research *37*, D93-D97. https://doi.org/10.1093/nar/gkn787.

Chang, Y.-H., Nishimura, S., Oishi, H., Kelly, V.P., Kuno, A., and Takahashi, S. (2018). TRMT2A is a novel cell cycle regulator that suppresses cell proliferation. Biochemical and Biophysical Research Communications. https://doi.org/10.1016/j.bbrc.2018.11.104.

Chatterjee, K., Nostramo, R.T., Wan, Y., and Hopper, A.K. (2018). tRNA dynamics between the nucleus, cytoplasm and mitochondrial surface: Location, location, location. Biochimica et Biophysica Acta (BBA) - Gene Regulatory Mechanisms *1861*, 373-386. https://doi.org/10.1016/j.bbagrm.2017.11.007.

Chen, V.B., Arendall, W. Bryan, III, Headd, J.J., Keedy, D.A., Immormino, R.M., Kapral, G.J., Murray, L.W., Richardson, J.S., and Richardson, D.C. (2010). MolProbity: all-atom structure validation for macromolecular crystallography. Acta Crystallographica Section D *66*, 12-21. https://doi.org/10.1107/S0907444909042073.

Chen, Z., Qi, M., Shen, B., Luo, G., Wu, Y., Li, J., Lu, Z., Zheng, Z., Dai, Q., and Wang, H. (2019). Transfer RNA demethylase ALKBH3 promotes cancer progression via induction of tRNA-derived small RNAs. Nucleic Acids Research *47*, 2533-2545. https://doi.org/10.1093/nar/gky1250.

Chendrimada, T.P., Gregory, R.I., Kumaraswamy, E., Norman, J., Cooch, N., Nishikura, K., and Shiekhattar, R. (2005). TRBP recruits the Dicer complex to Ago2 for microRNA processing and gene silencing. Nature *436*, 740-744. https://doi.org/10.1038/nature03868.

Cheng, Q.-Y., Xiong, J., Ma, C.-J., Dai, Y., Ding, J.-H., Liu, F.-L., Yuan, B.-F., and Feng, Y.-Q. (2020). Chemical tagging for sensitive determination of uridine modifications in RNA. Chemical Science *11*, 1878-1891. https://doi.org/10.1039/C9SC05094A.

Choe, B.K., and Taylor, M.W. (1972). Kinetics of synthesis and characterization of transfer RNA precursors in mammalian cells. Biochimica et Biophysica Acta (BBA) - Nucleic Acids and Protein Synthesis *272*, 275-287. https://doi.org/10.1016/0005-2787(72)90251-1.

Choudhury, S.A., Asefa, B., Webb, A., Ramotar, D., and Chow, T.Y.-K. (2007). Functional and genetic analysis of the Saccharomyces cerevisiae RNC1/TRM2: evidences for its involvement in DNA double-strand break repair. Molecular and Cellular Biochemistry *300*, 215-226. https://doi.org/10.1007/s11010-006-9386-1.

Chow, T.Y., and Resnick, M.A. (1987). Purification and characterization of an endo-exonuclease from Saccharomyces cerevisiae that is influenced by the RAD52 gene. Journal of Biological Chemistry *262*, 17659-17667.

Chujo, T., and Suzuki, T. (2012). Trmt61B is a methyltransferase responsible for 1-methyladenosine at position 58 of human mitochondrial tRNAs. RNA *18*, 2269-2276. https://doi.org/10.1261/rna.035600.112.

Cléry, A., Blatter, M., and Allain, F.H.T. (2008). RNA recognition motifs: boring? Not quite. Current Opinion in Structural Biology *18*, 290-298. https://doi.org/10.1016/j.sbi.2008.04.002.

Cléry, A., Sinha, R., Anczuków, O., Corrionero, A., Moursy, A., Daubner, G.M., Valcárcel, J., Krainer, A.R., and Allain, F.H.T. (2013). Isolated pseudo-RNA-recognition motifs of SR proteins can regulate splicing using a noncanonical mode of RNA recognition. Proceedings of the National Academy of Sciences *110*, E2802-E2811. https://doi.org/10.1073/pnas.1303445110.

Cong, R., Das, S., Ugrinova, I., Kumar, S., Mongelard, F., Wong, J., and Bouvet, P. (2012). Interaction of nucleolin with ribosomal RNA genes and its role in RNA polymerase I transcription. Nucleic Acids Research *40*, 9441-9454. https://doi.org/10.1093/nar/gks720.

Coussens, N.P., Kales, S.C., Henderson, M.J., Lee, O.W., Horiuchi, K.Y., Wang, Y., Chen, Q., Kuznetsova, E., Wu, J., and Chakka, S., et al. (2018). High-throughput screening with nucleosome substrate identifies small-molecule inhibitors of the human histone lysine methyltransferase NSD2. Journal of Biological Chemistry *293*, 13750-13765. https://doi.org/10.1074/jbc.RA118.004274.

Cowtan, K. (2006). The Buccaneer software for automated model building. Acta Crystallographica Section D *62*, 1002-1011. https://doi.org/10.1107/S0907444906022116.

Crotti, A., and Glass, C.K. (2015). The choreography of neuroinflammation in Huntington's disease. Trends in Immunology *36*, 364-373. https://doi.org/10.1016/j.it.2015.04.007.

Culver, B.P., Savas, J.N., Park, S.K., Choi, J.H., Zheng, S., Zeitlin, S.O., Yates, John R., III, and Tanese, N. (2012). Proteomic Analysis of Wild-type and Mutant Huntingtin-associated Proteins in Mouse Brains Identifies Unique Interactions and Involvement in Protein Synthesis *. Journal of Biological Chemistry *287*, 21599-21614. https://doi.org/10.1074/jbc.M112.359307.

Dai, W., Li, A., Yu, N.J., Nguyen, T., Leach, R.W., Wühr, M., and Kleiner, R.E. (2021). Activity-based RNA-modifying enzyme probing reveals DUS3L-mediated dihydrouridylation. Nature Chemical Biology. https://doi.org/10.1038/s41589-021-00874-8.

Davanloo, P., Sprinzl, M., Watanabe, K., Albani, M., and Kersten, H. (1979). Role of ribothymidine in the thermal stability of transfer RNA as monitored by proton magnetic resonance. Nucleic Acids Research *6*, 1571-1581. https://doi.org/10.1093/nar/6.4.1571.

Dominguez, C., and Allain, F.H.-T. (2006). NMR structure of the three quasi RNA recognition motifs (qRRMs) of human hnRNP F and interaction studies with Bcl-x G-tract RNA: a novel mode of RNA recognition. Nucleic Acids Research *34*, 3634-3645. https://doi.org/10.1093/nar/gkl488.

Dominissini, D., Moshitch-Moshkovitz, S., Schwartz, S., Salmon-Divon, M., Ungar, L., Osenberg, S., Cesarkas, K., Jacob-Hirsch, J., Amariglio, N., and Kupiec, M., et al. (2012). Topology of the human and mouse m6A RNA methylomes revealed by m6A-seq. Nature *485*, 201-206. https://doi.org/10.1038/nature11112.

Edelmann, F.T., Schlundt, A., Heym, R.G., Jenner, A., Niedner-Boblenz, A., Syed, M.I., Paillart, J.-C., Stehle, R., Janowski, R., and Sattler, M., et al. (2017). Molecular architecture and dynamics of ASH1 mRNA recognition by its mRNA-transport complex. Nature Structural and Molecular Biology *24*, 152 EP -. https://doi.org/10.1038/nsmb.3351.

Ellrichmann, G., Blusch, A., Fatoba, O., Brunner, J., Reick, C., Hayardeny, L., Hayden, M., Sehr, D., Winklhofer, K.F., and Saft, C., et al. (2017). Laquinimod treatment in the R6/2 mouse model. Scientific Reports *7*, 4947. https://doi.org/10.1038/s41598-017-04990-1.

Emsley, P., and Cowtan, K. (2004). Coot: model-building tools for molecular graphics. Acta Crystallographica Section D *60*, 2126-2132. https://doi.org/10.1107/S0907444904019158.

Etcheverry, T., Colby, D., and Guthrie, C. (1979). A precursor to a minor species of yeast $tRNA^{Ser}$ contains an intervening sequence. Cell *18*, 11-26. https://doi.org/10.1016/0092-8674(79)90349-0.

Evans, P. (2006). Scaling and assessment of data quality. Acta Crystallographica Section D *62*, 72-82. https://doi.org/10.1107/S0907444905036693.

Fan, H.-C., Ho, L.-I., Chi, C.-S., Chen, S.-J., Peng, G.-S., Chan, T.-M., Lin, S.-Z., and Harn, H.-J. (2014). Polyglutamine (PolyQ) Diseases: Genetics to Treatments. Cell Transplantation *23*, 441-458. https://doi.org/10.3727/096368914x678454.

Fisher, E.R., and Hayden, M.R. (2014). Multisource ascertainment of Huntington disease in Canada: Prevalence and population at risk. Movement Disorders *29*, 105-114. https://doi.org/10.1002/mds.25717.

Fleissner, E., and Borek, E. (1962). A new enzyme of RNA synthesis: RNA methylase. Proceedings of the National Academy of Sciences *48*, 1199-1203. https://doi.org/10.1073/pnas.48.7.1199.

Freed, E.F., Prieto, J.-L., McCann, K.L., McStay, B., and Baserga, S.J. (2012). NOL11, implicated in the pathogenesis of North American Indian childhood cirrhosis, is required for pre-rRNA transcription and processing. PLoS Genet *8*, e1002892-e1002892. https://doi.org/10.1371/journal.pgen.1002892.

French, S., and Wilson, K. (1978). On the treatment of negative intensity observations. Acta Crystallographica Section A *34*, 517-525. https://doi.org/10.1107/S0567739478001114.

Frye, M., and Watt, F.M. (2006). The RNA Methyltransferase Misu (NSun2) Mediates Myc-Induced Proliferation and Is Upregulated in Tumors. Current Biology *16*, 971-981. https://doi.org/10.1016/j.cub.2006.04.027.

Garriga-Canut, M., Agustín-Pavón, C., Herrmann, F., Sánchez, A., Dierssen, M., Fillat, C., and Isalan, M. (2012). Synthetic zinc finger repressors reduce mutant huntingtin expression in the brain of R6/2 mice. Proceedings of the National Academy of Sciences *109*, E3136-E3145. https://doi.org/10.1073/pnas.1206506109.

Gatchel, J.R., and Zoghbi, H.Y. (2005). Diseases of Unstable Repeat Expansion: Mechanisms and Common Principles. Nature Reviews Genetics *6*, 743. https://doi.org/10.1038/nrg1691.

Gautier, I., Tramier, M., Durieux, C., Coppey, J., Pansu, R.B., Nicolas, J.C., Kemnitz, K., and Coppey-Moisan, M. (2001). Homo-FRET microscopy in living cells to measure monomer-dimer transition of GFP-tagged proteins. Biophys J *80*, 3000-3008. https://doi.org/10.1016/S0006-3495(01)76265-0.

Giralt, A., Puigdellívol, M., Carretón, O., Paoletti, P., Valero, J., Parra-Damas, A., Saura, C.A., Alberch, J., and Ginés, S. (2011). Long-term memory deficits in Huntington's disease are associated with reduced CBP histone acetylase activity. Human Molecular Genetics *21*, 1203-1216. https://doi.org/10.1093/hmg/ddr552.

Go, C.D., Knight, J.D.R., Rajasekharan, A., Rathod, B., Hesketh, G.G., Abe, K.T., Youn, J.-Y., Samavarchi-Tehrani, P., Zhang, H., and Zhu, L.Y., et al. (2021). A proximity-dependent biotinylation map of a human cell. Nature *595*, 120-124. https://doi.org/10.1038/s41586-021-03592-2.

Gräslund, S., Sagemark, J., Berglund, H., Dahlgren, L.-G., Flores, A., Hammarström, M., Johansson, I., Kotenyova, T., Nilsson, M., and Nordlund, P., et al. (2008). The use of systematic N- and C-terminal deletions to promote production and structural studies of recombinant proteins. Protein Expression and Purification *58*, 210-221. https://doi.org/10.1016/j.pep.2007.11.008.

Gregersen, L.H., Schueler, M., Munschauer, M., Mastrobuoni, G., Chen, W., Kempa, S., Dieterich, C., and Landthaler, M. (2014). MOV10 Is a 5' to 3' RNA Helicase Contributing to UPF1 mRNA Target Degradation by Translocation along 3' UTRs. Molecular Cell *54*, 573-585. https://doi.org/10.1016/j.molcel.2014.03.017.

Griesche, N., Schilling, J., Weber, S., Rohm, M., Pesch, V., Matthes, F., Auburger, G., and Krauss, S. (2016). Regulation of mRNA Translation by MID1: A Common Mechanism of Expanded CAG Repeat RNAs. Frontiers in Cellular Neuroscience *10*. https://doi.org/10.3389/fncel.2016.00226.

Gu, X., Ivanetich, K.M., and Santi, D.V. (1996). Recognition of the T-Arm of tRNA by tRNA (m5U54)-Methyltransferase Is Not Sequence Specific. Biochemistry *35*, 11652-11659. https://doi.org/10.1021/bi9612125.

Gu, X., and Santi, D.V. (1991). The T-arm of tRNA is a substrate for tRNA (m5U54)-methyltransferase. Biochemistry *30*, 2999-3002. https://doi.org/10.1021/bi00226a003.

Guarguaglini, G., Battistoni, A., Pittoggi, C., Di Matteo, G., Di Fiore, B., and Lavia, P. (1997). Expression of the murine RanBP1 and Htf9-c genes is regulated from a shared bidirectional promoter during cell cycle progression. Biochemical Journal *325*, 277-286.

Gustafsson, C., and Björk, G.R. (1993). The tRNA-(m5U54)-methyltransferase of Escherichia coli is present in two forms in vivo, one of which is present as bound to tRNA and to a 3'-end fragment of 16 S rRNA. Journal of Biological Chemistry *268*, 1326-1331.

Gustafsson, C., Lindström, P.H., Hagervall, T.G., Esberg, K.B., and Björk, G.R. (1991). The trmA promoter has regulatory features and sequence elements in common with the rRNA P1 promoter family of Escherichia coli. Journal of Bacteriology *173*, 1757-1764. https://doi.org/10.1128/jb.173.5.1757-1764.1991.

Haag, S., Kretschmer, J., and Bohnsack, M.T. (2015). WBSCR22/Merm1 is required for late nuclear pre-ribosomal RNA processing and mediates N7-methylation of G1639 in human 18S rRNA. RNA *21*, 180-187. https://doi.org/10.1261/rna.047910.114.

Hasler, D., Lehmann, G., Murakawa, Y., Klironomos, F., Jakob, L., Grässer, F.A., Rajewsky, N., Landthaler, M., and Meister, G. (2016). The Lupus Autoantigen La Prevents Mis-channeling of tRNA Fragments into the Human MicroRNA Pathway. Molecular Cell *63*, 110-124. https://doi.org/10.1016/j.molcel.2016.05.026.

Hayano, T., Yanagida, M., Yamauchi, Y., Shinkawa, T., Isobe, T., and Takahashi, N. (2003). Proteomic Analysis of Human Nop56p-associated Pre-ribosomal Ribonucleoprotein Complexes. Journal of Biological Chemistry *278*, 34309-34319. https://doi.org/10.1074/jbc.M304304200.

Hayne, C.K., Schmidt, C.A., Haque, M.I., Matera, A.G., and Stanley, R.E. (2020). Reconstitution of the human tRNA splicing endonuclease complex: insight into the regulation of pre-tRNA cleavage. Nucleic Acids Research *48*, 7609-7622. https://doi.org/10.1093/nar/gkaa438.

Herzik, M.A., Wu, M., and Lander, G.C. (2019). High-resolution structure determination of sub-100 kDa complexes using conventional cryo-EM. Nature Communications *10*, 1032. https://doi.org/10.1038/s41467-019-08991-8.

Hicks, D.G., Janarthanan, B.R., Vardarajan, R., Kulkarni, S.A., Khoury, T., Dim, D., Budd, G.T., Yoder, B.J., Tubbs, R., and Schreeder, M.T., et al. (2010). The expression of TRMT2A, a novel cell cycle regulated protein, identifies a subset of breast cancer patients with HER2 over-expression that are at an increased risk of recurrence. BMC Cancer *10*, 108. https://doi.org/10.1186/1471-2407-10-108.

Ho, S.N., Hunt, H.D., Horton, R.M., Pullen, J.K., and Pease, L.R. (1989). Site-directed mutagenesis by overlap extension using the polymerase chain reaction. Gene *77*, 51-59. https://doi.org/10.1016/0378-1119(89)90358-2.

Hoang, C., and Ferré-D'Amaré, A.R. (2001). Cocrystal Structure of a tRNA Ψ55 Pseudouridine Synthase: Nucleotide Flipping by an RNA-Modifying Enzyme. Cell *107*, 929-939. https://doi.org/10.1016/S0092-8674(01)00618-3.

Hofacker, I.L. (2003). Vienna RNA secondary structure server. Nucleic Acids Research *31*, 3429-3431. https://doi.org/10.1093/nar/gkg599.

Hoogeveen, A.T., Willemsen, R., Meyer, N., Roolj, K.E., Roos, R.A., Ommen, G.-J.B., and Galjaard, H. (1993). Characterization and localization of the Huntington disease gene product. Human Molecular Genetics *2*, 2069-2073. https://doi.org/10.1093/hmg/2.12.2069.

Hopper, A.K., Furukawa, A.H., Pham, H.D., and Martin, N.C. (1982). Defects in modification of cytoplasmic and mitochondrial transfer RNAs are caused by single nuclear mutations. Cell *28*, 543-550. https://doi.org/10.1016/0092-8674(82)90209-4.

Hsiao, K., Zegzouti, H., and Goueli, S.A. (2016). Methyltransferase-Glo: a universal, bioluminescent and homogenous assay for monitoring all classes of methyltransferases. Epigenomics *8*, 321-339. https://doi.org/10.2217/epi.15.113.

Huntington, G. (1872). On chorea. Medical Surgery Reports *26*, 317-321.

Huttlin, E.L., Bruckner, R.J., Navarrete-Perea, J., Cannon, J.R., Baltier, K., Gebreab, F., Gygi, M.P., Thornock, A., Zarraga, G., and Tam, S., et al. (2021). Dual proteome-scale networks

reveal cell-specific remodeling of the human interactome. Cell *184*, 3022-3040.e28. https://doi.org/10.1016/j.cell.2021.04.011.

Huttlin, E.L., Bruckner, R.J., Paulo, J.A., Cannon, J.R., Ting, L., Baltier, K., Colby, G., Gebreab, F., Gygi, M.P., and Parzen, H., et al. (2017). Architecture of the human interactome defines protein communities and disease networks. Nature *545*, 505-509. https://doi.org/10.1038/nature22366.

Imami, K., Milek, M., Bogdanow, B., Yasuda, T., Kastelic, N., Zauber, H., Ishihama, Y., Landthaler, M., and Selbach, M. (2018). Phosphorylation of the Ribosomal Protein RPL12/uL11 Affects Translation during Mitosis. Molecular Cell *72*, 84-98.e9. https://doi.org/10.1016/j.molcel.2018.08.019.

Jain, A., and Vale, R.D. (2017). RNA phase transitions in repeat expansion disorders. Nature *546*, 243. https://doi.org/10.1038/nature22386.

Jäkel, S., Albig, W., Kutay, U., Bischoff, F.R., Schwamborn, K., Doenecke, D., and Görlich, D. (1999). The importin beta/importin 7 heterodimer is a functional nuclear import receptor for histone H1. EMBO Journal *18*, 2411-2423. https://doi.org/10.1093/emboj/18.9.2411.

Jia, G., Fu, Y., Zhao, X., Dai, Q., Zheng, G., Yang, Y., Yi, C., Lindahl, T., Pan, T., and Yang, Y.-G., et al. (2011). N6-Methyladenosine in nuclear RNA is a major substrate of the obesity-associated FTO. Nature Chemical Biology *7*, 885-887. https://doi.org/10.1038/nchembio.687.

Jiang, Y., Li, F., Wu, J., Shi, Y., and Gong, Q. (2017). Structural insights into substrate selectivity of ribosomal RNA methyltransferase RlmCD. PLoS ONE *12*, e0185226. https://doi.org/10.1371/journal.pone.0185226.

Jiang, Y., Wang, X., Bao, S., Guo, R., Johnson, D.G., Shen, X., and Li, L. (2010). INO80 chromatin remodeling complex promotes the removal of UV lesions by the nucleotide excision repair pathway. Proceedings of the National Academy of Sciences *107*, 17274-17279. https://doi.org/10.1073/pnas.1008388107.

Johansson, M.J.O., and Byström, A.S. (2002). Dual function of the tRNA(m(5)U54)methyltransferase in tRNA maturation. RNA *8*, 324-335.

Jonkhout, N., Tran, J., Smith, M.A., Schonrock, N., Mattick, J.S., and Novoa, E.M. (2017). The RNA modification landscape in human disease. RNA *23*, 1754-1769. https://doi.org/10.1261/rna.063503.117.

Jühling, F., Mörl, M., Hartmann, R.K., Sprinzl, M., Stadler, P.F., and Pütz, J. (2009). tRNAdb 2009: compilation of tRNA sequences and tRNA genes. Nucleic Acids Research *37*, D159-D162. https://doi.org/10.1093/nar/gkn772.

Jumper, J., Evans, R., Pritzel, A., Green, T., Figurnov, M., Ronneberger, O., Tunyasuvunakool, K., Bates, R., Žídek, A., and Potapenko, A., et al. (2021). Highly accurate protein structure prediction with AlphaFold. Nature *596*, 583-589. https://doi.org/10.1038/s41586-021-03819-2.

Kabsch, W. (2010). XDS. Acta Crystallographica Section D *66*, 125-132. https://doi.org/10.1107/S0907444909047337.

Kealey, J.T., Gu, X., and Santi, D.V. (1994). Enzymatic mechanism of tRNA (m5U54)methyltransferase. Biochimie *76*, 1133-1142. https://doi.org/10.1016/0300-9084(94)90042-6.

Keffer-Wilkes, L.C., Soon, E.F., and Kothe, U. (2020). The methyltransferase TrmA facilitates tRNA folding through interaction with its RNA-binding domain. Nucleic Acids Research. https://doi.org/10.1093/nar/gkaa548.

Keffer-Wilkes, L.C., Veerareddygari, G.R., and Kothe, U. (2016). RNA modification enzyme TruB is a tRNA chaperone. Proceedings of the National Academy of Sciences *113*, 14306-14311. https://doi.org/10.1073/pnas.1607512113.

Kelley, L.A., Mezulis, S., Yates, C.M., Wass, M.N., and Sternberg, M.J.E. (2015). The Phyre2 web portal for protein modelling, prediction and analysis. Nature Protocols *10*, 845-858. https://doi.org/10.1038/nprot.2015.053.

Kenny, P.J., Zhou, H., Kim, M., Skariah, G., Khetani, R.S., Drnevich, J., Arcila, M.L., Kosik, K.S., and Ceman, S. (2014). MOV10 and FMRP Regulate AGO2 Association with MicroRNA Recognition Elements. Cell Reports *9*, 1729-1741. https://doi.org/10.1016/j.celrep.2014.10.054.

Kersten, H., Albani, M., Männlein, E., Praisler, R., Wurmbach, P., and Nierhaus, K.H. (1981). On the Role of Ribosylthymine in Prokaryotic tRNA Function. European Journal of Biochemistry *114*, 451-456. https://doi.org/10.1111/j.1432-1033.1981.tb05166.x.

Khoddami, V., and Cairns, B.R. (2013). Identification of direct targets and modified bases of RNA cytosine methyltransferases. Nature Biotechnology *31*, 458-464. https://doi.org/10.1038/nbt.2566.

Kim, D.E., Chivian, D., and Baker, D. (2004). Protein structure prediction and analysis using the Robetta server. Nucleic Acids Research *32*, W526-W531. https://doi.org/10.1093/nar/gkh468.

Kimura, M., and Imamoto, N. (2014). Biological Significance of the Importin-β Family-Dependent Nucleocytoplasmic Transport Pathways. Traffic *15*, 727-748. https://doi.org/10.1111/tra.12174.

Knudsen, M., and Wiuf, C. (2010). The CATH database. Human Genomics *4*, 207-212. https://doi.org/10.1186/1479-7364-4-3-207.

Kordasiewicz, H.B., Stanek, L.M., Wancewicz, E.V., Mazur, C., McAlonis, M.M., Pytel, K.A., Artates, J.W., Weiss, A., Cheng, S.H., and Shihabuddin, L.S., et al. (2012). Sustained Therapeutic Reversal of Huntington's Disease by Transient Repression of Huntingtin Synthesis. Neuron *74*, 1031-1044. https://doi.org/10.1016/j.neuron.2012.05.009.

Kramer, K., Sachsenberg, T., Beckmann, B.M., Qamar, S., Boon, K.-L., Hentze, M.W., Kohlbacher, O., and Urlaub, H. (2014). Photo-cross-linking and high-resolution mass spectrometry for assignment of RNA-binding sites in RNA-binding proteins. Nature Methods *11*, 1064-1070. https://doi.org/10.1038/nmeth.3092.

Krendl, C., Shaposhnikov, D., Rishko, V., Ori, C., Ziegenhain, C., Sass, S., Simon, L., Müller, N.S., Straub, T., and Brooks, K.E., et al. (2017). GATA2/3-TFAP2A/C transcription factor network couples human pluripotent stem cell differentiation to trophectoderm with repression of pluripotency. Proceedings of the National Academy of Sciences *114*, E9579-E9588. https://doi.org/10.1073/pnas.1708341114.

Lafontaine, D.L.J. (2015). Noncoding RNAs in eukaryotic ribosome biogenesis and function. Nature Structural and Molecular Biology *22*, 11-19. https://doi.org/10.1038/nsmb.2939.

Laptev, I., Shvetsova, E., Levitskii, S., Serebryakova, M., Rubtsova, M., Bogdanov, A., Kamenski, P., Sergiev, P., and Dontsova, O. (2020). Mouse Trmt2B protein is a dual

specific mitochondrial metyltransferase responsible for m(5)U formation in both tRNA and rRNA. RNA Biology *17*, 441-450. https://doi.org/10.1080/15476286.2019.1694733.

Laskowski, R.A., MacArthur, M.W., Moss, D.S., and Thornton, J.M. (1993). PROCHECK: a program to check the stereochemical quality of protein structures. Journal of Applied Crystallography *26*, 283-291. https://doi.org/10.1107/S0021889892009944.

Lee, J.-M., Correia, K., Loupe, J., Kim, K.-H., Barker, D., Hong, E.P., Chao, M.J., Long, J.D., Lucente, D., and Vonsattel, J.P.G., et al. (2019). CAG Repeat Not Polyglutamine Length Determines Timing of Huntington's Disease Onset. Cell *178*, 887-900.e14. https://doi.org/10.1016/j.cell.2019.06.036.

Lee, J.Y., Lake, R.J., Kirk, J., Bohr, V.A., Fan, H.-Y., and Hohng, S. (2017). NAP1L1 accelerates activation and decreases pausing to enhance nucleosome remodeling by CSB. Nucleic Acids Research *45*, 4696-4707. https://doi.org/10.1093/nar/gkx188.

Lee, T.T., Agarwalla, S., and Stroud, R.M. (2004). Crystal Structure of RumA, an Iron-Sulfur Cluster Containing E. coli Ribosomal RNA 5-Methyluridine Methyltransferase. Structure *12*, 397-407. https://doi.org/10.1016/j.str.2004.02.009.

Lee, T.T., Agarwalla, S., and Stroud, R.M. (2005). A Unique RNA Fold in the RumA-RNA-Cofactor Ternary Complex Contributes to Substrate Selectivity and Enzymatic Function. Cell *120*, 599-611. https://doi.org/10.1016/j.cell.2004.12.037.

Lewis, C.J.T., Pan, T., and Kalsotra, A. (2017). RNA modifications and structures cooperate to guide RNA-protein interactions. Nature Reviews Molecular Cell Biology *18*, 202-210. https://doi.org/10.1038/nrm.2016.163.

Li, J., Wang, Y.-N., Xu, B.-S., Liu, Y.-P., Zhou, M., Long, T., Li, H., Dong, H., Nie, Y., and Chen, P.R., et al. (2020). Intellectual disability-associated gene ftsj1 is responsible for 2′-O-methylation of specific tRNAs. EMBO reports *21*, e50095. https://doi.org/10.15252/embr.202050095.

Li, Z., Michael, I.P., Zhou, D., Nagy, A., and Rini, J.M. (2013). Simple piggyBac transposon-based mammalian cell expression system for inducible protein production. Proceedings of the National Academy of Sciences *110*, 5004-5009. https://doi.org/10.1073/pnas.1218620110.

Li, Z., Wang, C., Wang, Z., Zhu, C., Li, J., Sha, T., Ma, L., Gao, C., Yang, Y., and Sun, Y., et al. (2019). Allele-selective lowering of mutant HTT protein by HTT–LC3 linker compounds. Nature *575*, 203-209. https://doi.org/10.1038/s41586-019-1722-1.

Liang, C., Xiong, K., Szulwach, K.E., Zhang, Y., Wang, Z., Peng, J., Fu, M., Jin, P., Suzuki, H.I., and Liu, Q. (2013). Sjoegren Syndrome Antigen B (SSB)/La Promotes Global MicroRNA Expression by Binding MicroRNA Precursors through Stem-Loop Recognition *. Journal of Biological Chemistry *288*, 723-736. https://doi.org/10.1074/jbc.M112.401323.

Lightfoot, H.L., and Hall, J. (2014). Endogenous polyamine function--the RNA perspective. Nucleic Acids Research *42*, 11275-11290. https://doi.org/10.1093/nar/gku837.

Lin, S., Liu, Q., Jiang, Y.-Z., and Gregory, R.I. (2019). Nucleotide resolution profiling of m7G tRNA modification by TRAC-Seq. Nature Protocols *14*, 3220-3242. https://doi.org/10.1038/s41596-019-0226-7.

Liu, F., Clark, W., Luo, G., Wang, X., Fu, Y., Wei, J., Wang, X., Hao, Z., Dai, Q., and Zheng, G., et al. (2016). ALKBH1-Mediated tRNA Demethylation Regulates Translation. Cell *167*, 816-828.e16. https://doi.org/10.1016/j.cell.2016.09.038.

Liu, J., Yue, Y., Han, D., Wang, X., Fu, Y., Zhang, L., Jia, G., Yu, M., Lu, Z., and Deng, X., et al. (2014). A METTL3-METTL14 complex mediates mammalian nuclear RNA N6-adenosine methylation. Nature Chemical Biology *10*, 93-95. https://doi.org/10.1038/nchembio.1432.

Loerch, S., and Kielkopf, C.L. (2015). Dividing and Conquering the Family of RNA Recognition Motifs: A Representative Case Based on hnRNP L. Journal of Molecular Biology *427*, 2997-3000. https://doi.org/10.1016/j.jmb.2015.06.009.

Lu, S., Wang, J., Chitsaz, F., Derbyshire, M.K., Geer, R.C., Gonzales, N.R., Gwadz, M., Hurwitz, D.I., Marchler, G.H., and Song, J.S., et al. (2020). CDD/SPARCLE: the conserved domain database in 2020. Nucleic Acids Research *48*, D265-D268. https://doi.org/10.1093/nar/gkz991.

Luo, X., Hsiao, H.-H., Bubunenko, M., Weber, G., Court, D.L., Gottesman, M.E., Urlaub, H., and Wahl, M.C. (2008). Structural and functional analysis of the E. coli NusB-S10 transcription antitermination complex. Molecular Cell *32*, 791-802. https://doi.org/10.1016/j.molcel.2008.10.028.

Ma, H., Wang, X., Cai, J., Dai, Q., Natchiar, S.K., Lv, R., Chen, K., Lu, Z., Chen, H., and Shi, Y.G., et al. (2019). N(6-)Methyladenosine methyltransferase ZCCHC4 mediates ribosomal RNA methylation. Nature Chemical Biology *15*, 88-94. https://doi.org/10.1038/s41589-018-0184-3.

Mach, M., Kersten, H., and Kersten, W. (1982). Regulation of tRNA methyltransferase activities by spermidine and putrescine. Inhibition of polyamine synthesis and tRNA methylation by α-methylornithine or 1,3-diaminopropan-2-ol in *Dictyostelium discoideum*. Biochemical Journal *202*, 153-162. https://doi.org/10.1042/bj2020153.

Madeira, F., Park, Y.m., Lee, J., Buso, N., Gur, T., Madhusoodanan, N., Basutkar, P., Tivey, A.R.N., Potter, S.C., and Finn, R.D., et al. (2019). The EMBL-EBI search and sequence analysis tools APIs in 2019. Nucleic Acids Research *47*, W636-W641. https://doi.org/10.1093/nar/gkz268.

Maggi, L.B., Kuchenruether, M., Dadey, D.Y.A., Schwope, R.M., Grisendi, S., Townsend, R.R., Pandolfi, P.P., and Weber, J.D. (2008). Nucleophosmin serves as a rate-limiting nuclear export chaperone for the Mammalian ribosome. Molecular and Cellular Biology *28*, 7050-7065. https://doi.org/10.1128/MCB.01548-07.

Malbec, L., Zhang, T., Chen, Y.-S., Zhang, Y., Sun, B.-F., Shi, B.-Y., Zhao, Y.-L., Yang, Y., and Yang, Y.-G. (2019). Dynamic methylome of internal mRNA N(7)-methylguanosine and its regulatory role in translation. Cell Research *29*, 927-941. https://doi.org/10.1038/s41422-019-0230-z.

Maraia, R.J., and Intine, R.V. (2002). La protein and its associated small nuclear and nucleolar precursor RNAs. Gene Expression *10*, 41-57.

Martin, J.L., and McMillan, F.M. (2002). SAM (dependent) I AM: the S-adenosylmethionine-dependent methyltransferase fold. Current Opinion in Structural Biology *12*, 783-793. https://doi.org/10.1016/S0959-440X(02)00391-3.

McCammon, M.T., and Parks, L.W. (1981). Inhibition of sterol transmethylation by S-adenosylhomocysteine analogs. Journal of Bacteriology *145*, 106-112. https://doi.org/10.1128/jb.145.1.106-112.1981.

McCampbell, A., Taylor, J.P., Taye, A.A., Robitschek, J., Li, M., Walcott, J., Merry, D., Chai, Y., Paulson, H., and Sobue, G., et al. (2000). CREB-binding protein sequestration by expanded polyglutamine. Human Molecular Genetics *9*, 2197-2202. https://doi.org/10.1093/hmg/9.14.2197.

Mei, L., Shen, C., Miao, R., Wang, J.-Z., Cao, M.-D., Zhang, Y.-S., Shi, L.-H., Zhao, G.-H., Wang, M.-H., and Wu, L.-S., et al. (2020). RNA methyltransferase NSUN2 promotes gastric cancer cell proliferation by repressing p57Kip2 by an m5C-dependent manner. Cell Death and Disease *11*, 270. https://doi.org/10.1038/s41419-020-2487-z.

Menon, R.P., Nethisinghe, S., Faggiano, S., Vannocci, T., Rezaei, H., Pemble, S., Sweeney, M.G., Wood, N.W., Davis, M.B., and Pastore, A., et al. (2013). The Role of Interruptions in polyQ in the Pathology of SCA1. PLOS Genetics *9*, e1003648. https://doi.org/10.1371/journal.pgen.1003648.

Mészáros, B., Erdős, G., and Dosztányi, Z. (2018). IUPred2A: context-dependent prediction of protein disorder as a function of redox state and protein binding. Nucleic Acids Research *46*, W329-W337. https://doi.org/10.1093/nar/gky384.

Meyer, K.D., Saletore, Y., Zumbo, P., Elemento, O., Mason, C.E., and Jaffrey, S.R. (2012). Comprehensive Analysis of mRNA Methylation Reveals Enrichment in 3′ UTRs and near Stop Codons. Cell *149*, 1635-1646. https://doi.org/10.1016/j.cell.2012.05.003.

Mi, H., Muruganujan, A., Casagrande, J.T., and Thomas, P.D. (2013). Large-scale gene function analysis with the PANTHER classification system. Nature Protocols *8*, 1551-1566. https://doi.org/10.1038/nprot.2013.092.

Mielcarek, M., Landles, C., Weiss, A., Bradaia, A., Seredenina, T., Inuabasi, L., Osborne, G.F., Wadel, K., Touller, C., and Butler, R., et al. (2013). HDAC4 Reduction: A Novel Therapeutic Strategy to Target Cytoplasmic Huntingtin and Ameliorate Neurodegeneration. PLOS Biology *11*, e1001717. https://doi.org/10.1371/journal.pbio.1001717.

Mohler, K., and Ibba, M. (2017). Translational fidelity and mistranslation in the cellular response to stress. Nature Microbiology *2*, 17117. https://doi.org/10.1038/nmicrobiol.2017.117.

Mohler, K., Mann, R., and Ibba, M. (2017). Isoacceptor specific characterization of tRNA aminoacylation and misacylation in vivo. Methods *113*, 127-131. https://doi.org/10.1016/j.ymeth.2016.09.003.

Monecke, T., Dickmanns, A., and Ficner, R. (2009a). Structural basis for m7G-cap hypermethylation of small nuclear, small nucleolar and telomerase RNA by the dimethyltransferase TGS1. Nucleic Acids Research *37*, 3865-3877. https://doi.org/10.1093/nar/gkp249.

Monecke, T., Dickmanns, A., Strasser, A., and Ficner, R. (2009b). Structure analysis of the conserved methyltransferase domain of human trimethylguanosine synthase TGS1. Acta Crystallographica Section D *65*, 332-338. https://doi.org/10.1107/S0907444909003102.

Murshudov, G.N., Skubak, P., Lebedev, A.A., Pannu, N.S., Steiner, R.A., Nicholls, R.A., Winn, M.D., Long, F., and Vagin, A.A. (2011). REFMAC5 for the refinement of macromolecular

crystal structures. Acta Crystallographica Section D *67*, 355-367. https://doi.org/10.1107/S0907444911001314.

Natchiar, S.K., Myasnikov, A.G., Kratzat, H., Hazemann, I., and Klaholz, B.P. (2017). Visualization of chemical modifications in the human 80S ribosome structure. Nature *551*, 472-477. https://doi.org/10.1038/nature24482.

Nedialkova, D.D., and Leidel, S.A. (2015). Optimization of Codon Translation Rates via tRNA Modifications Maintains Proteome Integrity. Cell *161*, 1606-1618. https://doi.org/10.1016/j.cell.2015.05.022.

Nguyen Ba, A.N., Pogoutse, A., Provart, N., and Moses, A.M. (2009). NLStradamus: a simple Hidden Markov Model for nuclear localization signal prediction. BMC Bioinformatics *10*, 202. https://doi.org/10.1186/1471-2105-10-202.

Niimi, T., Nureki, O., Yokogawa, T., Hayashi, N., Nishikawa, K., Watanabe, K., and Yokoyama, S. (1994). Recognition of the Anticodon Loop of tRNAIle 1 by Isoleucyl-tRNA Synthetase from Escherichia coli. Nucleosides and Nucleotides *13*, 1231-1237. https://doi.org/10.1080/15257779408012147.

Nollen, E.A.A., Garcia, S.M., van Haaften, G., Kim, S., Chavez, A., Morimoto, R.I., and Plasterk, R.H.A. (2004). Genome-wide RNA interference screen identifies previously undescribed regulators of polyglutamine aggregation. Proceedings of the National Academy of Sciences *101*, 6403-6408. https://doi.org/10.1073/pnas.0307697101.

Nordlund, M.E., Johansson, J.O., Pawel-Rammingen, U. von, and Byström, A.S. (2000). Identification of the TRM2 gene encoding the tRNA(m5U54)methyltransferase of Saccharomyces cerevisiae. RNA *6*, 844-860.

Ny, T., and Björk, G.R. (1977). Stringent regulation of the synthesis of a transfer ribonucleic acid biosynthetic enzyme: transfer ribonucleic acid(m5U)methyltransferase from Escherichia coli. Journal of Bacteriology *130*, 635-641. https://doi.org/10.1128/jb.130.2.635-641.1977.

Ou, X., Cao, J., Cheng, A., Peppelenbosch, M.P., and Pan, Q. (2019). Errors in translational decoding: tRNA wobbling or misincorporation? PLOS Genetics *15*, e1008017. https://doi.org/10.1371/journal.pgen.1008017.

Pan, T. (2013). Adaptive translation as a mechanism of stress response and adaptation. Annual Review of Genetics *47*, 121-137. https://doi.org/10.1146/annurev-genet-111212-133522.

Panjikar, S., Parthasarathy, V., Lamzin, V.S., Weiss, M.S., and Tucker, P.A. (2005). Auto-Rickshaw: an automated crystal structure determination platform as an efficient tool for the validation of an X-ray diffraction experiment. Acta Crystallographica Section D *61*, 449-457. https://doi.org/10.1107/S0907444905001307.

Panjikar, S., Parthasarathy, V., Lamzin, V.S., Weiss, M.S., and Tucker, P.A. (2009). On the combination of molecular replacement and single-wavelength anomalous diffraction phasing for automated structure determination. Acta Crystallographica Section D *65*, 1089-1097. https://doi.org/10.1107/S0907444909029643.

Pendleton, K.E., Chen, B., Liu, K., Hunter, O.V., Xie, Y., Tu, B.P., and Conrad, N.K. (2017). The U6 snRNA m(6)A Methyltransferase METTL16 Regulates SAM Synthetase Intron Retention. Cell *169*, 824-835.e14. https://doi.org/10.1016/j.cell.2017.05.003.

Percipalle, P., Clarkson, W.D., Kent, H.M., Rhodes, D., and Stewart, M. (1997). Molecular interactions between the importin α/β heterodimer and proteins involved in vertebrate

nuclear protein import11Edited by J. Karn. Journal of Molecular Biology *266*, 722-732. https://doi.org/10.1006/jmbi.1996.0801.

Pereira, M., Ribeiro, D.R., Pinheiro, M.M., Ferreira, M., Kellner, S., and Soares, A.R. (2021). m(5)U54 tRNA Hypomodification by Lack of TRMT2A Drives the Generation of tRNA-Derived Small RNAs. International Journal of Molecular Sciences *22*, 2941. https://doi.org/10.3390/ijms22062941.

Persson, B.C., Gustafsson, C., Berg, D.E., and Björk, G.R. (1992). The gene for a tRNA modifying enzyme, m5U54-methyltransferase, is essential for viability in Escherichia coli. Proceedings of the National Academy of Sciences *89*, 3995-3998. https://doi.org/10.1073/pnas.89.9.3995.

Pircs, K., Petri, R., Madsen, S., Brattås, P.L., Vuono, R., Ottosson, D.R., St-Amour, I., Hersbach, B.A., Matusiak-Brückner, M., and Lundh, S.H., et al. (2018). Huntingtin Aggregation Impairs Autophagy, Leading to Argonaute-2 Accumulation and Global MicroRNA Dysregulation. Cell Reports *24*, 1397-1406. https://doi.org/10.1016/j.celrep.2018.07.017.

Pöll, G., Braun, T., Jakovljevic, J., Neueder, A., Jakob, S., Woolford, John L., Jr., Tschochner, H., and Milkereit, P. (2009). rRNA maturation in yeast cells depleted of large ribosomal subunit proteins. PLoS ONE *4*, e8249-e8249. https://doi.org/10.1371/journal.pone.0008249.

Ponchon, L., Beauvais, G., Nonin-Lecomte, S., and Dardel, F. (2009). A generic protocol for the expression and purification of recombinant RNA in Escherichia coli using a tRNA scaffold. Nature Protocols *4*, 947. https://doi.org/10.1038/nprot.2009.67.

Ponchon, L., Catala, M., Seijo, B., El Khouri, M., Dardel, F., Nonin-Lecomte, S., and Tisné, C. (2013). Co-expression of RNA–protein complexes in Escherichia coli and applications to RNA biology. Nucleic Acids Research *41*, 150-150. https://doi.org/10.1093/nar/gkt576.

Powell, C.A., and Minczuk, M. (2020). TRMT2B is responsible for both tRNA and rRNA m^5U-methylation in human mitochondria. RNA Biology *17*, 451-462. https://doi.org/10.1080/15476286.2020.1712544.

Prieto, J.-L., and McStay, B. (2007). Recruitment of factors linking transcription and processing of pre-rRNA to NOR chromatin is UBF-dependent and occurs independent of transcription in human cells. Genes and Development *21*, 2041-2054. https://doi.org/10.1101/gad.436707.

Pütz, J., Florentz, C., Benseler, F., and Giegé, R. (1994). A single methyl group prevents the mischarging of a tRNA. Nature Structural Biology *1*, 580-582. https://doi.org/10.1038/nsb0994-580.

Ramesh, M., and Woolford, J.L. (2016). Eukaryote-specific rRNA expansion segments function in ribosome biogenesis. RNA *22*, 1153-1162. https://doi.org/10.1261/rna.056705.116.

Ranaei-Siadat, E., Fabret, C., Seijo, B., Dardel, F., Grosjean, H., and Nonin-Lecomte, S. (2013). RNA-methyltransferase TrmA is a dual-specific enzyme responsible for C(5)-methylation of uridine in both tmRNA and tRNA. RNA Biology *10*, 572-578. https://doi.org/10.4161/rna.24327.

Reilmann, R., Gordon, M.F., Anderson, K.E., Feigin, A., Tabrizi, S.J., Leavitt, B.R., Stout, J.C., Piccini, P., Borowsky, B., and Rynkowski, G., et al. (2019a). The Efficacy and Safety

Results of Laquinimod as a Treatment for Huntington Disease (LEGATO-HD) (S16.007). Neurology *92*, S16.007.

Reilmann, R., McGarry, A., Grachev, I.D., Savola, J.-M., Borowsky, B., Eyal, E., Gross, N., Langbehn, D., Schubert, R., and Wickenberg, A.T., et al. (2019b). Safety and efficacy of pridopidine in patients with Huntington's disease (PRIDE-HD): a phase 2, randomised, placebo-controlled, multicentre, dose-ranging study. The Lancet Neurology *18*, 165-176. https://doi.org/10.1016/S1474-4422(18)30391-0.

Rintala-Dempsey, A.C., and Kothe, U. (2017). Eukaryotic stand-alone pseudouridine synthases - RNA modifying enzymes and emerging regulators of gene expression? RNA Biology *14*, 1185-1196. https://doi.org/10.1080/15476286.2016.1276150.

Robert, X., and Gouet, P. (2014). Deciphering key features in protein structures with the new ENDscript server. Nucleic Acids Research *42*, 320-324. https://doi.org/10.1093/nar/gku316.

Rodrigues, F.B., Ferreira, J.J., and Wild, E.J. (2019). Huntington's Disease Clinical Trials Corner: June 2019. Journal of Huntington's Disease *8*, 363-371. https://doi.org/10.3233/JHD-199003.

Roux, K.J., Kim, D. in, and Burke, B. (2013). BioID: A Screen for Protein-Protein Interactions. Current protocols in protein science *74*, 19231–192314. https://doi.org/10.1002/0471140864.ps1923s74.

Rozov, A., Demeshkina, N., Khusainov, I., Westhof, E., Yusupov, M., and Yusupova, G. (2016). Novel base-pairing interactions at the tRNA wobble position crucial for accurate reading of the genetic code. Nature Communications *7*, 10457. https://doi.org/10.1038/ncomms10457.

Safra, M., Nir, R., Farouq, D., Vainberg Slutskin, I., and Schwartz, S. (2017a). TRUB1 is the predominant pseudouridine synthase acting on mammalian mRNA via a predictable and conserved code. Genome Research *27*, 393-406. https://doi.org/10.1101/gr.207613.116.

Safra, M., Sas-Chen, A., Nir, R., Winkler, R., Nachshon, A., Bar-Yaacov, D., Erlacher, M., Rossmanith, W., Stern-Ginossar, N., and Schwartz, S. (2017b). The m1A landscape on cytosolic and mitochondrial mRNA at single-base resolution. Nature *551*, 251-255. https://doi.org/10.1038/nature24456.

Santi, D.V., and Hardy, L.W. (1987). Catalytic mechanism and inhibition of tRNA (uracil-5-)methyltransferase: evidence for covalent catalysis. Biochemistry *26*, 8599-8606. https://doi.org/10.1021/bi00400a016.

Saudou, F., and Humbert, S. (2016). The Biology of Huntingtin. Neuron *89*, 910-926. https://doi.org/10.1016/j.neuron.2016.02.003.

Schindelin, J., Arganda-Carreras, I., Frise, E., Kaynig, V., Longair, M., Pietzsch, T., Preibisch, S., Rueden, C., Saalfeld, S., and Schmid, B., et al. (2012). Fiji: an open-source platform for biological-image analysis. Nature Methods *9*, 676-682. https://doi.org/10.1038/nmeth.2019.

Schöls, L., Bauer, P., Schmidt, T., Schulte, T., and Riess, O. (2004). Autosomal dominant cerebellar ataxias: clinical features, genetics, and pathogenesis. The Lancet Neurology *3*, 291-304. https://doi.org/10.1016/S1474-4422(04)00737-9.

Schosserer, M., Minois, N., Angerer, T.B., Amring, M., Dellago, H., Harreither, E., Calle-Perez, A., Pircher, A., Gerstl, M.P., and Pfeifenberger, S., et al. (2015). Methylation of

ribosomal RNA by NSUN5 is a conserved mechanism modulating organismal lifespan. Nature Communications *6*, 6158. https://doi.org/10.1038/ncomms7158.

Schultz, S.K.-L., and Kothe, U. (2020). tRNA elbow modifications affect the tRNA pseudouridine synthase TruB and the methyltransferase TrmA. RNA. https://doi.org/10.1261/rna.075473.120.

Schwartz, S., Bernstein, D.A., Mumbach, M.R., Jovanovic, M., Herbst, R.H., León-Ricardo, B.X., Engreitz, J.M., Guttman, M., Satija, R., and Lander, E.S., et al. (2014). Transcriptome-wide mapping reveals widespread dynamic-regulated pseudouridylation of ncRNA and mRNA. Cell *159*, 148-162. https://doi.org/10.1016/j.cell.2014.08.028.

Sears, R.M., May, D.G., and Roux, K.J. (2019). BioID as a Tool for Protein-Proximity Labeling in Living Cells. Methods in Molecular Biology *2012*, 299-313. https://doi.org/10.1007/978-1-4939-9546-2_15.

Sheldrick, G.M. (2002). Macromolecular phasing with SHELXE. Zeitschrift für Kristallographie - Crystalline Materials *217*, 644-650. https://doi.org/10.1524/zkri.217.12.644.20662.

Shenkman, M., Geva, M., Gershoni-Emek, N., Hayden, M.R., and Lederkremer, G.Z. (2021). Pridopidine reduces mutant huntingtin-induced endoplasmic reticulum stress by modulation of the Sigma-1 receptor. Journal of Neurochemistry *158*, 467-481. https://doi.org/10.1111/jnc.15366.

Shi, H., Chai, P., Jia, R., and Fan, X. (2020). Novel insight into the regulatory roles of diverse RNA modifications: Re-defining the bridge between transcription and translation. Molecular Cancer *19*, 78. https://doi.org/10.1186/s12943-020-01194-6.

Shirasaki, D.I., Greiner, E.R., Al-Ramahi, I., Gray, M., Boontheung, P., Geschwind, D.H., Botas, J., Coppola, G., Horvath, S., and Loo, J.A., et al. (2012). Network Organization of the Huntingtin Proteomic Interactome in Mammalian Brain. Neuron *75*, 41-57. https://doi.org/10.1016/j.neuron.2012.05.024.

Sibert, B.S., and Patton, J.R. (2011). Pseudouridine synthase 1: a site-specific synthase without strict sequence recognition requirements. Nucleic Acids Research *40*, 2107-2118. https://doi.org/10.1093/nar/gkr1017.

Sloan, K.E., Bohnsack, M.T., and Watkins, N.J. (2013). The 5S RNP Couples p53 Homeostasis to Ribosome Biogenesis and Nucleolar Stress. Cell Reports *5*, 237-247. https://doi.org/10.1016/j.celrep.2013.08.049.

Sloan, K.E., Warda, A.S., Sharma, S., Entian, K.-D., Lafontaine, D.L.J., and Bohnsack, M.T. (2017). Tuning the ribosome: The influence of rRNA modification on eukaryotic ribosome biogenesis and function. RNA Biology *14*, 1138-1152. https://doi.org/10.1080/15476286.2016.1259781.

Smith-Dijak, A.I., Sepers, M.D., and Raymond, L.A. (2019). Alterations in synaptic function and plasticity in Huntington disease. Journal of Neurochemistry *150*, 346-365. https://doi.org/10.1111/jnc.14723.

Steffan, J.S., Kazantsev, A., Spasic-Boskovic, O., Greenwald, M., Zhu, Y.Z., Gohler, H., Wanker, E.E., Bates, G.P., Housman, D.E., and Thompson, L.M. (2000). The Huntington's disease protein interacts with p53 and CREB-binding protein and represses transcription. Proceedings of the National Academy of Sciences *97*, 6763-6768. https://doi.org/10.1073/pnas.100110097.

Studier, F.W. (2005). Protein production by auto-induction in high-density shaking cultures. Protein Expression and Purification *41*, 207-234. https://doi.org/10.1016/j.pep.2005.01.016.

Suelves, N., Kirkham-McCarthy, L., Lahue, R.S., and Ginés, S. (2017). A selective inhibitor of histone deacetylase 3 prevents cognitive deficits and suppresses striatal CAG repeat expansions in Huntington's disease mice. Scientific Reports *7*, 6082. https://doi.org/10.1038/s41598-017-05125-2.

Sui, Y., and Wu, Z. (2007). Alternative Statistical Parameter for High-Throughput Screening Assay Quality Assessment. Journal of Biomolecular Screening *12*, 229-234. https://doi.org/10.1177/1087057106296498.

Sung, V.W., Iyer, R., Schilling, T., and Buzinec, P.N. (2017). Tetrabenazine Use in Patients With Huntington's Disease (HD) Chorea (P2.009). Neurology *88*, P2.009.

Suzuki, T. (2021). The expanding world of tRNA modifications and their disease relevance. Nature Reviews Molecular Cell Biology *22*, 375-392. https://doi.org/10.1038/s41580-021-00342-0.

Swaminathan, V., Kishore, A.H., Febitha, K.K., and Kundu, T.K. (2005). Human histone chaperone nucleophosmin enhances acetylation-dependent chromatin transcription. Molecular and Cellular Biology *25*, 7534-7545. https://doi.org/10.1128/MCB.25.17.7534-7545.2005.

Swinehart, W.E., Henderson, J.C., and Jackman, J.E. (2013). Unexpected expansion of tRNA substrate recognition by the yeast m1G9 methyltransferase Trm10. RNA *19*, 1137-1146. https://doi.org/10.1261/rna.039651.113.

Tabrizi, S.J., Leavitt, B.R., Landwehrmeyer, G.B., Wild, E.J., Saft, C., Barker, R.A., Blair, N.F., Craufurd, D., Priller, J., and Rickards, H., et al. (2019). Targeting Huntingtin Expression in Patients with Huntington's Disease. New England Journal of Medicine *380*, 2307-2316. https://doi.org/10.1056/NEJMoa1900907.

Tang, Z., Shu, H., Qi, W., Mahmood, N.A., Mumby, M.C., and Yu, H. (2006). PP2A Is Required for Centromeric Localization of Sgo1 and Proper Chromosome Segregation. Developmental Cell *10*, 575-585. https://doi.org/10.1016/j.devcel.2006.03.010.

Terwilliger, T. (2002). Automated structure solution, density modification and model building. Acta Crystallographica Section D *58*, 1937-1940. https://doi.org/10.1107/S0907444902016438.

The Gene Ontology Consortium (2021). The Gene Ontology resource: enriching a GOld mine. Nucleic Acids Research *49*, D325-D334. https://doi.org/10.1093/nar/gkaa1113.

Thongdee, N., Jaroensuk, J., Atichartpongkul, S., Chittrakanwong, J., Chooyoung, K., Srimahaeak, T., Chaiyen, P., Vattanaviboon, P., Mongkolsuk, S., and Fuangthong, M. (2019). TrmB, a tRNA m7G46 methyltransferase, plays a role in hydrogen peroxide resistance and positively modulates the translation of katA and katB mRNAs in Pseudomonas aeruginosa. Nucleic Acids Research *47*, 9271-9281. https://doi.org/10.1093/nar/gkz702.

Turi, Z., Lacey, M., Mistrik, M., and Moudry, P. (2019). Impaired ribosome biogenesis: mechanisms and relevance to cancer and aging. Aging *11*, 2512-2540. https://doi.org/10.18632/aging.101922.

Tzelepis, K., Rausch, O., and Kouzarides, T. (2019). RNA-modifying enzymes and their function in a chromatin context. Nature Structural & Molecular Biology *26*, 858-862. https://doi.org/10.1038/s41594-019-0312-0.

Uhlén, M., Fagerberg, L., Hallström, B.M., Lindskog, C., Oksvold, P., Mardinoglu, A., Sivertsson Ã…sa, Kampf C., Sjöstedt E., and Asplund A., et al. (2015). Tissue-based map of the human proteome. Science *347*, 1260419. https://doi.org/10.1126/science.1260419.

Urbonavičius, J., Jäger, G., and Björk, G.R. (2007). Amino acid residues of the Escherichia coli tRNA(m(5)U54)methyltransferase (TrmA) critical for stability, covalent binding of tRNA and enzymatic activity. Nucleic Acids Research *35*, 3297-3305. https://doi.org/10.1093/nar/gkm205.

Vagin, A., and Lebedev, A. (2015). MoRDa, an automatic molecular replacement pipeline. Acta Crystallographica Section A *71*, 19. https://doi.org/10.1107/S2053273315099672.

Vakiloroayaei, A., Shah, N.S., Oeffinger, M., and Bayfield, M.A. (2017). The RNA chaperone La promotes pre-tRNA maturation via indiscriminate binding of both native and misfolded targets. Nucleic Acids Research *45*, 11341-11355. https://doi.org/10.1093/nar/gkx764.

Van Haute, L., Lee, S.-Y., McCann, B.J., Powell, C.A., Bansal, D., Vasiliauskaitė, L., Garone, C., Shin, S., Kim, J.-S., and Frye, M., et al. (2019). NSUN2 introduces 5-methylcytosines in mammalian mitochondrial tRNAs. Nucleic Acids Research *47*, 8720-8733. https://doi.org/10.1093/nar/gkz559.

van Tran, N., Ernst, F.G.M., Hawley, B.R., Zorbas, C., Ulryck, N., Hackert, P., Bohnsack, K.E., Bohnsack, M.T., Jaffrey, S.R., and Graille, M., et al. (2019). The human 18S rRNA m6A methyltransferase METTL5 is stabilized by TRMT112. Nucleic Acids Research *47*, 7719-7733. https://doi.org/10.1093/nar/gkz619.

Venter, J.C., Adams, M.D., Myers, E.W., Li, P.W., Mural, R.J., Sutton, G.G., Smith, H.O., Yandell, M., Evans, C.A., and Holt, R.A., et al. (2001). The sequence of the human genome. Science *291*, 1304-1351. https://doi.org/10.1126/science.1058040.

Vilardo, E., Amman, F., Toth, U., Kotter, A., Helm, M., and Rossmanith, W. (2020). Functional characterization of the human tRNA methyltransferases TRMT10A and TRMT10B. Nucleic Acids Research. https://doi.org/10.1093/nar/gkaa353.

Voßfeldt, H., Butzlaff, M., Prüßing, K., Ní Chárthaigh, R.-A., Karsten, P., Lankes, A., Hamm, S., Simons, M., Adryan, B., and Schulz, J.B., et al. (2012). Large-Scale Screen for Modifiers of Ataxin-3-Derived Polyglutamine-Induced Toxicity in Drosophila. PLoS ONE *7*, e47452. https://doi.org/10.1371/journal.pone.0047452.

Walbott, H., Leulliot, N., Grosjean, H., and Golinelli-Pimpaneau, B. (2008). The crystal structure of Pyrococcus abyssi tRNA (uracil-54, C5)-methyltransferase provides insights into its tRNA specificity. Nucleic Acids Research *36*, 4929-4940. https://doi.org/10.1093/nar/gkn437.

Wang, H.-F., Takenaka, K., Nakanishi, A., and Miki, Y. (2011). BRCA2 and Nucleophosmin Coregulate Centrosome Amplification and Form a Complex with the Rho Effector Kinase ROCK2. Cancer Research *71*, 68-77. https://doi.org/10.1158/0008-5472.can-10-0030.

Wang, X., and Pan, T. (2016). Stress Response and Adaptation Mediated by Amino Acid Misincorporation during Protein Synthesis. Advances in Nutrition *7*, 773S-779S. https://doi.org/10.3945/an.115.010991.

Wang, X., Zhao, B.S., Roundtree, I.A., Lu, Z., Han, D., Ma, H., Weng, X., Chen, K., Shi, H., and He, C. (2015). N(6)-methyladenosine Modulates Messenger RNA Translation Efficiency. Cell *161*, 1388-1399. https://doi.org/10.1016/j.cell.2015.05.014.

Warkocki, Z., Krawczyk, P.S., Adamska, D., Bijata, K., Garcia-Perez, J.L., and Dziembowski, A. (2018). Uridylation by TUT4/7 Restricts Retrotransposition of Human LINE-1s. Cell *174*, 1537-1548. https://doi.org/10.1016/j.cell.2018.07.022.

Waterhouse, A., Bertoni, M., Bienert, S., Studer, G., Tauriello, G., Gumienny, R., Heer, F.T., de Beer, Tjaart A P, Rempfer, C., and Bordoli, L., et al. (2018). SWISS-MODEL: homology modelling of protein structures and complexes. Nucleic Acids Research *46*, 296-303. https://doi.org/10.1093/nar/gky427.

Watkins, N.J., Lemm, I., Ingelfinger, D., Schneider, C., Hoßbach, M., Urlaub, H., and Lührmann, R. (2004). Assembly and Maturation of the U3 snoRNP in the Nucleoplasm in a Large Dynamic Multiprotein Complex. Molecular Cell *16*, 789-798. https://doi.org/10.1016/j.molcel.2004.11.012.

Wernimont, A., and Edwards, A. (2009). In Situ Proteolysis to Generate Crystals for Structure Determination: An Update. PLoS ONE *4*, e5094. https://doi.org/10.1371/journal.pone.0005094.

Wertz, M.H., Mitchem, M.R., Pineda, S.S., Hachigian, L.J., Lee, H., Lau, V., Powers, A., Kulicke, R., Madan, G.K., and Colic, M., et al. (2020). Genome-wide In Vivo CNS Screening Identifies Genes that Modify CNS Neuronal Survival and mHTT Toxicity. Neuron *106*, 76-89.e8. https://doi.org/10.1016/j.neuron.2020.01.004.

Wiener, D., and Schwartz, S. (2021). The epitranscriptome beyond m6A. Nature Reviews Genetics *22*, 119-131. https://doi.org/10.1038/s41576-020-00295-8.

Winn, M.D., Ballard, C.C., Cowtan, K.D., Dodson, E.J., Emsley, P., Evans, P.R., Keegan, R.M., Krissinel, E.B., Leslie, A.G.W., and McCoy, A., et al. (2011). Overview of the CCP4 suite and current developments. Acta Crystallographica Section D *67*, 235-242. https://doi.org/10.1107/S0907444910045749.

Witkowska, D., and Rowińska-Żyrek, M. (2019). Biophysical approaches for the study of metal-protein interactions. Journal of Inorganic Biochemistry *199*, 110783. https://doi.org/10.1016/j.jinorgbio.2019.110783.

Wolin, S.L. (2016). Two for the price of one: RNA modification enzymes as chaperones. Proceedings of the National Academy of Sciences *113*, 14176-14178. https://doi.org/10.1073/pnas.1617402113.

Wolin, S.L., and Cedervall, T. (2002). The La Protein. Annual Review of Biochemistry *71*, 375-403. https://doi.org/10.1146/annurev.biochem.71.090501.150003.

Wong, Y.C., and Holzbaur, E.L.F. (2014). The regulation of autophagosome dynamics by huntingtin and HAP1 is disrupted by expression of mutant huntingtin, leading to defective cargo degradation. Journal of Neuroscience *34*, 1293-1305. https://doi.org/10.1523/JNEUROSCI.1870-13.2014.

Xiang, Y., Laurent, B., Hsu, C.-H., Nachtergaele, S., Lu, Z., Sheng, W., Xu, C., Chen, H., Ouyang, J., and Wang, S., et al. (2017). RNA m6A methylation regulates the ultraviolet-induced DNA damage response. Nature *543*, 573-576. https://doi.org/10.1038/nature21671.

Xie, Y., Yao, L., Yu, X., Ruan, Y., Li, Z., and Guo, J. (2020). Action mechanisms and research methods of tRNA-derived small RNAs. Signal Transduction and Targeted Therapy *5*, 109. https://doi.org/10.1038/s41392-020-00217-4.

Yan, Y., Di Zhang, Zhou, P., Li, B., and Huang, S.-Y. (2017). HDOCK: a web server for protein–protein and protein–DNA/RNA docking based on a hybrid strategy. Nucleic Acids Research *45*, W365-W373. https://doi.org/10.1093/nar/gkx407.

Yang, X., Yang, Y., Sun, B.-F., Chen, Y.-S., Xu, J.-W., Lai, W.-Y., Li, A., Wang, X., Bhattarai, D.P., and Xiao, W., et al. (2017). 5-methylcytosine promotes mRNA export - NSUN2 as the methyltransferase and ALYREF as an m(5)C reader. Cell Research *27*, 606-625. https://doi.org/10.1038/cr.2017.55.

Yankova, E., Blackaby, W., Albertella, M., Rak, J., Braekeleer, E. de, Tsagkogeorga, G., Pilka, E.S., Aspris, D., Leggate, D., and Hendrick, A.G., et al. (2021). Small-molecule inhibition of METTL3 as a strategy against myeloid leukaemia. Nature *593*, 597-601. https://doi.org/10.1038/s41586-021-03536-w.

Youkharibache, P., Veretnik, S., Li, Q., Stanek, K.A., Mura, C., and Bourne, P.E. (2019). The Small β-Barrel Domain: A Survey-Based Structural Analysis. Structure *27*, 6-26. https://doi.org/10.1016/j.str.2018.09.012.

Zeitlin, S., Liu, J.-P., Chapman, D.L., Papaioannou, V.E., and Efstratiadis, A. (1995). Increased apoptosis and early embryonic lethality in mice nullizygous for the Huntington's disease gene homologue. Nature Genetics *11*, 155-163. https://doi.org/10.1038/ng1095-155.

Zhang, K., Lentini, J.M., Prevost, C.T., Hashem, M.O., Alkuraya, F.S., and Fu, D. (2020). An intellectual disability-associated missense variant in TRMT1 impairs tRNA modification and reconstitution of enzymatic activity. Human Mutation *41*, 600-607. https://doi.org/10.1002/humu.23976.

Zhang, S., Binari, R., Zhou, R., and Perrimon, N. (2010). A genomewide RNA interference screen for modifiers of aggregates formation by mutant Huntingtin in Drosophila. Genetics *184*, 1165-1179. https://doi.org/10.1534/genetics.109.112516.

Zhao, X., and Horne, D.A. (1997). The Role of Cysteine Residues in the Rearrangement of Uridine to Pseudouridine Catalyzed by Pseudouridine Synthase I. Journal of Biological Chemistry *272*, 1950-1955. https://doi.org/10.1074/jbc.272.3.1950.

Zheng, G., Dahl, J.A., Niu, Y., Fedorcsak, P., Huang, C.-M., Li, C.J., Vågbø, C.B., Shi, Y., Wang, W.-L., and Song, S.-H., et al. (2013). ALKBH5 is a mammalian RNA demethylase that impacts RNA metabolism and mouse fertility. Molecular Cell *49*, 18-29. https://doi.org/10.1016/j.molcel.2012.10.015.

Zhong, S., Li, H., Bodi, Z., Button, J., Vespa, L., Herzog, M., and Fray, R.G. (2008). MTA Is an Arabidopsis Messenger RNA Adenosine Methylase and Interacts with a Homolog of a Sex-Specific Splicing Factor. The Plant Cell *20*, 1278-1288. https://doi.org/10.1105/tpc.108.058883.

Zhong, W., Koay, A., Ngo, A., Li, Y., Nah, Q., Wong, Y.H., Chionh, Y.H., Ng, H.Q., Koh-Stenta, X., and Poulsen, A., et al. (2019). Targeting the Bacterial Epitranscriptome for Antibiotic Development: Discovery of Novel tRNA-(N1G37) Methyltransferase (TrmD) Inhibitors. ACS Infectious Diseases. https://doi.org/10.1021/acsinfecdis.8b00275.

Acknowledgements

“The whole is greater than the sum of its parts”. In this spirit I want to thank the people that made this work possible. First and foremost, I would like to express my gratitude to Dierk Niessing for giving me the opportunity to carry out my PhD thesis in his group. I am truly thankful for his great mentorship, supportive and encouraging advice, and his believe in me, even when I doubted myself. Thanks to all members of my Thesis Advisory Committee, Dierk Niessing, Kamyar Hadian, Giulia Rossetti, Aaron Voigt and Roberst Janowski for constructive discussions, suggestions and for sharing their scientific perspective. Moreover, I would like to thank my collaboration partners, especially Aaron Voigt, who shared his vision and incredible excitement about TRMT2A. Thanks to Irmi for her help with cellular experiments. A huge thanks goes to Michael and Giulia for sharing their bioinformatics expertise and *in silico* predictions. Thanks to Luisa, Monika and Henning for the fruitful collaboration on crosslinking and mass spectrometry. Additionally, I would like to thank Steffi and Anne for a great collaboration on the BioID and Co-IP project. Thanks to André for ITC support and Kenji for very useful advice on the enzymatic assay. I am very grateful for the helpful feedback on my thesis from Lena, Jana, Sabrina and Tom.

Importantly, I would like to thank former and present members of the Niessing group at HMGU in Munich. Annika, Jana and Simone for helping me with my first steps in the lab. Elena for her generous and patient supervision. Rob for mentoring and offering me insights into the world of crystallography. Marcel for his help in the BioID project. Lena and Sabrina for lively discussions and support with cell culture work. Arun for challenging me on the TRMT2A project. My student Marina for her assistance and patience. Vera and Simi for technical and administrative support; without them the lab would not run as well as it does. The relaxed working atmosphere, countless coffee breaks together and gatherings outside the lab made this time a whole lot of fun! I want to extend my thank you to the Ulm University Niessing group: Tom for his advice regarding methyltransferases, Wieland for help with Biacore, Anne for administrative support, as well as Sandra and Thomas for discussions and advice. I would like to thank HMGU, especially the STB members for a truly memorable time amongst working colleagues and friends. Not to forget skiing retreats and culinary adventures.

Thanks to my friends Dominik, Kyra, Laura, Philipp, Daria, Till, Anja, Charlotte, Chris and Conny, for sitting in the same boat and for motivational, cheerful speeches. A heartfelt thanks goes to Katharina, who showed me the importance of little achievements. Finally, I wish to thank my family: To my sister Brigitte for always standing by me. To my parents Johanna and Max, as well as to my grandparents, for their love and unconditional support. To my in-law family for their encouraging thoughts. Importantly, a deep-felt thank you to Ankur for his patience and incontestable believe in me throughout the years.